

**Femtosecond spectroscopy of charge-transfer  
dynamics in self-assembled Pd(II) based  
donor-acceptor/host-guest cages and  
heterobinuclear alkyne-bridged  
W(II)-Ru(II) and W(II)-Ir(III) complexes**

**Dissertation**

for the award of the degree

**"Doctor rerum naturalium"**

(Dr.rer.nat.)

of the Georg-August-Universität Göttingen

within the doctoral program chemistry

of the Georg-August University School of Science (GAUSS)

submitted by

**Jan-Hendrik Georg Günther Borter**

from Hannover (germany)

Göttingen, 2023

## **Thesis Committee**

Prof. Dr. Dirk Schwarzer  
Dynamics at surfaces  
Max-Planck-institute for multidisciplinary sciences (MPI)  
Institute for physical chemistry (IPC)  
Georg-August-Universität Göttingen

Prof. Dr. Sven Schneider  
Institute for inorganic chemistry (IAC)  
Georg-August-university Göttingen

Prof. Dr. Inke Siewert  
Institute for inorganic chemistry (IAC)  
Georg-August-university Göttingen

## **Members of the Examination Board**

Reviewer:

Prof. Dr. Dirk Schwarzer  
Dynamics at surfaces  
Max-Planck-institute for multidisciplinary sciences (MPI)  
Institute for physical chemistry (IPC)  
Georg-August-Universität Göttingen

Second Reviewer:

Prof. Dr. Sven Schneider  
Institute for inorganic chemistry (IAC)  
Georg-August-university Göttingen

Further members of the Examination Board:

Prof. Dr. Inke Siewert  
Institute for inorganic chemistry (IAC)  
Georg-August-university Göttingen

Prof. Dr. Franc Meyer  
Institute for inorganic chemistry (IAC)  
Georg-August-university Göttingen

Prof. Dr. Martin Suhm  
Institute for physical chemistry (IPC)  
Georg-August-Universität Göttingen

Dr. Oliver Bünermann  
Institute for physical chemistry (IPC)  
Georg-August-Universität Göttingen

Date of the oral examination: 04.08.2023

「人は何かの犠牲なしに何も得ることはできない。  
何かを得るためには同等の代価が必要になる。  
それが、錬金術における『等価交換』の原則だ。  
その頃僕らは、それが世界の真実だと信じていた」

**“hito wa nanika no gisei nashi ni, nani mo eru koto wa dekinai.  
nanika wo eru tame ni wa, doutou no daika ga hitsuyou ni naru.  
sore ga, renkinjutsu ni okeru “toukakoukan” no gensoku da.  
sono koro, bokura wa sore ga sekai no shinjitsu da to shinjiteita.”**

**“One cannot obtain anything without first sacrificing something.  
In order to obtain anything something of equal value is required.  
That is the principle of equivalent exchange in alchemy.  
At that time we believed this to be the true way of the world.”**

Alphonse Elric, Fullmetal alchemist



## Table of contents

1	Abstract .....	1
2	Theory.....	3
2.1	Molecular dynamics and spectroscopy .....	4
2.1.1	Matter-radiation interaction .....	4
2.1.2	Relaxation dynamics following electronic excitation .....	5
2.1.3	Charge-transfer transitions .....	7
2.1.4	Infrared spectroscopy.....	8
2.1.5	Pump-probe spectroscopy .....	11
2.1.6	Laser .....	13
2.2	Nonlinear optics .....	15
2.2.1	Radiation induced polarization.....	15
2.2.2	Sum frequency, second and fourth harmonic generation (SFG, SHG, FHG) .....	16
2.2.3	difference frequency generation (DFG) .....	17
2.2.4	phase matching condition .....	17
2.2.5	Self-focussing, -defocussing and -phase modulation .....	18
2.2.6	White light continuum generation (WLG).....	18
2.2.7	Tunable optical parametric amplifier (OPA).....	19
3	Experimental setup.....	21
3.1	Overview.....	22
3.2	UV/vis-pump-UV/vis-probe spectroscopy setup.....	23
3.2.1	General setup .....	23
3.2.2	Measurement area .....	25
3.2.3	Pump option 1: linear SHG/THG setup.....	26
3.2.4	Pump option 2: OPA + frequency mixer .....	28
3.2.5	Electronic control and synchronization.....	31
3.3	UV/vis-pump-midIR-probe spectroscopy setup .....	32
3.3.1	General setup .....	32
3.3.2	SHG/THG with external group velocity correction.....	33
3.3.3	CPA.....	34
3.3.4	OPA.....	37
3.3.5	Detection .....	38
3.3.6	Electronic control and synchronization.....	40
3.4	Sample cells .....	41
3.5	Data acquisition and processing.....	43
3.5.1	Time-resolved UV/vis measurement.....	43

3.5.2	Time-resolved midIR measurement.....	44
3.5.3	data interpretation .....	46
4	Projects .....	49
4.1	Project 1: donor-acceptor charge-transfer in self-assembling Pd(II) complexes.....	51
4.1.1	Introduction .....	51
4.1.2	Previous work on the PTZ ligand.....	52
4.1.3	Phenothiazine-fluorenone-donor-acceptor cage .....	54
4.1.4	Triphenylamine-fluorenone-donor-acceptor cage .....	68
4.1.5	Phenothiazine-anthraquinone-host-guest cage .....	76
4.1.6	Conclusion project 1 .....	83
4.2	Project: metal-to-metal charge-transfer and vibrational relaxation of carbonyl ligands in tungsten-alkyne complexes OC-W(II)-L, OC-W(II)-L-Ru(II)(bpy) <sub>2</sub> PF <sub>6</sub> and OC-W(II)-L-Ir(III)(ppy) <sub>2</sub> 85	
4.2.1	Dewar-Chatt-Duncanson model .....	86
4.2.2	Mononuclear OC-W-L complex.....	88
4.2.3	Heterobinuclear [OC-W-L-Ru(bpy) <sub>2</sub> ] <sup>+</sup> complex .....	97
4.2.4	Heterobinuclear OC-W-L-Ir(ppy) <sub>2</sub> complex.....	108
5	Appendix .....	113
6	References .....	115
7	Acknowledgements.....	119
8	Curriculum vitae.....	121
9	Publications.....	121







# 1 Abstract

Using femtosecond UV/vis-pump-UV/vis-probe and -midIR-probe absorption spectroscopy the charge-transfer dynamics of self-assembling donor-acceptor Pd(II) coordination cages and heterobinuclear alkyne-bridged W(II)-Ru(II) and W(II)-Ir(III) complexes were investigated.

The cages consisted of ligands with the following chromophore backbones:

- Phenothiazine (PTZ)-donor and fluorenone (FLO)-acceptor
- Triphenylamine (TPA)-donor and fluorenone (FLO)-acceptor
- Phenothiazine (PTZ)-donor/host and anthraquinone (ANQ)-acceptor/guest

The first two complexes both consisted of donor and acceptor ligands forming a cage molecule, the third complex was a bare donor cage built around the acceptor as a host-guest compound. A general pattern was discovered for all of them: photoexcitation of specifically the donor created the donor  $S_1$  state, from which charge-transfer processes lead to the generation of a short-lived donor radical cation  $D^{\bullet+}$  as was deduced from the time-resolved UV/vis spectra, where bands similar to a chemically oxidized donor cage  $[Pd_2D_4]^{4+}$  were observed. Those bands decay with at least two different time constants indicating multiple charge-transfer partners. For the donor-acceptor cages three time constants with  $\tau_1 \approx 1$  ps,  $\tau_2 \approx 100$  ps and  $\tau_3 > 1$  ns were attributed to a ligand-to-metal charge-transfer (LMCT) from donor to Pd(II) and two donor-acceptor charge-transfers (DACT) from donor to acceptor that were assigned to a CT towards an acceptor in cis, the other in trans position to the excited donor. The acceptor radical anion  $A^{\bullet-}$  was identified via time-resolved midIR spectroscopy, where, despite practically pure donor excitation, both donor and acceptor bleaches as well as excited state peaks, that were assigned to  $D^{\bullet+}$  and  $A^{\bullet-}$  via DFT calculations and spectra of the chemically oxidized/reduced analogues, appeared simultaneously. For the host-guest cage a CT between donor and acceptor was observed as well, however, the  $A^{\bullet-}$  was only identified in the time-resolved UV/vis spectra and time-resolved midIR measurements were not possible because the compound was not soluble in any solvent with sufficient IR transparency. The ratio of LMCT to DACT was 60:40 for the PTZ-FLO cage, 50:50 for the TPA-FLO cage and for the PTZ-ANQ-host-guest cage 56:44.

The heterobinuclear tungsten complexes both showed ultrafast generation of a triplet metal-to-ligand charge-transfer state ( $^3MLCT$ ) upon photoexcitation that was not converted into a metal-to-metal charge-transfer (MMCT) given the small blue-shift in the time-resolved midIR spectra compared to the large shift in the FTIR spectra upon oxidation, but most likely led to a slight reduction of electron density at the W(II). Subsequent relaxation to the electronic ground state within about 60 ps resulted in the vibrational excitation of the anharmonic carbonyl stretching vibration, which was immediately achieved in the mononuclear tungsten complex due to ultrafast internal conversion. Additionally, in the W(II)-Ru(II) complex a far red shifted peak was observed that could not be safely identified, but is assumed to stem from a side-on coordinated carbonyl.



## 2 Theory

In order to be able to understand the results of time-resolved UV/vis and midIR spectroscopy, a deep understanding of the interactions between matter and electromagnetic radiation, molecular electronic structures and relaxation dynamics of their excited states as well as the experimental setup is necessary as the spectra can become rather complex. Therefore, the following chapters will cover the basics of molecular spectroscopy (chapter 2.1.1), the most common relaxation processes following electronic excitation (chapter 2.1.2) and frequently observed electronic transitions in transition metal complexes (chapter 2.1.3). In the next chapters the necessary information to interpret data gained from infrared (chapter 2.1.4) and pump-probe absorption spectroscopy (chapter 2.1.5) are presented followed by a brief introduction to the formation and properties of a laser beam (chapter 2.1.6), which are needed to create an array of effects used in time-resolved spectroscopy. Those effects are summarized under the subject of nonlinear optics (chapter 2.2) and will be covered in the next chapters starting with the foundation, radiation induced polarization in matter (chapter 2.2.1), followed by the sum frequency and difference frequency generation (chapters 2.2.2 and 2.2.3) and the basics on white light continuum generation (chapter 2.2.4-2.2.6). Finally, a short introduction to the optical parametric amplification (chapter 2.2.7) is provided, which will, however, be discussed in much more detail in the following experimental section.

## 2.1 Molecular dynamics and spectroscopy

The interaction of matter with radiation with well-defined properties can provide a lot of information about the latter. For this reason, spectroscopic methods are probably the most wide spread techniques to analyse materials of any kind. Many of those complex interactions and subsequent dynamics are covered in the following chapters.

### 2.1.1 Matter-radiation interaction

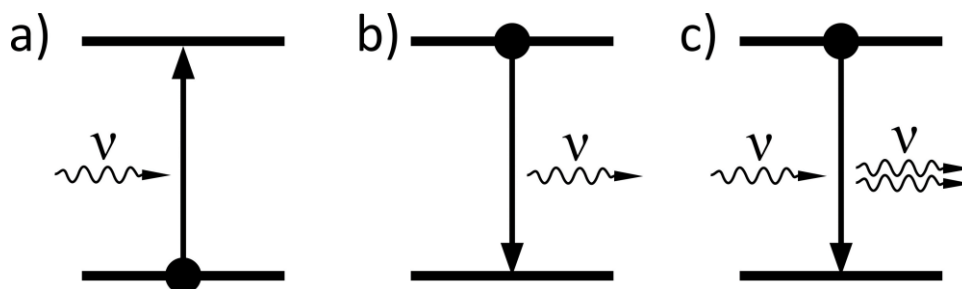


Fig. 1: three basic types of matter-radiation interaction. A) absorption, b) spontaneous emission, c) stimulated emission.

In order to investigate photoinduced dynamics, whether they are induced by natural sources like sunlight regarding photovoltaic applications or artificial ones like laser light used to read and write data from data carriers, spectroscopic methods are the most straight forward approach since they specifically deal with the interaction of matter and electromagnetic (EM) radiation.

According to Bohr's frequency condition<sup>[1]</sup>, matter can absorb a photon only if its energy

$$E_{\text{ph}} = h\nu = \frac{hc}{\lambda} = hc_{\text{ph}}\tilde{\nu} \quad \text{eq. 001}$$

with  $h$  as the Planck constant,  $\nu$  as the frequency,  $\lambda$  the wavelength and  $\tilde{\nu}$  as the wavenumber of the photon, equals the difference between the energy of two states

$$\Delta E = E_2 - E_1 = E_{\text{ph}} \quad \text{eq. 002}$$

the atoms, molecules or composites thereof that constitute the matter can assume. By absorbing a suitable photon, the system is transitioning from the energetically lower to the higher of the two states. On the other hand, a photon can be emitted upon transition from an energetically higher to a lower state obeying eq. 002, which can happen spontaneously or be stimulated by irradiating the system with a photon with the same energy. While a spontaneously emitted photon has random polarization and phase position and is released in a random direction, the properties of a photon from stimulated emission equal those of the stimulant. This characteristic is essential for the operation of a laser.

Absorption, spontaneous emission and stimulated emission are the three basic types of interaction between matter and electromagnetic radiation. Spectroscopic methods that emerge from these interactions use Bohr's frequency condition, the connection between photon energy and transitions between states, to examine the properties of a specific matter since the energy of its states and therefore also their energy differences are characteristic for a molecular system or structures within the system. By measuring the photon energies at which an absorption occurs, these systems or subsystems can be identified.

A system can perform many different transitions. For each type of transition, a typical range of photon absorption/emission energies can be determined. Ultraviolet (UV) to visible (vis) radiation can be used for transitions of the electronic system in a molecule, while infrared (IR) radiation generally induces transitions in molecular vibrations. Electronic transitions can create interesting properties in a molecule, most notably here is the separation of charges, but they often effect large sections of a molecule, which is why they can be rather unspecific to identify the responsible functional groups. The range of middle infrared (midIR) especially, on the other hand, covers vibrational transitions of such functional groups found in many metal organic complexes like carbonyl ( $-\text{C}=\text{O}$ ), cyano ( $-\text{C}\equiv\text{N}$ ) and hydroxy ( $-\text{O}-\text{H}$ ) groups among many others. Accordingly, those groups and sections of a molecule connected to them can be probed in a more isolated way to gain a more refined picture of structures and other properties of a molecule. By measuring the energy and the amount of light that is absorbed or emitted from a sample

There are several different spectroscopic methods that can be classified by the type of transitions that are observed or the range of the energy of the photons that correlates with it and their mode of measurement among others. The following chapters will be limited to absorption spectroscopy with UV/vis and midIR radiation.

Tab. 1: ranges of wavelength  $\lambda$ , frequency  $\nu$ , wavenumber  $\tilde{\nu}$  and energy  $E$  of UV, VIS, IR and midIR radiation.

	UV	VIS	IR			
			midIR			
$\lambda / \text{nm}$	100	380	780	3000	50000	1000000
$\nu / \text{THz}$	3000	789	385	100	6	0.3
$\tilde{\nu} / \text{cm}^{-1}$	100000	26316	12820.5	3330	200	10
$E / 10^{-23}\text{J}$	198645	52275	25467	6615	397	19.86
$E / \text{eV}$	12.39	3.26	1.59	0.413	0.025	0.00124

## 2.1.2 Relaxation dynamics following electronic excitation

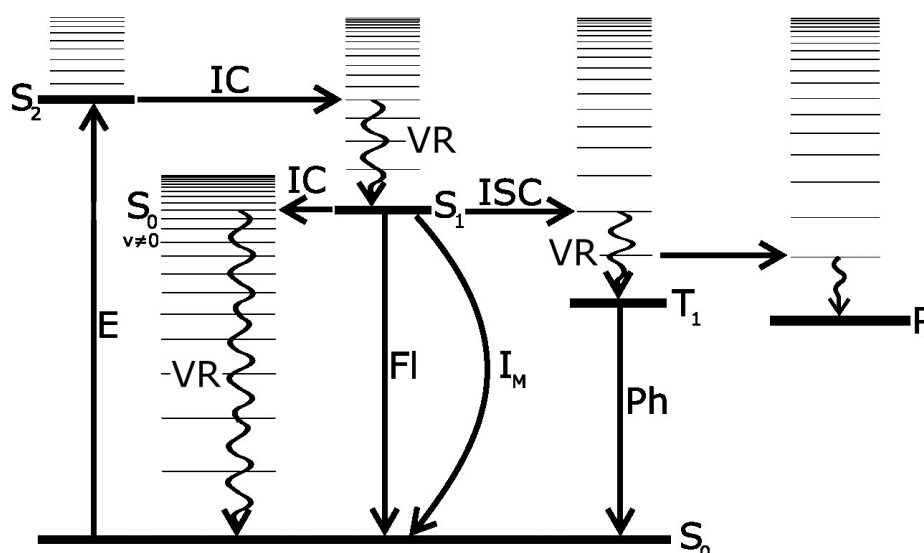


Fig. 2: Jablonski diagram of typical electronic and vibrational states and transitions following electronic excitation from an electronic singlet ground state to a higher excited electronic singlet state. Thick lines represent electronic states, thin lines the associated vibrational states, straight arrows electronic transitions and waves arrows vibrational transitions. Abbreviations:  $S_n$ : electronic singlet state  $n$ ,  $T_m$ : electronic triplet state  $m$ ,  $P$ : undefined electronic state of a photoproduct,  $v$ : quantum number for vibrational states, IC: internal conversion, ISC: intersystem crossing, VR: vibrational relaxation,  $I_M$ : impact relaxation,  $M$ : impact partner, Fl: fluorescence, Ph: phosphorescence.

The dynamics of absorption and emission in a molecular system rarely involve only two states. Especially the excitation of electronic states leads to a series of ultrafast relaxation processes that very few measurement techniques are able to follow, one of them being ultrafast time-resolved pump-probe absorption spectroscopy. In order to understand the results of this technique using visible or ultraviolet light for excitation, it is important to understand those dynamics, which are depicted in a simplified manner using a Jablonski diagram<sup>[2]</sup> (see. Fig 2).

As was mentioned before, illuminating a molecule with photons of a specific energy can induce a transition between two states, if the difference in energy between them equals the photon energy. In the case of ultraviolet to visible light and transition metal organic complexes electronic transitions are generally induced.

In the schematic in fig. 2 a molecular system with a singlet ground state  $S_0$  is assumed, which is the more common case, though a triplet or higher multiplicity ground state is possible and the following relaxation dynamics in those cases are very similar. A photoinduced transition  $E$  from the electronic ground state more often than not leads to a state with the same the multiplicity or spin state, since transitions with spin change are regarded as forbidden, which means they are much less likely, though not impossible. From the resulting electronically excited singlet state  $S_n$  the molecular system can transform the introduced energy via several paths. If the system is excited into a higher electronically excited state with for example  $n=2$ , it will first of all transition into an energetically lower lying excited state of equal multiplicity via internal conversion (IC). The rate for radiationless electronic transitions like IC depends on the overlap between the vibrational wavefunctions of the states involved or the magnitude of the corresponding Franck-Condon factor, which tends to be greater for states with smaller energy gaps as is often the case for medium to large sized molecules due to their high density of excited electronic states. Accordingly, most electronically excited transition metal complexes end up in the lowest electronically excited state of a given multiplicity within  $<100$  fs, before any other electronic transition can occur (Kasha 1950).

Since the atoms in the molecule cannot immediately follow the quasi-instantaneous change in electron density distribution from electronic excitation, the molecule is not in its equilibrium state, but a vibrationally excited state. The energy difference between the corresponding electronic states is distributed among multiple vibrational modes within the molecule depending on how much they are coupled to the electronic states. In order to relax into the vibrational ground state of the respective electronic state the energy is dissipated to other vibrational modes within the molecule (intramolecular vibrational relaxation IVR) or to other molecules in the vicinity, primarily the solvent molecules or bath. The effectiveness of the energy transfer of those vibrational relaxations VR (sometimes also called vibrational energy relaxation VER) again depends on how well the respective states are coupled.

From the energetically lowest excited singlet state  $S_1$  multiple electronic transitions are possible, though they don't have the same probability to occur. Which of the transitions can be observed depends on the electronic and by extension on the molecular structure and can therefore be tuned through careful design of the molecule, in the case of transition metal complexes especially the ligands.

Systems with a very short-lived  $S_1$  state often directly return to the electronic ground state  $S_0$ . Due to the usually rather large energy gap between ground state  $S_0$  and first electronically excited state  $S_1$  compared to the gap between adjacent electronically excited states like  $S_1$  and  $S_2$  this transition produces an electronic state with rather high vibrational excitation. Since a population of higher vibrational states can also be achieved by heating (though the population distributions differ dramatically), the result is often called a vibrationally hot or just hot electronic ground state. The

vibrational relaxation happens over the afore mentioned pathways and generally takes about 10-100 ps.

Another path directly back to the ground state is the transfer of energy to an impact partner M. This impact relaxation  $I_M$ , however, requires a partner capable of receiving the energy by having two states with a matching energy gap, a long lifetime of the excited state for the necessary bimolecular interaction and is only relevant at high concentrations of the partner to ensure high probability of an impact.

Last but not least, an  $S_1 \rightarrow S_0$  transition can also occur by emitting a photon with energy equal to the energy gap. As was mentioned before, this transition can happen either spontaneously or stimulated by another photon. In the spontaneous case emission without change in multiplicity is called fluorescence Fl. Due to the energy losses related to the preceding relaxation processes the energy of the emitted photon is generally smaller than the energy of the absorbed one.

Though transitions between states of different multiplicity are forbidden according to quantum chemical theory, relativistic considerations like spin-orbit coupling give an explanation why they can nevertheless occur and are actually quite prominent in transition metal complexes especially of heavy metals. The heavier the metal, the more electronic states it possesses and the mixing and coupling of states increases enabling transitions between different spin states, which are called intersystem crossing (ISC). A transition for example from  $S_1$  to  $T_1$ , however, still tends to occur at lower rates than IC, but they can be used to trap a system in a longer-lived electronic state since a return back to the electronic ground state involves another spin transition that can be hindered with an appropriate molecular design. Triplet lifetimes from a few picoseconds to several nanoseconds

Such a long-lived triplet state is especially useful for charge separated states that require a long lifetime to extract the charges before recombination. For the same reason a chemical reaction to any photoproduct P is also more likely from the triplet than the singlet state. This way a product can be created that is not accessible from the electronic ground state by using a part of the supplied photon energy to break or built new bonds.

In the absence of any intervention, the  $T_1$  state eventually needs to relax back to the ground state. If there is no other possible path, this happens via photon emission similar to fluorescence Fl. This transition, which is distinguished from Fl, because it necessitates a forbidden spin transition, is called phosphorescence Ph. Mirroring the processes of Fl the Ph photon energy is generally lower than that of Fl in the same system due to the energy losses along the preceding path.

### 2.1.3 Charge-transfer transitions

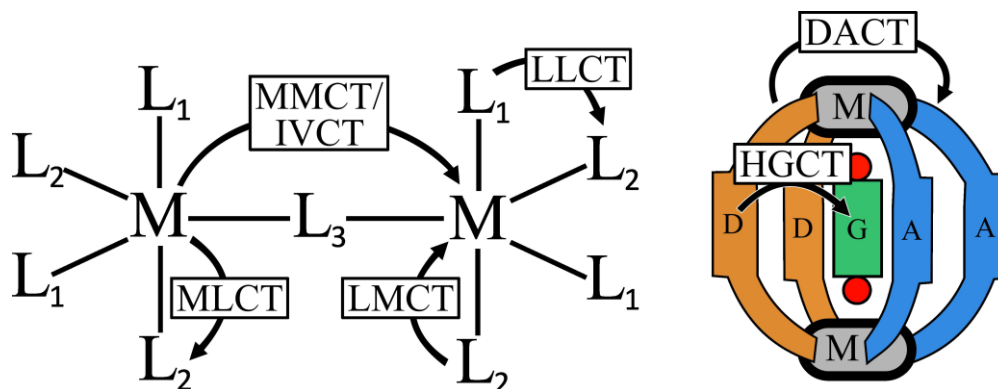


Fig. 3: depiction of electron transfer directions in common charge-transfer transitions.

Up until now the states and transitions have only been characterized by their energy, which determines the wavelength an absorption or emission appears in a spectrum, and the multiplicity, which contributes to the probability a transition can occur due to selection rules forbidding certain transitions. Since a transition between electronic states induced by electromagnetic radiation is always accompanied by a shift of the electron density in a molecule, the direction of the change in electron density is commonly used to classify transitions especially in transition metal complexes<sup>[3]</sup>.

Aside from transition that are confined or localized to a part of the molecule like d-d-transitions in a metal centre, often referred to as metal centred (MC) transition, or inter ligand (IL, sometimes also LC for ligand centred) transition that typically involve transitions between  $\pi$  and  $\pi^*$  orbitals, charge-transfer transitions are of particular interest, since they offer a path to a separation of charges that can be picked up to create a current. Though a transfer of a full electron in the sense of a redox reaction is often implied with a charge-transfer, it is not required in current language.

Frequently appearing charge-transfer transitions are depicted in fig. 3. A commonly observed process in a transition metal complex is the metal-to-ligand charge-transfer (MLCT) transition. A lot less instances of the reverse, a ligand-to-metal charge-transfer (LMCT), are known for complexes in the ground state due to the fact that the occupation of the ligand states is often energetically more favourable than of the metal states, but in the excited state this relation can be inverted.

Complexes with multiple different ligands can perform ligand-to-ligand charge-transfer (LLCT) transitions. If the donors are specifically designed to pass and receive an electron, creating a cation and an anion, these transitions are referred to as donor-acceptor charge transfer (DACT) transitions. An even more specific term used in this thesis is a host-to-guest charge transfer (HGCT), that applies to molecules, whose acceptor is embedded in the cavity of the donor or a molecule involving the donor.

In bi-/multinuclear complexes with two/multiple metal cores, either different elements or the same element in different oxidation states, metal-to-metal charge-transfer (MMCT) transitions can be observed given a suitable connecting ligand is used. In the case of the mentioned mixed valence compounds, the term intervalence charge-transfer (IVCT) is used alternatively, though this expression is sometimes extended to analogue complexes with different metals.

It needs to be emphasized that a common habit is to not only use these abbreviations for a transition, but also for the state resulting from it or even, for a series of relaxation processes, using the same scheme to describe a state relative to another state, typically the ground state, referring to a corresponding hypothetical direct transition.

## 2.1.4 Infrared spectroscopy

The vibrations of a molecular bond can be approximated with a spring connecting two masses stretching and compressing. The contained energy is constantly transformed between kinetic and potential energy. The latter is described by a cubic potential <sup>[4]</sup>(see fig. 4 left) of the form

$$V(r) = \frac{1}{2}Dr^2 \quad \text{Eq. 003}$$



The parameter  $r$  is the displacement of the spring or bond from its state of lowest potential energy, the equilibrium distance  $r_e$  between the masses or atoms, and the force constant  $D$  describes the stiffness of the spring which equates with the bond strength of a molecule.

Solving the Schrödinger equation with this potential gives the vibrational energy states a molecule can occupy according to this model:

$$E(v) = hv_m \left( v + \frac{1}{2} \right) \quad \text{with } v = 0, 1, 2, 3, \dots \quad \text{eq. 004}$$

or if the energy is depicted in units of  $\text{cm}^{-1}$  simply

$$\tilde{E}(v) = \tilde{\nu}_m \left( v + \frac{1}{2} \right) \quad \text{with } v = 0, 1, 2, 3, \dots \quad \text{eq. 005}$$

with the vibrational quantum number  $v$  and the molecular vibrational frequency  $\nu_m$  or wavenumber  $\tilde{\nu}_m$ . Since there is no way to reach a state below the zero point energy at  $v = 0$ , it can be subtracted to use it as a new base line:

$$\tilde{E}(v) = \tilde{\nu}_0 v \quad \text{eq. 006}$$

A transition would then according to eq. 002 be induced by a photon of the energy

$$\tilde{E}(v + n) - \tilde{E}(v) = n\tilde{\nu}_0 \quad \text{eq. 007}$$

The frequency of the photon and therefore also the position in an IR spectrum is directly connected to the bond strength  $D$  via

$$\tilde{\nu}_0 = \frac{1}{2\pi c} \sqrt{\frac{D}{m_{\text{eff}}}} \quad \text{eq. 008}$$

where  $c$  is the velocity of light and  $m_{\text{eff}}$  the reduced mass, which is

$$m_{\text{eff}} = \frac{m_1 \cdot m_2}{m_1 + m_2} \quad \text{eq. 009}$$

for diatomic molecules.

The intensity of a vibrational transition peak is related to the transition dipole moment  $\mu_{ij}$  between the states  $i$  and  $j$  (with  $j > i$ )

$$I_{ij} \sim \mu_{ij}^2 \quad \text{eq. 010}$$

which is calculated via the integral

$$\mu_{ij} = \langle \psi_i(r) | \hat{\mu}(r) | \psi_j(r) \rangle = \int_{-\infty}^{+\infty} \psi_i^*(r) \cdot \hat{\mu}(r) \cdot \psi_j(r) dr \quad \text{eq. 011}$$

Using a Taylor series for the dipole moment

$$\mu(r) = \mu_{r=0} + r \left( \frac{d\mu(r)}{dr} \right)_{r=0} \quad \text{eq. 012}$$

This equation can be simplified to

$$\mu_{ij} = \mu_{r=0} \cdot \langle \psi_i(r) \cdot \psi_j(r) \rangle + \left( \frac{d\mu(r)}{dr} \right)_{r=0} \langle \psi_i(r) | r | \psi_j(r) \rangle \quad \text{eq. 013}$$

since  $\mu$  and its derivative are both constants independent of  $r$  that can be removed from the integral. The first integral in this equation is always zero for a harmonic oscillator, because the wavefunctions of all vibrations are orthogonal towards each other. For the same reason the second one is only non-zero for  $n = \pm 1$ , provided the derivative of  $\mu$  is non-zero as well. Accordingly, for a harmonic oscillator only a single transition frequency at

$$\Delta\tilde{E} = \tilde{E}(v+1) - \tilde{E}(v) = \tilde{\nu}_0 \quad \text{eq. 014}$$

can be observed and only if the molecule has a permanent or at least a by the respective vibration inducible dipole moment. It can even be shown that the second integral in eq. 013 and by inference the peak intensity and therefore also the cross section of absorption and stimulated emission depends linearly on the quantum number of the two states:

$$r_{ij} = \langle \psi_i(r) | \hat{r} | \psi_j(r) \rangle = \sqrt{\frac{\hbar}{2m_{\text{eff}}\nu_m}} (\delta_{i+1,j}\sqrt{i+1} + \delta_{i,j+1}\sqrt{j+1}) \quad \text{eq. 015}$$

In this equation  $\hbar$  represents the reduced Planck constant,  $m_{\text{eff}}$  the reduced mass of the molecular vibration and  $\delta$  the Kronecker delta, which is one for equal indices and zero for different ones. With this equation and considering a proportional relation between peak intensity  $I_{ij}$  and absorption cross section  $\sigma_{ij}$  ( $I_{ij} \sim r_{ij} \sim \sigma_{ij}$ ) two simple relations for absorption ( $\delta_{i,j+1}$ ) and stimulated emission ( $\delta_{i+1,j}$ ) can be made<sup>[5]</sup>:

$$\sigma_{v+1,v} = (v+1) \sigma_{10} \quad \text{with } v = 1, 2, 3, \dots \quad \text{eq. 016}$$

$$\sigma_{v+1,v} = \sigma_{v,v+1} \quad \text{eq. 017}$$

These relations have a minor influence on the spectrum of a harmonic oscillator, but become relevant, when the possible transitions don't overlap at one peak.

For most molecules the model of the harmonic oscillator is insufficient to accurately describe the energy and transitions of vibrational states, especially at high displacements, where a molecule is approaching dissociation. In these cases of anharmonic oscillations, often described with the Morse potential<sup>[4]</sup> (see fig. 4 right)

$$V(r) = D_e(1 - e^{-\beta r})^2 \quad \text{eq. 018}$$

with the dissociation constant  $D_e$  and  $\beta$  as an equivalent to the force constant  $D$ , the resulting energy eigenvalues

$$\tilde{E}(v) = \tilde{\nu}_e \left( v + \frac{1}{2} \right) - \chi_e \tilde{\nu}_e \left( v + \frac{1}{2} \right)^2 \quad \text{with } v = 0, 1, 2, 3, \dots \quad \text{eq. 019}$$

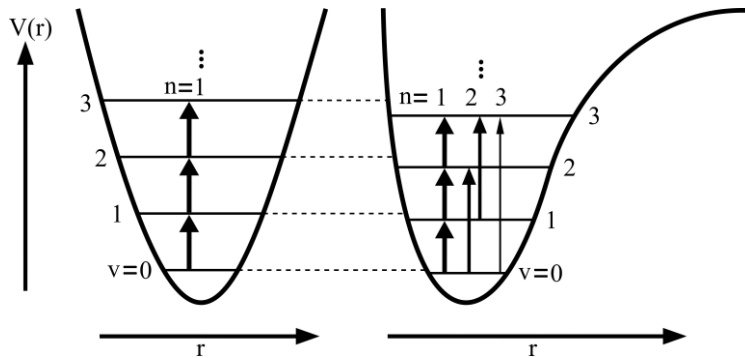


Fig. 4: potential energy curve  $V(r)$  of harmonic (left) and anharmonic (right) oscillator. Allowed transitions are indicated with arrows. Transition probabilities are implied by arrow thickness.

are slightly smaller than their harmonic counterpart. They can again be related to the zero point energy<sup>[6]</sup> instead of the minimum of the potential via

$$\tilde{E}(v) = \tilde{\nu}_0 v - \chi_0 \tilde{\nu}_0 v^2 \quad \text{eq. 020}$$

with

$$\tilde{\nu}_0 = \tilde{\nu}_e - \chi_e \tilde{\nu}_e \quad \text{eq. 021}$$

and

$$\chi_e \tilde{\nu}_e \approx \chi_0 \tilde{\nu}_0 \quad \text{eq. 022}$$

The transitions are then calculated with

$$\tilde{E}(v+n) - \tilde{E}(v) = \tilde{\nu}_0 n - \chi_0 \tilde{\nu}_0 (2vn + n^2 - n) \quad \text{eq. 023}$$

It is apparent that the transitions of an anharmonic oscillator are not overlapping at the fundamental  $\tilde{\nu}_0$ , but they are shifted by the anharmonicity  $2\chi_0 \tilde{\nu}_0$  for transitions with  $n = \pm 1$ . Moreover, transition with  $n \neq 1$ , so-called overtones, are allowed (though they are less likely than the fundamental) for the anharmonic oscillator and can be observed at slightly less than double the frequency of the fundamental which provides another possibility to obtain the anharmonicity.

## 2.1.5 Pump-probe spectroscopy

Though there are a lot of more or less intricate spectroscopic methods available, which all have their advantages and disadvantages, the most common one is without a doubt the absorption spectroscopy. The principle is simple: a sample, for transition metal complexes usually dissolved in an organic solvent and contained in a sample cell, is illuminated by a beam of known or measured intensity  $I_0$ . Behind the sample the beam intensity  $I$  is measured again. The radiation source can be monochromatic or polychromatic, meaning it can have a very narrow range of wavelengths, ideally only one, or a broad spectrum of wavelengths. If a utilized wavelength is appropriate for inducing a transition within the sample, it can be absorbed and the intensity  $I_0$  is reduced upon passing the sample according to the Beer-Lambert law<sup>[7]</sup>

$$I = I_0 e^{-\kappa cd} = I_0 10^{-\epsilon cd} \quad \text{eq. 024}$$

The bigger the logarithmic/decadic absorption coefficient  $\kappa/\epsilon$  (a measure of the probability of a molecule to absorb a suitable photon, which is a function of the wavelength  $\lambda$  and temperature  $T$  and directly connected to the absorption cross section), the higher the concentration  $c$  of the sample molecules (which increases the probability of a photon to meet a sample molecule while passing the cell) and the longer the distance  $d$  the beam travels through the sample solution (further increasing the probability of an interaction), the lower the intensity  $I$  becomes. For a given temperature  $T$ , concentration  $c$  and cell thickness  $d$  a measurement of  $I$  and  $I_0$  as a function  $\lambda$  generates  $\epsilon(\lambda)$  ( $\kappa$  is rarely used), which can be plotted against the corresponding wavelength  $\lambda$  to receive the absorption spectrum of the sample. In infrared spectroscopy the spectrum is typically shown as the transmission

$$T_{IR}(\tilde{\nu}) = \frac{I}{I_0} \quad \text{eq. 025}$$

while indicating concentration, cell thickness and temperature. UV/vis absorption spectra often depict the absorbance

$$A_{UV/vis}(\lambda) = -\log_{10}(T) = \log_{10}\left(\frac{I_0}{I}\right) \quad \text{eq. 026}$$

When measuring a sample under moderate conditions, for example room temperature and low beam intensity, the sample is usually situated in its electronic ground state and many vibrations that absorb in the midIR are sparsely populated in higher vibrational states, which is easily understood when looking at the Boltzmann distribution

$$N_{i+1} = N_i e^{-\frac{\Delta E}{k_B T}} \quad \text{eq. 027}$$

where  $N_{i+1}$  and  $N_i$  are the populations of two energy levels with an energy level difference  $\Delta E$  and  $k_B$  is the Boltzmann constant. This means that the steady state (due to the constant irradiation) absorption spectrum typically has only transitions from the ground state. However, a sample can also be excited into another state first, which is subsequently probed to get information of the excited state. Given enough time after excitation the sample can relax from the initial excited state to other states via mechanisms that were discussed in chapter 2.1.2. Each state has its own spectrum due to their energy level and applicable selection rules and can therefore potentially be identified. This relation is used in pump-probe spectroscopy setups to uncover the dynamics of samples upon photoexcitation.

For this setup two pulsed radiation sources (often generated from one beam, but the use of two or even more synchronized devices is also possible) are needed: the pump beam for the initial excitation of the sample and the probe beam, which illuminates the sample and its intensity is measured after passing it similar to the measurement of a steady state or ground state spectrum. The delay between pump excitation and probe measurement can be set between measurements either electronically or by varying the path one of the beams must travel. The latter is achieved using a translational stage. This device holds two mirrors that reflect a beam back at two times  $90^\circ$  mounted on a platform that can be moved forth and back. The further the stage is moved back, the longer the beam path becomes and the later a pulse arrives at the cell. Since electronic transitions of transition metal complexes in solution typically happen in a range of several picoseconds ( $10^{-12}$  s) down to only a few femtoseconds ( $10^{-15}$  s), appropriately short pulses of around or even less than 100 fs have to be created, which is only possible with lasers, whose principle of operation will be intensively covered in the next chapters.

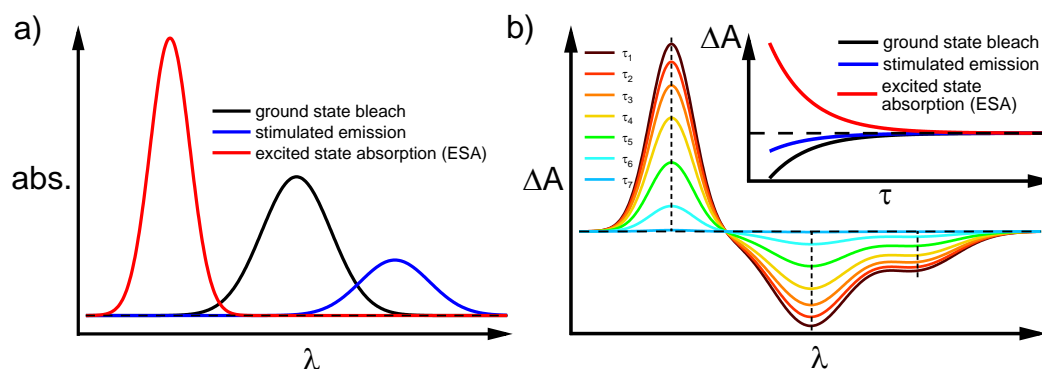


Fig. 5: three types of absorption bands (a) and how they appear and decay in a pump-probe spectrum (b)). Inlet shows the transients of the bands at the wavelength indicated by the dashed line.

The pump pulse generally cannot excite every molecule in its path, but only a fraction according to the absorption cross sections of each component in the sample. Unfortunately, the probe pulse cannot distinguish between excited and non-excited molecules. It measures the sum of the spectra of all components upon arrival. In order to only receive the changes induced in the sample by the pump pulse a spectrum without pump excitation, basically the ground state spectrum, is subtracted creating a difference spectrum

$$\Delta A(\lambda) = \log_{10} \left( \frac{I_0}{I_{pump}} \right) - \log_{10} \left( \frac{I_0}{I_{no\ pump}} \right) \quad \text{eq. 028}$$

If the pump pulse didn't induce a change or the sample completely reverted back to the state before excitation,  $\Delta A(\lambda)$  is zero since both pumped and not-pumped spectra are equal.

There are several ways to measure spectra without pump excitation in quick succession for example using a rotating wheel with holes, a chopper, cutting every second pulse or permanently splitting off a portion of the probe beam as a reference, which has the added benefit that pulse fluctuations can be removed as well.

In a pump-probe difference spectrum three general types of bands can be distinguished (also see fig. 5):

Since the ground state is less populated in favour of the excited states the ground state absorption bands get weaker. In the difference spectrum this creates a negative band called (ground state) bleach.

The population of excited states increases the absorption at their designated bands. A positive band appears in the difference spectrum designated excite state absorption (ESA).

The excited state cannot only absorb, it can also be stimulated to emit by the probe pulse. Just like the ground state bleach the detector receives more light after excitation, however, not due to less absorption, but more emission than without pump excitation. Therefore, stimulated emission also creates negative bands in the difference spectrum.

Another type of band that is frequently encountered in time-resolved UV/vis spectra is the hot ground state band, which is typically observed after a quick relaxation back to the ground state. Since the pump energy cannot be dissipated into the surroundings quickly enough, it is transferred to vibrational excitations. This leads to absorption bands that are broadened towards lower energy since the vibrationally excited molecules need less energy to reach a certain excited state. In the difference spectrum this often creates a negative band at the centre of the bleach and a broad positive one on its low-energy side.

## 2.1.6 Laser

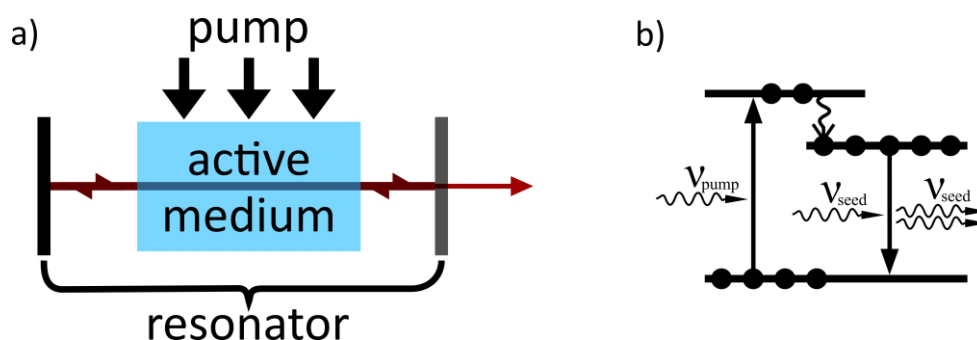


Fig. 6: a) schematic setup of a simple laser (a) and energy level diagram of an active medium with a 3-level system.

A laser is a device that uses stimulated emission to create a high intensity beam of coherent, ideally monochromatic, practically collimated radiation. Basic idea is to put a photon into a two-state system that is already in its excited state and receive a second photons with the same properties due to the mechanism of stimulated emission in order to achieve an amplification (therefore the acronym laser: “light amplification by stimulated emission of radiation”). Those photons could again be used to induce stimulated emission in other excited molecules to perpetuate an exponentially growing cascade. A simple setup for a laser to achieve this is depicted in fig. 6 a). The so-called pump is supplying the energy needed to put the active medium, that performs the stimulated emission, into its excited state. There are many pump methods available, most of which are based on optical excitation like flash lamps and laser diodes. Two mirrors form a resonator or cavity that creates standing waves (modes) by reflecting the emitted photons back and forth through the active medium to achieve continuous amplification. The initial photon can be derived from spontaneous emission, but this is rather inefficient due to the randomness of direction and timing and therefore other sources, especially other, smaller lasers are typically used to “seed” the emission.

Since an incoming photon can induce both stimulated emission and absorption, two processes whose transition rates

$$\frac{dN_{ij}}{dt} = N_i u(\nu) B_{ij} \quad \text{eq. 029}$$

and

$$\frac{dN_{ji}}{dt} = N_j u(\nu) B_{ji} \quad \text{eq. 030}$$

with  $B_{ij} = B_{ji}$  only differ by the population of the two states  $i$  and  $j$ , amplification is only achieved at population inversion  $N_j > N_i$ . In a two-state system, however, an equal population of both states  $N_j = N_i$ , where the probability for both processes is the same, is the upper limit no matter the beam intensity represented in eq. 029 and eq. 030 by the photon density  $u(\nu)$ . Spontaneous emission additionally lowers the population of the excited state without contributing a meaningful amount to the amplification due to the random emission direction.

In order to achieve population inversion, the processes of absorption and stimulated emission are decoupled using an active medium that has at least three states as is depicted in fig. 6 b). After excitation into state 1 the system quickly relaxes into a comparatively long-lived state 2, where population is stored until it is cleared by the seed. This way an inversion between state 0 and 2 can be achieved without the impossible pump induced inversion between state 0 and 1.

Beside the population inversion a second condition must be met for laser operation: the gain from illuminating the active medium must surpass the losses from absorption, scattering, diffraction, misalignments among others. This condition becomes especially relevant for the extraction of a laser beam from the cavity, for example if one of the cavity mirrors is slightly transparent, as this equals another loss, but it can also be used to produce high-intensity laser pulses. Using a so-called Q-switch the losses within the cavity are artificially boosted to avoid clearing the active medium from the emissive state while it is pumped, storing more and more energy until the switch starts the lasing process releasing the energy in a short burst, a pulse, whose duration depends partially on the type of Q-switch.

There are many other methods to produce pulsed laser beams like cutting pulses out of a continuous beam or mode locking. The latter is a common method for an active medium like a titanium: sapphire (Ti:Sa) crystal with a broad emission band to create ps/fs pulses.

The properties of a laser beam can be manipulated in many ways both inside and outside the cavity. In the chapters describing the experimental setups used for this thesis further discussions for some of those methods will be provided.

## 2.2 Nonlinear optics

The properties of radiation from typically incoherent sources used in UV/vis and IR spectroscopy (low intensity, polychromatic, random direction and phase) are sufficient to measure ground state spectra, but the necessary temporal and spatial resolution necessary for the investigation of ultrafast processes like the dynamics after electronic excitation in molecules can only be delivered by lasers. Especially the high intensity, which are a result of the defined direction and phase relation, opens up a large variety of techniques that are not accessible otherwise. Most of these techniques require the interaction with crystals of a specific material, whose polarization responds nonlinearly to high-intensity EM radiation creating completely new beam properties. The following chapters will give an introduction to the field of nonlinear optics and some commonly used applications of it.

### 2.2.1 Radiation induced polarization

In the concept of wave-particle dualism, EM radiation has properties of both a particle (then it is referred to as a photon) and a wave that is propagating in space. This wave has an electric and a magnetic field component that are both oscillating with the same frequency  $\nu$  proportional to its energy according to eq. 001. Just like a macroscopic electric or magnetic field, EM waves can move charges. In a material both electrons and nuclei can be moved by those fields, though the comparatively heavy nuclei cannot follow the quick changes of the fields in UV and vis radiation, while electrons on the other hand are often capable to do so. Consequently, the electron density around the nuclei of a molecule is periodically displaced by the electric field  $E(t)$  from the previously balanced state by following the EM field, which creates a local electric dipole moment in the molecules that adds up to a macroscopic polarization

$$P(t) = \epsilon_0 \chi^{(1)} E(t) \quad \text{eq. 031}$$

within the material. The constants  $\epsilon_0$  and  $\chi^{(1)}$  refer to the electrical field constant and the linear electric susceptibility. Due to the linear correlation between electrical field and induced dipole moment/polarization the incoming wave can leave the material without change in its frequency. Accordingly, phenomena of matter-radiation interactions without a change in radiation frequency are assigned to the subject of linear optics.

Similar to the force needed to displace a spring from its equilibrium state, which can be described by the model of the harmonic oscillator, the linear relation between  $P$  and  $E$  only applies to small displacements. With coherent high intensity radiation, as can be generated with lasers, the correspondingly strong electric field creates a nonlinear response of the electric dipoles as the electrons cannot exactly follow the guidance of the electric field at large displacements. Due to this anharmonicity, susceptibilities of higher order become relevant to the polarization

$$P(t) = \epsilon_0 \chi^{(1)} E(t) + \epsilon_0 \chi^{(2)} E^2(t) + \epsilon_0 \chi^{(3)} E^3(t) + \dots \quad \text{eq. 032}$$

of the material. The additional terms give rise to a great number of optical phenomena that are summarized under the term of nonlinear optics. Many of these phenomena are frequently used for frequency and beam profile conversion to access a wide variety of beam properties. The most important ones for the experimental setup presented in this thesis will be discussed shortly in the following chapters.

## 2.2.2 Sum frequency, second and fourth harmonic generation (SFG, SHG, FHG)

When two superimposed laser beams are passing a suitable nonlinear crystal at the same time, two photons of frequencies  $\nu_1$  and  $\nu_2$  can merge into one photon and generate the sum frequency

$$\nu_3 = \nu_1 + \nu_2 \quad \text{eq. 033}$$

The crystal does not have to possess a fitting energy gap between two states for each photon. It is assumed that the photons are inducing transitions into so called virtual states (Shore 1979). Those states should not exist according to quantum chemical considerations and are therefore presumed extremely short-lived compared to transitions to real states with similar energy gaps. Consequently, they need to be occupied in quick succession, which is only sufficiently probable at high beam intensities.

A special variation of SFG is the degenerate case, where both incoming photons have the same frequency  $\nu_1 = \nu_2$ , which means only one beam with sufficient intensity is needed. The result is the generation of a photon with exactly twice the frequency

$$\nu_3 = \nu_1 + \nu_2 = 2\nu_1 \quad \text{eq. 034}$$

and energy. Accordingly, the product is called second harmonic of  $\nu_1$ , the incoming beam is often referred to as the fundamental. With a second crystal it is possible to generate a second harmonic of  $\nu_3$ , which is equivalent to fourth harmonic generation of  $\nu_1$ .

SFG, SHG and especially SHG are frequently used to obtain higher energy photons from a given laser beam, thus without the need to use another laser for the required frequency.

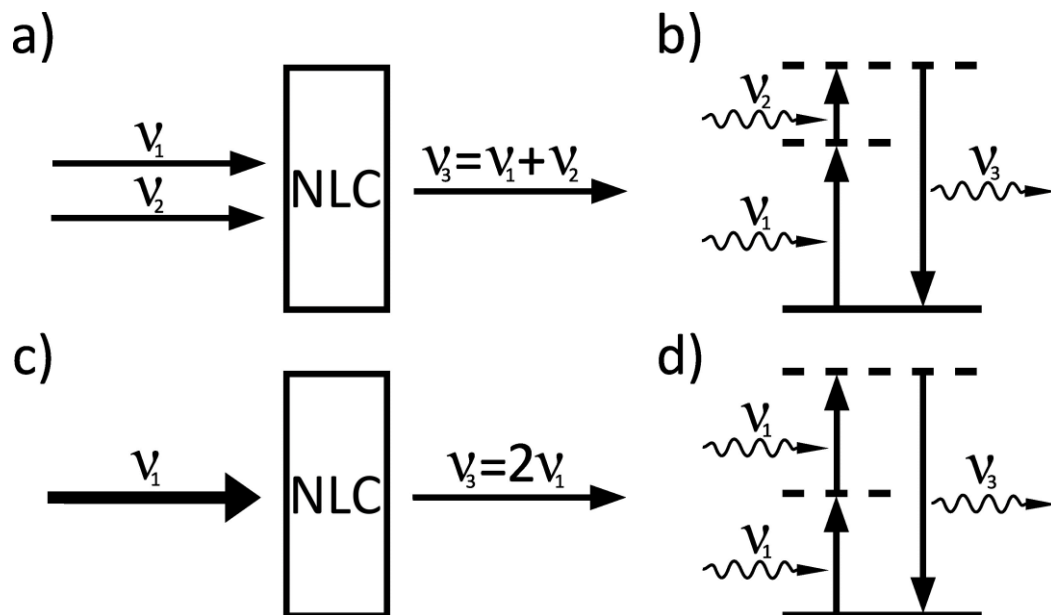


Fig. 7: schematic depicting the sum frequency (a) and second harmonic generation (c) and corresponding energy level diagrams (b) and d). Abbreviations: NLC: nonlinear crystal,  $\nu$ : frequency.



## 2.2.3 difference frequency generation (DFG)

Similar to the SFG, two laser beams can also be used to generate the difference frequency

$$\nu_3 = \nu_1 - \nu_2 \quad \text{eq. 035}$$

In this case, photon 1 is absorbed, inducing a transition to a virtual state with higher energy, but photon 2 is then stimulating a transition to another, energetically lower lying virtual state under emission of a photon with the same properties as photon 2 similar to the afore mentioned stimulated emission. From the second virtual state photon 3 is then emitted with the difference frequency.

DFG can not only be used to create radiation with lower energy than the incoming beams, for example to obtain IR radiation from visible light, but also to amplify one beam at the expense of another due to the quasi-stimulated emission. It is then referred to as optical parametric amplification (OPA). For this purpose, beam 1, the pump beam, usually has a higher intensity than beam 2 and basically serves as the energy source for the amplification process of beam 2, the seed. Photons generated with the same properties as photon 2 are called signal, those with the difference frequency idler.

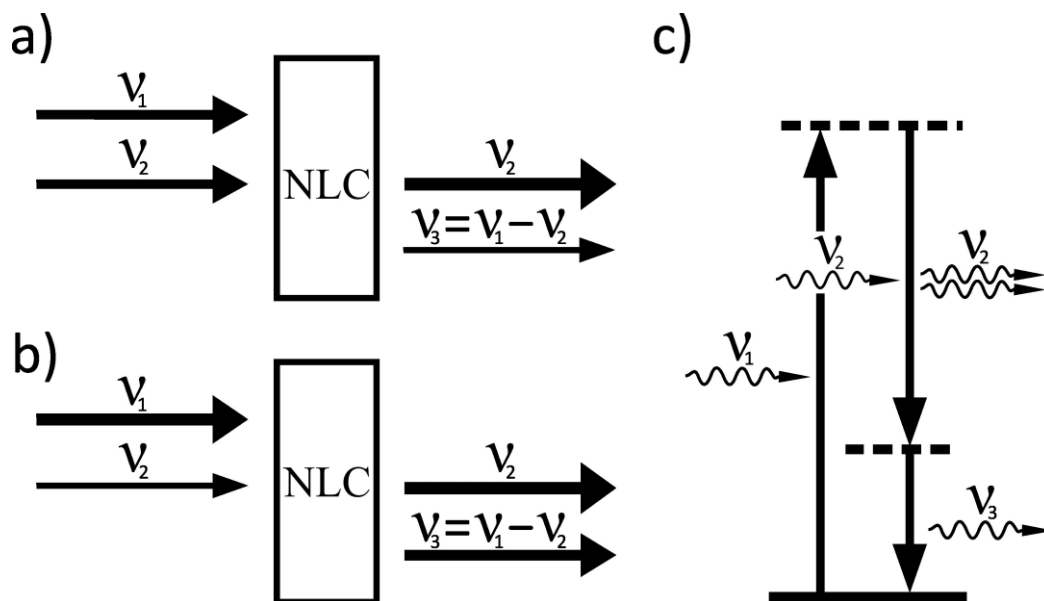


Fig. 8: schematic depicting the difference frequency generation (a) and optical parametric amplification (b)) and corresponding energy level diagram (c)). Abbreviations: NLC: nonlinear crystal,  $\nu$ : frequency.

## 2.2.4 phase matching condition

During propagation through a nonlinear material a new wave can be generated at every layer of molecules. Since the refractive index  $n$  (and due to the connection

$$c = \frac{c_0}{n} \quad \text{eq. 036}$$

also the propagation velocity  $c$ ) of a wave is dependent on the wavelength, the wave created from a nonlinear effect and the fundamental slowly diverge temporally from one another as one is

moving faster through the material than the other. The result is that the phase of a wave generated at each layer is slightly shifted relative to the previous one, which leads to a periodic intensity progression due to constructive and destructive interference. In order to achieve phase matching, the refractive indices of incoming and created wave need to be equal. The most common method for that is the use of birefringent crystals as the nonlinear medium. Those create two waves with different phase velocities, the ordinary (o) and extraordinary (ao) wave. The refractive index of the latter is dependent on the angle towards the crystal's optical axis. Consequently, a crystal orientation with

$$n_o(v_1) = n_{ao}(v_2) \quad \text{eq. 037}$$

exists. In this case the intensity of the nonlinearly generated outgoing beam increases quadratically with the distance travelled through the crystal until an upper limit, in theory full conversion, is reached.

The phase matching condition is very important to unlock the full potential of nonlinear effects for frequency conversion, since the conversion efficiency is otherwise very low.

## 2.2.5 Self-focussing, -defocussing and -phase modulation

While the nonlinear effects mentioned prior are all a result of the second order susceptibility, self-focussing and -defocussing (also referred to as optical Kerr-effect) and self-phase matching arise from the susceptibility of third order.

Above a certain intensity threshold that is primarily found in pulsed laser beams the refractive index  $n$  becomes dependent on the intensity  $I$  according to

$$n = n_0 + \gamma I = n_0 + \Delta n \quad [8] \quad \text{eq. 038}$$

with  $n_0$  as the refractive index without irradiation,  $\gamma$  as the nonlinear refractive index coefficient and  $\Delta n$  as the intensity-dependent change of the refractive index. Since the intensity profile of a typical laser beam can often be described with a two-dimensional gauss distribution that possesses a maximum in its centre, the corresponding gradient of the refractive index in the material as described by eq. 038 leads to refraction towards the centre of the beam (self-focussing) at positive  $\gamma$  and away from the beam centre (self-defocussing) at negative  $\gamma$ .

Due to the connection of  $n$  to  $c$  according to eq. 036 the phase velocity becomes intensity dependent as well leading to self-phase modulation. This effect can be used to shorten laser pulses, since it can produce slightly shifted new frequencies that can be compressed by wavelength dependent dispersion media (see chirped pulse amplification in chapter 3.3.3). It is also assumed to contribute to the generation of a white light continuum, which will be discussed in the next chapter.

## 2.2.6 White light continuum generation (WLG)

A white light continuum (WLC, sometimes also referred to as supercontinuum) is a product of several nonlinear effects commonly used for example as a source of a broad spectrum for spectroscopical purposes ranging from ultraviolet to near infrared (NIR) or as a seed for tunable optical parametric amplification. The exact interaction of the nonlinear effects depends on the used material (sapphire, yttrium-aluminium-garnet, calcium fluoride) and its geometry (bulk crystal, fibre) as well as the beam intensity and pulse duration, but self-focussing and the generation of filaments is at the centre of most explanations.

In order to create a WLC a spectrally narrow seed beam is focussed into a crystal suitable for WLG, where it is further focussed due to self-focussing (see fig. 9). Because of the high intensities a plasma, basically an area with ionized molecules and their separated electrons, is generated, either through multiphoton ionization or avalanche ionization<sup>[9]</sup> that lowers the refractive index in the area. The more the beam is focussed, the more plasma is generated, the more the refractive index is decreased and the more the beam is defocussed, which lowers the plasma density until the beam is refocussed. The periodically focussed and defocussed beam traversing the crystal is called a filament.

The plasma in the filament is one of the causes used to explain the generation of the broad white light continuum as it compresses the laser pulses, which is accompanied by a spectral broadening according to the Fourier principle. A mixture of other nonlinear effects like SHG, SFG, DFG, four wave mixing and self-phase modulation is additionally broadening and shaping the white light spectrum.

Though the white light contains a variety of wavelengths, the polarization of the seed beam is adopted. The beam profile consists of diverging concentric circles, that can be collimated and refocussed by suitable mirrors.

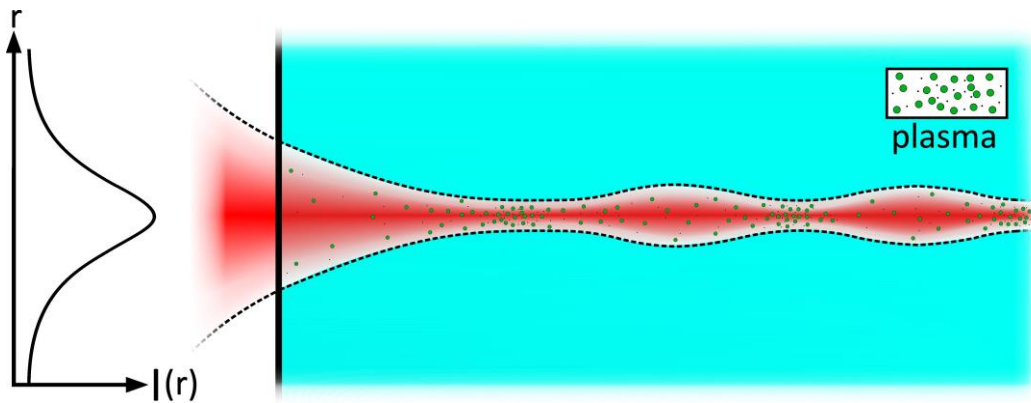


Fig. 9: filamentation of a laser beam of gaussian intensity profile  $I(r)$  upon focussing into a suitable nonlinear crystal.

## 2.2.7 Tunable optical parametric amplifier (OPA)

In a tunable OPA all the afore mentioned nonlinear effects come together. A white light continuum seed beam and its high intensity fundamental as the pump beam are focussed into a nonlinear crystal to generate the difference frequency. Which wavelength range of the white light is amplified and which idler wavelength is created is selected by the crystal orientation meeting the respective phase matching condition. With this setup a wide range of wavelengths is accessible. For this thesis two two-stage tunable OPA were used to obtain amplified NIR signal and idler beams: one to produce an intense beam with a wavelength in the UV to NIR range from SFG, SHG and FHG, another to create about  $100\text{ cm}^{-1}$  broad midIR spectra from their difference frequency. The specific structure of both OPA will be described in detail in chapter 3.2.4 and 3.3.4.



### 3 Experimental setup

Ultrafast dynamics require ultrafast techniques to measure them. The relaxation dynamics that follow electronic excitation in transition metal complexes can take as much as several microseconds<sup>[10],[11]</sup>, but also down to only a few femtoseconds<sup>[12]</sup>. For this reason, femtosecond UV/vis-pump-UV/vis-probe and UV/vis-pump-midIR-probe absorption spectroscopy was used to investigate charge-transfer dynamics of the given complexes. The corresponding experimental setups are highly complex regarding optical installations, electronic coordination and data processing. They will be described in detail in the following chapters. At first a short overview is provided comparing both setups (chapter 3.1). Then, starting with the time-resolved UV/vis setup (chapter 3.2), a more detailed view on the setup including the composition of the laser system is provided (chapter 3.2.1) before the measurement area with the probe detection (chapter 3.2.2) and the two options to create a pump beam (chapter 3.2.3 and 3.2.4) are described in detail. The chapter is concluded by a rather outline of the electronic connections. The coverage of the time-resolved midIR setup (chapter 3.3) has a similar structure: after a general overview of the laser system and the main sections following it (chapter 3.3.1), the latter will be described in detail. Those consist of a compartment for the second or third harmonic to create the pump beam (chapter 3.3.2), a chirped pulse amplifier (chapter 3.3.3), whose output powers an optical parametric amplifier (chapter 3.3.4), and a detection area that also includes a crystal for the difference frequency generation (chapter 3.3.5). This part is again concluded by a description of the electronic connections. The last two chapters deal with the cells the samples are contained in during a measurement (chapter 3.4) and finally the data acquisition, processing and interpretation (chapter 3.5).

### 3.1 Overview

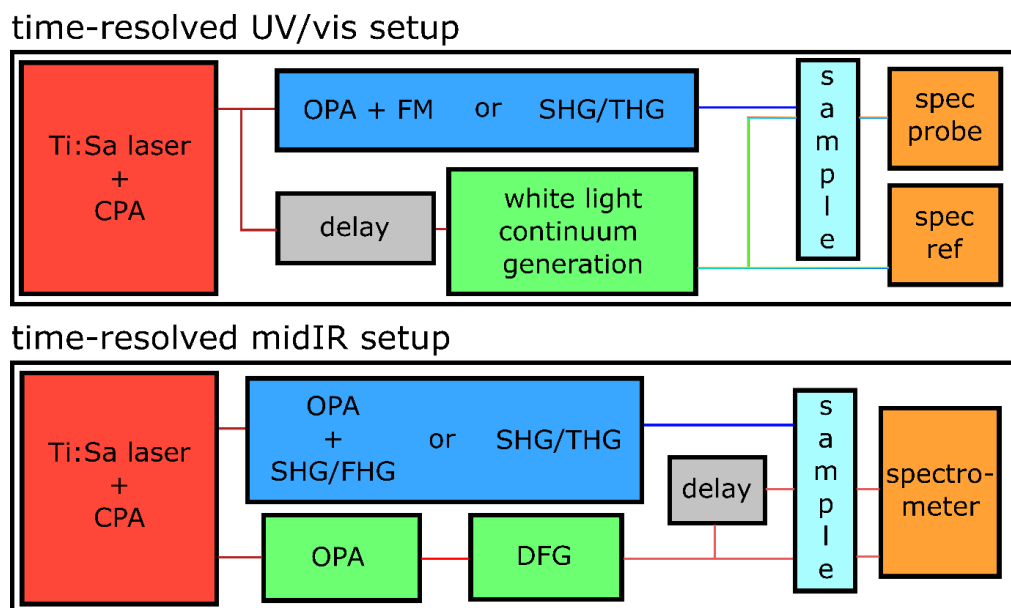


Fig. 10: rough outline of the time-resolved UV/vis and midIR spectroscopy setup. Ti:Sa: titanium doped sapphire, CPA: chirped pulse amplification, OPA: optical parametric amplifier, FM: frequency mixing (including second and fourth harmonic and sum frequency generation and wavelength separation), SHG: second harmonic generation, THG: third harmonic generation, FHG: fourth harmonic generation, DFG: difference frequency generation, spec probe/ref: spectrometer for probe and reference beam.

In order to investigate the ultrafast mechanisms that occur after excitation of electronic states of a sample via ultraviolet or visible light, two time-resolved spectroscopic methods were used: time-resolved UV/vis-pump-UV/vis-probe and time-resolved UV/vis-pump-midIR-probe absorption spectroscopy.

Since both setups use the pump-probe technique, their general structure is very similar as is illustrated in fig. 10. The basis is a Ti:sa (titanium doped sapphire crystal) solid state laser with CPA (chirped pulse amplification) unit that produce a pulsed beam with a wavelength of 800 nm that serves as fundamental for both pump and probe generation. The pump wavelength can be selected either from a tuneable OPA (optical parametric amplifier) or by creating the second or third harmonic (SHG/FHG) of the fundamental and every second pulse is removed by a chopper wheel in order to obtain data with and without pump excitation. The probe is delayed relative to the pump beam via translational stage and a reference is split off before it crosses the pump beam in the sample and is measured with a spectrometer.

Obviously, owed to the respective spectral measurement ranges there have to be differences. The most meaningful one is the shaping of the probe beam, where different optical effects are utilized. A UV/vis probe spectrum is achieved via white light continuum generation by focussing the Ti:Sa laser beam into a CaF<sub>2</sub> crystal, while the difference frequency of idler and signal beam from an OPA produce an about 100 cm<sup>-1</sup> broad midIR spectrum. Other deviations, for example the position of the delay stage and the reference beam splitter, reflect the beam properties and available instrumentation or just grew historically. The intricacies of both setups will be discussed in the following chapters.

## 3.2 UV/vis-pump-UV/vis-probe spectroscopy setup

### 3.2.1 General setup

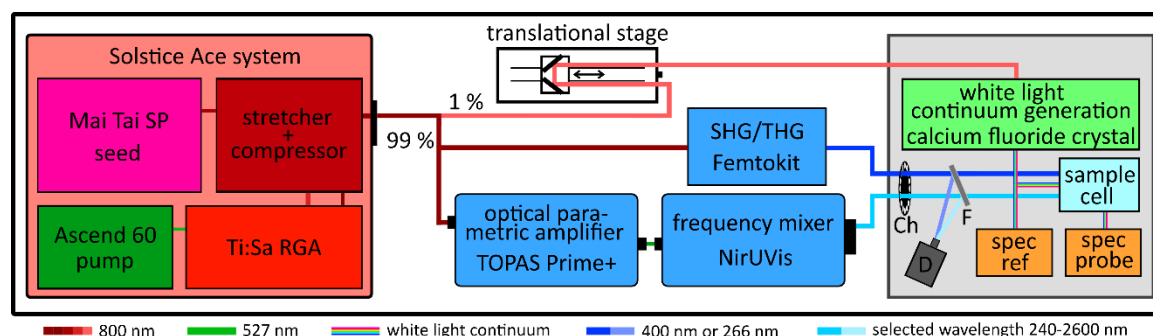


Fig. 11: schematic depiction of the time-resolved UV/vis setup. Abbreviations: Ch: chopper wheel, F: step variable metallic neutral density filter, D: photodiode, spec ref/probe: spectrometer for reference/probe beam detection.

Before the measurements the time-resolved UV/vis setup was moved into another laboratory. The basic setup, which was established in many other sources before, was adopted primarily regarding the electronic configurations (including the measurement program) and the optics concerning the beam detection. However, the opportunity was used to update the laser system as well as the conversion units for the pump beam. Hence the old Clark MRX-CPA 2001 laser of Clark MRX Inc. (a frequency-doubled  $\text{Er}^{3+}$ -doped fiber laser with chirped pulse amplification (CPA) emitting at 775 nm) was replaced by the Spectra-Physics Solstice Ace Ti:Sa oscillator/regenerative amplifier system. A schematic depiction of the setup is given in fig 11.

The Solstice Ace consists of four main sections. Centre unit is the regenerative amplifier that comprises a Ti:Sa oscillator. It is seeded by the Mai Tai Sp, a mode-locked Ti:Sa laser pumped by a diode-pumped, intracavity frequency-doubled Nd:YVO<sub>4</sub> laser that produces a 532 nm cw beam. The seed output was set to 800 nm central wavelength. The pump energy for the amplifier is provided by the Ascend 60, a diode-pumped, Q-switched, frequency doubled Nd:YLF laser that emits a pulsed, green 527 nm beam with a power of 35 W at a repetition rate of 1 kHz.

In short, the seed beam is passing the stretcher, amplified in the RGA's Ti:Sa crystal by the pump beam and then compressed again (details on the procedure of chirped pulse amplification will be given in chapter 3.3.3 looking at a home-built setup). The result is a pulsed beam with a down to less than 35 fs pulse duration at 800 nm wavelength and a repetition rate of 1 kHz. The pulse duration was measured with the PulseScout2 autocorrelator (Newport) to be about 50 fs.

Unfortunately, the laser had some stability issues. Right after installation the output power exceeded 5 W, but multiple times it gradually decreased to below 4 W over the duration of only a few months, sometimes accompanied by a slight shift of the beam direction, and even a designated Spectra-Physics laser technician was not able to retrieve the original settings. The actual maximum power that was achieved under optimal conditions was about 4.8 W and with regular short readjustments about 4.5 W could be maintained, which was sufficient for most measurements.

After leaving the enclosure, the output beam is split into a pump and a probe beam. Due to the high energy of the new laser system the transmission of the first mirror with 99 % reflectivity used to deliver the beam to the pump frequency conversion units was more than enough to run the whole probe section, meaning no additional beam splitter was needed.

The rest of the high output energy was used to power a commercial computer-controlled optical parametric amplifier (OPA) TOPAS Prime+ and associated frequency mixer NirUVis (Light conversion, Spectra-Physics). Those devices provide access to any pump wavelength in the range of 240-2600 nm with output energies of a few  $\mu\text{J}$  up to several hundred  $\mu\text{J}$  depending on the selected wavelength and effort put into the adjustment. A detailed description will be given in the next chapters.

Though the setup of TOPAS Prime+ and NirUVis is highly automated and covers a wide range of wavelengths, it is not without flaws. Due to the mentioned instability of energy and direction of the input beam the required high energy for certain wavelengths to create a homogeneous and stable output could not always be generated. Sadly, this was especially problematic for the frequently used wavelengths close to 400 nm. Moreover, this also demanded frequent manual recalibrations of the computer-controlled parts. Therefore, the more reliable, less demanding SHG/THG Femtokit FK-800-050 from Eksma Optics was integrated as an alternative. Pump beams with 400 nm and 266 nm wavelength can be set up with this arrangement in a very short amount of time and almost independently of the current laser adjustment. The rather simple structure and operating principle will be dealt with in chapter 3.2.3.

In order to be able to use the SHG/THG line a flip mirror was added right behind the “beam splitter” mirror. After passing a Galilei telescope and compensating for the distance travelled inside the TOPAS via several mirrors and a translation stage for rough beam path adjustments, the beam is guided to the Femtokit using two apertures.

Leaving either of the two pump options, a series of four dichroic mirrors DM, the first of which is moved to the selected beam line, is used to clear the beam of any residual beam fractions, which is especially important for the SHG/THG, and delivered to the sample cell C in the measurement area. The structure of the utilized sample cells will be covered in chapter 3.4 after the description of the time-resolved midIR setup as two of the three cells were useable in both the UV/vis and midIR spectral regions.

The probe beam is traversing an equally long path as the pump beams to ensure that pump and probe pulse fractions that were generated from the same pulse simultaneously arrive at the sample cell. A delay between both pulses is achieved with a 16 cm translational stage (M-415.DG, Physik Instrumente) equipped with two mirrors arranged like a corner reflector. Accordingly, the probe beam passes the stage two times resulting in a maximum delay of a little more than 1 ns. One aperture before and one after the stage were used to make sure the beam is not moving while operating the stage. It is then entering the measurement area, which will be described in detail in the next chapter, together and parallel to the pump beam.



### 3.2.2 Measurement area

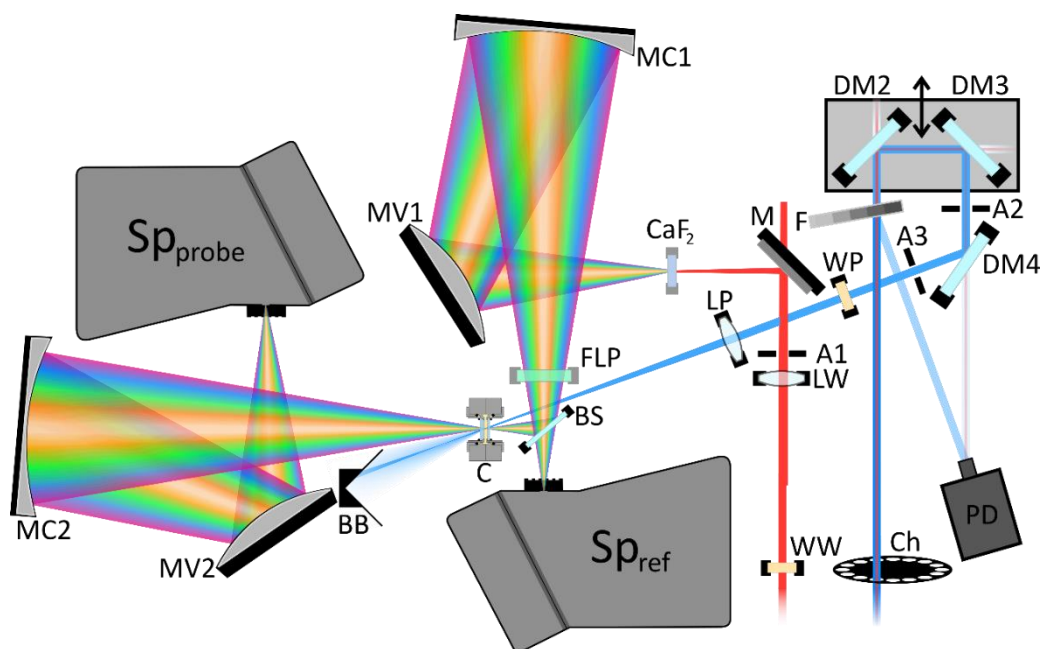


Fig. 12: pump, probe and reference beam trajectories through sample cell and into the respective spectrometers. Abbreviations: F: variable metallic neutral density filter, LP: lens pump, LW: lens for white light generation, CaF<sub>2</sub>: calcium fluoride crystal for white light generation, MC: concave aluminium mirrors, MV: convex aluminium mirrors, FLP: longpass filter ( $\lambda_{\text{cutoff}}=750$  nm), BS: beam splitter ( $R_s=50\%$ ) for splitting into probe and reference beam, C: sample cell, BB: beam block for pump,  $Sp_{\text{probe}}+Sp_{\text{ref}}$ : spectrometer consisting of an imaging spectrograph and a 256 pixel linear imaging sensor for probe and reference beam.

On the way to the sample cell, the pump beam passes a chopper wheel Ch that cuts out every second pulse from the pulse train to be able to get the pump induced absorption changes by calculating the difference spectrum later. The information whether a spectrum was recorded with or without pump excitation, is gained either from the residual transmitting the last dichroic mirror DM4 or from the reflected beam part from a step variable metallic neutral density filter F that is also used to tune down the pump energy. A last aperture A3 is added for fine adjustments. In order to avoid nonlinear effects, especially multiphoton absorption, the pump energy was reduced to preferably  $<1 \mu\text{J}$ . Behind the cell the pump beam and its scattered radiation are blocked by separating it from the white light with a beam blocker BB.

The white light continuum spectrum that is ultimately used to measure the time-resolved UV/vis spectra, is generated by focussing the probe beam with a lens LW ( $f=200$  mm) into a CaF<sub>2</sub> crystal of 2 mm thickness. The ingoing power is reduced with the aperture in front of the translation stage to create an intense, but homogeneous and stable spectrum. Since the nonlinear effects causing this wavelength conversion tend to destroy the material, it is moved up and down constantly with a home-built device. The diverging white light is then focussed into the sample cell C and spatially overlapped with the pump beam. In order avoid aberrations (chromatic aberration and astigmatism) a combination of a convex and a concave mirror MV1 and MC1, which are aligned with a  $90^\circ$  angle between incoming and outgoing beam is used. A longpass filter FLP ( $\lambda_{\text{cutoff}}=750$  nm) removes the 800 nm fundamental. About 6 cm before the sample cell, the white light continuum is split into two fractions by a beam splitter, that has a 50 % reflectivity on s-polarized light. A  $\lambda/2$  waveplate WW behind the translation stage rotates the probe polarisation for equal splitting. The transmitted part is directly entering an imaging spectrograph  $Sp_{\text{ref}}$  (CP140-1825, Horiba) dispersing the spectrum onto a 256 pixel linear image sensor (NMOS S3901-256Q,

Hamamatsu) as an undisturbed reference, while the reflected part is passing the sample cell C and being refocussed with the similar mirror combination MV2 and MC2 into a second structurally identical spectrometer  $Sp_{\text{probe}}$ . The spectral response range of the sensor is 200-1000 nm, though the available setup records a range of about 390 nm that was set to 340-730 nm by default and shifted up to 780 nm for some measurements.

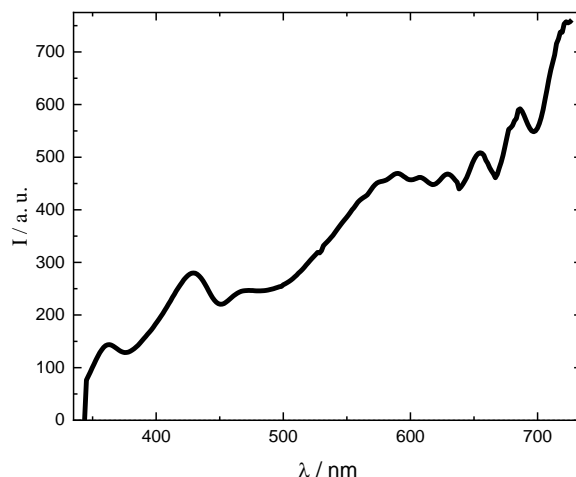
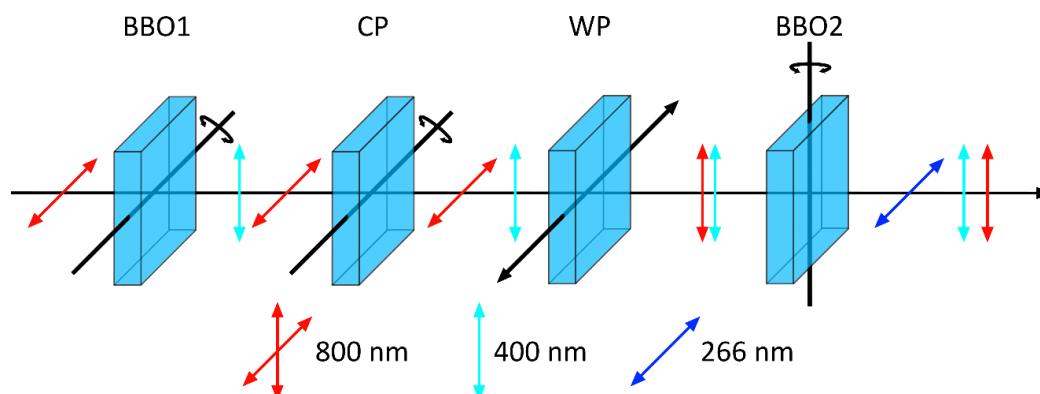


Fig. 13: white light continuum spectrum generated with the time-resolved UV/vis setup.

Pump and probe beam enter the sample cell under an angle of approximately  $10^\circ$ . The pump polarisation is set to  $54.7^\circ$  relative to the probe polarisation with a tuneable waveplate WP to minimize molecular rotational effects in solution. Both beams are focussed, though the probe beam's focal point ( $f = 200$  mm) is inside the cell, while the pump's ( $f = 250$  mm) is behind it. The consequently larger beam diameter (probe:  $80 \mu\text{m}$ , pump:  $200 \mu\text{m}$ ) and therefore lower radiation density prevents the occurrence of unwanted nonlinear optical effects especially within the cell windows and ensures excitation of the complete probe illuminated volume.

### 3.2.3 Pump option 1: linear SHG/THG setup



14: Schematic of the Femtokit for SHG/THG in the time-resolved UV/vis setup. Arrow direction indicates polarization, relative position represents relative delay between pulses of same origin before the subsequent optic. Abbreviations: BBO1: type 1 SHG BBO, P-coated at 400-800 nm, CP: compensation plate consisting of calcite, AR-coated at 800+400 nm, WP: zero order dual waveplate, optically contacted, AR-coated at 800+400 nm, works as  $\lambda/2$  waveplate at 800 nm and as  $\lambda$  waveplate at 400 nm, BBO2: type 1 THG BBO, p-coated at 400-800 nm+266 nm. Adapted from manual to Eksma Optics Femtokit FK-800-050.

Since Kasha's rule<sup>[13]</sup> states that an electronically excited system quickly decays to the lowest electronically excited state of a given multiplicity because of the very fast internal conversion compared to other transitions like ISC and especially radiative relaxation (Kasha 1950), the exact wavelength for electronic excitation of (especially heavier) transition metal complexes is most often inconsequential for the measurement of time-resolved UV/vis and midIR spectra with a temporal resolution of about 100 fs as long as the corresponding absorption coefficient  $\epsilon$  is high enough as the molecules tend to end up in the lowest electronically excited state within <100 fs. Hence, in most cases only two excitation wavelengths, one in the visible, one in the ultraviolet range of the electromagnetic spectrum, are sufficient for electronic excitation.

The Femtokit can generate either the second (400 nm) or the third (266 nm) harmonic from an 800 nm pulsed beam with a pulse duration of 30-70 fs. It works with less than 10 % of the input energy used for the TOPAS Prime+. Combined with its easy application the Femtokit is the preferred setup to generate the pump beam for the time-resolved UV/vis measurements.

The kit consists of four components that are aligned linearly: a type 1 BBO crystal, a calcite plate, a zero-order dual waveplate and finally a second type 1 BBO crystal.

Since the 800 nm input beam is polarized horizontally, the first BBO crystal is mounted with a vertical rotation axis to adjust the phase matching angle. Passing through the crystal, two photons with 800 nm wavelength create the second harmonic with double the frequency or half the wavelength in perpendicular (vertical) polarization superimposing the 800 nm fundamental. Due to the group velocity dispersion the 800 nm fundamental travels faster through the crystal than the generated 400 nm product giving the former a lead over the latter. The following calcite plate inverts the lead. After passing through the waveplate, that rotates the polarization of the fundamental by 90°, while the second harmonic is rotated by 180° effectively maintaining its polarization, both beams arrive simultaneously at the second BBO crystal mounted with a vertical rotation axis matching the vertical polarization. There one photon with 800 nm and one with 400 nm generates the horizontally polarized sum frequency of 266 nm, which equals the third harmonic of three 800 nm photons.

Due to the linear alignment and relatively wide aperture (BBO crystals: 6 mm, plates: 25 mm, beam diameter: about 4 mm) of the optics, the Femtokit can quickly be set up by aligning the input beam with two apertures and adjusting the optic's angles without considering slight beam movement. If only the second harmonic is needed, the second BBO crystal can either be rotated to miss the phase-matching angle or removed completely.

The beam emerging from this SHG/THG setup is a superposition of the fundamental and all created harmonics. Since it does not include any optics to separate the different wavelengths, a series of dichroic mirrors was used to extract the desired wavelength, while delivering the beam to the sample.

## 3.2.4 Pump option 2: OPA + frequency mixer

### 3.2.4.1 Optical parametric amplifier TOPAS Prime+

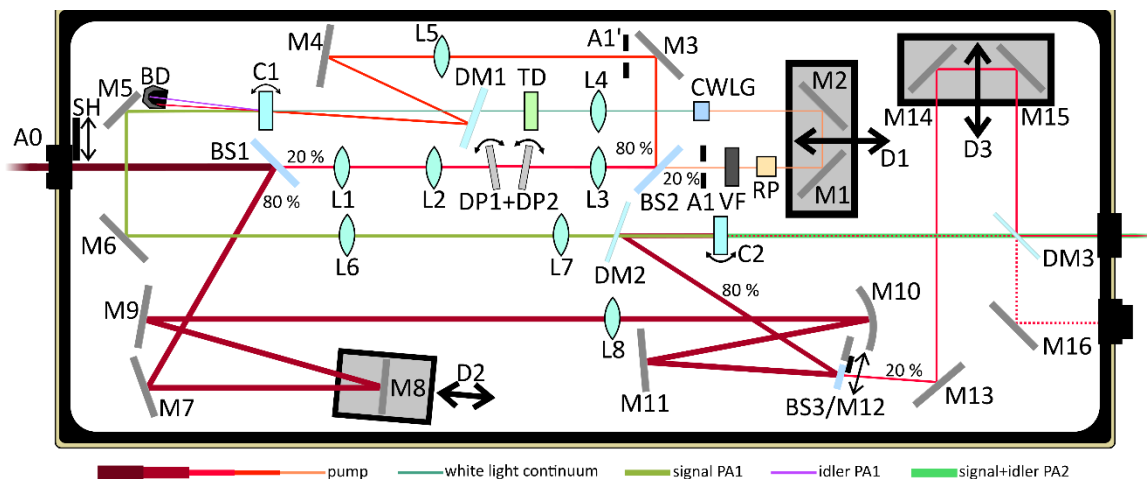


Fig. 15: Optics and beam path in TOPAS Prime+. Abbreviations: A0, A1, A1': apertures, SH: shutter, M1-M16: mirrors, L1-L8: lenses, BS1, BS2, BS3: beam splitters, DM1, DM2, DM3: dichroic mirror, D1, D2, D3: delay stages for PA1, PA2 and fresh pump, DP1, DP2: Brewster angled plates, VF: variable density filter, RP: half-wave plate, CWLG: nonlinear crystal for white light generation, C1, C2: nonlinear crystals for parametric amplification, TD: dispersive plate, BD: beam dump.

In some cases, the selective excitation at a specific wavelength is necessary, either to reach an electronic state that is capable to transition via mechanisms other than IC (for example ISC that is not possible from the lowest excited electronic state) or avoid excitation of specific parts of the sample via a low absorption coefficient as will be important for the donor-acceptor cages. The system of TOPAS Prime+ plus NirUVis frequency mixer can offer exactly that: the generation of a pump beam with a wavelength of 240-2600 nm.

The TOPAS Prime+ is a commercial, in part computed-controlled two-stage OPA that can create an output beam with a wavelength in the range of 1160-2600 nm with 10-20 nm bandwidth using a pulsed, ultrafast, high-power (at least 0.15 mJ, under normal operation about 4 mJ), 800 nm input beam. The configuration used for the time-resolved UV/vis measurements is depicted in fig. 15 and will be described in detail in the following section.

In general, the input is separated into three beams. The mayor part (80-98 % depending on the pump energy) serves as pump for the second amplification stage PA2. From the residual another 80 % are used as pump for the first amplification stage PA1 while the rest is used to create a white light continuum that acts as seed for PA1. The resulting signal beam of PA1 is then used as seed for PA2.

The input beam enters the setup through the aperture A0 in parallel polarisation to the beam plane and passes an opened shutter towards a beam splitter BS1 that reflects the mentioned pump portion for PA2. The transmitting part passes a two-lens telescope L1+L2 that adjusts the beam diameter to be able to pass two Brewster angled plates BP1+BP2. The following lens L3 is used to focus about 20 % of the beam (transmitting the second beam splitter BS2 with reflectivity of about 80%) into a crystal CWLG to create the white light continuum. The aperture A1 and variable density filter VF are used to tune the beam power to obtain a homogeneous and stable white light. The highly divergent beam is then refocused with lens L4 into the nonlinear crystal C1 where the first amplification occurs.

The required pump beam for PA1 consists of the 80 % reflected by BS2 after L3, which creates a focus point before lens L5 that refocuses the beam not into, but right behind crystal C1 in order to not damage it or create any undesirable products of other nonlinear effects due to high intensities. The power can be optimized manually with aperture A1'. The pump beam is then aligned with the seed via a dichroic mirror that transmits the white light, but is highly reflective for 800 nm. Both are, however, not superimposed collinearly, but at a slight angle. In the crystal the seed is amplified via difference frequency generation with the pump. A corresponding idler beam is generated in the process. Due to the beam arrangement the pump beam, the amplified signal beam and the generated idler beam leave the crystal under a corresponding angle and can therefore be easily separated from each other. Pump and idler can be disposed of to the right of mirror M5 in a beam dump BD while the signal beam is delivered to the second amplification stage PA2 via M5 and M6.

In order to be able to choose a wavelength from the white light to amplify, it is stretched in time using a dispersive plate TD. The red part of the spectrum then arrives at C1 before the blue part. By moving the computer-controlled translational stage with mirrors M1 and M2 the beam path length of the white light relative to the pump beam can be controlled. In doing so the part of the spectrum that passes C1 at the same time as the pump is set for amplification. The crystal angle is adjusted accordingly to meet the phase-matching condition. Depending on the wavelength and assuming good settings, the amplified signal beam can have energies of 1-3  $\mu\text{J}$ .

Before crystal C2 for PA2 the diverging signal beam generated from PA1 is collimated and adjusted in diameter with the two-lens telescope L6+L7 and transmitting through the dichroic mirror DM2, which is used to superimpose the signal beam with the pump beam that was separated earlier with BS1. In contrast to PA1, the beams are aligned collinearly since all beam fractions can be used in the later frequency mixing.

In order to ensure the temporal overlap inside C2, the pump beam is redirected with several high reflective mirrors (and a telescope consisting of L8 and M10 to adjust the beam diameter) matching the beam path of pump and seed from BS1 to C2. M8 can be used for rough adjustments, though this is in most cases not necessary and discouraged since it would affect all following alignments. Fine adjustments can be achieved via the afore mentioned Brewster plates. Those are mounted onto computer-controlled rotation stages and can be rotated a few degrees around the Brewster angle against each other creating a small beam path variation without a noticeable displacement.

As was already mentioned, signal, idler and pump can be used in several types of frequency mixing. The setup used in the experiments includes an optional arrangement to replace the residual pump fraction of PA2 with a fresh one, which enhances the properties of wavelengths obtained from sum frequency generation of pump with signal or idler (about 460-600 nm). For that purpose, mirror M12 can be automatically switched with a third beam splitter BS3 via flip mechanism. The transmitting 20 % are temporally aligned with the beam resulting from PA2 by passing a translational stage with mirrors M14 and M15 and spatially with dichroic mirror DM3, that at the same time extracts the old pump fraction on its back side and into a beam dump via M16.

The output of the TOPAS Prime+ consists of the fresh pump fraction and the amplified signal and idler beams. The latter are polarized vertically or horizontally relative to the pump and hence input beam, have an energy of tens to hundreds of  $\mu\text{J}$  (again depending on the wavelength) and can cover a spectral range of 1160-1600 nm or 1600-2600 nm, respectively. In order to obtain wavelengths in the visible and even ultraviolet range, the beams are delivered directly towards the frequency mixing unit NirUVis.

### 3.2.4.2 Frequency mixer NirUVis

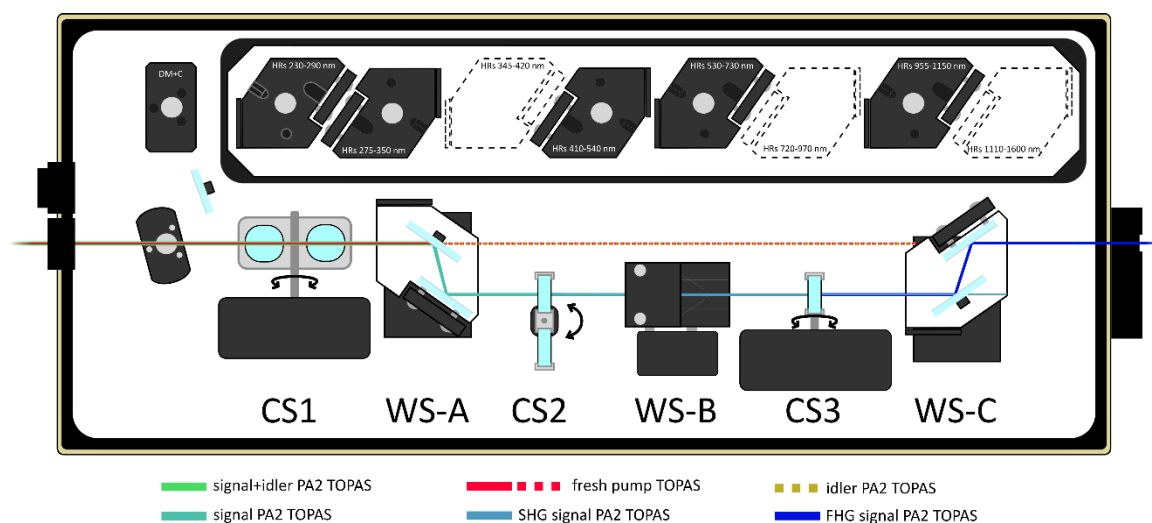


Fig. 16: schematic of the frequency mixer for SFG, SHG and FHG of the TOPAS prime+ output. Abbreviations: CS: rotational state for nonlinear crystals, WS: wavelength separators.

The NirUVis can generate the second harmonic, fourth harmonic and sum frequency from the three components of the output beam of the TOPAS Prime+ by using three nonlinear crystals on computer-controlled rotational stages CS. This opens up a wide range of wavelengths, from about 240 nm to 2600 nm.

In order to select a specific wavelength, all unnecessary beam parts need to be removed. For this purpose, so called wavelength separators WS are inserted on magnetic mounts between the crystals. Those WS consist of two dichroic mirrors that have a high reflectivity for s-polarized radiation in a certain wavelength range. Beam fractions that don't meet the criteria for high reflectivity transmit the first mirror and leave the WS without a meaningful interference or are simply blocked. A suitable beam on the other hand is reflected two times and exits the WS with a displacement of 30 mm. Since the polarisations of signal and idler are orthogonal to each other and their wavelengths are (most of the time) non-degenerate, they can be easily separated from each other with these devices.

The setup has four magnetic mounts, one each behind a crystal (positions WS-A, WS-B and WS-C) to insert a WS for the relevant wavelengths and a special one (DM+C) before the first crystal to remove the signal fraction from the input beam. The latter only consists of one dichroic mirror reflecting the signal beam and a compensator element C that restores the original trajectory of the other fractions after they were slightly displaced upon transmitting the dichroic mirror. At the end of the setup, the resulting beam can exit via one of four output port G1-G4. They take up to three displacements from the WS into account.

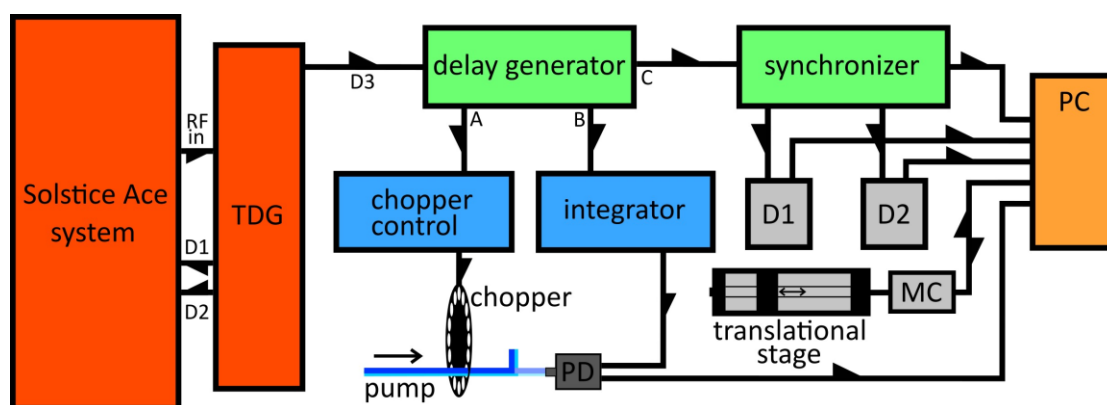
Not all configurations can be discussed here due to the high number of possible combinations of beams, crystals and wavelength separators. Hence only the fourth harmonic generation using the signal fraction of the input beam (FHS), which has been applied for all pump wavelengths that have been used in the measurements, will be described in the following paragraphs.

This configuration can output wavelengths from 345 nm to 425 nm. Since the signal beam is needed for this setup, the DM+C unit was not used. Furthermore, the first crystal is rotated 90° so that the input beam passes over it. At the magnetic mounts the wavelength separators with high

reflectivity for 1110-1600 nm (WS-A), 720-970 nm (WS-B) and 345-420 nm (WS-C) are attached (though other combinations for FHS are possible). WS-A and WS-C are positioned horizontally, while WS-B is vertically owing to the polarisation of the respective beams. Accordingly, the reflected beam is displaced right (WS-A), down (WS-B) and then left (WS-C).

The first WS separates the signal fraction from the transmitting rest of the beam. Within the second crystal the second harmonic is created from the signal beam, whose unconverted fraction is disposed of at WS-B, while the product beam is reflected towards crystal three. Here the fourth harmonic is finally generated, which is cleared from its fundamental with WS-C and delivered to output port G4 with an energy of at least 10 uJ.

### 3.2.5 Electronic control and synchronization



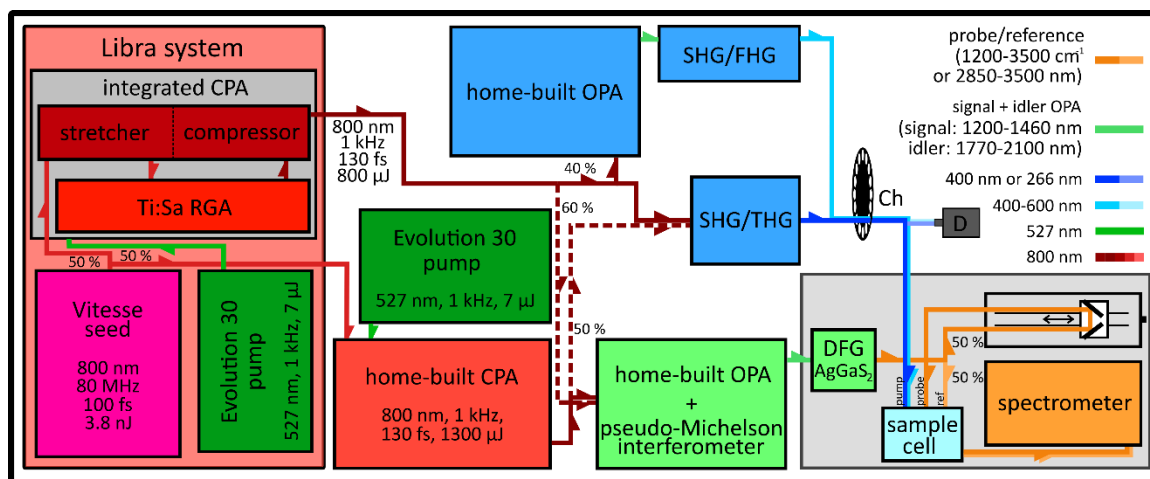
17: Schematic depiction of connections between electronics relevant for the coordination in a time-resolved UV/vis measurement. Abbreviations: RF in: signal recorded from a photodiode measuring the 84 MHz Mai Tai Sp seed laser pulse train, TDG: timing and delay generator, D1-D3: delays created by the TDG, A/B/C: delays created by the delay generator, PD: photodiode to measure the pump pulse train, D1/D2: detector for probe and reference beam, MC: translational stage motor control, PC: computer for data acquisition and device control.

Despite the new laser system, the electronic configuration of the time-resolved UV/vis setup was transferred completely from the trigger for the delay generator onward. Accordingly, the details can be retraced elsewhere<sup>[14],[15]</sup>. Fig. 17 gives an overview of the connections.

Central part of the synchronization is the seed beam in the Solstice Ace laser system, which is measured via photodiode behind a cavity mirror and send as a corresponding electrical signal of 84 MHz as the master clock to the timing and delay generator TDG (Spectra Physics) provided with the laser system. The TDG creates several delays of 1 kHz repetition rate to synchronize the rest of the setup. Delay D1 and D2 trigger the pump pulse generation and the Pockels cell of the RGA within the Solstice Ace system. A third delay gives an external trigger to a second delay generator (DG535 Four Channel Digital Delay/Pulse Generator, Stanford Research Systems, Inc.). From there three more delays are introduced for the chopper control, the integration control of the photodiode that measures the pump pulse timing and a home-built circuit (called synchronizer in fig. 17). The latter triggers the spectrometer for probe and reference and manages the sequential reading of the pixels in the detector diode arrays. Both signals are simultaneously handed to the computer for data processing, where the translational stage is also controlled via a precision motor controller (C-844, Physik Instrumente).

## 3.3 UV/vis-pump-midIR-probe spectroscopy setup

### 3.3.1 General setup



18: schematic depiction of the time-resolved midIR setup. Abbreviations: CPA: chirped pulse amplifier, Ti:Sa RGA: regenerative amplifier with titan sapphire crystal as gain medium, OPA: optical parametric amplifier, DFG: difference frequency generation, SHG: second harmonic generation, THG: third harmonic generation, Ch: chopper wheel, D: photodiode.

The time-resolved midIR setup and its constant updates have been described in multiple publications before. The basic principle and similarities to the time-resolved UV/vis setup were shown before in chapter 3.1. In the following chapters the different sections of the setup will be covered in detail.

At the centre of the setup is the Vitesse laser (Coherent) as a component of the Libra laser system (Coherent). The Vitesse uses an oscillator cavity with a Ti:Sa crystal as its gain medium and generates a red pulsed laser beam at 800 nm central wavelength with repetition rate of 80 MHz, a 100 fs pulse duration and a pulse energy of about 3.8 nJ. The pump energy is provided by the cw diode pumped Nd:YVO<sub>4</sub> laser Verdi (Coherent). It creates a >5 W continuous wave beam at 1064 nm central wavelength that is frequency-doubled to 532 nm using a water-cooled LBO (LiB<sub>3</sub>O<sub>5</sub>) crystal.

The beam emerging from the Vitesse laser is then split into two equal portions that each is amplified in one of two CPAs, one as an integrated part of the Libra system, the other from a structurally very similar home-built CPA unit. Both amplifiers use the same basic structure as the one included in the Solstice Ace system of the time-resolved UV/vis setup: a stretcher, a Ti:Sa oscillator, a suitable pump laser and a compressor. For both the integrated and the home-built CPA one cw diode pumped Q-switched Nd:LYF<sub>4</sub> laser (Evolution 30, Coherent) each provides the pump energy. It creates a pulsed beam with a repetition rate of 1 kHz and an energy of about 7  $\mu\text{J}$  at 527 nm central wavelength due to intra-cavity frequency-doubling of the 1053 nm emission of the Nd:LYF<sub>4</sub> crystal. The outputs of both CPA are very similar: a pulsed beam at 800 nm central wavelength, 1 kHz repetition rate and about 130 fs pulse duration. The difference in energy comes from the replacement of the old degraded grating in the compressor of the home-built CPA resulting in an increase in output energy from about 800  $\mu\text{J}$  to up to 1300  $\mu\text{J}$ . The structure and operating principle of the three CPA will be described in detail in chapter 3.3.3 at the example of the home-built arrangement.



By default, the output of the integrated CPA is used to produce the pump beam, while the one from the home-built CPA powers the conversion units for the probe beam generation. The independent control of the amplifier timings allows to pick different pulses for amplification (one out of 80.000 pulses according to the different repetition rates of amplifier (1 kHz) and seed laser (80 MHz = 80.000 kHz)). This means that, beside the physical delay between pump and probe via a translational stage, an electronic delay up to about 800  $\mu\text{s}$  (limited by detector electronics) in 12.5 ns steps is possible, though the necessary changes in the measurement program could not be implemented properly, yet.

Inspired by previous setups, beam splitters were put behind the CPAs to be able to use pump and probe with only one of the amplifiers in case the other is not working properly for example when a pump laser needs to be fixed. Accordingly, the separated beam fraction is either directed to the respective beam line (pump or probe) or disposed of in a beam dump.

In order to create midIR radiation for the probe beam, the respective 800 nm beam fraction first passes a home-built optical parametric amplifier, that generates and amplifies two NIR beams, so called signal and idler. Those beams are then superimposed spatially and temporally with a pseudo-Michelson interferometer. Both OPA and interferometer are covered in detail in chapter 3.3.4.

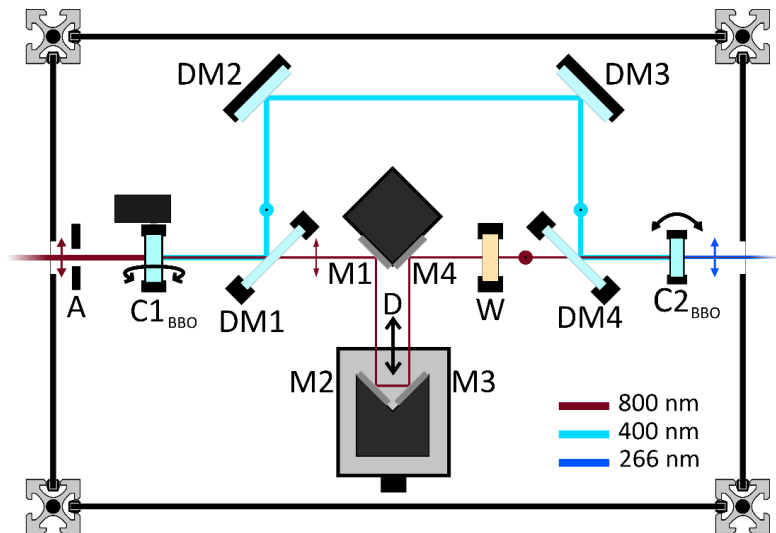
By focussing the beams into a AgGaS<sub>2</sub> crystal in the measurement area a broad midIR beam is obtained via difference frequency generation (DFG) of signal and idler. A reference beam is then separated with a beam splitter and after the rest of the probe beam passes a translational stage, both transmit the sample cell before entering the spectrometer. The rather complex arrangements in the measurement area will be described in chapter 3.3.5.

For the pump beam, two options are available: either an OPA structurally similar to the one for the probe beam (which will not be described further, since it is basically covered with the probe-OPA and was not used for the presented projects anyway) plus two consecutive BBO crystals (crystal 1: vertical rotation,  $\theta = 23.4^\circ$ ,  $\varphi = 90^\circ$ , crystal 2: horizontal rotation,  $\theta = 29.2^\circ$ ,  $\varphi = 90^\circ$ ) to create the fourth harmonic (FHG) of the idler beam or a home-built setup to obtain the second or fourth harmonic of the 800 nm input beam can be used. The latter applies the same principle as the Femtokit from the time-resolve UV/vis setup, but uses a more hands-on approach. It will be described in chapter 3.3.2.

From there the pump beam passes a chopper wheel removing every other pulse which is monitored by a photodiode that measures a residual that transmits a dichroic mirror highly reflective for the respective pump wavelength (400 nm or 266 nm). The pump beam is purged from residuals by seven dichroic mirrors in total, while compensating for the path the probe beam travels inside the OPA, before it enters the measurement area towards the sample cell.

### 3.3.2 SHG/THG with external group velocity correction

The SHG/THG unit of the time-resolved midIR setup in principle works the same as the Femtokit of the time-resolved UV/vis setup: the 400 nm second harmonic is created from the 800 nm fundamental, the group velocity difference is corrected, the polarization of the fundamental is adjusted and finally the third harmonic is generated via sum frequency of fundamental and second harmonic. The setups differ, however, in the method they use for the group velocity dispersion correction. Instead of a calcite plate, their temporal overlap is ensured via a translational stage along the beam path of the fundamental that is separated from the second harmonic by a dichroic mirror and later realigned after adjustment of the polarization.



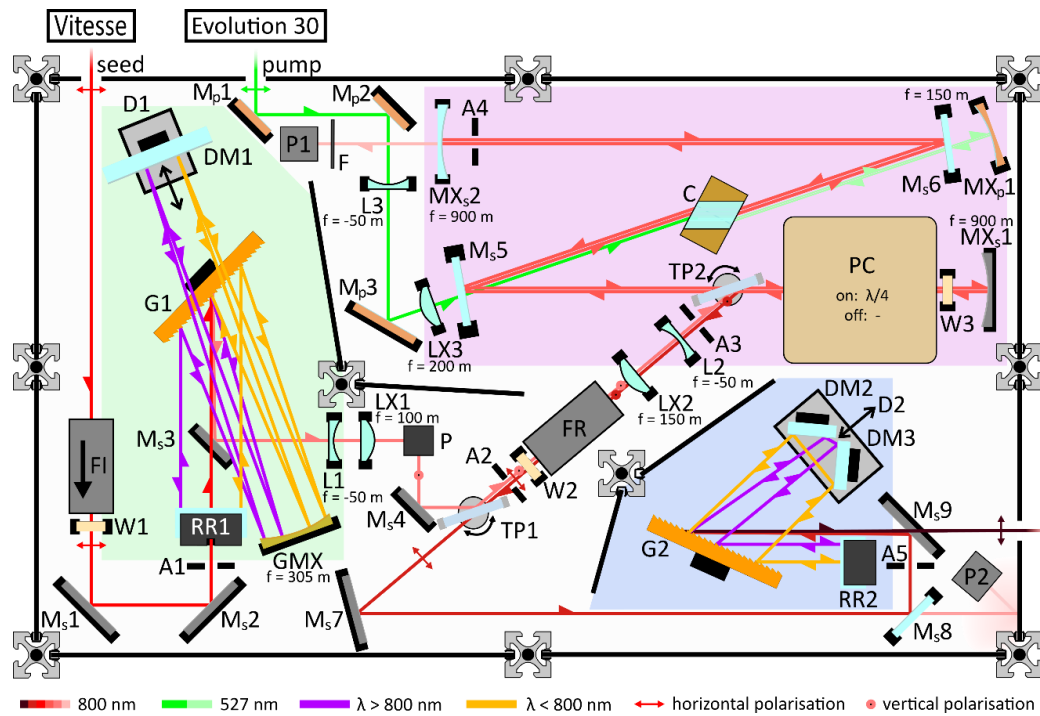
19: Schematic of the SHG/THG arrangement in the time-resolved midIR setup. Abbreviations: M: mirrors HR 800 nm, DM: dichroic mirror HR 400 nm, A: aperture, C1<sub>BBO</sub>: BBO crystal  $\theta = 29.2^\circ$ ,  $\varphi = 90^\circ$ , C2<sub>BBO</sub>: BBO crystal  $\theta = 44.3^\circ$ ,  $\varphi = 90^\circ$ , W:  $\lambda/2$  waveplate at 800 nm set at  $90^\circ$  rotation, D: translational stage for delay between 400 nm and 800 nm beam path.

The correct delay can easily be monitored with the brightness of the resulting beam on a target: the brighter the beam, the more efficient the THG. In case the SHG is needed, either the delay is set far off the optimum or the fundamental is blocked at the translational stage.

### 3.3.3 CPA

A regenerative amplifier of the type used in the presented setups is able to amplify an input beam by a factor of about  $10^6$ . Output energies of up to 1.5 mJ are easily accessible. In order to reach such high energies, the chirped pulse amplification (CPA) technique is used. The idea is to stretch a beam temporally using its finite spectral width, amplifying it in a regenerative amplifier (RGA) and then compressing it back to ideally its former pulse width. The initial stretching or chirp of the pulses prevents damage to the optics and allows higher amplifications in the RGA without the use of more expensive materials. The RGA basically works like a laser. The input beam serves as a seed beam that is amplified by passing an active medium pumped by another intense laser within a cavity.

The home-built CPA in the time-resolved midIR setup is seeded by a portion of the Vitesse seed laser inside the Libra laser system. It exits the system through a designated outlet and is deflected directly into the CPA compartment. At first the beam passes a combination of a Faraday Isolator FI and a  $\lambda/2$  waveplate W1 both set to a rotation of the polarisation plane of  $45^\circ$ . It prevents the seed laser from damage that may be inflicted by amplified pulses reflected back from the amplifier due to possible misalignments. While the Faraday Isolator always rotates in the same fixed direction, the waveplate does so from the perspective of the incident beam. For the incoming beam this leads to a compensation of both contributions leaving the polarization unchanged, while they add up for the returning beam resulting in vertical polarization that is ejected by the Faraday Isolator.



20: Schematic depiction of the home-built CPA used for the probe generation in the midIR setup. Superimposed returning beams are either shown next to each other or indicated by an arrow. Background color coding: green: stretcher, purple: amplifier, blue: compressor. Abbreviations:  $M_s$ : flat mirrors HR 800 nm,  $M_p$ : flat mirrors HR 527 nm,  $MX_s$ : convex mirrors HR 800 nm,  $MX_p$ : convex mirrors HR 527 nm, DM: dichroic mirror HR 800 nm, L: concave lens, LX: convex lens, A: apertures, FI: Faraday Isolator, W1+W2:  $\lambda/2$  waveplates, set to  $45^\circ$  rotation of polarisation, W3:  $\lambda/4$  waveplate, G1+G2: reflective diffraction gratings, 2000 grooves/mm, D1+D2: translational stages, GMX: convex gold mirror, RR: retro reflector, P: periscope, TP: thin film polarizer, FR: Faraday rotator, PC: Pockels cell, C: Ti:Sa crystal mounted in a cooling block, P1+P2: photo diodes, F: absorptive neutral density filter.

Hereafter, the beam is entering the stretcher section via two mirrors  $M_s1$  and  $M_s2$ . It passes through a hole between the two mirrors of the vertical retro reflector RR1 and over stretcher outlet mirror  $M_s3$  directly onto a reflective diffraction grating G1. This optic disperses the beam by reflecting it under an angle depending on the wavelength. The portion of the beam's about 40 nm bandwidth with longer wavelengths are reflected under smaller, the ones with shorter wavelengths under bigger angles compared to the central wavelength of 800 nm. This introduces the desired stretch or chirp of the pulse since the beam path through the stretcher becomes longer and the delay therefore greater with decreasing wavelength akin to positive group-velocity dispersion. After diffraction, the at first spatially broadened beam hits a concave gold mirror GMV positioned at the first diffraction maximum of the grating, that focusses the beam onto a flat dichroic mirror DM1 with high reflectivity around 800 nm. From there it is reflected to the gold mirror and back to the grating that is diffracting the beam for a second time. Due to a slight tilt of DM1 the beam can then hit the retro reflector RR1 returning the beam passing all stretcher optics in reverse with a vertical shift downwards and hence leaves the section via  $M_s3$ .

Subsequently, the beam diameter is widened with a Galilei telescope and the plane of polarization is turned from horizontally to vertically by passing a periscope. With this polarization the beam is totally reflected by the thin film polarizers TP1 and TP2 into the amplifier cavity. Between the polarizers another  $\lambda/2$  waveplate W2, a Faraday Rotator FR and a Galilei telescope are placed in the beam path. The telescope reduces the beam diameter. The W2/FR combination works similar to the FI/W1 one before the stretcher as the incoming beam's polarization is unchanged, while the polarization of the outgoing amplified beam is rotated from vertical to horizontal. However, the latter beam is not ejected, but separated from the former by transmitting through the polarizer TP1.

Right after entering the cavity between the concave mirrors  $MX_s1$  and  $MX_s2$ , the beam is passing a Pockels cell PC and a  $\lambda/4$  waveplate W3. In its voltage free state, the Pockels cell is not affecting the polarization of the beam, so only the waveplate changes it to circular polarisation. After back reflection at the first cavity end mirror  $MX_s1$ , the beam is again only transformed by the waveplate, resulting in horizontal linear polarization. This allows the beam to transmit through the polarizer TP2 and remain in the cavity for amplification. The cavity itself is folded in a z-shape by mirrors  $M_s5$  and  $M_s6$  with a water-cooled Ti:Sa crystal C in the focus of the cavity end mirrors. The pulse built-up can be monitored with a photodiode P1 measuring a residual transmitted through  $MX_s2$ .

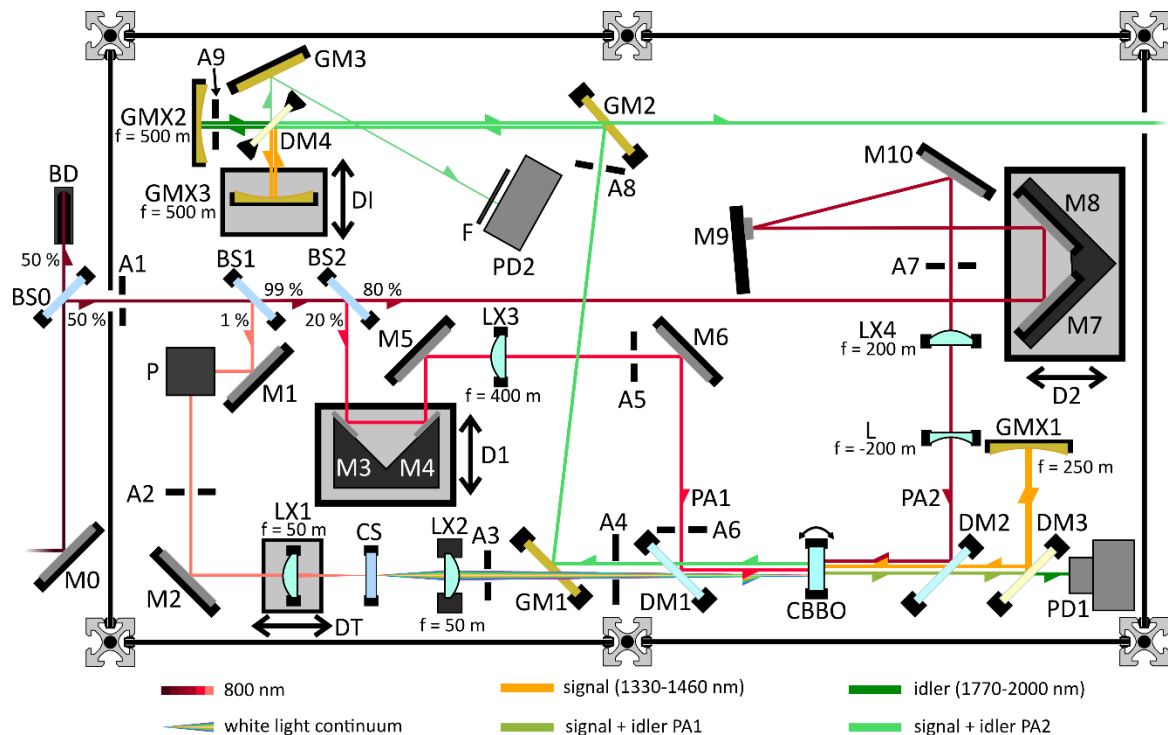
The energy for amplification is provided by another Evolution 30 pump laser structurally identical to the one inside the Libra laser system. The beam is aligned with the seed beam in the cavity by mirrors  $M_p1$ ,  $M_p2$  and  $M_p3$  and focussed into the Ti:Sa crystal via lens LX3 while transmitting through  $M_s5$ . After the crystal it passes through  $M_s6$  and is reflected and refocussed back into the crystal by the concave mirror  $MX_p1$ .

When the seed beam is passing the crystal, it receives the pump energy stored inside the crystal via stimulated emission resulting in its amplification. Mirror  $MX_s2$  returns the beam back enabling a second traversing through the crystal. In order to prevent a pulse from leaving the cavity for multiple round trips of amplification, a voltage is applied to the Pockels cell that then operates like a  $\lambda/4$  waveplate. The pulse passes both PC and W3 twice, rotating the polarization by  $180^\circ$  maintaining the horizontal polarization, and is therefore held inside the cavity as long as the voltage is upheld.

Following a few round trips within the cavity the amplified pulse is ejected by releasing the voltage and being reflected by TP2 due to its resulting vertical polarization. On its way back the Galilei telescope is widening the beam diameter and, as mentioned before, the beam polarization is rotated by  $90^\circ$  by the FR/W2 combination, enabling it to transmit through TP1. Mirrors  $M_s7$ ,  $M_s8$  and  $M_s9$  then deliver the beam to the compressor section.

The compressor is reversing the effect of the stretcher by inverting the wavelength dependence of the beam path. Portions with longer wavelength travel a longer path than those with shorter wavelengths like a material with negative group-velocity dispersion would do. Coming from mirror  $M_s9$  the beam is diffracted by a grating G2 structurally identical to G1. An arrangement of two mirrors positioned at an angle of  $90^\circ$  towards each other on a translational stage returns the beam with a horizontal shift for a second diffraction. The spatially broad beam then hits a vertical retro reflector to introduce a vertical shift upwards in order to leave the CPA compartment above  $M_s9$  after following the preceding beam path in reverse passing the grating four times. The resulting beam has a diameter of about 5 mm, a pulse duration of about 100 fs and a mean energy of 1.3 mJ. The beam energy after amplification can be monitored for optimization by a second photodiode P2 that measures radiation of a residual beam scattered on the wall of the CPA encasing after transmitting through  $M_s8$ . The compression needed for ideal operation of the following OPA can be adjusted via translational stage D2.

### 3.3.4 OPA



21: Optics and beam paths in the OPA for midIR probe pulse generation of the time-resolved midIR setup. Beams that are superimposed or vertically offset are depicted side by side for clarity. Abbreviations: M: mirrors HR 800 nm, A: apertures, BS: beam splitters, DM1+DM2: dichroic mirrors HR 800 nm, HT 1100-1600 nm, DM3+DM4: dichroic mirrors HR 1170-1470 nm, HT 1650-2500 nm, GM1+GM2: gold mirrors, GMX: concave gold mirrors, L1-L4: concave lenses, LX: convex lens, PD1, PD2: photodiodes, D1, D2: delay stages PA1 + PA2, DT: delay stage of lens for white light generation, DI: delay stage for pseudo-Michelson-interferometer, P: periscope, Cs: sapphire crystal, CBBO: BBO crystal  $\theta = 27^\circ$ ,  $\varphi = 0^\circ$ .

Just as was described for the time-resolved UV/vis setup, the optical parametric amplifier for the time-resolved midIR setup was merely used to amplify a given seed beam, but rather to generate a beam with tunable wavelength. This OPA consists of two collinear amplification stages that occur in the same BBO crystal to create NIR radiation to later generate midIR radiation via DFG<sup>[16],[17]</sup>.

As was mentioned before, the output of the preceding CPA unit is not directly fed to the OPA, but deflected to a beam splitter BS0 with 50% reflectivity at 800 nm wavelength, which means about 600-700  $\mu\text{J}$  are used for operation. The transmitting 50% is generally disposed of in a beam dump BD, though an arrangement for pump generation has been set up in case the internal CPA unit of the Libra system is not working properly.

Right after entering the OPA compartment and passing a first aperture A1 for alignment, the beam is split into three fractions by two beam splitters BS1 and BS2. The first one reflects 1% of the beam as seed for the first amplification stage, the second one separates 20% from the residual for the pump of the first amplification stage and the transmitting portion is used as pump for the second stage.

The seed beam is at first deflected into a periscope P shifting it upwards, then passes aperture A2 and is reflected towards a lens that focusses the beam just behind a Ti:Sa crystal. The emerging white light continuum is focussed into a BBO crystal, but not before traveling barely over a gold mirror GM1 (usually a minor portion of the lower part of the beam is blocked by the mirror) and through a dichroic mirror DM1. A2 is used control stability and quality of the white light.

The first pump beam passes a translational stage to ensure the temporal overlap of pump and seed in the BBO crystal, a lens to create a focus in the crystal and two apertures A5 and A6 for alignment. The pump is adjusted with M6 to hit DM1 at the point where the seed leaves it after transmitting and both beams are aligned collinearly. In the BBO crystal the seed beam is amplified by the pump via difference frequency generation while an idler beam is created as a side product. The BBO crystal is mounted with a vertical rotational axis. Depending on the angle, the phase-matching condition is met for a specific range of wavelengths of the white light. Behind the crystal the signal and idler beam transmit through DM2 while the residual pump is reflected and since only the signal is needed, it is separated by DM3. The idler is used to monitor and optimize the temporal and spatial overlap of pump and seed with photodiode PD1.

The signal beam serves as seed for the second amplification stage. It is returned to and focussed via the concave gold mirror GMX1 with a slight tilt downwards into the crystal about 2 mm below the beams of the first stage. The pump beam is traveling over translational stage D2, aligned by aperture A7, superimposed with the signal/seed beam at and with DM2 and focussed into the BBO crystal with lenses LX4 and L. Again, the seed is amplified and an idler beam is generated at the expense of the pump beam. The residual pump is separated by the dichroic mirror DM1 and signal and idler can hit the gold mirror GM1 below the incoming white light.

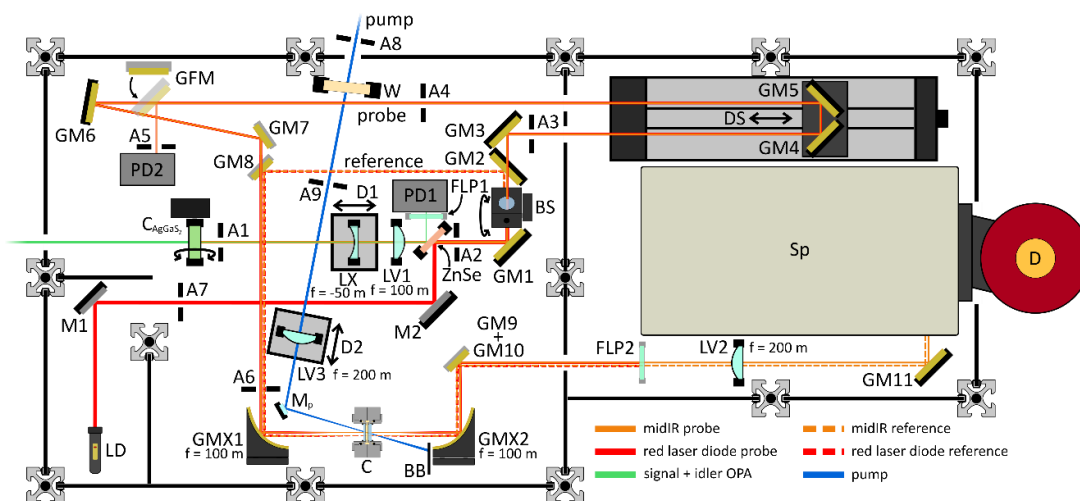
At this point the collinearity and temporal matching in both amplification stages can be verified. Due to secondary nonlinear processes signal and idler are superimposed by weak green and yellow beams, that can be used to adjust the angle between respective seed and pump beams. A weak blue beam created from the pump indicates a temporal mismatch in the second amplification stage.

In order to ensure the temporal overlap of the spatially superimposed signal and idler after amplification for the subsequent midIR formation via difference frequency generation, the beams are directed towards a pseudo-Michelson-interferometer with a gold mirror GM2. It separates signal and idler by reflecting the latter with a dichroic mirror DM4 towards a concave gold mirror GMX3 on a translational stage DI moved with a piezoelectric motor and corresponding control (Piezo Driver PD 3, Spindler & Hoyer). The signal beam transmits DM4 and is returned by a fixed gold mirror GMX2 that is identical to GMX3. On their way back both beams are realigned traveling slightly upwards to pass over GM2 and out of the OPA compartment. A minor fraction of both beams exits the interferometer towards gold mirror GM3 interfering with each other. The resulting beam intensity, which is recorded via photodiode PD2, correlates with the delay between signal and idler. With this information the temporal match can be adjusted using DI targeting local and global interference maximum for optimal alignment.

### 3.3.5 Detection

The last compartment contains the final frequency conversion unit to create midIR radiation, a translational stage for pump-probe delay adjustment, the sample cell, a spectrometer and a detector.

Coming from the pseudo-Michelson interferometer, the signal and idler beams of the OPA are focussed into a AgGaS<sub>2</sub> crystal to create the difference frequency between them. It can be rotated around a horizontal rotational axis perpendicular to the beam trajectory in order to meet the phase-matching angle corresponding to the wavelengths of the created signal-idler pair. With this setup a range of 1300-3500 cm<sup>-1</sup> is available, but the intensity drops significantly below 1400 cm<sup>-1</sup> and above 2300 cm<sup>-1</sup>. Due to the intense absorption of gaseous CO<sub>2</sub> and water in the air in large parts of this range, the compartment is constantly flooded with dry nitrogen gas on measurement days. On days with high humidity, silica dry pearls can be added to adsorb water.



22: Schematic depiction of the midIR generation and measurement area. Abbreviations: M: flat mirrors HR 800 nm, GM: flat gold mirrors, A: apertures, LX concave lens, LV, convex lens, D1+D2: translational stages for lens focus adjustment, ZnSe: zinc selenide plate, FLP: longpass filter ( $\lambda_{\text{cutoff}}=2400$  nm), PD: photodiode, LD: laser diode, BS: beam splitter, DS: translational stage for pump-probe delay, GFM: gold flip mirror, GMX: concave gold mirror, C: sample cell, SP: spectrometer, D: detector, W:  $\lambda/2$  waveplate for 400 nm or 266 nm,  $M_p$ : flat mirror plate HR 400nm or 266 nm, BB: beam blocker,  $C_{\text{AgGaS}_2}$  = nonlinear  $\text{AgGaS}_2$  crystal for midIR generation from OPA signal and idler,  $\theta=45^\circ$ ,  $\varphi=41.5^\circ$ .

The diverging beam is collimated with a Galilei-telescope LX+LV1 and then hitting a ZnSe plate that is transparent in the midIR, but reflects radiation with higher or lower wavelength, including signal, idler and other secondary beam components. The reflected part is passing a longpass filter FLP1 to remove beam fractions in the visible range and the remaining intensity is measured by photodiode PD1, which can be used as a second control mechanism especially for the spatial overlap of signal and idler in the pseudo-Michelson-interferometer. Since the transmitting midIR beam is invisible, it is superimposed with the red beam of a laser diode LD at the back of the ZnSe plate in order to be able to adjust it further on.

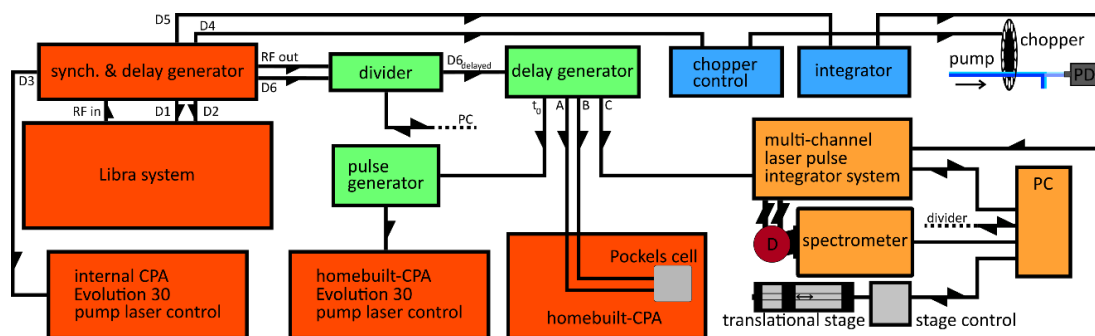
With the visible aid, the beam is deflected into a beam splitter BS that splits off a reference beam. The beam splitter is built similar to a wavelength separator except it does not contain dichroic mirrors, but a  $\text{BaF}_2$  plate and a gold mirror. The former transmits a fraction of the beam depending on the angle of incidence while the rest is reflected downwards to the gold mirror leaving the beam splitter parallel to the transmitted portion with a down shift. In order to avoid repeated reflections creating a series of pulses, the surfaces of the  $\text{BaF}_2$  plate are not perfectly parallel to each other, but angled at about  $1^\circ$ . The beam splitter is rotated to create a 50:50 split of the beam.

The reference beam hits the gold mirror GM2 traveling a short way towards the sample cell to arrive before the probe beam, which crosses over GM2 and is reflected by GM3. From there it traverses a computer-controlled motorized 250 mm translational stage (M-ILS250CCL, Newport Corp.) that can introduce a probe pulse delay of up to 1.6 ns. The pump path is usually set so that a pump-probe delay of -200 ps to 1300 ps is possible. The rest of the stage provides room for corrections of the zero-delay point. After this, the beam passes the gold mirrors GM6 and GM7 and is aligned 15 mm above the reference beam.

Both beams are then focussed into the sample cell with a spherical parabolic gold mirror GMX1, crossing paths in the cell, and after leaving it collimated with another spherical parabolic gold mirror GMX2 that is mirror inverted to GMX1. The vertically stacked mirrors GM9 and GM10, the upper one of which is used for the reference, the lower one for the probe, deflect the beams. They then pass a longpass filter FLP2, removing the red beam of the laser diode, are focussed with lens LV2 and enter the spectrometer Sp (Chromex 250is, Bruker optics) via mirror GM11.

The grating within the spectrometer diffracts probe and reference according to their wavelengths and focuses the spectrally separated beams onto each of a 32 pixel HgCdTe diode array of a detector D cooled with liquid nitrogen (MCT-32/2-10, Infrared associates Inc.).

### 3.3.6 Electronic control and synchronization



23: Schematic depiction of connections between electronics relevant for the coordination in a time-resolved midIR measurement. Abbreviations: RF in: signal recorded from a photodiode measuring the 80 MHz Vitesse seed laser pulse train, RF out: undisturbed output of the RF in, D1-D6: delays created by the synchronization and delay generator SDG Elite,  $D6_{\text{delayed}}$ : D6 delayed by a multiple of 12.5 ns,  $t_0$ : undisturbed output of  $D6_{\text{delayed}}$ , A/B/C: delays of created by the delay generator, PD: photodiode to measure the pump pulse train, D: detector, PC: computer for data acquisition and device control.

The electronic makeup of the time-resolved midIR setup has been altered even more often than the optical structure, though this mostly entailed a change in the connections of delay outputs. The most notable change preceding the measurements was the inclusion of a device for the electronic delay control between pump and probe. This, however, did not influence the general functioning of the setup and, since the electronic delay was not used in the presented measurements, it was set to zero electronic delay. A schematic depiction of the connections between electronics that were relevant for the coordination during an experiment is shown in fig 23.

Starting point is the optical output of the Vitesse seed laser that is measured with a photodiode inside the Libra system. The resulting electrical 80 MHz signal is passed to a synchronization and delay generator (SDG Elite, Coherent) and serves as a master clock for the SDG. From there all timings of the pump section are synchronized directly using pulsed electrical signals of 1 kHz repetition rate. The voltage of the Pockels cell inside the Libras CPA unit is controlled via two delays and the internal Evolution 30 pump laser is synchronized with it. A home-built device called chopper control receives another signal from the SDG and controls the chopper wheel, which is positioned in a way that the pump pulses are not cut off. A photodiode that measures a fraction of the pump pulse behind the chopper wheel, integrates the irradiated light over time even from scattered light by building up a corresponding charge. A home-built integrator activates it shortly before a pump pulse arrives and lets it release its charge shortly afterwards. Only every second pump pulse passes the chopper wheel, which means that every other measurement of the photodiode only releases a minor charge (due to the scattered light). This information is transferred to a multi-channel laser pulse integrator system (IR-6416, Infrared Systems Development Corporation), which also receives spectral data from the detector, which can then be sorted into data recorded with and without pump excitation.

For the electronic pump-probe delay option the probe section control is centred at a second delay generator (DG535 Four Channel Digital Delay/Pulse Generator, Stanford Research Systems, Inc.). The external trigger of the delay generator does not come directly from the SDG, but from a home-built device called divider. It receives an 80 MHz and a 1 kHz output from the SDG and



creates a 1 kHz electrical signal that can be delayed by up to 80.000 times 12.5 ns relative towards the respective pump pulse, which is controlled by a computer. All subsequent timings are then delayed accordingly.

With the delays coming from the delay generator the Pockels cell of the home-built CPA and the corresponding pump laser (via a pulse generator (model 8011A, Hewlett Packard)) are synchronized. Moreover, a delay sets the timing of the multi-channel integrator similar to the pump photodiode, though the integration duration is set with the computer.

The computer also reads and sets the position of the probe delay stage and of the grating in the spectrometer, which are later translated into delay time and wavelength at a respective pixel on the detector. That information is finally synchronized with the data received from the multi-channel integrator.

### 3.4 Sample cells

For the sample cell three options were available. Less demanding samples, e. g. without (significant) susceptibility to exposure to water (either within the solvent or airborne) and/or oxygen can be probed in a 2 mm far UV quartz cuvette (Starna, transmission: 170-2700 nm) capped by a Teflon plug. A magnetic stir bar is added to the cuvette and rotated from the outside by a motorised magnet to constantly supply fresh sample into the illuminated volume. For compounds with a minor sensitivity, the plug is sealed with parafilm. Those cells were used for some quick first time-resolved UV/vis measurements on the cage molecules.

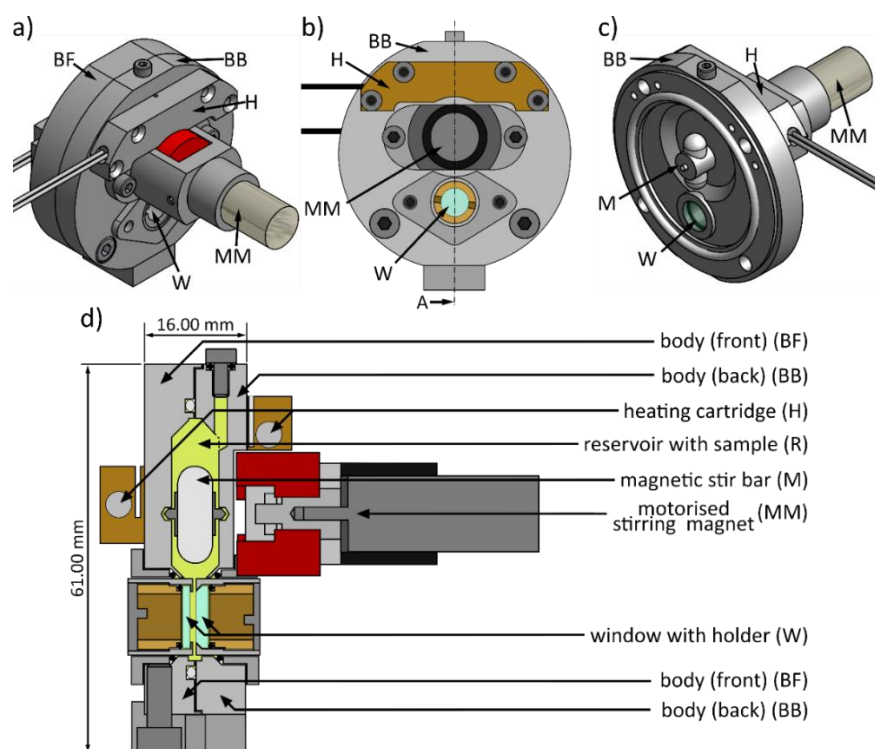


Fig. 24: Schematics of the heatable hermetic stainless-steel cell. a) angled view of the back side, b) rear view, c) angled view of the inner side of the back half, d) cross section perpendicular to b) at A.

Highly fragile samples are transferred from inside an inert gas filled glove box into an air-tight custom stainless-steel cell consisting of two halves with each one 1 mm thick  $\text{CaF}_2$  window transparent for both UV/vis and mid IR radiation sealed with Teflon and Perfluoroelastomer (FFKM) O-rings. It encloses a volume of about 3 mL due to a reservoir above the windows that is constantly stirred by a magnetic stir bar moved from the back of the cell by a motorised stirring magnet powered by a tunable laboratory power supply (RNG 1502, MC Power) at about 8 V. The base cell was described before, but it was modified in two aspects (see fig. 24). The windows, once glued to the steel body, are now encased in structures that can be fixed with variable distances between them creating optical paths down to 0.6 mm. Additionally, the sealing O-rings are more resistant than the two-component glue to a greater variety of solvents. For particularly strongly absorbing samples and solvents, windows with a conical cut were purchased and the casings were tailored accordingly to create a level surface. With those conical windows on both sides of the cell arbitrarily small optical paths can be achieved, though viscosity and surface tension of the solution pose a limit since the sample mobility between the windows might get reduced. For all measurements presented here, a plane window for the front and a conical for the back side of the cell were used. The second modification is the addition of heating cartridges and a thermal sensor to the front and back of the cell close to the reservoir to enable temperature dependent measurements up to about 120 °C. The cartridges are powered by a laboratory DC power supply (Digi 35, Voltcraft) at 24 V and controlled by a Eurotherm 3216 temperature regulator.

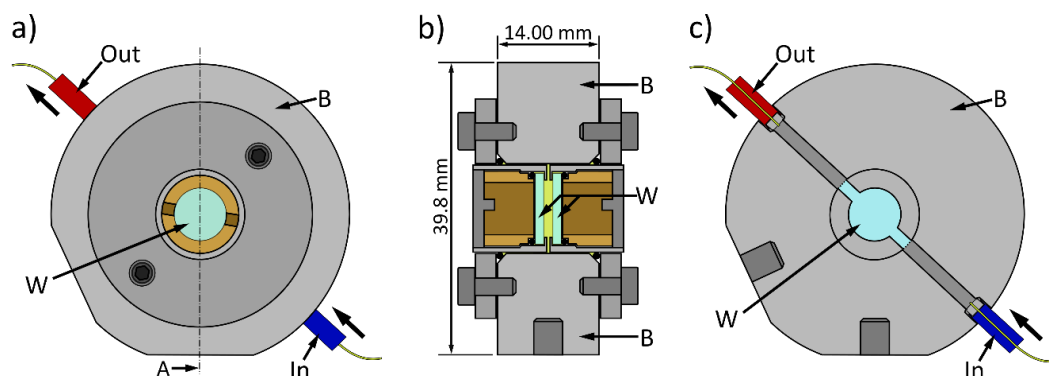


Fig. 25: Schematics of the stainless-steel flow cell. a) front view, b) cross section perpendicular to a) at A, c) cross section parallel to a). Abbreviations: B: cell body, W: window in holder, In: inlet from pump, Out: outlet back to pump.

Some samples are irreversibly converted into photoproducts upon excitation, reducing the educt concentration during a measurement whenever hit by a pulse. At high conversion rates this can be observable at the gradually decreasing or increasing absorption at certain wavelengths and pump-probe delays. Spectra of such compounds can be measured in a stainless-steel flow-through cuvette or flow cell, where the solution is pumped in a circle between a 10 mL reservoir and the cell by a magnetic drive gear pump (GA-X21.P8FS.B, Micropump). Due to the large volume the photoproduct is diluted and the educt concentration is approximately unchanged, however, a proportionally high amount of compound is needed. The cell consists of a singular body that can hold the same windows and respective casings as the heatable hermetic stainless-steel cell. Accordingly, the optical path can be adjusted from both sides as well. The sample solution is pumped through Teflon tubes (inner dia.: 0.75 mm, outer dia.: 1.59 mm, Techlab) connected via fittings with cutting rings (1/4" or 6.35 mm UNF, Techlab) into the lower corner of the cell, passes the space between the windows, leaves the cell on the opposite side, where it flows through another tube back into the reservoir of the pump. Since the measurements on the cage molecules were not reproducible with the simple quartz cuvettes, the irreversible formation of a photoproduct presumably connected to a charge transfer was assumed. Therefore, all final time-resolved UV/vis and midIR measurements were conducted in the flow cell. The optical path was adjusted to 0.9 mm.

## 3.5 Data acquisition and processing

### 3.5.1 Time-resolved UV/vis measurement

#### 3.5.1.1 Data acquisition

The measurements as well as the preceding adjustments were controlled with a program that was created by Dr. Arne Walter in Vee Pro<sup>[14]</sup>. Details about its operating principle are described in his thesis.

Occasionally the wavelength of the pixels of both detectors were calibrated using well-known emission lines of mercury and neon lamps. Additionally, before a measurement the offset due to the surrounding light conditions the detectors pick up is subtracted since they work in the visible range.

In the adjustment tab of the program the current measured spectra are depicted, typically averaged over 100-300 pulses. With the help of this visualization the probe and reference beam are adjusted to reach the detectors. The white light continuum was set to a stable, at best uniform intensity over the whole spectrum using the aperture before the translational stage.

Depending on the selected pump option the fundamental was either just passed through the SHG/THG compartment or into the TOPAS prime+ and frequency mixer units, which were set to the respective wavelength and optimized using the provided programs. The pump is then arranged to pass the chopper wheel without cutting pulses and its intensity is attenuated with the variable metallic neutral density filter and finetuned with an aperture. Subsequently, it is roughly overlapped with the probe beam within the sample cell.

For the exact spatial and temporal overlap two dyes were used: stilbene for the lower pump wavelengths around 266 nm and coumarin 153 for those around 400 nm. Both were diluted in ethanol. These dyes produce very intense difference spectra and have long lifetimes in their excited states, which makes finding the overlaps very easy. At first the spatial overlap is found by crossing the pump with the probe beam until a signal is visible in the program. This signal is then optimized and the pump intensity is set to produce a moderately intense spectrum. The temporal overlap is then found by moving the translational stage forth until the probe beam arrives at the sample cell before the pump. Right before the zero delay point waves appear on top of the sample spectrum that stem from Raman signals of the solvent (Ahrens 2017). Due to the dispersion of the white light the temporal overlap of the red part of the spectrum is a little later than that of the blue part. The zero point is set somewhere within this range.

Before a measurement a file needs to be set up that gives the program the information at which delays spectra should be recorded. This file does, however, not contain the delays themselves, but codes them with the number of steps and the width of each step. The information is then translated within the program. During a measurement the delays are passed several times. This helps to identify, if a sample gets destroyed during a measurement as the intensity of the spectrum slowly changes between each run. Usually, 2-3 runs are used with 200 pulses averaged for each spectrum that is put out.

For every sample measurement a solvent measurement is needed with equal settings to avoid introducing additional noise when the solvent is subtracted during data processing. At the same day one measurement of the solvent is sufficient for all samples.

### 3.5.1.2 Data processing

Data processing was achieved with scripts in MatLab® R2017b that were created during preceding theses<sup>[14],[15],[18]</sup>. The general function will be described here. Further details are referred to in the corresponding publications.

The measurement file that is output by the computer consists of one column with 257 rows, the delay time and corresponding 256 intensities measured by each pixel, times the number of delays that were measured. In a first step this file is converted to a matrix with delays in the first column, wavelengths, which are pulled from the calibration file, in the first row and the intensities at the corresponding entries. If the spectra did not significantly change between the runs, all spectra at the same delay are averaged. From spectra measured at negative delays, meaning when the pump arrived after the probe pulse at the sample, a baseline is created that is subtracted from all spectra. Due to the group velocity dispersion, the speed at which light travels through a material depends on the wavelength. Accordingly, the red part of the white light continuum arrives faster than the blue part at the sample. This dispersion is corrected using a polynomial of typically third or fourth order (see fig. 26). The same procedure is applied to the sample and the solvent measurement, the latter of which is subsequently subtracted from the former with a scaling factor that is derived from comparison of the intensities of the Raman signals from the solvent that appear close to the zero delay point. The resulting data matrix is typically plotted as spectra depending on the delay time or as transients for different wavelengths

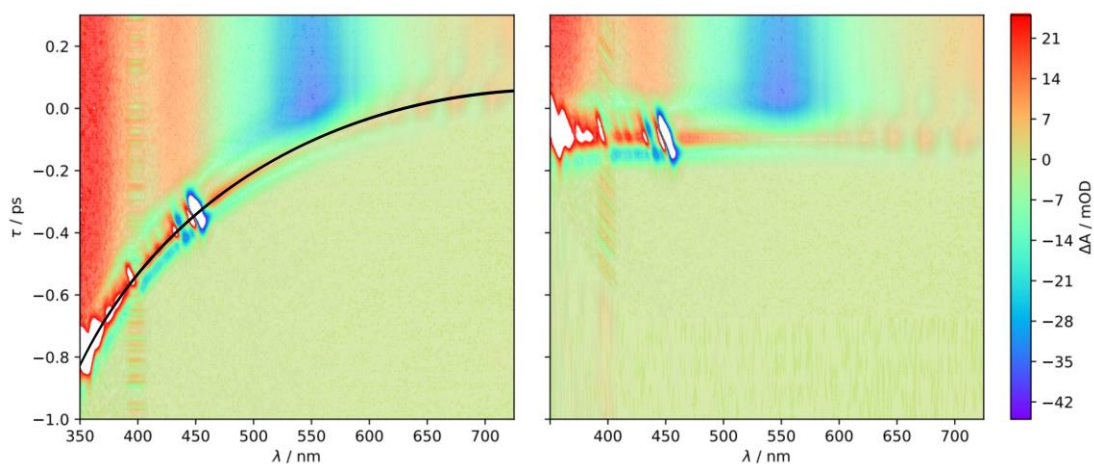


Fig. 26: time-resolved UV/vis data before (left) and after (right) dispersion correction.

## 3.5.2 Time-resolved midIR measurement

### 3.5.2.1 Data acquisition

Since the spectral window of a measurement is limited to about  $100 \text{ cm}^{-1}$  (depending on the central wavenumber) and further narrowed by the non-uniform intensity of the midIR beam, a typical time-resolved midIR measurement consists of multiple measurements at slightly shifted central wavenumbers that are merged during the data processing step. The measurement control and first processing are done via a program written in LabVIEW™. The details can be learned from previous publications<sup>[15],[19],[20],[21]</sup>.

A few days before a measurement the OPA and, if necessary, the CPA are adjusted to gain a high-intensity low-noise midIR beam. The program depicts the intensity of both probe, reference and pump intensity that arrive at the detector or respective photodiode averaged over a specified number of pulses (during the adjustment 100-300 pulses) and calculates the difference spectrum on the spot. In a first step the central wavelength measured by the detector is selected with the program and the BBO and Ag<sub>2</sub>Ga<sub>2</sub>S crystal orientation are adjusted accordingly. For the first measurement the wavenumber of the most intense absorption peak in the ground state IR spectrum of the sample is selected. The slit width at the entrance of the detector is modified in the program to receive a good signal without oversaturating the diode array.

The pump beam is adjusted to pass the chopper wheel without cutting off pulse fractions, passes a  $\lambda/2$  waveplate to rotate the polarization to the magic angle ( $54.7^\circ$ ) towards the probe beam and is roughly overlapped with the probe beam at the position, where the sample is measured. In the measurement program, an intensity threshold for the signal from the photodiode measuring the pump pulses is set between the value with and without pump to enable the program to distinguish between related spectra.

To find the spatial and temporal overlap between pump and probe a silicon wafer or a germanium plate is used as a test sample. Both generate very intense long-lived signals over almost the complete available spectrum from their UV/vis pump induced band gap transition. At first the spatial overlap is found by moving the pump beam over the probe beam on the sample surface until a signal of the test sample is visible in the measurement program. With apertures and neutral filters, the pump intensity is then adjusted to, if possibly, below 1  $\mu\text{J}$ , but at least a value with which a bleach signal is visible. When the signal is optimized, the stage is moved via the program until it vanishes to find the rough temporal overlap. From a short measurement around this stage position the exact time of zero pump-probe delay is found and calibrated in the program.

Before a measurement a number of parameters is entered into the program: the central wavenumber of the measurement, the delay times that transfer to delay stage positions and the number of times each delay is measured, the number of pulses averaged for each spectrum (for a measurement 1000-2000 pulses) and some comments regarding pump intensity, sample concentration and other details.

After a measurement, the central wavenumber is moved by 10-50  $\text{cm}^{-1}$  in the program and the crystals are adjusted accordingly. Given a correct beam alignment in the OPA, this should not affect the beam intensity arriving at the detector. The new central wavenumber is filed in the program and the measurement is started under the same conditions.

### 3.5.2.2 Processing

The time-resolved midIR spectra were processed completely by a program written by Hendrik Vennekate. The details are described in his thesis<sup>[19]</sup>.

Similar to the processing of the time-resolved UV/vis data the spectra at the same delays were averaged given the intensity does not change significantly in between runs. Then a baseline was generated from some spectra with negative delays of at least -20 ps and subtracted from all spectra (fig. 27 b)). The spectra are linearly shifted and tilted and therefore have to be further offset-corrected (fig. 27 c)). This procedure is repeated for all measurements, which are subsequently merged together.

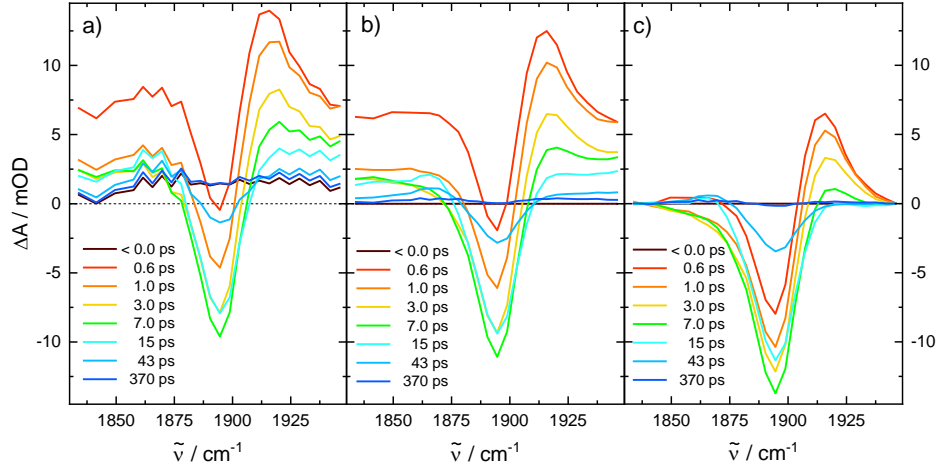


Fig. 27: time-resolved midIR data processing. a) raw data, b) baseline subtracted, c) offset aligned.

### 3.5.3 data interpretation

The decay of a state regarding a single relaxation process with the time constant  $\tau$  can generally be described with an exponential function of the shape<sup>[4]</sup>

$$s(t) = A_0 \cdot e^{-\frac{t-t_0}{\tau}} \quad \text{eq. 039}$$

With  $t_0 = 0$ . Before excitation the signal stays at zero due to the mentioned baseline correction and would jump up right to the value of the amplitude  $A$ , if the pump beam would be an infinitely short burst of energy. This is factored in with the Heaviside-function (Abramowitz 1972)

$$H(t) = \begin{cases} 0 & \text{at } t < 0 \\ 0.5 & \text{at } t = 0 \\ 1 & \text{at } t > 0 \end{cases} \quad \text{eq. 040}$$

that must be multiplied with  $s(t)$  to receive the system response function

$$r(t) = s(t) \cdot H(t) \quad \text{eq. 041}$$

However, the real pulse width induces a gradual excitation and must therefore be accounted for in the evolution of the response function  $s(t)$ . Assuming a temporal pulse profile of gaussian shape

$$g(t) = \frac{1}{\sigma\sqrt{2\pi}} \cdot e^{-\frac{1}{2}\left(\frac{t-t_0}{\sigma}\right)^2} \quad \text{eq. 042}$$

for the instrument response function the convolution of  $r(t)$  with  $g(t)$  must be generated to accurately describe the measured signal:

$$I(t) = \int_{-\infty}^{+\infty} r(t') \cdot g(t-t') dt' \quad \text{eq. 043}$$

$$= \frac{1}{2} A \cdot e^{-\frac{\sigma^2 - 2\tau(t-t_0)}{2\tau^2}} \cdot \left( \operatorname{erf} \left( \frac{\tau(t-t_0) - \sigma^2}{\sqrt{2}\sigma\tau} \right) + 1 \right)$$

Multiple parallel relaxation paths can be described with a sum of their respective response functions

$$I(t) = \sum_i^n \frac{1}{2} A_i \cdot e^{-\frac{\sigma^2 - 2\tau_i(t-t_0)}{2\tau_i^2}} \cdot \left( \operatorname{erf} \left( \frac{\tau_i(t-t_0) - \sigma^2}{\sqrt{2}\sigma\tau_i} \right) + 1 \right) \quad \text{eq. 044}$$

$I(t)$  can also be used to approximately describe more complex relaxation processes, but a correct analysis in these cases can usually only be attempted by setting up a suitable kinetic model with the corresponding rate equations and solving the resulting equation system regarding the population of the different states.

No matter the chosen approach, in order to receive the desired parameters, especially the time constants  $\tau_i$  and the amplitudes  $A_i$ , the respective functions have to be fitted to the measured data by varying the parameters  $A_i$ ,  $\tau_i$ ,  $\sigma$  and  $t_0$ . If multiple wavelengths of the same measurement were fitted simultaneously, a time constant  $\tau_i$  was set equal for all fits. From this global analysis the amplitudes as a function of the wavelength can be generated.

A plot of the amplitudes  $A_i(\lambda)$  vs  $\lambda$  for the respective time constant  $\tau_i$  are called decay associated spectra (DAS). These spectra show at which wavelength a measured signal rises or falls with the corresponding time constant. Each DAS spectrum therefore depicts the decaying bands of one state and the growing bands of newly populated ones. Since those bands are frequently superimposed in UV/vis spectra, it is rarely possible to generate a spectrum of an excited state from them, but sometimes additional information about the relaxation processes can be gained.

For the data analysis according to eq. 044, the program OriginPro® 2022 was used. The construction of a kinetic model, solution of the corresponding rate equation systems and fitting of data to the model was achieved by the program Mathcad 15.0.

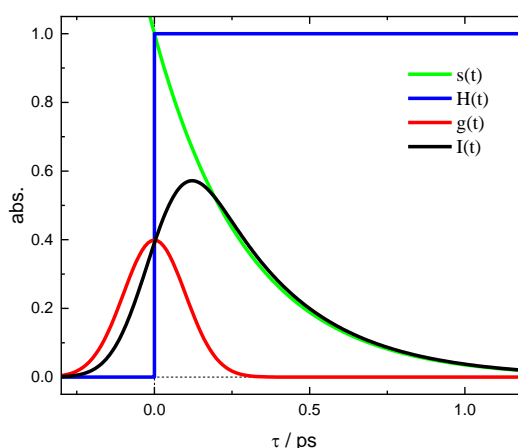


Fig. 28: exponential function  $s(t)$ , Heaviside function  $H(t)$ , gauss function  $g(t)$  and resulting response function  $I(t)$  for the kinetic data analysis.





## 4 Projects

The demand for renewable sustainably produced energy is constantly rising not just for environmental, but also financial reasons. The harvesting of practically unlimited energy sources that are freely available for almost everyone like wind and solar energy is in the long term undoubtedly preferable to sources like coal, oil, gas or nuclear energy that have to be tediously mined, can cause environmental damage both in the short- and long-term and/or will inevitably run dry. Especially the conversion of sun light into electricity is an intensively researched field that generated a plethora of approaches most of which involve the well-known solar cells. The typical solar cell consists of silicon or other inorganic semiconductor materials with high efficiencies of 27.6% for the popular single crystal silicon cell up to 47.6% for recently developed highly efficient multijunction cells<sup>[22]</sup>. Though these cells more often than not recuperate their cost within their life cycle, the initial high expenses present a major obstacle for most people. Therefore, there is a great effort to create cheaper organic or at least hybrid solar cells. Their comparatively low efficiency of about 10-15%<sup>[23]</sup> was considerably improved in the last years approaching 20%<sup>[24]</sup>. Aside from the costs, organic solar cells have many other advantages: they are flexible, light, work with weak or diffuse light and can be tailored to the spectrum of the sun. Moreover, the developed materials can also be used for other applications like light emitting diodes (OLEDs), sensors and or transistors. These are more than enough reasons to search for suitable new materials.

A requirement of a material for the use in those electronic devices is the generation of charges, more importantly separated charges or more specifically an electron and its corresponding hole. In the typical semiconductor solar cells charges are separated via photoinduced transition from the valence into the conduction bands, which are superpositions of a multitude of atomic or molecular states in a crystal structure that practically equal a continuum contrary. The excitation does not directly create an electron that can be harvested at an electrode, but a hydrogen atom-like state, the exciton, due to the electrostatic attraction to the positively charged hole. In order to be able to use the charges they have to be separated before the charges recombine. This can happen during the diffusion of the charges through the material. The longer the lifetime of the exciton is, the more likely it is that the charges get separated and can reach the respective electrode.

The equivalent of excitons in organic molecules and transition metal complexes is a charge-transfer state. The electrons are transferred between two sections of the molecule, but are bound electrostatically as a pair of radicals until the charges are separated and can be removed at an electrode. The primary objective to improve the efficiency of solar cells and other devices based on photoinduced charge separation is to extend the lifetime of the respective charge-transfer state by stabilizing it. In the context of this thesis two approaches are presented and investigated.

The first project group in chapter 4.1 deals with self-assembled cage molecules that are built from donor- and acceptor-type ligands coordinated by Pd(II) cations. The ligands consist of a chromophore backbone that is covalently connected via a linker to an anchor group, in all three cases a pyridyl ring, that coordinates to the palladium. Excitation of either of the chromophores is supposed to induce a ligand-to-ligand charge-transfer (LLCT) between donor and acceptor (DACT). The idea is that the coordination instead of a covalent bond between donor and acceptor reduces electronic coupling hindering an electron-hole recombination, while at the same time providing the possibility of self-healing as those complexes can reconnect autonomously. Additionally, their size can be tailored via the linker to increase the donor-acceptor distance further reducing the probability of recombination<sup>[25]</sup>. The reduced coupling, however, can also

decrease the probability a CT even occurs. Moreover, due to the autonomous assembling several different conformers can be assembled. These problems have already been observed with a cage complex with ligands based on phenothiazine (PTZ) as a donor and anthraquinone (ANQ) as an acceptor that performed photoinduced charge-transfer, but did not only form statistically mixed cages, but mixed double cages.

The first two projects address these issues by not only introducing the backbones fluorenone (FLO) and triphenylamine (TPA) as new chromophores, but also by using their different length and inflection to force a specific coordination. The third project on the other hand uses a different approach. Using a cage purely with ligands with a PTZ backbone the acceptor is moved from a cage building block to a host inside the cage. This reduced the distance, but potentially increases the coupling and might be used to secure or transport reactive molecules or serve as a reactive centre akin to enzymes<sup>[26]</sup>. These projects demonstrate that the morphology of these self-assembling cage complexes can be controlled while maintaining the ability to perform the desired charge-transfer.

The second project group in chapter 4.2 approaches the challenge to improve the CT lifetime from another angle. Since a CT state produces radicals on both sides, molecules in such states tend to have side reactions. In order to prevent those reactions a second reaction step, be it a coupled proton transfer or a second CT, could be used to stabilize the first one. For this purpose two photoactive centres based on Ru(II) and Ir(III) polypyridine complexes were coupled to a W(II) complex to each create a heterobinuclear complex. The photocentres are well-known for their efficient conversion into a triplet metal-to-ligand charge-transfer (<sup>3</sup>MLCT) state. From this state a subsequent metal-to-metal charge-transfer (MMCT) coming from the W(II) is proposed. In order to maximize the potential coupling between the metals the smallest ditopic ligand, an alkyne with two donor groups imitating a phenylpyridyl ligand (ppy), is bound to the Ru(II)/Ir(III) while the W(II) is side-on coordinated to the alkyne  $\pi$ -bond. Though a pure MMCT could not be observed, this project showed rich photophysics regarding electron density shifts within the complex and especially an unusually efficient vibrational energy transfer to an anharmonically vibrating carbonyl ligand.

## 4.1 Project 1: donor-acceptor charge-transfer in self-assembling Pd(II) complexes

### 4.1.1 Introduction

Self-assembling complexes have a rather rich history. Beside rather simple structures like cages<sup>[27],[28],[29]</sup>, grids<sup>[30]</sup> and rings<sup>[31]</sup> more complex configurations like interpenetrated knots<sup>[32],[33]</sup> and cages<sup>[34],[35],[36]</sup> are already well-known. Though the simple batch synthesis is a huge advantage for their potential commercial viability, it is often connected to uncertainties in the primary structure that is constructed. And the number of possibilities rises with the number of components added to the components, which can create a broad distribution of properties. Therefore, it makes sense to look for methods to control the assembling process or at least heavily favour one structure over the other. Since the synthesis of covalent bridges is counterproductive to the point of self-assembling, the morphology of the ligands themselves is a reasonable approach. The question arises then, however, how much the ligand morphology can be changed to generate a specific structure without dramatically changing the properties of the complex.

This consideration plays a primary role for self-assembling donor-acceptor cages that are supposed to perform charge-transfer transitions. The ligands in those complexes should be as long as possible to build distance between donor and acceptor for a long lifetime of the CT state, but long ligands create large cavities within the cage that can be filled with nodes of other cages as was observed for a phenothiazine (PTZ) and an anthraquinone (ANQ) based ligand that formed intercalated double cages both in their pure donor and acceptor cages  $[\text{Pd}_4\text{D}_8]^{8+}$  and  $[\text{Pd}_4\text{A}_8]^{8+}$  as well as in the mixed cage  $[\text{Pd}_4\text{D}_m\text{A}_{8-1}]^{8+}$ . Though the mixed cage actually was able perform a DACT<sup>[34],[35]</sup>, there was room for improvement regarding morphology control.

To prevent the uncontrolled formation of cage structures new ligands were introduced to force a defined cage morphology and investigated with time-resolved UV/vis and midIR spectroscopy on their relaxation dynamics after photoexcitation to evaluate if they can perform a DACT as well. In chapter 4.1.3 a cage made from PTZ and fluorenone (FLO) based ligands is covered, chapter 4.1.4 deals with a cage that switches the PTZ for a triphenylamine (TPA) ligand. In chapter 4.1.5 a different approach is examined, where the acceptor is wrapped inside the cavity of the donor cage with a similar PTZ ligand. But before all of that the bedrock for these projects, the time-resolved measurements on the PTZ-ANQ cage by Dr. Jennifer Zimara, former Ahrens, are shortly summarized.

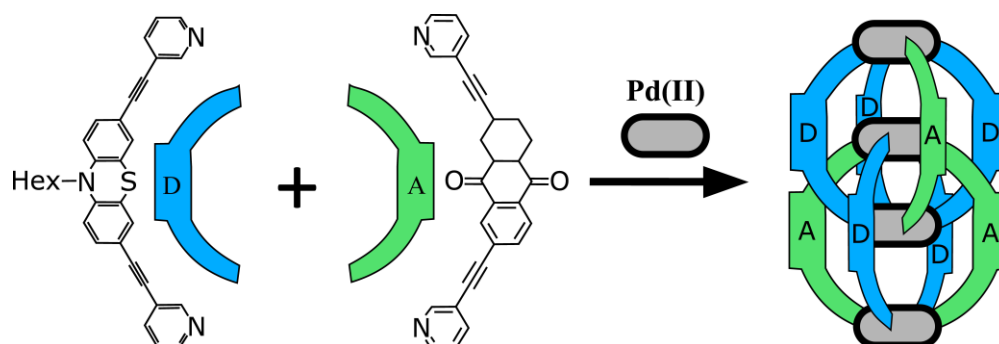


Fig. 29: molecular structure of the PTZ donor and ANQ acceptor ligands and one example structure from a statistical distribution of mixed cages.

## 4.1.2 Previous work on the PTZ ligand

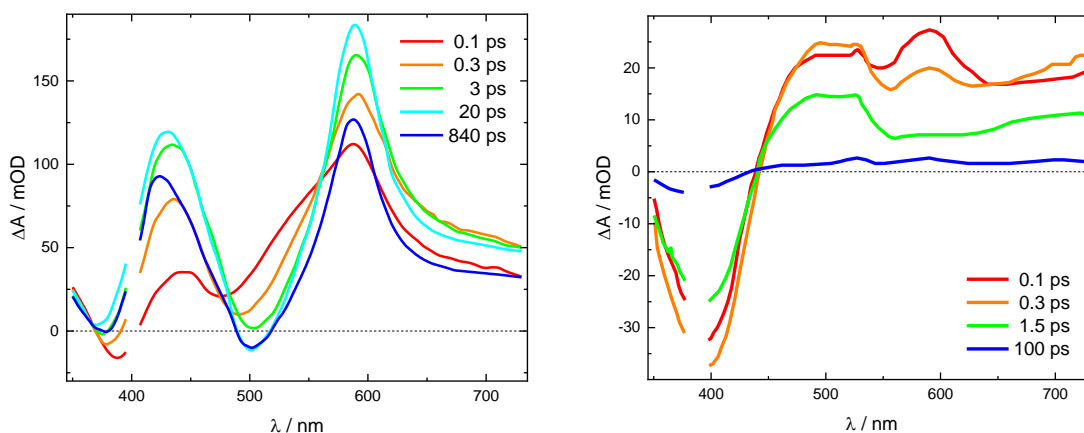


Fig. 30: time-resolved UV/vis spectra of the free PTZ donor ligand (left) and the PTZ donor cage  $[\text{Pd}_2\text{D}_4]^{4+}$  in acetonitrile at selected pump-probe delays after excitation at 400 nm. Data reproduced after Frank et al.<sup>[34]</sup>.

PTZ and ANQ are frequently used chromophores that are especially useful in cage structures due to their reversible and via side chains tunable oxidation or reduction potentials<sup>[37]</sup> and simultaneous structural integrity<sup>[36]</sup>.

Excitation of the PTZ donor ligand at 400 nm in acetonitrile leads to a long-lived excited state that is assigned to an intramolecular charge transfer (ICT)<sup>[15]</sup> with a broad excited state absorption band with two maxima at about 435 nm and 590 nm intersected at 390 nm by the ground state bleach and at about 480 nm by a fluorescence band<sup>[34]</sup>. Within a few picoseconds the excited state absorption and emission spectra increase in intensity, hence it can be assumed that both occur from the same excited singlet state. During this evolution the emission spectrum shifts to lower energies<sup>[35]</sup> indicating vibrational or structural relaxation possibly including solvent relaxation due to an intramolecular charge transfer within the PTZ ligand. These initial evolutions can be described by two time constants  $\tau_1 = 0.3$  ps and  $\tau_2 = 7.6$  ps. After the relaxation the spectrum keeps almost completely unchanged in accordance with the long lifetimes of multiple phenothiazine derivatives<sup>[38],[39]</sup>.

The time-resolved midIR spectra corroborated those measurements<sup>[35]</sup>. Upon excitation at 400 nm both bleaches and very intense excited state peaks appear, the latter of which grow with a time constant of  $\tau_1 = 2$  ps in reasonable agreement with the 0.3 ps and 7 ps from the transient UV/vis spectra. The high intensity of the excited state compared to the ground state absorption further reinforces the interpretation of the transition at 400 nm as an ICT as it would potentially produce a larger dipole derivative. The long lifetime  $\tau_3 \gg 1$  ns again coincides with the long-lived fluorescent singlet excited state. However, a second time constant  $\tau_2 = 120$  ps was necessary to fit the decay satisfactorily, which was assumed to come from a shorter-lived conformer.

Complexation with Pd(II) completely changes the spectral properties of the donor ligand. The overall transient UV/vis absorption (fig. 30 right) is a lot weaker. Evidence for the ICT singlet excited state appears right upon illumination with a band at 590 nm that is very short-lived though ( $\tau_1 = 0.2$  ps). Accordingly, the emission is almost completely quenched. During the singlets decay, a spectral pattern, superimposed by the ground state bleach at 390 nm, with remarkable similarities (especially the characteristic peak at 530 nm) to the electrochemically generated difference spectrum of the oxidized donor cage<sup>[34]</sup> or the ground state absorption spectrum of PTZ derivative radical cations<sup>[40]</sup> emerges. Slight differences can be explained with the disparity

between photophysical one-electron transition and uncontrollable electrochemical oxidation, but the semblance clearly indicates the formation of one radical cation of the PTZ ligand in the cage. The transition is attributed to an LMCT to one of the Pd(II) ions directly coordinated to the excited PTZ ligand. This charge separated state, however, has a very short lifetime ( $\tau_{CT} = 1.3$  ps) and the cage returns back to its electronic ground state via back electron transfer (BET) within about 6 ps. A residual of unknown origin remains after 100 ps. Though there is no clear evidence, an LMCT between cages of a double-cage could be assumed for this longer time constant. The presumably small Pd-PTZ electronic coupling compared to the coordination within a cage would support the small band intensities due to the low transition probability and a rather long lifetime ( $\tau = 0.9$  ns) for the BET.

The transient midIR data show ground state bleaches along with one peak at  $1585\text{ cm}^{-1}$  that decays with a time constant of  $\tau_1 = 1.1$  ps after excitation at 400 nm. The position of the excited state peak matches reasonably well with DFT calculations of the donor radical cation  $D^{\bullet+}$  that predict a peak at  $1559\text{ cm}^{-1}$ . During the decay of the  $D^{\bullet+}$  peak weak absorptions on the low energy side of the bleaches appear with a decay time constant of  $\tau_2 = 15$  ps. They were attributed to vibrational cooling of the hot electronic ground state that is generated after BET from the LMCT state as was proposed from the time-resolved UV/vis data. The initial singlet excited state was probably not observed due to its low intensity because of the ultrashort lifetime compared to the free ligand. The absence of a second intense peak that should appear at  $2184\text{ cm}^{-1}$  according to DFT calculations was attributed to an overestimation of the donor radical cations ethynyl stretching mode. Again, some residual remains at the same peak positions and with a similar proportion to what was observed in the time-resolved UV/vis spectra, though there is no excited state peak of the donor radical cation left. Overall, the proposal of  $D^{\bullet+}$  formation via LMCT and subsequent back electron transfer was strengthened by time-resolved midIR spectroscopy.

The time-resolved UV/vis and midIR spectra of the mixed PTZ-ANQ cage show signals of both  $D^{\bullet+}$  and the acceptor radical anion  $A^{\bullet-}$  as was deduced from comparisons to spectra of the electrochemically generated analogues<sup>[34]</sup> and DFT calculations<sup>[35]</sup>. The interpretation was a successful ligand-to-ligand or donor-acceptor charge-transfer (LLCT/DACT) from PTZ to ANQ that due to the statistical distribution of PTZ and ANQ in the cage has a lifetime of 1 ps to > 1 ns.

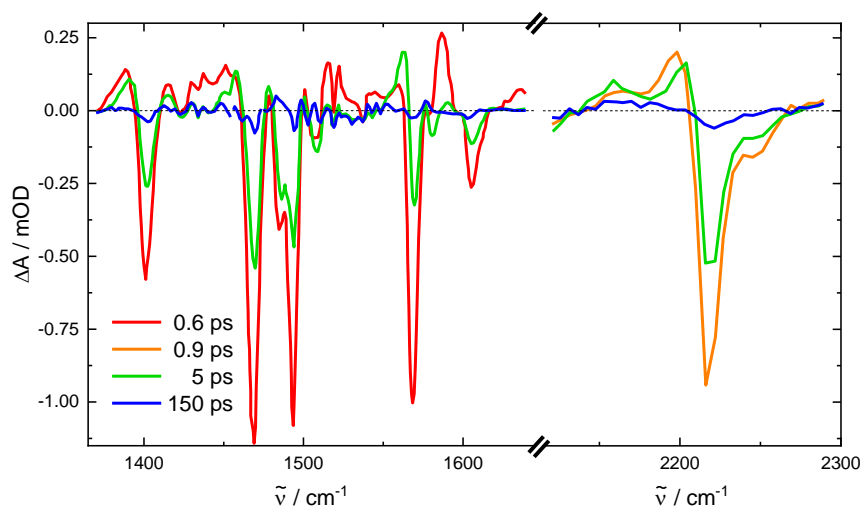


Fig. 31: transient midIR difference absorption spectra of the phenothiazine donor cage  $[\text{Pd}_2\text{D}_4]^{4+}$  in  $\text{CD}_3\text{CN}$  ( $1340\text{--}1670\text{ cm}^{-1}$ ) and  $\text{CD}_2\text{Cl}_2$  ( $2120\text{--}2285\text{ cm}^{-1}$ ) at selected pump-probe delays after excitation at 400 nm. Data reproduced after Ahrens et al.<sup>[35]</sup>.

## 4.1.3 Phenothiazine-fluorenone-donor-acceptor cage

### 4.1.3.1 Introduction

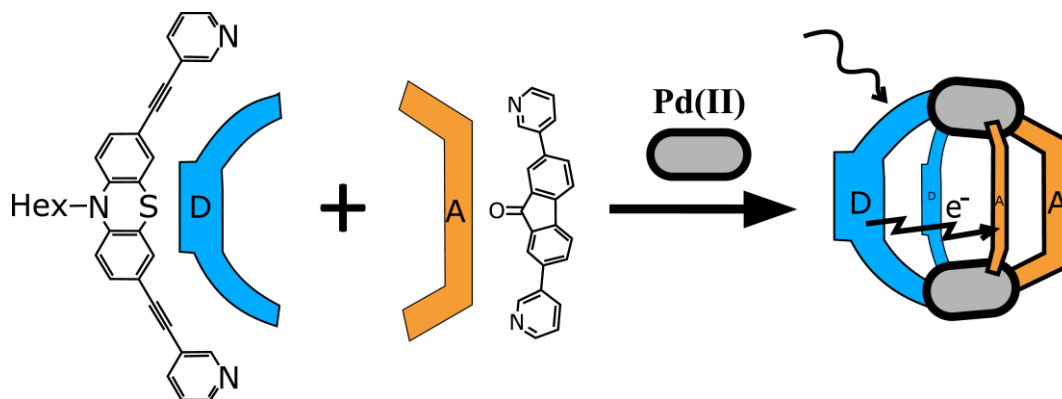


Fig. 32: molecular structure of the PTZ donor and FLO acceptor ligands and schematic structure of the mixed cage.

The first donor-acceptor cage, synthesized by Dr. Kai Wu, was built from the same PTZ donor ligand as in the PTZ-ANQ cage and a new fluorenone based acceptor ligand FLO. Similar to PTZ, FLO is a well-known chromophore that is frequently used as an acceptor in donor-acceptor dyads and polymers<sup>[41]</sup>.

The PTZ ligands consists of the PTZ backbone with a hexyl-group on the nitrogen for increased solubility in organic solvents and two 3-pyridyl-anchor-groups connected in 3,7-position to the backbone via ethynyl-groups. The FLO based acceptor ligand that has two pyridyl-groups directly connected in 2,7-position. Due to their vastly different length and inclination those two ligands are only assembling in one conformation: a single cage with two donor and two acceptor ligands binding onto the Pd(II) in cis-position towards each other forming  $[\text{Pd}_2\text{D}_2\text{A}_2]^{4+}$ .

Unlike the mixed cage, the FLO ligand alone forms three different coordination structures with Pd(II) with the general chemical formula  $[\text{Pd}_n\text{A}_{2n}]^{2n+}$ <sup>[42]</sup>: a triangular ring structure with three Pd(II) ions connected by two ligands per edge ( $\text{Pd}_3\text{A}_6$ ), a tetrahedron with Pd(II) at the corners, four edges with one ligand and two ligands at two opposing edges each ( $\text{Pd}_4\text{A}_8$ ), and an octahedron with six Pd(II) corners and one ligand per edge ( $\text{Pd}_6\text{A}_{12}$ ). In acetonitrile the ring (fig. 33) represents the mayor component, in DMSO-d6 it is the only one verifiable via 1H-NMR and ESI-MS.

The fluorenone part can rotate between the pyridyl-groups. In the ring structure one C=O-group is pointing outside, while the other one is oriented directly towards the first presumably interacting with the  $\pi$ -system<sup>[42]</sup>.

It must be noted that the ligand does not have a perfectly planar  $\pi$ -system as the structure especially at the double-edges requires a rotation between backbone and anchor out of the plane. The tilt reduces the overlap between their  $\pi$ -sub-systems and thus influences the contribution of the pyridyl-group to the electronic structure of the parent fluorenone.

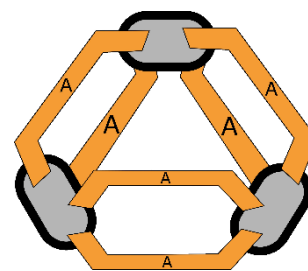


Fig. 33: schematic structure of the fluorenone-type acceptor cage ring  $\text{Pd}_3\text{A}_6$ .

### 4.1.3.2 Ground state spectra

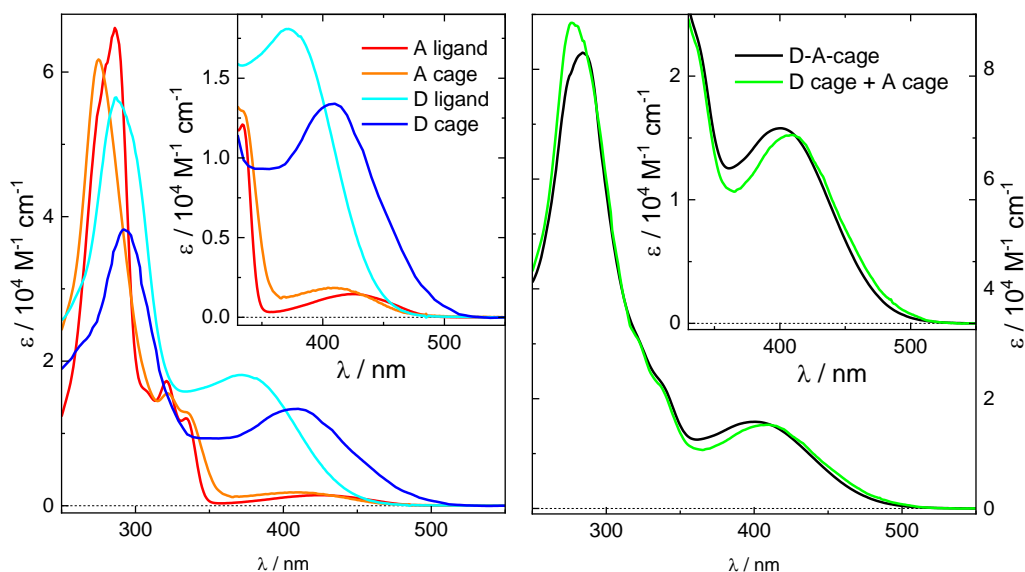


Fig. 34: ground state UV/vis spectra (a) of the PTZ donor and FLO acceptor ligand and their respective homomeric Pd(II) cage structures  $[\text{Pd}_2\text{D}_4]^{4+}$  and  $[\text{Pd}_3\text{A}_6]^{6+}$  and (b) of the mixed donor-acceptor cage  $[\text{Pd}_2\text{D}_2\text{A}_2]^{4+}$  and the sum of donor cage and acceptor cage  $[\text{Pd}_2\text{D}_4]^{4+} + [\text{Pd}_3\text{A}_6]^{6+}$ . The inlets show a zoom on the range used for excitation in the time-resolved spectra. Donor and donor cage spectra were provided by Marina Frank, the acceptor and acceptor cage spectra were measured by Jacopo Tessarolo, the mixed cage by Kai Wu. All spectra were measured in acetonitrile.

The pump wavelength for the time-resolved measurements is selected to only or at least primarily excite the donor. Any signal that can be assigned to the acceptor must then be generated by interaction with the donor, possibly in the form of a desired DACT. In order to find an appropriate excitation wavelength and understand from which electronic situation the following dynamics evolve, ground state UV/vis absorption spectra were recorded (see fig. 34) and interpreted. Since the donor has been reused for the project at hand, ligand and cage have been measured by Marina Frank before<sup>[36]</sup> and will be shortly revisited here.

The donor PTZ ligand has a strong sharp absorption maximum at 289 nm and a weaker broad one at 376 nm. The former can be interpreted as a local excitation confined to the phenothiazine moiety, since it is barely shifted by different substituents<sup>[43],[44]</sup> or complexation with Pd(II) in a coordination cage (maximum at 293 nm). The broader band corresponds to a  $\pi \rightarrow \pi^*$  transition. It has been shown by DFT calculations of phenothiazines with suitable substituents in 3,7-position that this transition has charge transfer character as charge density is moved from the heteroatoms towards the side-groups<sup>[43],[44]</sup>. Accordingly, this band is shifted to 407 nm in the donor cage since more electron withdrawing substituents tend to induce a bathochromic shift in 3,7-substituted phenothiazines<sup>[43],[44]</sup>. It is unlikely that this band transformed into a ligand-to-metal charge-transfer upon Pd(II) coordination as neither shape nor intensity and maximum wavelength change considerably and no additional band indicating a charge-transfer is apparent. The corresponding time-resolved UV/vis and midIR measurements support this interpretation<sup>[34],[35]</sup>.

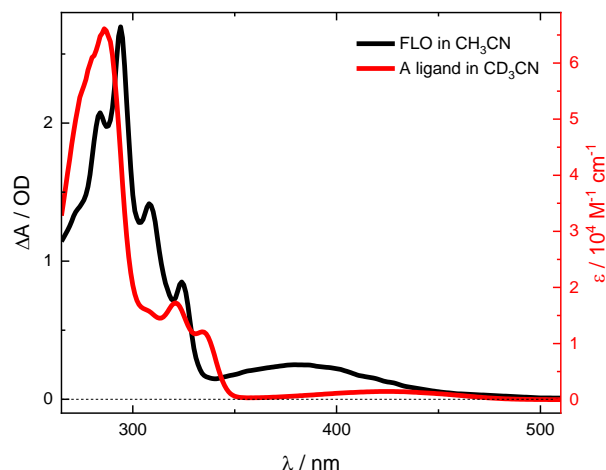


Fig. 35: ground state UV/vis absorption spectrum of fluorenone FLO and the free fluorenone-type acceptor ligand A in acetonitrile. Data for FLO reproduced from Gerbich<sup>[45]</sup>.

The acceptor spectrum is typical for a fluorenone derivative: a sharp band at 286 nm, two smaller bands at 321 nm and 335 nm that are interpreted as one slightly vibrationally resolved transition and a broad very weak band at about 426 nm. All three are generally assigned to  $\pi \rightarrow \pi^*$  transitions<sup>[46]</sup>. While the electron-withdrawing properties of the pyridyl-groups and its contribution to the  $\pi$ -system did not have much of an influence on the high energy bands when compared to the pure backbone (see fig. 35: 292 nm, 307 nm, 324 nm<sup>[45][47]</sup>), the low energy one is shifted dramatically (380 nm<sup>[45]</sup>) by adding the pyridyl-substituents. Again, the considerable influence of the substituents on the band position is a strong indicator for the charge transfer character of the transition.

DFT calculations on several 2,7-substituted fluorenones show an electron density shift from the  $\pi$ -system onto the carbonyl group<sup>[48],[49]</sup> between HOMO/HOMO-1 and LUMO/LUMO+1, that not necessarily involves the substituents, but is influenced by them<sup>[50]</sup>. The exact nature of the low energy band is still debated. An energy diagram by Kobayashi and Nagakura is commonly used to describe the energy levels of singlet and triplet states as a function of solvent polarity<sup>[51]</sup>. Back then this band was only ascribed to the  $S_0$ - $S_1$  transition while the bands at 307 nm and 324 nm were regarded as  $S_0$ - $S_3$  and  $S_0$ - $S_2$  bands<sup>[52]</sup>. More recently the 380 nm band is interpreted as a coupled  $S_0$ - $S_1$  plus  $S_0$ - $S_2$  band. Though the  $S_1$  and  $S_2$  states energetically drift apart with increasing solvent polarity, the spectrum only changes slightly. Therefore, the assignment might still stand. Unfortunately, there is no consistency on how much  $n \rightarrow \pi^*$  character the weak low energy band has and if the  $n \rightarrow \pi^*$  or  $\pi \rightarrow \pi^*$  transitions are stabilized in polar solvents<sup>[45],[49]</sup>. However, all the works agree in that the involvement of an  $n \rightarrow \pi^*$  state is necessary for an ISC from the  $S_1$  to the  $T_1$  state, which is not observed in polar solvents like acetonitrile.

In the cage the acceptor ligand bands are slightly blue shifted (275 nm, 321 nm, 335 nm, 408 nm) This has also been observed for ANQ<sup>[34]</sup>.

The absorption spectrum of the mixed cage has close resemblance with the sum of the donor and acceptor cage spectra. It has one intense band at 284 nm with small shoulders on the low energy side and a broad one at 400 nm. A small blue-shift compared to the sum of donor and acceptor cage is visible and could stem from the different angle of coordination compared to the homoleptic cages. The low energy band is almost identical to the corresponding one in the donor cage. This could indicate little interaction between ligands. Moreover, no new band is observed, hence a charge transfer from the ground state is unlikely and presumably only happens from an excited state.



### 4.1.3.3 FLO ligand

#### 4.1.3.3.1 Time-resolved UV/vis spectra

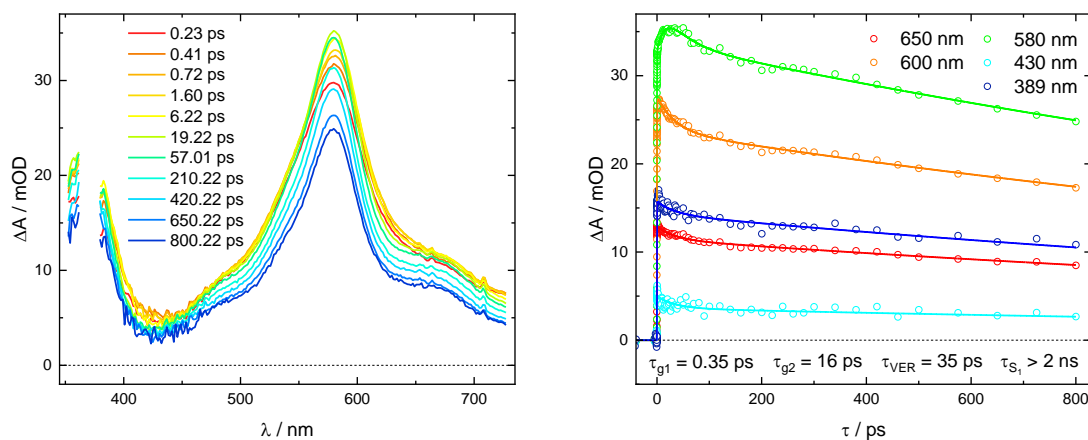


Fig. 36: transient UV/vis difference absorption spectra of the free fluorenone acceptor ligand in DMSO (2.5 mM) at selected pump-probe delays after excitation at 375 nm (0.5  $\mu$ J) (left), time traces at notable wavelengths (right). Lines represent multiexponential fit with  $\tau_{g1}=0.35$  ps,  $\tau_{g2}=16$  ps,  $\tau_3=35$  ps and  $\tau_{S1}>2$  ns.

As was mentioned before, the polarity of the solvent plays a vital role for the photophysics of fluorenones<sup>[51]</sup>. In polar solvents like DMSO and even more so in acetonitrile the lowest excited singlet state has  $\pi \rightarrow \pi^*$  character. Since all triplet states with lower energy also have  $\pi \rightarrow \pi^*$  character, an ISC to these states is symmetry forbidden, hence IC and fluorescence are the most likely relaxation paths for electronically excited states.

Accordingly, after excitation at 375 nm the time-resolved UV/vis spectra of the FLO ligand (fig. 36 left) show the formation of a very long-lived state with a lifetime beyond 1 ns as has been shown for fluorenone (18 ns (in acetonitrile)<sup>[53]</sup>, 16 ns (in acetonitrile)<sup>[54]</sup>, 15.1 ns (in DMSO)<sup>[54]</sup>) and other derivatives (10 ns (2,7-bis(phenylethyn-1-yl)fluoren-9-one (PAFO27) in THF)<sup>[49]</sup>) in polar solvents. Thus, the corresponding excited state can be assigned to an  $S_1$  state with  $\pi \rightarrow \pi^*$  character that slowly decays via photon emission and internal conversion.

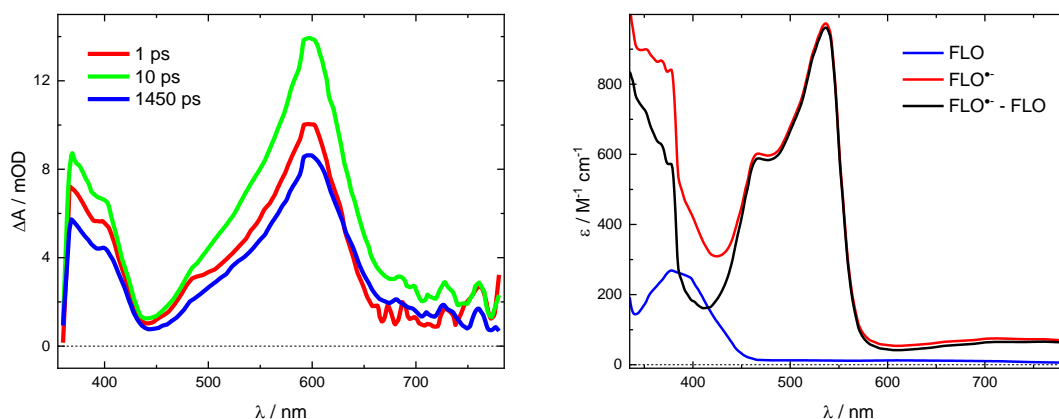


Fig. 37: time-resolved UV/vis spectra of PAFO27 in THF at selected pump-probe delays after excitation at 400 nm. Data reproduced after Neckers et al.<sup>[49]</sup> (left); ground state UV/vis absorption spectra of fluorenone, its anion and difference spectrum simulated from both spectra. Data reproduced after Ward et al.<sup>[55]</sup>.

The spectra consist of one intense excited state band at 579 nm with a low energy shoulder at about 665 nm, one band at 370 nm that is covered by the ground state bleach of the 335 nm band and thus might be centred at a lower wavelength, and a ground state bleach of the charge-transfer-like transition at 430 nm. The intense band is not fully formed right after excitation, but grows biexponentially with a time constant  $\tau_{g1} = 0.35$  ps and  $\tau_{g2} = 16$  ps, and shows some minor narrowing with  $\tau_{VR} = 35$  ps that might indicate some vibrational or structural relaxation.

Very profound spectral similarities were found with the afore mentioned fluorenone derivatives in THF (see fig. 37 left)<sup>[49]</sup>. After the initial rise with  $\tau_1 = 0.33$ - $0.44$  ps PAFO27 has both an intense band at 600 nm and a smaller one at 390 nm together with a ground state bleach at 440 nm. Here the shoulder does not appear on the low, but the high energy side of the intense band. Following a period of constant absorption of about 20 ps the spectrum decays with a time constant  $> 1.5$  ns.

The authors compared the excited state spectra to the fluorenone radical anion spectrum in dichloromethane at  $-55^\circ\text{C}$ <sup>[55]</sup>, which can be viewed as an extreme case of the charge transfer character if a lot of charge density from the substituents is focussed on the carbonyl-group of the fluorenone moiety as was found from DFT calculations for the  $S_0$ - $S_1$  transition of PAF27<sup>[49]</sup>. The FLO radical anion has increased absorption at 380 nm compared to the neutral species and an additional band at 536 nm with a high energy shoulder at 468 nm (see fig. 37 right), which could be affected by solvent polarity<sup>[55]</sup> or the size of the  $\pi$ -system. The similarities between the excited state spectra of PAF27 and the FLO radical anion spectrum are reasonable and applicable to the FLO acceptor ligand measurements. The viability of this comparison will be further supported by the time-resolved midIR spectra of the acceptor cage.

Similar spectroscopic data were obtained from time-resolved measurements on fluorenone itself<sup>[45]</sup>. After excitation at 400 nm a strong band appears at 490 nm together with a weaker band at 580 nm and a band at about 400 nm. The spectral shifts of the bands compared to the FLO ligand at hand are likely due to the pyridyl-substituent's influence on the energy levels of the electronic states. This can in turn change the effect of the pump excitation. While the  $S_1$  bands of fluorenone appear within the experimental resolution at 400 nm excitation, they rise from slightly blue-shifted broader bands at 305 nm excitation in about 20 ps. Though the initial spectra show striking similarities to vibrationally hot spectra of the  $S_1$  state, the changes were attributed to a  $S_3$ - $S_1/S_2$  transition via internal conversion by comparison to time-resolved photoionization spectra in the gas phase<sup>[45],[53]</sup>. The  $S_0$ - $S_1/S_1$  transition in fluorenone appears at 380 nm, but stretches from 330 nm to 430 nm, hence only the low energy side is covered by the 400 nm pump pulses. At 305 nm excitation clearly the  $S_3$  state will be occupied.

For the pyridyl derivative only the  $S_1$  or  $S_2$  state can be achieved from 385 nm excitation at the low energy CT-like transition at 430 nm. The initial rise in band intensity can therefore not be explained by an  $S_3$ - $S_2/S_1$  transition. A transition between  $S_2$  and  $S_1$ , which is likely for the acceptor cage as will be shown with the corresponding time-resolved midIR spectra, is possible and their strong correlation would explain the spectral similarities. Other mechanisms like a very slow charge separation can unfortunately not be completely ruled out, but would be more suitable for the fast rise time as was suggested for PAF27<sup>[49]</sup>. Solvent dipole reorientation as well as the influence of the rotatable pyridyl substituent can be discussed. However, with those approaches a spectral shift would be expected as ground and excited state would be affected differently.

Overall, it can be concluded that by photo-excitation at about 400 nm the  $S_1$  state is eventually achieved from a spectroscopically unresolved precursor, possibly the  $S_2$  state, and cannot cross over to a triplet state in the polar solvent DMSO due to its  $\pi \rightarrow \pi^*$  character. It therefore lives for several nanoseconds and decays primarily via fluorescence (also see emission spectrum in [42]) and IC. Due to the similarities of the excited state spectra to the fluorenone radical anion spectrum the ability of the acceptor to receive charges is plausible.

### 4.1.3.4 FLO cage

#### 4.1.3.4.1 Time-resolved UV/vis spectra

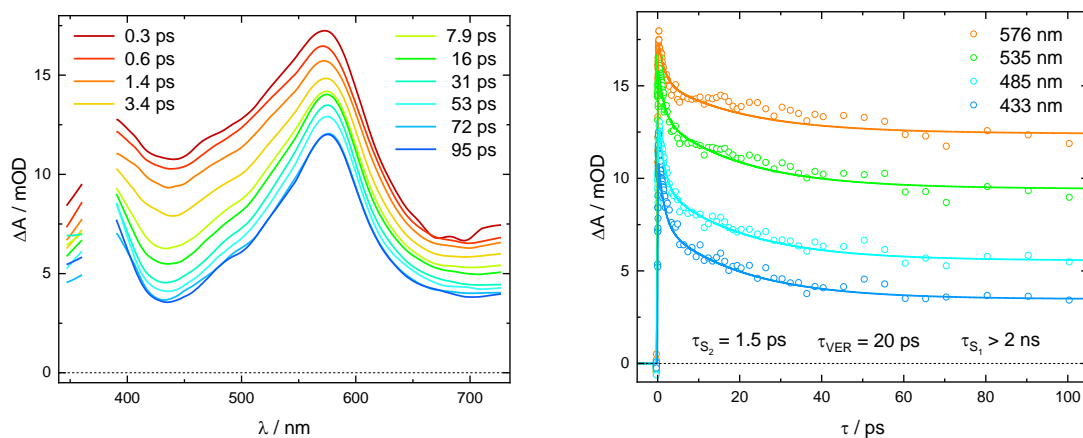


Fig. 38: time-resolved UV/vis spectra of the acceptor cage  $[\text{Pd}_3\text{A}_6]^{6+}$  in DMSO (0.26 mM ligand concentration) at selected pump-probe delays after excitation at 375 nm (0.46  $\mu\text{J}$ ) (left); time traces at selected wavelengths (circles) with corresponding tri-exponential fits (solid lines) (right).

In contrast to the donor, the acceptor is less affected by Pd(II) coordination (see fig. 38). The same pattern has already been observed with an anthraquinone acceptor<sup>[34],[35]</sup>.

Two excited state bands at 575 nm and below 380 nm appear along with the ground state bleach, however, they are much broader to the point that they overlap. There is no shoulder on the low energy side of the 575 nm band, but there might be one on the high energy side at about 480 nm. The bands emerge within the experiment's temporal resolution and, unlike the uncoordinated ligand, don't rise subsequently, but rather decay with a time-constant of 1.5 ps. After minor narrowing or possibly a decay of a broad background absorption signal with  $\tau_2 = 20$  ps the absorption reaches a plateau. Due to the similarities the remaining spectrum will be attributed to transitions from the  $S_1$  state of the ligand. The increased band width might be a consequence of the complexation: it creates different environments around the ligands on each edge of the ring structure due to their different orientation and related different rotational angles between fluorenone backbone and pyridyl anchor.

As fluorenone has been shown to draw electron density from side chains in 2,7-position<sup>[49]</sup>, an intramolecular charge transfer between pyridyl- and fluorenyl-sub-units is reasonable and the speed of BET would be influenced by the backbone-anchor angle. Aside from the aromatic hydrogen atoms the pyridyl-group and the free ligand would therefore prefer a rather planar structure in order to stabilize via delocalization the  $\pi$ -system over the whole molecule. In the Pd(II) ring complex on the other hand a tilt is strongly favoured<sup>[42]</sup> resulting in a weaker coupling and consequently a comparatively longer BET time.

There is little information on the nature of the initial decay as it basically doesn't change the shape of the spectrum except for the band width. The time-resolved midIR spectra in the next chapter, however, will show that another electronic state preceding the  $S_1$  is needed in order to explain the occurring peaks and their evolution as about 30% of the pump-excited ensemble ends up in a vibrationally hot ground state within a few picoseconds.

#### 4.1.3.4.2 Time-resolved midIR spectra

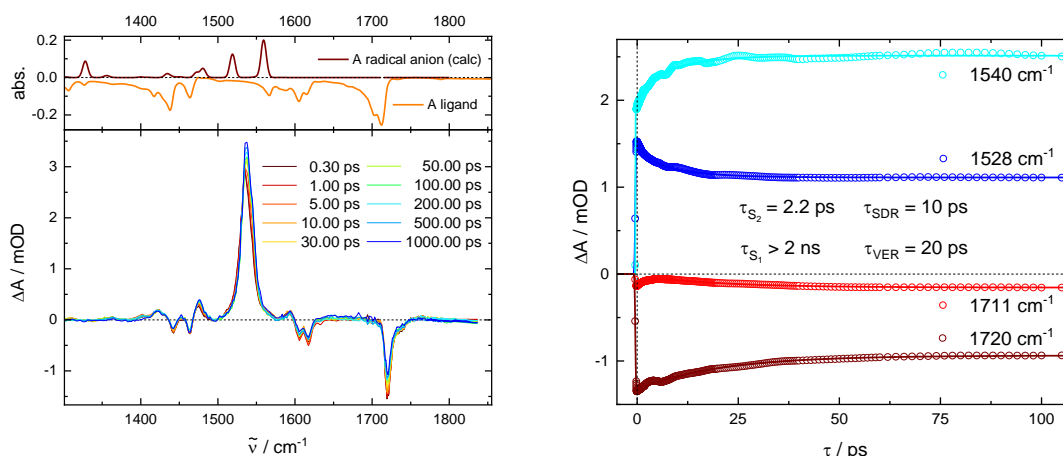


Fig. 39: DFT calculated IR spectrum of the acceptor radical anion A<sup>•-</sup> and ATR-IR spectrum of the free FLO acceptor ligand A (top left); time-resolved midIR spectra of the acceptor cage [Pd<sub>3</sub>A<sub>6</sub>]<sup>6+</sup> in deuterated acetonitrile (0.26 mM ligand concentration) at selected pump-probe delays after excitation at 400 nm (1.0 μJ) (bottom left); time traces at selected wavelengths (circles) with corresponding tri-exponential fits (solid lines) (right).

Since no clean ground state IR spectrum is available for the acceptor cage, the free ligand spectrum is used to identify ground state bleaches (fig. 39 top left). Though there are small differences in wavenumber and relative intensity, the peaks can be assigned quite easily.

Right after excitation at 400 nm bleaches at 1442 cm<sup>-1</sup>, 1463 cm<sup>-1</sup>, 1605 cm<sup>-1</sup>, 1617 cm<sup>-1</sup> and especially the very intense carbonyl stretch vibration at 1720 cm<sup>-1</sup> appear (fig. 39 bottom left). Simultaneously, excited state peaks at 1422 cm<sup>-1</sup>, 1474.5 cm<sup>-1</sup>, 1535 cm<sup>-1</sup> and 1593 cm<sup>-1</sup> emerge.

Following the assumption that regarding the fluorenone backbone the electronically excited state S<sub>1</sub> of the ligand resembles the ground state of the fluorenone radical anion, corresponding peaks are expected. The model structure shows a shift of the carbonyl stretch vibration to lower wavenumber at 1540 cm<sup>-1</sup> upon single-electron reduction as the electron occupies an antibonding orbital with regard to the C=O double bond increasing the single-bond character thereby weakening the bond strength<sup>[56]</sup>. The electron density is shifted onto a then highly partial negatively charged oxygen atom that results in even more intense vibrational C-O transitions. There is excellent agreement for the acceptor cage with the peak at 1535 cm<sup>-1</sup>. This observation again corroborates the proposed analogy of excited state and anion.

On a closer look, the peak at 1535 cm<sup>-1</sup> actually consists of two overlapping transitions at 1535.1 cm<sup>-1</sup> and 1543.4 cm<sup>-1</sup> that shift about 1-1.5 cm<sup>-1</sup> to 1536.5 cm<sup>-1</sup> and 1544.4 cm<sup>-1</sup>. The same effect is observed for the peak at 1474.5 cm<sup>-1</sup> moving to 1476 cm<sup>-1</sup> over time. A very similar feature was noticed in time-resolved IR measurements on fluorenone in deuterated acetonitrile before<sup>[57]</sup>. The authors found three excited state absorption peaks in the region 1492-1576 cm<sup>-1</sup> and using TD-DFT calculations they assigned these peaks to vibrational transitions in the electronically excited state S<sub>1</sub>: a very intense peak at 1542.4 cm<sup>-1</sup> (a) that corresponds to the approximately isolated C=O stretch vibration, a low-energy shoulder at 1533.2 cm<sup>-1</sup> (a') that represents a coupled vibration of the C=O bond together with the aromatic system and a small peak at 1495.7 cm<sup>-1</sup> (d) that belongs to the aromatic system itself. There are obviously some differences in central wavenumber and relative intensity due to the pyridyl-substituent and constraints imposed by the ring structure, but the general pattern applies very well to the acceptor cage.

The peak position as a function of delay time was fitted biexponentially with  $\tau_1 = 1.1$  ps and  $\tau_2 = 10.5$  ps by Fukui et al. and was explained with vibrational cooling of the hot  $S_1$  state by dissipating the excess energy into intramolecular modes and the surrounding solvent molecules via anharmonic coupling to low-frequency bath modes<sup>[57]</sup>. The simultaneous increase in peak intensity might be a result of the solvent molecules rotating and rearranging to accommodate the increasing charge separation within the fluorenone.

Very similar results are achieved for the corresponding peaks of the FLO acceptor cage. A sum of Lorentzian functions

$$I_{\tau}(\tilde{\nu}) = \sum_i A_i \frac{\Delta\tilde{\nu}_i^2}{4} \frac{1}{(\tilde{\nu} - \tilde{\nu}_{0,i})^2 + \left(\frac{\Delta\tilde{\nu}_i}{2}\right)^2} + I_0 \quad \text{eq. 045}$$

can be used to fit the peaks for several delay times. Since peak a and a' are mostly overlapping, the amplitude of the latter is comparatively small and the spectra consist of rather few points, an automated fit is close to impossible and a manual fit is extremely tedious, so a single Lorentzian was used as an approximation for a and a'. Plotting the obtained peak centre  $\tilde{\nu}_0$  versus the delay time  $\tau$  of the spectrum that was fitted, a peak shift from  $1535.37 \text{ cm}^{-1}$  to  $1538.16 \text{ cm}^{-1}$  can be observed (see fig. 40). The time trace of the shift can then be fitted biexponentially with  $\tau_1=1.3$  ps and  $\tau_2=10$  ps. The former coincides quite well with the first time constant derived from the time-resolved UV/vis measurements.

This would mean that the broad decay with  $\tau_1$  (UV/vis) = 1.5 ps derived from the time-resolved UV/vis spectra is caused by cooling of the hot  $S_1$  state. As was alluded for the acceptor ligand before, however, an expected spectral shift was not observed for the acceptor cage.

Another approach, however, works similarly well. Considering a transition between two electronic states with slightly different central wavenumbers due to their similar electronic structure as was proposed for the transient UV/vis spectra, the shift would be a result of one state's peaks decaying while the peaks of the other are emerging. On a close look a quasi-isoestic point can even be observed.

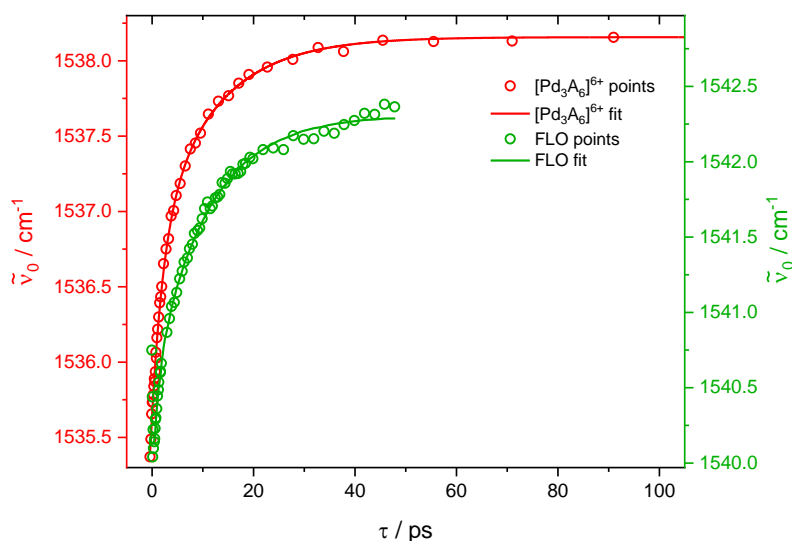


Fig. 40: plot of the fitted peak maximum of the C-O stretching vibrations a and a' according to eq. 045 versus the delay time and corresponding biexponential fit for the FLO cage  $[\text{Pd}_3\text{A}_6]^{6+}$  and fluorenone. The latter was reproduced from Fukui et al.<sup>[57]</sup>.

From an early spectrum and one after the “shift” is completed, the peak parameters of the respective states can be gained with a fit of three Lorentzian functions (see Tab. 2). It should then be possible to simulate all intermediate spectra with a weighted sum according to eq. 046.

$$\begin{aligned}
 I(\tilde{\nu}) &= A_{0.3 \text{ ps}} \cdot I_{0.3 \text{ ps}}(\tilde{\nu}) + A_{100 \text{ ps}} \cdot I_{100 \text{ ps}}(\tilde{\nu}) \\
 &= A_{0.3 \text{ ps}} \cdot \left( I_{a,0.3 \text{ ps}}(\tilde{\nu}) + I_{a',0.3 \text{ ps}}(\tilde{\nu}) + I_{d,0.3 \text{ ps}}(\tilde{\nu}) \right) \\
 &+ A_{100 \text{ ps}} \cdot \left( I_{a,100 \text{ ps}}(\tilde{\nu}) + I_{a',100 \text{ ps}}(\tilde{\nu}) + I_{d,100 \text{ ps}}(\tilde{\nu}) \right)
 \end{aligned}
 \tag{eq. 046}$$

The simulations suit the measured spectra reasonably well. Plotting the weighting parameters  $A_{0.3 \text{ ps}}$  and  $A_{100 \text{ ps}}$  against the delay of the simulated spectrum again gives a progression that can be fitted very well with a biexponential decay with  $\tau_1 = 2 \text{ ps}$  and  $\tau_2 = 10 \text{ ps}$  (fig. 41).

Though this interpretation has its merits, it also comes with some contradictions. An increase in peak intensity together with a blue-shift is theoretically possible, but unlikely considering prior knowledge of the electronic states of fluorenone. It would require a higher C=O dipole moment, meaning more partial negatively charged oxygen, while at the same time gaining bond strength by increasing the double-bond character. The latter, however, is supposed to be achieved by withdrawing electron density from the antibonding C-O orbital.

In one way or the other, the final excited state has a lifetime far beyond 2 ns and can safely be assigned to the  $S_1$  state when comparing to the time-resolved UV/vis data. However, the fact that all bleaches (except for the peak at  $1463 \text{ cm}^{-1}$  because of the overlap with the moving excited state peak d) decay to about 70% of their original intensity while the excited state peaks don't lose but rather gain intensity needs to be taken into account. The decay happens with a time constant of about 20 ps, typical for vibrational energy relaxation. There is also a positive peak at the low-energy edge of the C=O bleach (about  $1710 \text{ cm}^{-1}$ ) that disappears within the same time and could therefore be indication for the vibrationally hot ground state, although it is unusually weak.

Tab. 2: Lorentzian fit parameters used to fit the three peaks d, a and a' in the transient midIR spectra at 0.3 ps and 100 ps according to eq. 045 and eq. 046.

0.3 ps	A	$\tilde{\nu}_0/\text{cm}^{-1}$	$\Delta\tilde{\nu}/\text{cm}^{-1}$	100 ps	A	$\tilde{\nu}_0/\text{cm}^{-1}$	$\Delta\tilde{\nu}/\text{cm}^{-1}$
d	0.30271	1474.99	10.85	d	0.38849	1476.06	11.52
a	2.79375	1534.91	15.05	a	2.89421	1536.29	13.80
a'	0.57804	1542.98	10.57	a'	1.19808	1543.72	9.95

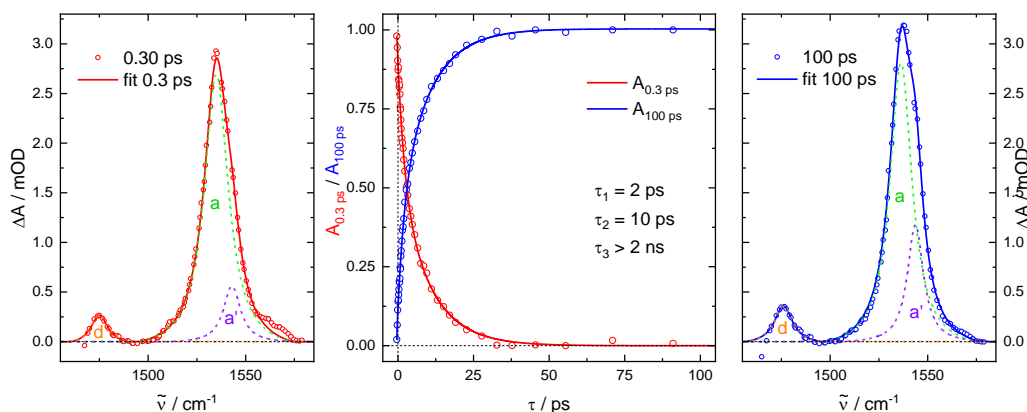


Fig. 41: Fit of the time-resolved midIR spectra of the FLO cage  $[\text{Pd}_3\text{A}_6]^{6+}$  at 0.3 ps (left) and 100 ps (right) according to eq. 046 and plot of the weighting parameters  $A_{0.3 \text{ ps}}$  and  $A_{100 \text{ ps}}$  fitted to the time-resolved midIR spectra versus the delay time including biexponential fits.

As the  $S_1$  state, however, has a very long lifetime, another preceding electronic state is necessary from which both the  $S_1$  and  $S_0$  state are populated to achieve vibrational excitation. Both the energy dissipation and the electronic transition approach are able to include this precondition. The former would necessitate an  $S_2$  state shorter-lived than the experiments temporal resolution as there would be no spectral evidence for it in the midIR. The ultrafast IC would produce the first reliable spectra with 30% hot  $S_0$  state and 70% hot  $S_1$  state that would indicate their excess energy dissipation via bleach decay and excited state peak shifts. The latter approach, on the other hand, would assign the excited state peaks in the beginning to the  $S_2$  state. As it decays both the slightly blue-shifted  $S_1$  and the vibrationally hot  $S_0$  peaks appear and show some solvent reorientation or vibrational energy relaxation. Both cases end in a plateau in accordance with the long lifetime of the  $S_1$  state that was also derived from the time-resolved UV/vis measurements.

As the increase in intensity of the excited state peaks in the midIR and the broad decay in the UV/vis better match the electronic transition approach, it will be used further on, however, the alternatives should be borne in mind.

### 4.1.3.5 PTZ-FLO donor-acceptor cage

#### 4.1.3.5.1 Time-resolved UV/vis spectra

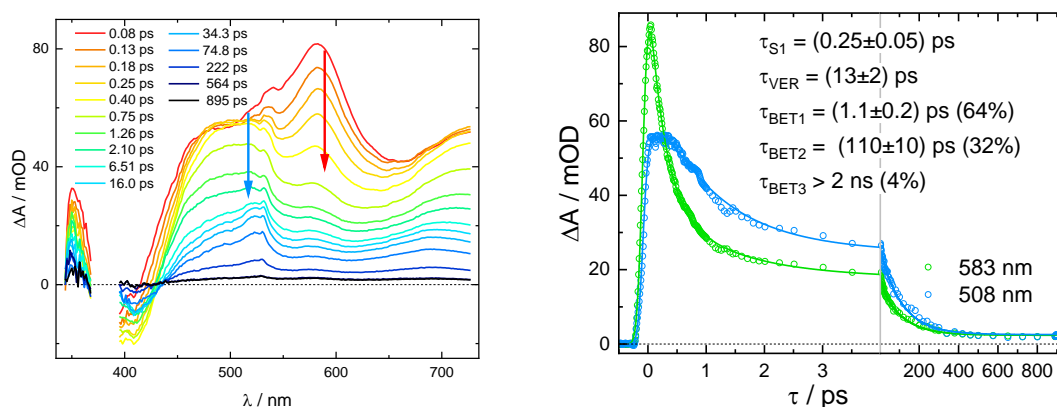


Fig. 42: time-resolved UV/vis spectra at selected pump-probe delays (left) and transient data (circles) of the PTZ-FLO donor-acceptor cage  $[\text{Pd}_2\text{D}_2\text{A}_2]^{4+}$  in deuterated acetonitrile (0.1 mM cage concentration) at different wavelengths after excitation at  $\lambda_{\text{pump}} = 385 \text{ nm}$  (0.45  $\mu\text{J}$ ) with corresponding quinquexponential fits (solid lines) and fitted time constants (right).

When measuring the time-resolved UV/vis spectra of the mixed donor acceptor cage system (fig. 42), the pump wavelength has been deliberately adjusted to a region of minimal ground state absorption by the acceptor ligand with at the same time at least decent absorption by the donor. Any acceptor related signal can then be considered to originate from the donor excitation. With the corresponding setup the pump wavelength is freely selectable within the range mentioned before. In order to not deviate too much from the previous measurements on the donor and donor cage, 385 nm was selected. At this wavelength the absorption coefficients of both donor systems are about five to ten times higher than the ones of the acceptor system, that have a minimum at this point.

The desired donor-acceptor charge-transfer should generate both donor radical cation and acceptor radical anion bands at the same time in the time-resolved spectra. Interestingly, they look almost entirely like the PTZ donor cage spectra, which of course only have evidence for the cationic species.

The first spectra clearly show bands of the quickly decaying donor  $S_1$  state. The intense band at 583 nm might also match the  $S_2/S_1$  band of the acceptor ligand at 579 nm, but the second one at 425 nm, that can be more easily recognised from subtracting early spectra for example at 0.08 ps and 0.25 ps or from the decay associated spectra, unambiguously mirrors the second donor  $S_1$  band at 435 nm rather than the one from the acceptor at about 370 nm.

As the  $S_1$  spectrum vanishes with  $\tau_{S_1} = 0.25$  ps, a drop in absorption at the bleach at about 395 nm hints at a transition not back into the ground state, but another state that, recognising the similarities of the spectra to those generated electrochemically as has been shown before for the donor cage, includes the donor radical cation. The direct  $S_1-D^{*\dagger}$  transition is also apparent when looking at the time traces around 500 nm, where something close to an isosbestic point is indicated by nearly unchanging absorption for a few hundred femtoseconds.

The first spectra, though possessing the very specific structure at 532 nm, initially differ from the oxidized donor cage in that the high-energy side is more intense and the band in the red part of the spectrum is red-shifted above 700 nm. In a less pronounced way this was also observed for the donor cage. Over a few ten picoseconds ( $\tau = 13$  ps) of possibly structural adaptation to the new electronic state, however, the time-resolved spectra gradually match those of the electrochemically generated derivative more closely. Any remaining differences again likely reflect the differing number of oxidized ligands in the respective cage.

The  $D^{*\dagger}$  bands initially decay with  $\tau_{BET_1} = 1.1$  ps, close to what was observed for the donor cage, but only to about 36% of the original intensity. Another 32% decays with  $\tau_{BET_2} = 110$  ps and a remainder of 4% persists beyond the experimentally available pump-probe delay. Though the late spectra are rather weak, they undoubtedly have the shape of the  $D^{*\dagger}$  spectra and a corresponding assignment is supported by time-resolved midIR spectra. From the isosbestic point at 437 nm a return to the ground state via back electron transfer is evident.

Unfortunately, there is no spectral indication of the whereabouts of the electron that is removed from the donor in the transient UV/vis spectra. From the donor cage spectra, it can be deduced that the short-lived  $D^{*\dagger}$  state is created from an LMCT to one of the Pd(II) metal ions of the cage. For the other two decays the time-resolved midIR spectra unmistakably show a connection to acceptor anionic signals providing proof that a donor-acceptor CT via an excited state was indeed achieved with the PTZ-FLO pair as will be discussed in detail in the next chapter.

When looking at the cage structure it can even be speculated on the nature of the transitions regarding the longer two time constants. Most straight forward would be an assignment of the electron transfer from a donor to either an adjacent or opposing acceptor as those obviously can receive an electron and their positions slightly differ in distance of the redox-active centres relative to the donor. According to considerations regarding charge separation, distance and lifetime, the charge-transfer to the acceptor in trans position would then be associated with the longer lifetime as the distance is slightly larger, but properties such as the geometry could have a greater impact. Other interpretations, for example the rotation of the FLO backbone, are less likely, since the shape of the spectra doesn't change after the decay of the donor  $S_1$  state. Due to the lack of any evidence for the acceptor radical anion or any acceptor species in the transient UV/vis spectra, however, such scenarios cannot be disregarded completely.

Without the time-resolved midIR spectra a donor-acceptor charge-transfer could hardly be considered, especially since moderately intense spectra from intramolecular charge-transfer transitions in acceptor and acceptor cage were observed after excitation with the same pump beam and the anionic species was expected to produce even more intense ones. It is possible that the absorption cross sections of transitions from the generated  $A^{\bullet-}$  are simply very weak, but it would require a measurement of the extinction coefficient of  $A^{\bullet-}$  compared to  $D^{*\dagger}$  to evaluate those considerations.



In the end, clear evidence for the creation of cages with  $D^{\bullet+}$  ligands from exciting the donor to its  $S_1$  state is given with the transient UV/vis spectra. The cationic spectra decay with three time constants that most likely relate to three recipients of the electron missing in the donor. The shortest one can be safely assigned to the Pd(II) ions creating  $Pd(II)Pd(I)DD^{\bullet+}A_2$ . The other two can only be characterized further with the help of time-resolved midIR spectra, as there is no band that can be attributed to the acceptor in the transient UV/vis spectra. With the additional information shown in the next chapter and consideration of the cage structure a DACT to an acceptor in cis and trans position to the donor can be assumed.

#### 4.1.3.5.2 Time-resolved midIR spectra

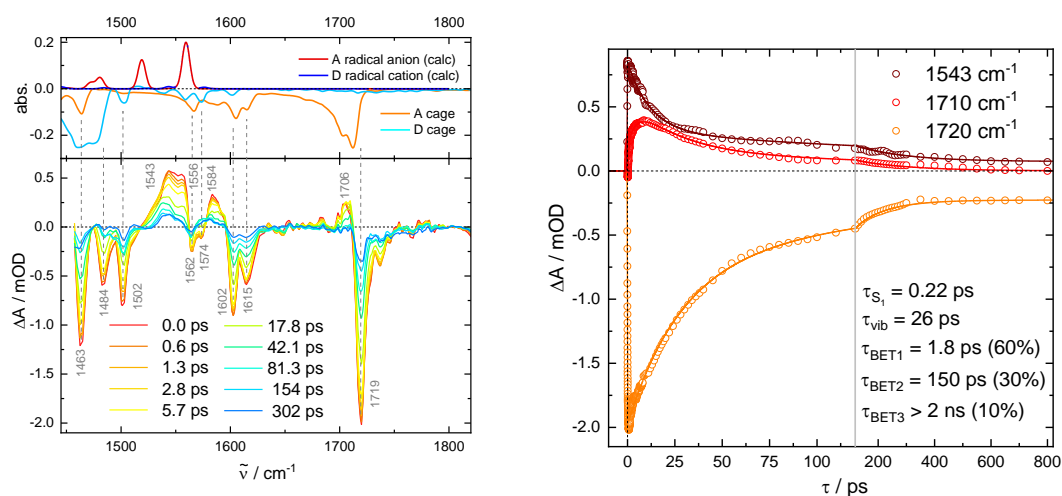


Fig. 43: DFT calculated IR spectra of the donor radical cation  $D^{\bullet+}$  and the acceptor radical anion  $A^{\bullet-}$  and FTIR spectra of the PTZ donor cage  $[Pd_2D_4]^{4+}$  and the FLO acceptor cage  $[Pd_3A_6]^{6+}$  (top left); time-resolved midIR spectra of the PTZ-FLO donor-acceptor cage  $[Pd_2D_2A_2]^{4+}$  in deuterated acetonitrile (0.26 mM ligand concentration) at selected pump-probe delays after excitation at 400 nm (2.3  $\mu J$ ) (bottom left); time traces at selected wavelengths (circles) with corresponding quinquexponential fits (solid lines) (right).

As was mentioned before, the excitation wavelength was chosen to explicitly excite the donor due to its much higher absorption coefficient. Accordingly, upon excitation at 400 nm donor bleaches that were also observed in the donor cage<sup>[35]</sup>, though in part slightly shifted, appear at 1463  $cm^{-1}$ , 1484  $cm^{-1}$ , 1484  $cm^{-1}$ , 1574  $cm^{-1}$  and 1602  $cm^{-1}$  (fig. 43). Additionally, however, all bleaches familiar from the acceptor cage emerge at the same time. The peaks at 1562  $cm^{-1}$ , 1615  $cm^{-1}$  and 1719  $cm^{-1}$  are well separated, while the others superimpose the donor bleaches at 1463  $cm^{-1}$  and 1602  $cm^{-1}$ .

Looking at the absorption coefficient at 400 nm in the homoleptic donor and acceptor cages, the bleaches are expected to resemble the sum of their respective IR spectra in a ratio of about 7:1, however, they are much more similar to an equal proportion (see fig. 44). This is a first indication that changes in the acceptor are connected to the excited donor.

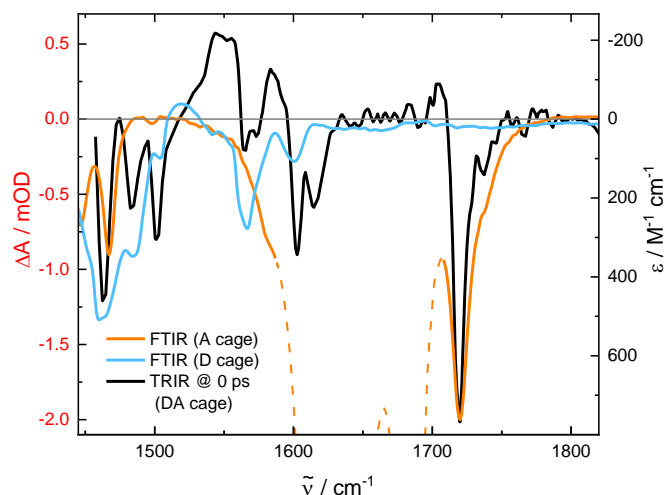


Fig. 44: FTIR spectra of PTZ donor cage  $[\text{Pd}_2\text{D}_4]^{4+}$  and the FLO acceptor cage  $[\text{Pd}_3\text{A}_6]^{6+}$  and time-resolved midIR spectrum of the PTZ-FLO donor-acceptor cage  $[\text{Pd}_2\text{D}_2\text{A}_2]^{4+}$  at close to 0 ps.

As was described before for the donor cage, the donor  $S_1$  state, clearly visible in the time-resolved UV/vis spectra, has no corresponding indicator in the midIR (fig. 43 left). Instead, there is immediate evidence for both the donor radical cation  $\text{D}^{\bullet+}$  and the acceptor radical anion  $\text{A}^{\bullet-}$  from excited state peaks. The former is represented by a peak at  $1584\text{ cm}^{-1}$  very close to what was observed in the donor cage. Two further peaks at  $1543\text{ cm}^{-1}$  and  $1556\text{ cm}^{-1}$  can be associated with the acceptors isolated C=O and combined C=O-aryl vibrations known from its  $S_1$  state, that was characterised as charge-transfer-like and similar to the fluorenone radical anion regarding the carbonyl group due to negative charge density from side-groups transferring to the carbonyl oxygen. Since the acceptor  $S_1$  state cannot have been achieved directly from pump excitation as was discussed prior and the peaks don't emerge upon the decay of the donor peaks, like for example in a resonant energy transfer, but appear instantly, the most evident interpretation is the creation of  $\text{A}^{\bullet-}$  via electron transfer from the donor.

Because of the different electronic structure those anion peaks are slightly blue-shifted and split further apart compared to the  $S_1$  state in the homoleptic acceptor cage. The third peak might also be present, but is superimposed by bleaches somewhere around  $1500\text{ cm}^{-1}$  hence their intensities are slightly smaller than what is expected. In general, the peak amplitudes in the range  $1450\text{--}1600\text{ cm}^{-1}$  are a little less reliable because the many overlapping peaks make it nearly impossible to merge the individual measurements with a consistent baseline. This might also be the reason for the surprisingly low intensity of the  $\text{A}^{\bullet-}$  peaks that are supposedly very high due to the strong dipole moment of the carbonyl group, though the different electronic structure of the anion compared to the  $S_1$  state certainly has an influence on that as well.

Both ground and excited state peaks generally decay with three time constants. The long time constants  $\tau_2 = 150\text{ ps}$  and  $\tau_2 \geq 2\text{ ns}$  coincide very well with those derived from the decay of the donor radical cation in the time-resolved UV/vis data. The fact that those time constants also appear in both the donor radical cation and acceptor radical anion peaks indicate the generation of two donor-acceptor charge-transfer species. There is unfortunately no further evidence regarding the relative position of the ligands (cis/trans) involved.

In the transient UV/vis spectra the short time constant was associated with BET from the short-lived LMCT state. Its mayor proportion of 64% of the overall generated  $\text{D}^{\bullet+}$  species should not contribute to any acceptor signal, which would at a first glance contradict the 1:1 ratio of donor and acceptor bleach contributions. However, the transition from the donor  $S_1$  state to a  $\text{D}^{\bullet+}$  of any

kind in the cage leaves excess energy that does not need to only dissipate (for example vibrationally) via the donor but also via the acceptor. The same is true for the following back electron transfer. Consequently, the arising vibrationally hot molecules in their electronic ground state have broad peaks slightly red-shifted in relation to their corresponding bleaches, particularly visible at the peaks at  $1556\text{ cm}^{-1}$ ,  $1592\text{ cm}^{-1}$  and  $1706\text{ cm}^{-1}$ , and can thus create acceptor bleaches even without the formation of the  $A^{\bullet-}$ . Following those relations, the decay of the hot peaks and of the share of the bleaches associated with those vibrationally hot molecules therefore mirrors the fast BET of the short-lived donor radical cation species  $\text{Pd(I)D}^{\bullet+}$  in the transient UV/vis data. Fittingly, about 60% of the bleach amplitudes decrease with the corresponding time constant of about  $\tau_{\text{VR}} = 20\text{ ps}$  while the species associated with the other two,  $\tau_2$  and  $\tau_3$ , contribute 30% and 10%, respectively. These ratios are in excellent agreement with the time-resolved UV/vis data.

Since both donor and acceptor bleaches decay with similar three time constants and amplitude ratios, one could assume that all three related species involve a DACT state. This would, however, raise the question what this third state would look like as there are only two plausible possibilities an electron could be transferred to the acceptor and furthermore the measurements on the donor cage clearly show a lot of similarities regarding the short time constant. It is possible that the LMCT from D to  $\text{Pd(II)}$  causes an electron density shift that also affects the acceptor and produces similarly intense peaks as the  $S_1$  or  $A^{\bullet-}$ , but for an ultimate conclusion on that more information on the FLO ligand is needed.

#### 4.1.3.6 Conclusion

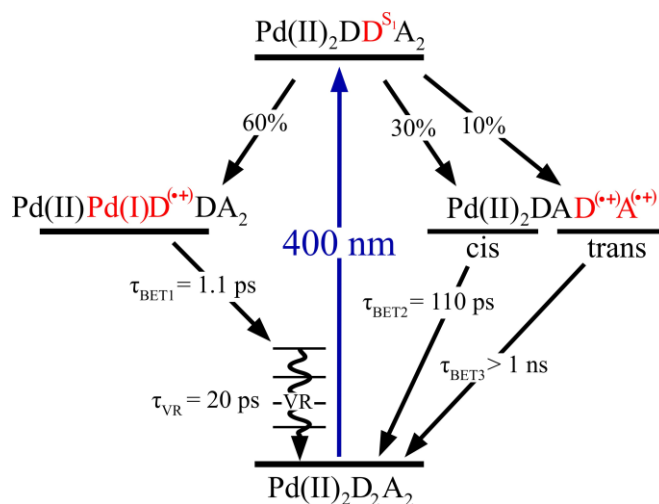


Fig. 45: energy level diagram depicting the relaxation processes within the PTZ-FLO donor-acceptor cage  $[\text{Pd}_2\text{D}_2\text{A}_2]^{4+}$  after excitation at 400 nm.

Through the combined information of time-resolved UV/vis and midIR spectra of the PTZ-FLO donor-acceptor cage  $[\text{Pd}_2\text{D}_2\text{A}_2]^{4+}$  strong evidence is gained that a photoinduced DACT is occurring from excitation of the PTZ donor at 400 nm. The time-resolved UV/vis spectra clearly show excited state spectra of the PTZ  $S_1$  state followed by characteristic PTZ  $D^{\bullet+}$  bands, that decay with three time constants. The time-resolved midIR spectra provide evidence for the FLO  $A^{\bullet-}$  both through the appearance of acceptor bleaches and excited state peaks that can be assigned to  $A^{\bullet-}$  with the help of DFT calculations. By comparison to the time-resolved UV/vis spectra of the donor cage the short decay time constant of  $D^{\bullet+}$  can be attributed to a BET from the  $\text{Pd(II)Pd(I)DD}^{\bullet+}\text{A}_2$  LMCT state. The longer time constants must be connected to DACT. Though a final conclusion about them cannot be provided, DACT to ligands in cis and trans position can be assumed.

## 4.1.4 Triphenylamine-fluorenone-donor-acceptor cage

### 4.1.4.1 Introduction

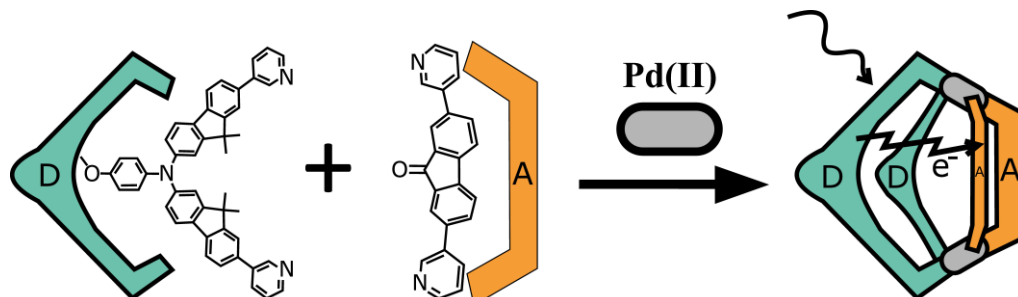


Fig. 46: molecular structure of the TPA donor and FLO acceptor ligands and schematic structure of the mixed cage.

The second donor-acceptor system by Jacopo Tessarolo (see fig. 46) uses the same concept as the one by Kai Wu: a difference in ligand length and inflection between donor and acceptor to force a certain morphology.

While the same fluorenone acceptor was used, the donor was changed to an even further bent much larger molecule. The backbone is based on triphenylamine (TPA), where one phenyl-ring has a methoxy-group in para-position. The other two are part of 9,9-dimethyl-9H-fluorene (further on abbreviated with FLN) connectors linking the backbone to 3-pyridyl-groups again serving as anchors.

Upon complexation with Pd(II) the TPA donor ligand D builds cages of the form Pd<sub>2</sub>D<sub>4</sub> in either acetonitrile or DMSO. Each ligand has, at least in the crystal, one fluorene's methyl-group pointing inside and one outside the cage reducing stress through bending of the ligand intended for the mixed cage and to prevent formation of non-stoichiometric D-A-cages. Two neighbouring ones have their upper methyl-groups while the other two have their lower ones inside. The amine in the centre of the ligand disrupts a potential delocalization over the whole molecule in the electronic ground state as the nitrogen is planar trigonally bound, but the substituents are oriented in a propeller shape<sup>[58]</sup>. Though it allows to further alleviate stress from the inflection, this flexibility could hinder the intended goal of morphology control.

Fortunately, the donor-acceptor cage only forms one structure like the one from Kai Wu: two donors and two acceptors coordinate two Pd(II) ions in a square-planar pattern, both in cis-position. The TPA donor further increases the angle between the Pd-coordination planes compared to the PTZ one. All methyl- and carbonyl-groups point towards the inside of the cage with a slight rotation between fluorene/fluorenone-backbone and their corresponding pyridyl-anchor.

All in all, in the case of the donor-acceptor-pair based on triphenylamine and fluorenone the concept of differing ligand length and inflection in order to ensure the formation of one cage structure was a success as well. With the time-resolved UV/vis and -midIR measurements it shall be demonstrated that the TPA-FLO cage is also able to perform a DACT upon photoexcitation of the TPA donor ligand. Similar to the PTZ-FLO cage, a successful DACT can be assumed if evidence is given for the creation of the FLO anion without it directly being excited itself. The following chapters will provide exactly this evidence.

### 4.1.4.2 Ground state spectra

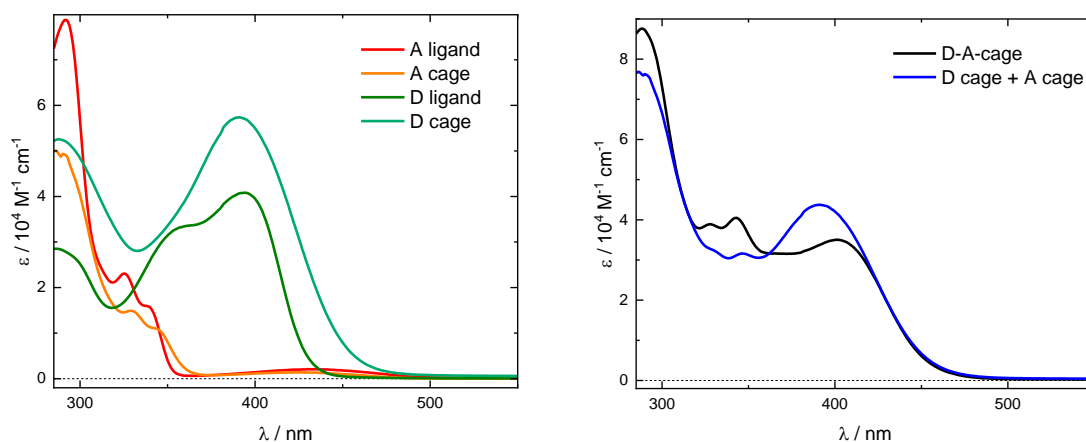


Fig. 47: ground state UV/vis absorption spectra (a) of the TPA donor and FLO acceptor ligand and their respective homomeric Pd(II) cage structures  $[\text{Pd}_2\text{D}_4]^{4+}$  and  $[\text{Pd}_3\text{A}_6]^{6+}$  and (b) of the mixed donor-acceptor cage  $[\text{Pd}_2\text{D}_2\text{A}_2]^{4+}$  and the sum of donor cage and acceptor cage  $[\text{Pd}_2\text{D}_4]^{4+} + [\text{Pd}_3\text{A}_6]^{6+}$ . All spectra were measured in DMSO-d6 by Jacopo Tessarolo.

Due to low solubility of TPA donor and donor cage in acetonitrile time-resolved UV/vis spectra were measured in deuterated dimethylformamide (DMSO-d6).

The UV/vis spectra of acceptor and acceptor cage in DMSO-d6 (fig. 47) are very similar to those in acetonitrile, though they are unexpectedly red-shifted (A ligand: 292 nm, 325 nm, 338 nm, 433 nm; A cage: ca. 285 nm, 330 nm, 335 nm, 424 nm) considering the lower polarity of the solvent.

The spectrum of the donor shows three absorption bands. The band at 287 nm corresponds to a local  $\pi \rightarrow \pi^*$  transition within the triphenylamine (TPA) moiety<sup>[59]</sup> that is typical for TPA with weakly electron-withdrawing phenyl substituents like methoxy-groups<sup>[60]</sup>. The similarly intense band at 394 nm is attributed to a transition within the  $\pi$ -system of the FLN branches<sup>[61],[62],[63]</sup>. The small shoulder at 357 nm might stem from the TPA localized transition that can appear if C3 symmetry is broken<sup>[59]</sup>. However, it could also be a shoulder that frequently appears at fluorene derivatives and might come from a HOMO-1  $\rightarrow$  LUMO transition. Though the ligand consists of both a typical electron donor (TPA) and acceptor (FLN) there is no charge transfer band in the NIR region<sup>[60],[64],[65]</sup>.

As expected, the complexation into the cage does only have a tangent effect on the position of the localized TPA transition (290 nm). The FLN transition is not shifted much as well (390 nm) presumably because its HOMO and LUMO are influenced equally strong by the Pd(II) ions due to similarities in electron density<sup>[63]</sup>. The band is generally broader and has no shoulder anymore.

Again, the donor-acceptor cage spectrum resembles the sum of the homoleptic cage spectra. However, the intensity of the acceptor band is significantly increased while the intensity of the donor bands is decreased. This suggests some electronic interaction between donor and acceptor ligands in the ground state. There are no new bands though, meaning there is most likely no direct donor-acceptor charge-transfer excitation accessible via the electronic ground state.

### 4.1.4.3 TPA ligand

#### 4.1.4.3.1 Time-resolved UV/vis spectra

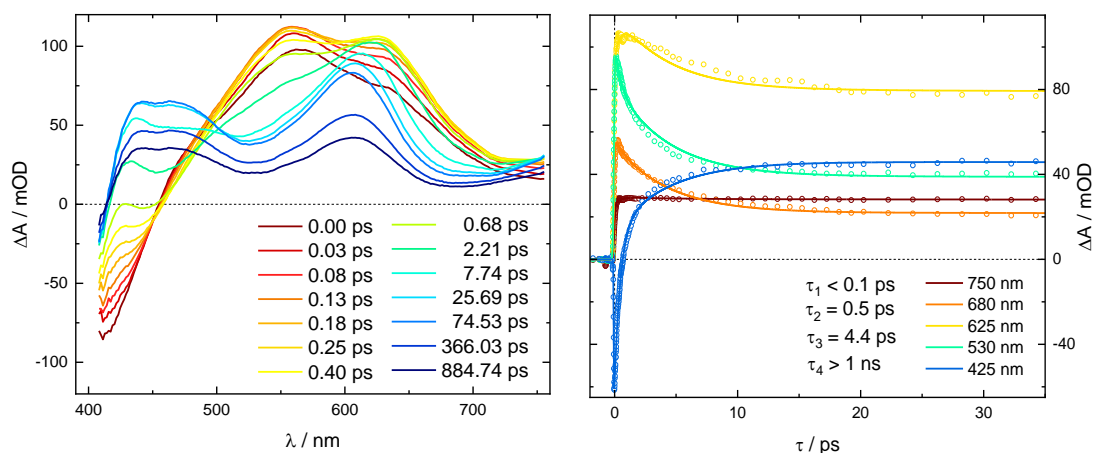


Fig. 48: time-resolved UV/vis spectra at selected pump-probe delays (left) and transient data (circles) of the TPA donor ligand D in DMSO-d<sub>6</sub> (0.227 mM ligand concentration) at different wavelengths after excitation at  $\lambda_{\text{pump}} = 375$  nm (0.19  $\mu\text{J}$ ) with corresponding tetraexponential fits (solid lines) and fitted time constants (right).

The time-resolved UV/vis spectra of the donor ligand upon excitation at  $\lambda_{\text{pump}} = 375$  nm in fig. 48 are highly complex due to the fact that it on its own includes the acceptor and fluorescent fluorene derived from the previously described fluorenone.

Right after excitation an excited state absorption band centred at 560 nm and a negative difference absorbance below 455 nm appear. When compared to the ground state absorption spectrum, it is apparent that this band cannot merely be a ground state bleach, but must include stimulated emission at about 425 nm. Since the excitation at 375 nm is assumed to induce a transition within the fluorene moiety, it could be attributed to a fluorescent band from the yet unrelaxed first singlet excited state  $S_1$  of the fluorene moiety.

A second absorption maximum at 625 nm is emerging with  $\tau_1 < 100$  fs. Time-resolved measurements on different triphenylamines show similar bands associated with the amine moiety<sup>[66]</sup>. Though the TPA is not directly excited at 375 nm, it is intertwined with the fluorene as one of the phenyl-groups and is therefore connected to the excitation. It could be assumed that the excitation at the fluorene induces a transition in the TPA as is insinuated for the TPA-FLO connection.

With the decay of the 560 nm band with  $\tau_2 = 0.5$  ps the stimulated emission at 425 nm also disappears while shifting to higher wavelengths and two new bands with less intensity emerge at 425 nm and above 730 nm. Those bands are a good indication for the formation of  $\text{TPA}^+$  when comparing to the oxidized donor cage (see fig. 49), where oxidation is most likely happening on the amine nitrogen. A similar spectral pattern was observed for fluorene-arylamine copolymers with 3-5 mol% amine content (the whole spectrum is red-shifted due to the extended  $\pi$ -system of the polymer)<sup>[67]</sup>. There, these new bands were linked to the fluorene singlet excited state that transforms into a charge transfer state  $\text{TPA}^+ + \text{FLN}^-$ .

At about 2 ps, when the 560 nm band has not fully vanished yet, the amine band at 625 nm starts to shift to 605 nm while at the same time a positive band at about 465 nm rises lifting up the  $\text{TPA}^+$  band at 425 nm. After this transformation ( $\tau_3 = 4.4$  ps) the remaining bands persist beyond 1 ns.

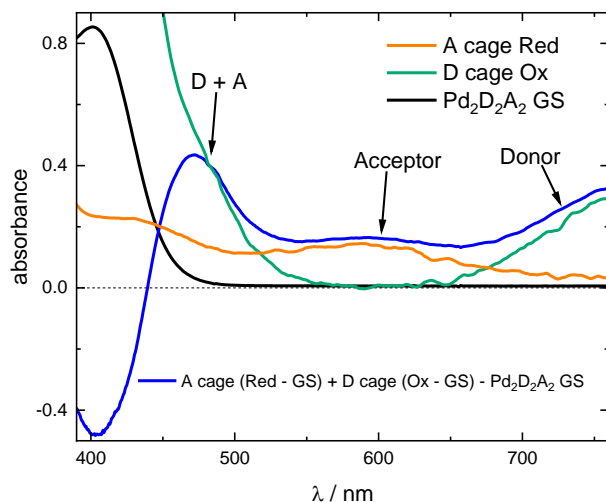


Fig. 49: ground state UV/vis absorption spectra of the TPA-FLO donor-acceptor cage  $[\text{Pd}_2\text{D}_2\text{A}_2]^{4+}$  (black), of the chemically oxidized TPA donor cage  $[\text{Pd}_2\text{D}_4]^{8+}$  (green) and the chemically reduced FLO acceptor cage  $[\text{Pd}_3\text{A}_6]$  in acetonitrile. The sum of those spectra (blue) should resemble a difference spectrum of the DACT state in the  $[\text{Pd}_2\text{D}_2\text{A}_2]^{4+}$  cage. All spectra were measured by Jacopo Tessarolo.

With the current information a reliable assignment of the bands with their complex transformations is not possible. Initial excitation of the fluorene moiety is likely considering the interpretation of the ground state UV/vis spectrum and there is evidence for a  $\text{TPA}^+$  with the bands at 425 nm and above 730 nm. However, the bands don't seem to grow and decay simultaneously, which could indicate the excitation into two different states or branching of the first relaxation step.

#### 4.1.4.4 TPA cage

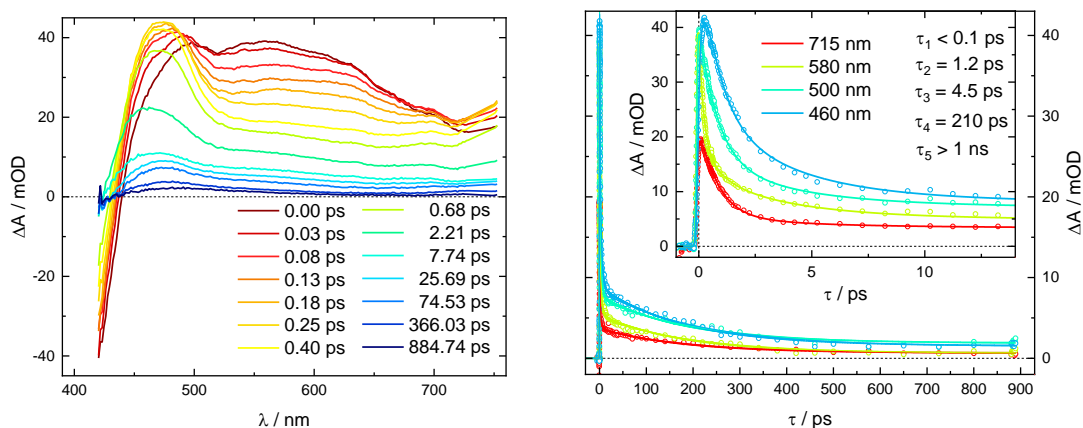


Fig. 50: time-resolved UV/vis spectra at selected pump-probe delays (left) and transient data (circles) of the donor cage  $[\text{Pd}_2\text{D}_4]^{4+}$  in DMSO-d<sub>6</sub> (0.221 mM ligand concentration) at different wavelengths after excitation at  $\lambda_{\text{pump}} = 375$  nm (0.19  $\mu\text{J}$ ) with corresponding quinquexponential fits (solid lines) and fitted time constants (right).

The time-resolved UV/vis spectra of the TPA donor cage  $[\text{Pd}_2\text{D}_4]^{4+}$  are shown in fig. 50. They are completely different from the spectra of the free donor ligand. Right upon excitation at  $\lambda_{\text{pump}} = 375$  nm a broad excited state absorption over the whole spectrum appears with maxima

at about 500 nm and 570 nm and the ground state bleach at below 450 nm. Similar to the free ligand, bands at 470 nm (considering the overlapping bleach the real maximum is probably lower) and above 730 nm grow within the first 200 fs ( $\tau_1 \approx 100$  fs), which again can be assigned to the generation of the TPA<sup>+</sup>.

The preceding state, according to the UV/vis spectrum an FLN excited state, has similarities to the time-resolved UV/vis spectra of the FLO acceptor cage, which has an excited state band of the S<sub>1</sub> state at 575 nm. Although there is no FLO in the molecule, FLN has a similar molecular structure and spectroscopic properties. It can be assumed that the less polar FLN produces a weaker absorption band of its S<sub>1</sub> state that is, just like the FLO ligand, severely broadened in the cage. However, since this band vanishes upon the creation of the supposed TPA<sup>+</sup> bands, the most evident explanation is that the relaxation of the FLN S<sub>1</sub> state induces an LMCT to a Pd(II) centre, which is reasonable considering the interconnection of FLN and TPA and similar observations for the PTZ donor ligands.

Three major components for the decay of the bands stand out: an initial fast decay with  $\tau_2 = 1.2$  ps, a comparatively slow one with  $\tau_4 = 210$  ps and a residual that lives beyond 1 ns. The fifth time constant  $\tau_3 = 4.5$  ps is probably caused by vibrational relaxations. Due to the similarities to the PTZ-FLO cage these time constants could be interpreted with three different BET, however, the TPA cage has no acceptor ligand and there is no explicit spectral evidence for an excited or CT state of the FLN moiety.

Time-resolved midIR spectroscopy could provide further evidence for the nature of these states, but since solubility issues currently don't allow such measurements, assumptions have to suffice. One distinguishing feature could come from the flexibility of the donor ligand. Two different morphologies of the ligand can be identified at least in the crystal. It is possible that one of these significantly hinders the BET, which would account for two time constants. Additionally, the para-methoxy-phenyl-group could be able to receive charge from the amine as an alternative acceptor. However, this assignment requires more knowledge of the electronic structure of this part of the ligand.

#### 4.1.4.5 TPA-FLO cage time-resolved UV/vis spectra

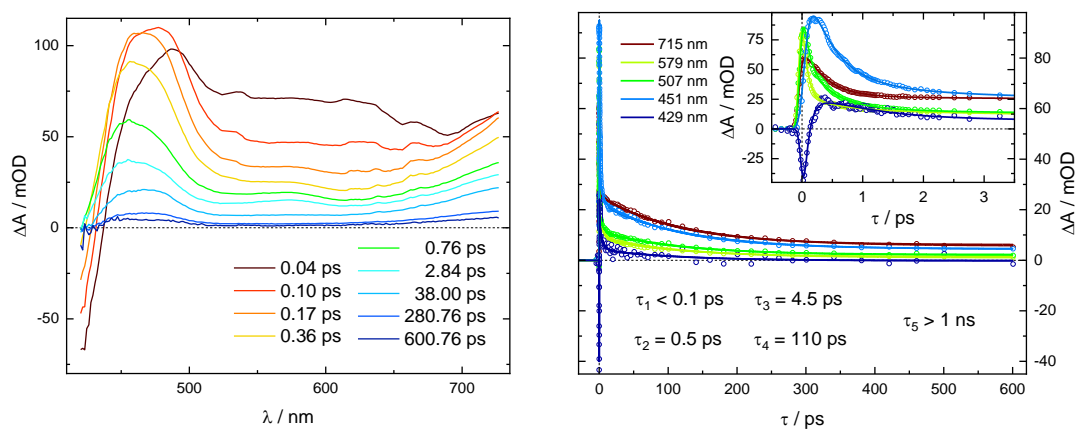


Fig. 51: time-resolved UV/vis spectra at selected pump-probe delays (left) and transient data (circles) of the TPA-FLO donor-acceptor cage [Pd<sub>2</sub>D<sub>2</sub>A<sub>2</sub>]<sup>4+</sup> in acetonitrile (0.25 mM ligand concentration) at different wavelengths after excitation at  $\lambda_{\text{pump}} = 400$  nm (1.3  $\mu$ J) with corresponding quinaexponential fits (solid lines) and fitted time constants (right).



The time-resolved UV/vis spectra of the TPA-FLO donor-acceptor cage  $[\text{Pd}_2\text{D}_2\text{A}_2]^{4+}$  after excitation at  $\lambda_{\text{pump}} = 400 \text{ nm}$  in fig. 51 (data was measured in acetonitrile and at 400 nm excitation for better comparison to the time-resolved midIR spectra, but measurements in DMSO-d6 and at 375 nm excitation were identical) have a lot of similarities to the spectra of the donor cage  $[\text{Pd}_2\text{D}_4]^{4+}$ : an initial broad band at about 575 nm that decays within 200 fs ( $\tau_1 < 100 \text{ fs}$ ) and bands at 470 nm and above 730 nm appear, which decay with primarily three time constants ( $\tau_2 = 0.5 \text{ ps}$ ,  $\tau_4 = 110 \text{ ps}$  and  $\tau_5 > 1 \text{ ns}$ ). A comparison of normalized time traces of  $[\text{Pd}_2\text{D}_4]^{4+}$  and  $[\text{Pd}_2\text{D}_2\text{A}_2]^{4+}$  (see fig. 52) shows higher absorption of the  $[\text{Pd}_2\text{D}_2\text{A}_2]^{4+}$  cage after the initial decay of the FLN  $S_1$  state at the presumed TPA<sup>+</sup> bands and simultaneously a band at 575 nm appears that can be attributed to the absorption of the FLO anion  $A^{\cdot-}$  by comparison to the ground state UV/vis spectrum of the reduced FLO cage (see fig. 48), which would be a first indication of a successful DACT from TPA to FLO.

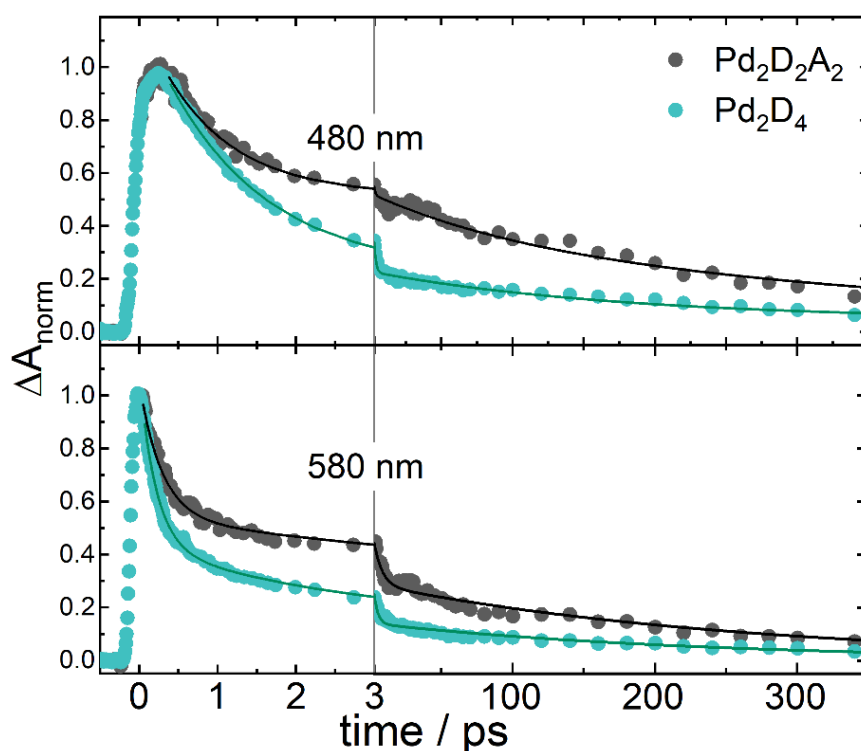


Fig. 52: comparison of normalized time traces of TPA donor cage  $[\text{Pd}_2\text{D}_4]^{4+}$  and TPA-FLO donor-acceptor cage  $[\text{Pd}_2\text{D}_2\text{A}_2]^{4+}$  at 480 nm and 580 nm. Note the change in scaling at 3 ps.

#### 4.1.4.6 TPA-FLO cage time-resolved midIR spectra

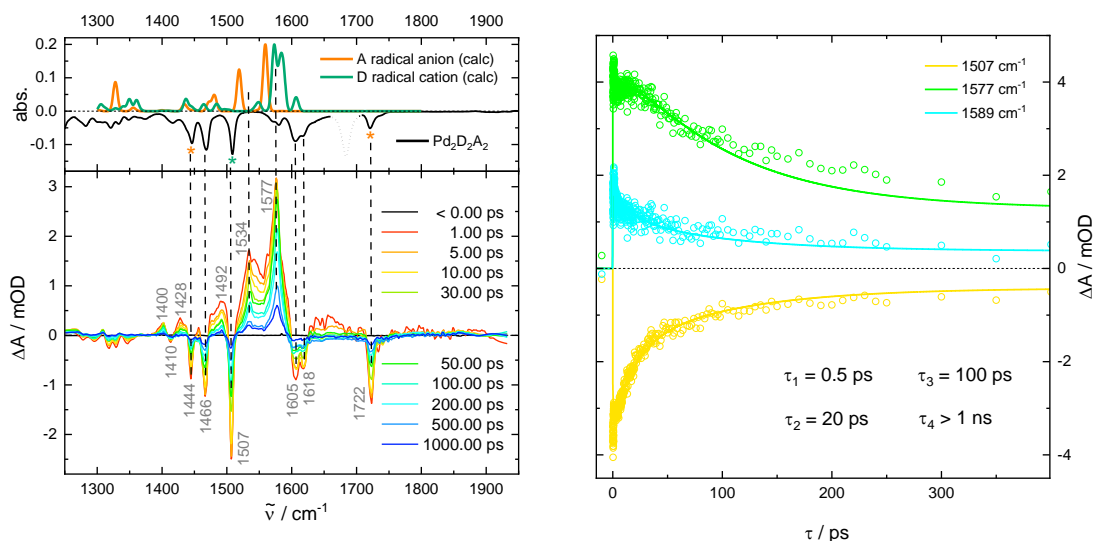


Fig. 53: ground state FTIR spectrum of the TPA-FLO cage  $[\text{Pd}_2\text{D}_2\text{A}_2]^{4+}$  (black) and calculated IR spectra for TPA $^{\bullet-}$  and FLO $^{\bullet+}$  (top left). DFT calculation were performed by Jacopo Tessarolo; time-resolved midIR spectra of  $[\text{Pd}_2\text{D}_2\text{A}_2]^{4+}$  in acetonitrile (0.25 mM) at selected pump-probe delays after excitation at 400 nm (1.1  $\mu\text{J}$ ) (bottom left); transient data (circles) of the time-resolved midIR measurement of  $[\text{Pd}_2\text{D}_2\text{A}_2]^{4+}$  at selected peaks with corresponding tetraexponential fits (solid lines) and fitted time constants (right).

The time-resolved midIR spectra of the TPA-FLO donor-acceptor cage  $[\text{Pd}_2\text{D}_2\text{A}_2]^{4+}$  after excitation at  $\lambda_{\text{pump}} = 400 \text{ nm}$  (fig. 53) show clear evidence for a DACT. Upon excitation of the donor ligand TPA not only the ground state bleaches of the donor appear, most importantly the strong peak at  $1507 \text{ cm}^{-1}$ , but also bleaches of the acceptor are visible, first and foremost intense the C=O stretching vibration at  $1722 \text{ cm}^{-1}$  and the C-C stretching vibrations of the aromatic system at  $1444 \text{ cm}^{-1}$ . Several other ground state vibrations are bleached as well ( $1410 \text{ cm}^{-1}$ ,  $1466 \text{ cm}^{-1}$ ,  $1605 \text{ cm}^{-1}$  and  $1618 \text{ cm}^{-1}$ ), but they at least partially overlap and can therefore not be used for an unambiguous assignment.

Aside from the bleaches two major excited state peaks appear as well: the thoroughly analysed C-O stretching vibration of the FLO anion at  $1534 \text{ cm}^{-1}$ , slightly red-shifted compared to the analogue signal in the PTZ-FLO cage, and a peak at  $1577 \text{ cm}^{-1}$ , which is in good agreement with experimentally gained shifts due to the removal of an electron from TPA $^{[68]}$  and with DFT calculated spectra (see fig. 53 top left) and therefore assigned to the TPA donor radical cation.

The bleaches decay with three time constants ( $\tau_2 = 20 \text{ ps}$ ,  $\tau_3 = 100 \text{ ps}$  and  $\tau_4 > 1 \text{ ns}$ ) that can be explained similarly to those of the PTZ-FLO cage: the long time constants belong to DACT in cis and trans direction, which is again just an assumption, and the short one is associated with vibrational relaxation that follows BET from the LMCT state. This interpretation is consistent for both the time-resolved UV/vis and midIR spectra and in comparison to the PTZ-FLO cage complex. However, very similar results were derived from the time-resolved UV/vis measurements of the donor cage  $[\text{Pd}_2\text{D}_4]^{4+}$ , which makes it less conclusive (time-resolved midIR spectra could unfortunately not be measured due to a lack of solubility in solvents appropriate for the spectral range). On the other hand, there is clearly a difference in the time-resolved UV/vis spectra at the TPA $^+$  bands and an FLO anion  $\text{A}^{\bullet-}$  band is visible without direct excitation.



## 4.1.5 Phenothiazine-anthraquinone-host-guest cage

### 4.1.5.1 Introduction

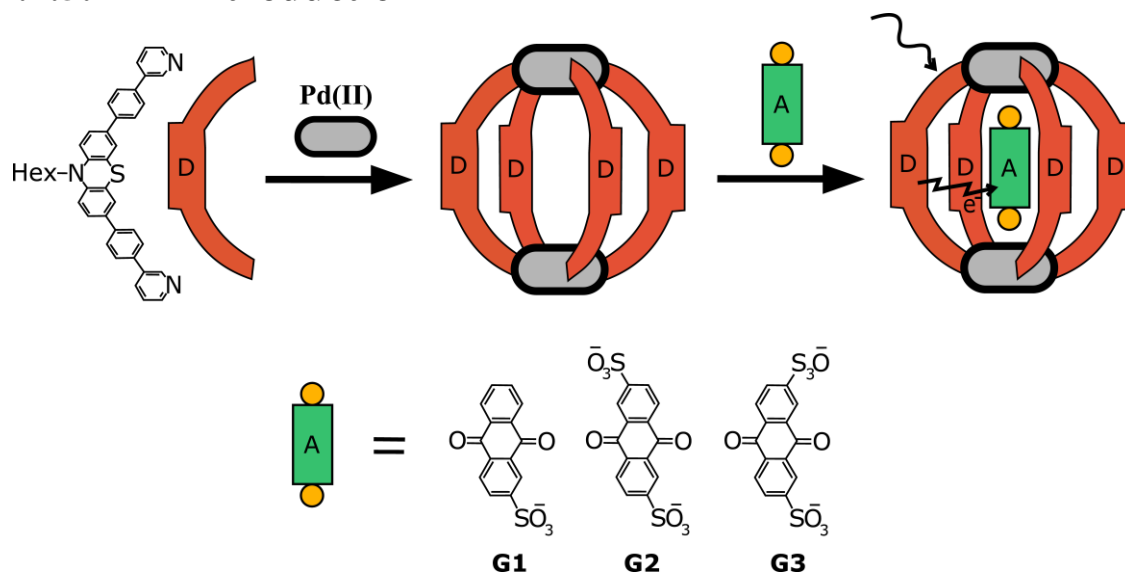


Fig. 55: molecular structure of the PTZ donor, the acceptors G1, G2, and G3 and schematic structure of the host-guest cage.

The third donor-acceptor system (fig. 55) takes a different approach: the cage is built solely of donor ligands, while the acceptor is embedded into the cavity of the cage as a guest molecule.

A donor very similar to the one of the first system was used consisting of a phenothiazine backbone and 3-pyridyl-anchor-groups. However, in order to scale up the size of the cavity a 1,4-phenyl-group was used instead of an ethynyl-group which increased the ligand length by about 3 Å<sup>[26]</sup>.

Interestingly, though the same basic structure was used, this ligand exclusively forms single cages with the same structure as the ones present in the double-cages of the other phenothiazine-derivative: four donor ligands coordinate two Pd(II) ions each in a square-planar geometry with their pyridyl-nitrogen aligning their phenothiazine sulphur towards the centre of the constructed cage.

As guest molecules three different anthraquinone-sulfonate and -disulfonate derivatives were used. While anthraquinone-2,7-disulfonate (G3) could not be integrated into the cage (and will therefore not be mentioned further on), host-guest-complexes with anthraquinone-2-sulfonate (G1) and anthraquinone-2,6-disulfonate (G2) were successfully created as demonstrated by NMR spectroscopy and single-crystal X-ray diffraction<sup>[26]</sup>.

The cavity of the host cage is large enough for one guest molecule. The sulfonate-groups are directed towards and close to the  $\alpha$ -protons of the ligands pyridyl-anchors while phenylene protons stabilize the guest from a comparable distance. The aromatic system of the anthraquinone does not seem to show any significant interaction with the host though, which was proposed due to the large distance of more than 7 Å between the respective aromatic systems<sup>[26]</sup>.

### 4.1.5.2 Ground state spectra

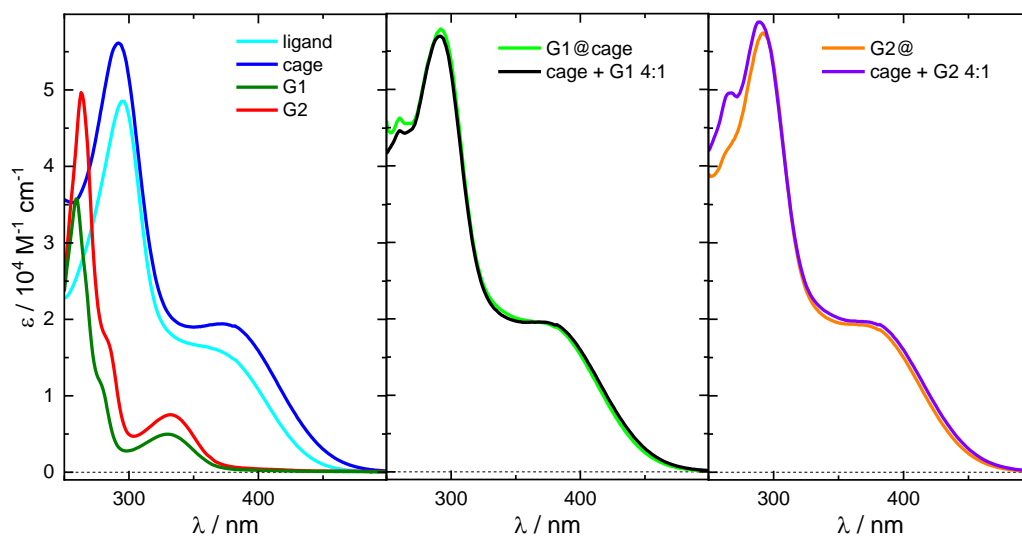


Fig. 56: ground state UV/vis spectra of the free PTZ donor ligand, its respective homomeric Pd(II) host cage structures  $[\text{Pd}_2\text{D}_4]^{4+}$  and the free guest molecules G1 and G2 (left), of the host-guest structure  $\text{G1}@[Pd_2D_4]^{4+}$  and the sum of host cage  $[\text{Pd}_2\text{D}_4]^{4+}$  and free guest G1 and (middle) and of the host-guest structure  $\text{G2}@[Pd_2D_4]^{4+}$  and the sum of host cage  $[\text{Pd}_2\text{D}_4]^{4+}$  and free guest G2. All spectra were measured in DMSO by Sudhakar Ganta.

Since the structure of the donor ligand is very similar to the one of the first donor-acceptor cage, the spectra look very much alike (see fig. 56 and fig. 34). Both the local phenothiazine and the  $\pi$ -systems charge transfer transition are only minimally shifted (295 nm and 362 nm), but overlap more, making the latter look more like a shoulder of the former.

Within the cage the high energy band at 292 nm and especially the low energy band at 373 nm is not shifted as much as with the double-cage of the ethynyl-derivative. It can be reasoned that the interaction between ligands of different cages in the double cage could have caused the strong red-shift.

Both guest molecules G1 and G2 share the spectral pattern of anthraquinone-sulfonates in solution<sup>[69]</sup>: an intense sharp band at 259 nm and 263 nm with a low-energy shoulder at 278 nm and 283 nm and a weak broad band at 330 nm and 332 nm, respectively, that are attributed via DFT calculations for G1 to an aromatic  $\pi \rightarrow \pi^*$ , a benzenoidic and an  $n \rightarrow \pi^*$  transition<sup>[70]</sup>. All of those include the sulfonate group to some extent. Due to the second sulfonate-group of the disulfonated derivative all bands are slightly red-shifted presumably owing to the extension of the  $\pi$ -system.

The addition of the monosubstituted anthraquinone G1 into the cage cavity induces minute differences to the spectrum compared to the sum of its parts: the band maxima at 372 nm, 292 nm and 260 nm are almost identical. Only the increased intensity of the latter might hint at some form of host-guest communication.

The disubstituted derivative G2 on the other hand has a slightly stronger band shift (370 nm, 292 nm, 266 nm) and more importantly a quite significant decrease in the intensity of anthraquinones intense aromatic  $\pi \rightarrow \pi^*$  transition indicating significant host-guest interaction. Unfortunately, there is no band of a charge transfer between phenothiazine backbone and the acceptor guest at about 630 nm as was predicted by DFT calculation<sup>[26]</sup>.

### 4.1.5.3 Time-resolved UV/vis spectra

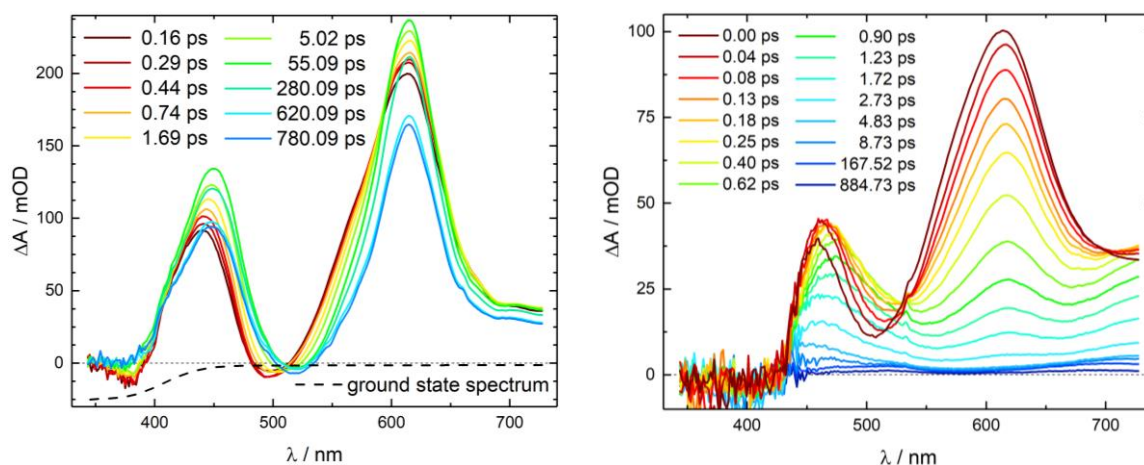


Fig. 57: time-resolved UV/vis spectra of the PTZ donor ligand D (left) and the host cage [Pd<sub>2</sub>D<sub>4</sub>]<sup>4+</sup> (right) in acetonitrile (0.28 mM ligand concentration) at selected pump-probe delays after excitation at 400 nm (0.45 μJ).

The time-resolved UV/vis spectra of the free donor ligand, the donor cage and both host-guest cages were excited at  $\lambda_{\text{pump}} = 400$  nm. At this wavelength all samples have an absorption band, which is the PTZ IL charge-transfer-like transition. This ensures that specifically the donor is excited so that any signal from the guest acceptor molecule is a result of an interaction, preferably a charge-transfer, with the donor.

The spectra of the free donor ligand (fig. 57 left) look very similar to those of the analogue with the ethynyl-linker. Upon excitation they show two absorption bands centred at 445 nm and 613 nm with a minimum at around 500 nm. Over a few picoseconds the first maximum shifts to 450 nm and the minimum to about 520 nm, however, the spectrum barely decays for the whole measurement indicating a long lifetime  $> 2$  ns of the corresponding state.

Just like the analogue, the spectra are interpreted as a superposition of a strong excited state absorption of the long-lived charge-transfer-like  $S_1$  state with superimposing stimulated emission from this state, which is consistent with observations of other PTZ compounds<sup>[38]</sup>.

Coordination of the donor completely quenches the steady-state fluorescence<sup>[26]</sup> from the  $S_1$  state and accordingly the time-resolved UV/vis spectrum almost completely decays within about 5 ps (see fig. 57 right). It initially consists, very similar to the free ligand, of two excited state maxima at 455 nm and 613 nm and a minimum at about 500 nm and is therefore assigned to the  $S_1$  state of the ligand. Because of the red-shifted ground state spectrum, the band at 500 nm is weaker and slightly red shifted compared to the free ligand. The drastically shorter lifetime of  $S_1$  implies that a new relaxation pathway is opened upon complexation. An evident interpretation would be an LMCT from ligand to Pd(II) creating [Pd(II)Pd(I)D<sub>3</sub>D<sup>•+</sup>]<sup>4+</sup>.

During the first few hundred femtoseconds the excited state bands decay while a section of a band above 700 nm grows. Comparison with the oxidized cage [Pd<sub>2</sub>D<sub>4</sub><sup>•+</sup>]<sup>8+</sup>, which has a band at 700 nm, further supports the generation of the donor radical cation D<sup>•+</sup> (see fig. 58). The shift of that band between those spectra could be explained with the fact that only one electron is transferred upon photoexcitation. At the same time, the minimum at 500 nm shifts to 530 nm, possibly due to the growth of the second band of D<sup>•+</sup> at about 530 nm and the subsiding of the stimulated emission from the depopulating  $S_1$  state. The subsequent decay can be attributed to the BET.

Addition of G1 into the cavity of the donor cage does not change the time-resolved UV/vis spectra (fig. 60 right). This might confirm the from the ground state UV/vis spectrum suspected lack of host-guest interaction, but the calculation of the binding constant ( $K_b \approx 140 \text{ M}^{-1}$  [26], 1% encapsulated at the used concentrations) reveals that at the low concentrations used in the experiments the fraction of cages that were filled with this guest is actually rather small anyway so any eventual changes would most likely be undetectable. The disulfone variant G2 on the other hand is quite efficiently encapsulated ( $K_b \approx 1.16 \cdot 10^5 \text{ M}^{-1}$  [26], 84% encapsulated at the used concentrations) and introduces a small, but noticeable difference in the spectra. Beside the slightly smaller intensity of the  $S_1$  band at 613 nm, it also seemingly shifts to 601 nm, which is actually the appearance of a new band. It can be reasoned that this band is an indication for the reduced guest anion  $G2^{2-}$ , which has a band at 575 nm (see fig. 58), generated via HGCT. The difference might be again caused by the different charge of the  $G2^{2-}@[Pd_2D_3D^{*+}]^{4+}$  compared to the chemically reduced form or by interactions with the electric field of the positively charged cage with two  $Pd^{2+}$  cations and one  $D^{*+}$ .

The influence of the guest can also be observed with the changed transient signal in fig. 59 (other transients show similar changes). Due to the additional relaxation path of  $S_1$  the initial decay is slightly faster. Though the difference is small, the high quality and low noise of the measurements guarantee the validity of the observation. Subsequently, a slower decay compared to the cage without guest represents the relaxation from the HGCT state back to the ground state via BET.

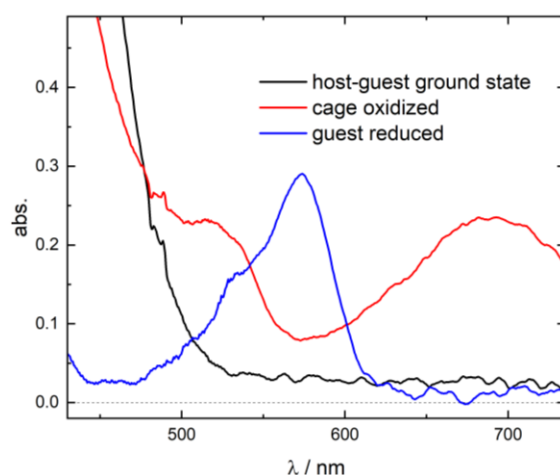


Fig. 58: arbitrarily scaled absorption spectrum of the ground state of  $G2@[Pd_2D_4]^{4+}$ , the oxidized cage  $[Pd_2D_4]^{8+}$  and the reduced guest  $G2^{2-}$ .

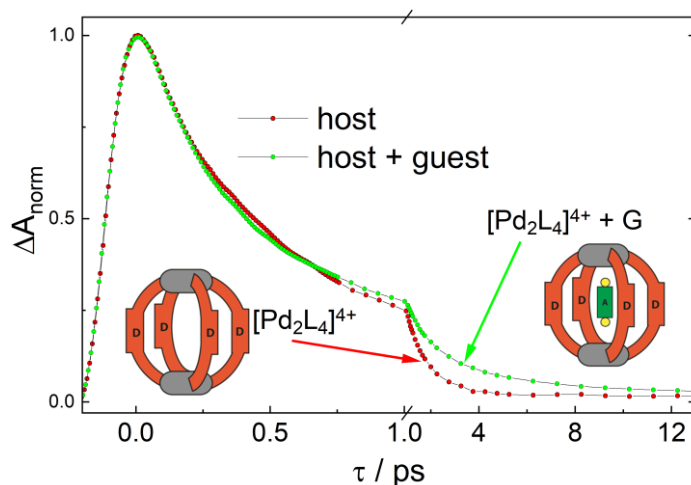


Fig. 59: transient data (dots) of the time-resolved UV/vis measurement of  $[Pd_2D_4]^{4+}$  (red) and  $G2@[Pd_2D_4]^{4+}$  (green) after excitation at  $\lambda_{pump} = 400 \text{ nm}$  at 613 nm.

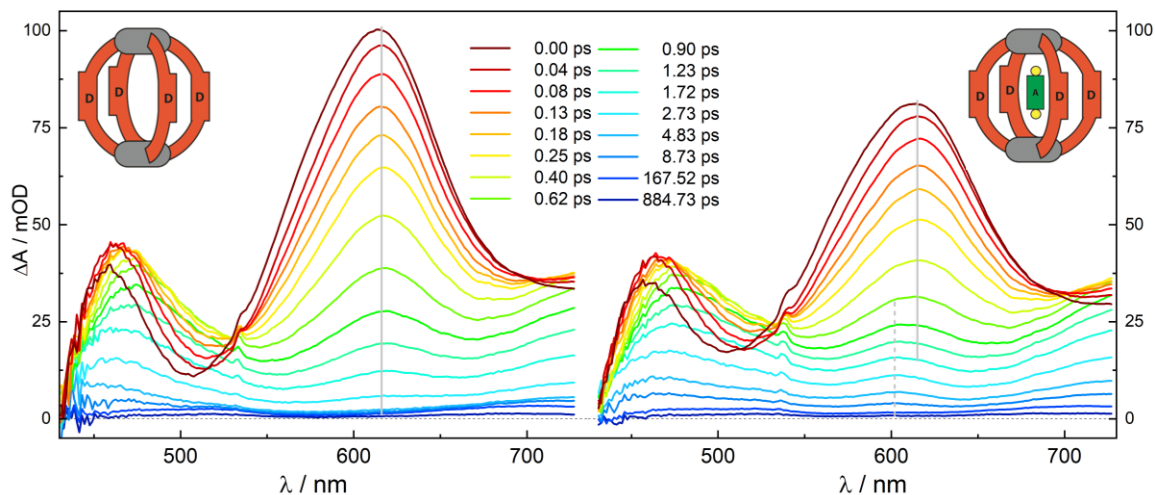


Fig. 60: comparison of the time-resolved UV/vis spectra of the PTZ host cage  $[\text{Pd}_2\text{D}_4]^{4+}$  (left) and the host-guest cage  $\text{G2}@\text{[Pd}_2\text{D}_4]^{4+}$  in acetonitrile (0.28 mM ligand concentration) at selected pump-probe delays after excitation at 400 nm (0.45  $\mu\text{J}$ ).

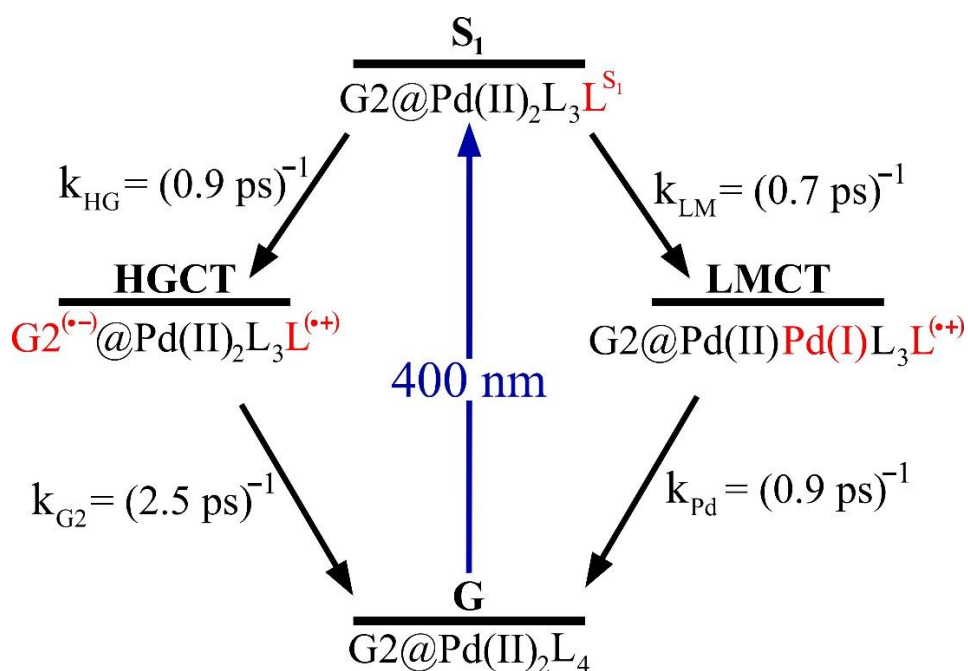


Fig. 61: energy level diagram depicting the proposed relaxation dynamics of  $\text{G2}@\text{[Pd}_2\text{D}_4]^{4+}$  upon excitation at 400 nm.

In order to receive accurate time constants and from those a relative yield of LMCT and HGCT, a kinetic model was constructed according to the energy level diagram in fig. 61. After photoexcitation of one D ligand in a cage to its  $S_1$  state two relaxation paths are available: the LMCT from D to Pd(II) creating  $\text{G2}@\text{[Pd(II)Pd(I)D}_3\text{D}^{\bullet+}]^{4+}$  with  $k_{\text{LM}}$  or the HGCT forming  $\text{G2}^{\bullet-}@\text{[Pd}_2\text{D}_3\text{D}^{\bullet+}]^{4+}$  with  $k_{\text{HG}}$ . Both then decay with their respective rate constant  $k_{\text{Pd}}$  and  $k_{\text{G2}}$  back to the ground state via BET. According to this model the following rate equations were established:



$$\frac{d[S_1]}{dt} = -(k_{LM} + k_{HG})[S_1] \quad \text{eq.047a}$$

$$\frac{d[LMCT]}{dt} = k_{LM}[S_1] - k_{Pd}[LMCT] \quad \text{eq.047b}$$

$$\frac{d[HGCT]}{dt} = k_{HG}[S_1] - k_{G1}[HGCT] \quad \text{eq.047c}$$

$$\frac{d[G]}{dt} = k_{Pd}[LMCT] + k_{G1}[HGCT] \quad \text{eq.047d}$$

By numerically solving this equation system, the time dependence of the concentration of the four proposed species abbreviated  $S_1$ , LMCT, HGCT and G was gained with the initial concentration of  $S_1$  set to one, the others to zero. The absorption time traces  $\Delta A(\lambda, t)$  were then fitted at four probe wavelength (474 nm, 505 nm, 613 nm, and 720 nm) to receive the rate constants. For this purpose, the concentration  $c_i(t)$  of all spectrally visible species, which are the  $S_1$  state of D  $L^{S_1}$ , the donor radical cation  $L^{(\bullet+)}$  and the guest radical anion  $G2^{\bullet-}$ , multiplied by their respective absorption cross section  $\sigma(i, \lambda)$  were added together

$$\Delta A(\lambda, t) = \sum_i \sigma(i, \lambda) c_i(t) \quad \text{eq.048}$$

in consideration of the relations  $[L^{(\bullet+)}] = [LMCT] + [HGCT]$  and  $[G2^{\bullet-}] = [HGCT]$ .

At first the data of the donor cage  $[Pd_2D_4]^{4+}$  were fitted excluding the HGCT path. From this the rate constants  $k_{LM} = (0.7 \pm 0.1 \text{ ps})^{-1}$  and  $k_{Pd} = (0.9 \pm 0.2 \text{ ps})^{-1}$  were gained. In the subsequent fit of the host-guest cage data these constants were assumed unaffected by the addition of the guest G2. The time constants received from this fit are  $k_{HG} = (0.9 \pm 0.2 \text{ ps})^{-1}$ ,  $k_{G1} = (2.5 \pm 0.3 \text{ ps})^{-1}$ .

The experimental data and fit curves are depicted in fig. 62. They show good agreement for all four wavelengths and both samples supporting the validity of the model. The inset with the relative populations of all spectrally visible species shows the high concentrations of the guest radical anion  $G2^{\bullet-}$ . This is also reflected in the yield calculated from the rate constants

$$\Phi_{HGCT} = \frac{k_{HG}}{k_{HG} + k_{LM}} = 44\% \quad \text{eq.049}$$

The yield shows that despite the small changes in the spectrum a significant share of the guest G2 is performing the desired HGCT.

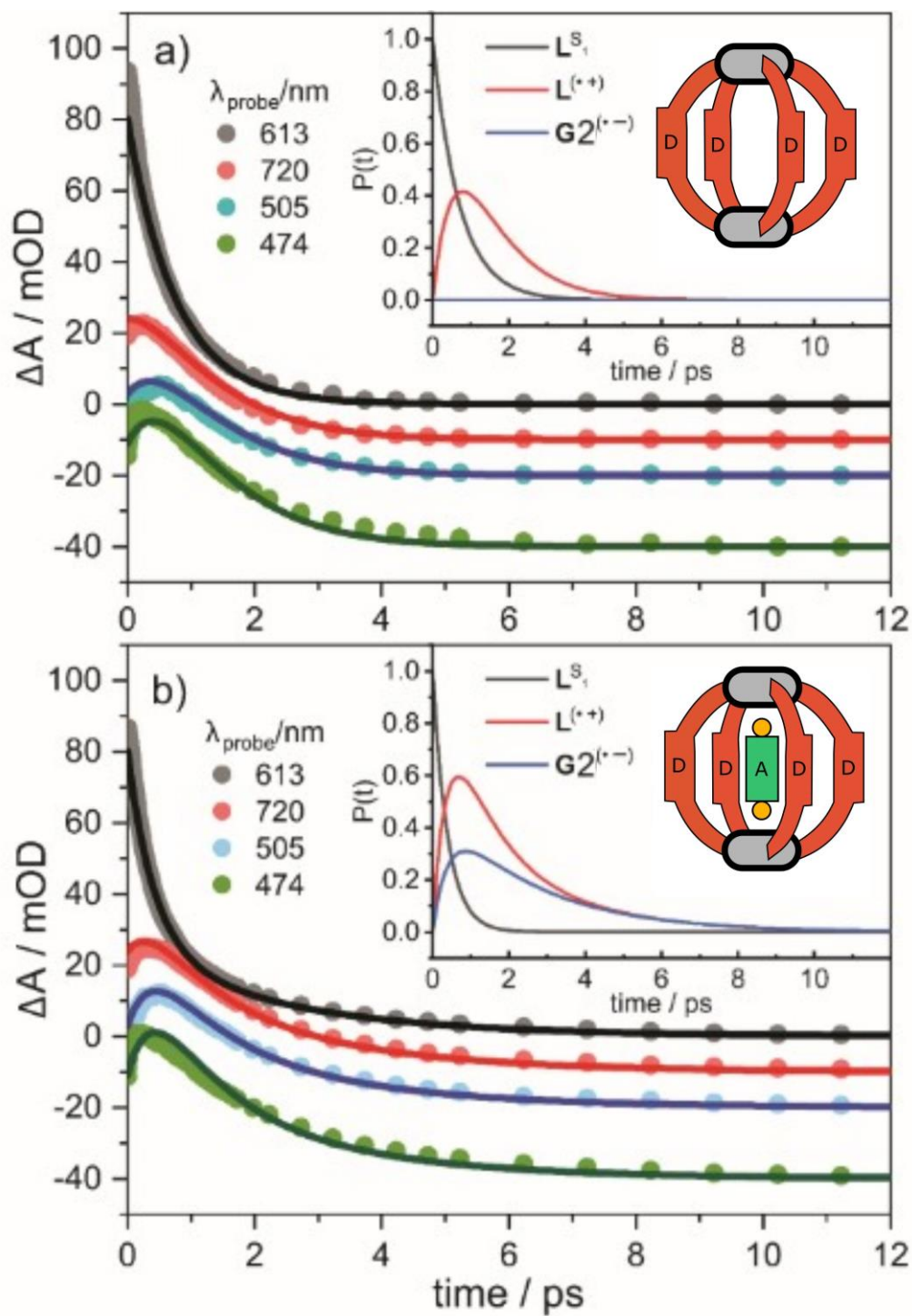


Fig. 62: transient data (dots) and fits of the kinetic model (solid lines) of the time-resolved UV/vis measurement of  $[\text{Pd}_2\text{D}_4]^{4+}$  (a) and  $\text{G2}@\text{[Pd}_2\text{D}_4]^{4+}$  (b) after excitation at  $\lambda_{\text{pump}} = 400 \text{ nm}$  at four different wavelengths. The insets show the relative populations of the spectrally visible states according to the fitted model.

## 4.1.6 Conclusion project 1

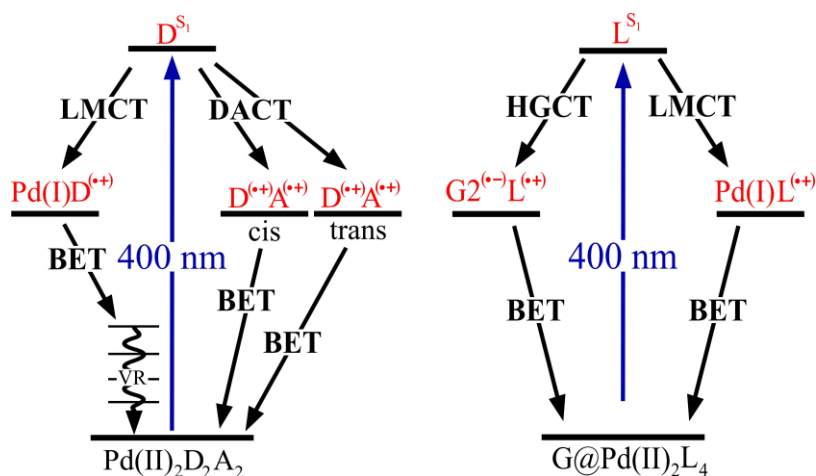


Fig. 63: general energy level diagram depicting the relaxation processes within donor-acceptor (left) and host-guest (right) Pd(II) cage complexes after excitation at 400 nm.

The analysis of time-resolved UV/vis and midIR spectra of all three self-assembling donor-acceptor cage systems very convincingly proved charge-transfer dynamics occurring after excitation at 400 nm. In all cases the charge-transfer process originated from the  $\text{S}_1$  state of the donor, which generated the predominant signals in the time-resolved UV/vis spectra. The identification of the donor radical cation from the subsequent transition happened primarily by comparing data from the chemically oxidized donor cage. However, these signals do not by themselves prove a donor-acceptor CT since they also appear upon the LMCT transition to the Pd(II) cation. For the two traditional cage structures, where both donor and acceptor constitute the cage, the definitive evidence that the acceptor received the negative charge was provided with the time-resolved midIR spectra. The very intense peaks of the acceptor radical anion, in these cases the carbonyl stretching vibration of fluorenone, appeared at the same time as those of the donor radical cation and together with the corresponding ground state bleaches, although the pump wavelength was selected to specifically only excite the donor.

Issues with the solubility of the complexes hindered the analysis severely, since often no suitable solvent for the time-resolved midIR measurements was available that both does not absorb in the necessary spectral ranges and enables concentrations above the point where the complexes significantly decompose. Nevertheless, it was possible to find evidence for a host-to-guest charge-transfer for the corresponding complex by fitting a kinetic model to the available data despite the almost invisible manifestation of bands from the guest radical anion.

The results for all three complexes and the previous PTZ-ANQ Pd(II) cage show a general pattern: the excitation of the donor leads to a short-lived singlet state that upon relaxation primarily transitions to an LMCT state with a lifetime of about 1 ps. The introduction of an acceptor into the system, whether as a cage building block or within the cage cavity, can open an additional relaxation path: the desired DACT/HGCT. The yield of this second path ranges between 30 and 50% of the  $\text{S}_1$  population. Those cages with two different donor-acceptor distances all showed a relaxation time constant of about 100 ps and a second one with more than a nanosecond. Though there is no solid prove yet, the association with the D-A distance of the ligands in cis/trans position is evident. This concept is also at play in the host-guest cages, where the very short distance results in a similarly short lifetime of the HGCT state, but the yield is accordingly rather high.



## 4.2 Project: metal-to-metal charge-transfer and vibrational relaxation of carbonyl ligands in tungsten-alkyne complexes OC-W(II)-L, OC-W(II)-L-Ru(II)(bpy)<sub>2</sub>PF<sub>6</sub> and OC-W(II)-L-Ir(III)(ppy)<sub>2</sub>

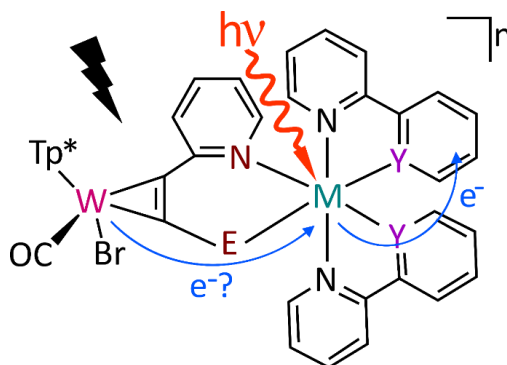


Fig. 64: schematic structure of the heterobinuclear W(II)-Ru(II)/Ir(III) complexes.

Ruthenium and iridium are very useful metal centres when it comes to the generation of charge-transfer states since they mediate a very fast spin transition due to their large spin-orbit coupling. The resulting triplet MLCT states have very long lifetimes and a correspondingly high phosphorescence yield<sup>[71],[72]</sup>, which is mandatory to achieve a consecutive two-electron transfer in high yields for the stabilization of the excitonic radical pair. As a two-step reaction already has a lower probability for success, it is paramount to increase the efficiency of the second step by establishing a strong electronic coupling between redox centres, which is often reduced due to the influence of the bridging connector. It is therefore reasonable to use the smallest bridge possible. Connecting ligands that can fulfil these conditions are alkynes. As the smallest ditopic ligand they can side-on connect to one metal centre via their  $\pi$ -system and serve as a bidentate ligand with two donor substituents for the other<sup>[8]</sup>. Especially the  $\pi$ -connection can mediate quite well as it not only pushes charge to the metal site, but also receives charge from the metal via  $\pi$ -back bonding according to the Dewar-Chatt-Duncanson (DCD) model.

With this approach heterobinuclear transition metal complexes built from a Ru(II)- or Ir(III)-polypyridine side and a W(II) carbonyl side connected by an alkyne with two donor substituents imitating a phenylpyridine ligand were constructed (see fig. 64), that are supposed to perform a photoinduced LMCT from the Ru/Ir centre to the polypyridine ligands, which should trigger a subsequent MMCT from the W(II). The carbonyl ligand on the tungsten in this case serves as a marker that is very sensitive to the electron density around the metal as it also connects via  $\pi$ -back bonding and can therefore be used in time-resolved midIR spectroscopy to monitor any charge transfer around the W(II).

In order to investigate the dynamics following electronic excitation of the photocentres Ru(II)(bpy)<sub>2</sub> and Ir(III)(ppy)<sub>2</sub> both complexes and the mononuclear building block surrounding the W(II) centre (see fig. 65) were measured using time-resolved UV/vis and midIR spectroscopy. Those measurements will show that a full MMCT cannot be observed, but that the energy transfer still is efficient as a highly vibrationally excited anharmonic carbonyl stretching vibration appears.

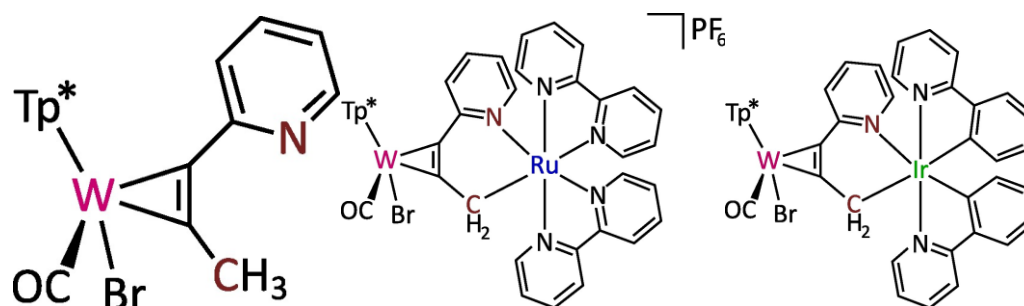


Fig. 65: Molecular structures of the complexes OC-W-L (left), [OC-W-L-Ru(bpy)<sub>2</sub>]<sup>+</sup> (middle) and OC-W-L-Ir(ppy)<sub>2</sub> (right).

## 4.2.1 Dewar-Chatt-Duncanson model

Electronic excitation of the binuclear tungsten complexes in the visible spectral range is expected to induce a metal-to-metal charge-transfer either directly or via intermediate stages. Such a transition inevitably would involve the creation of W(III) from W(II), which would be rather difficult to identify with time-resolved UV/vis spectra and barely visible in the midIR, if it weren't for the carbonyl ligand connected to the tungsten centre. This group possesses a very intense absorption peak corresponding to the C-O stretching vibration, whose position in the midIR spectrum strongly depends on the electron density on the connected transition metal. This behaviour is typically explained with  $\sigma$ -donation to the metal and especially  $\pi$ -acceptance of the carbonyl from the metal according to the Dewar-Chatt-Duncanson (DCD) model<sup>[74],[75]</sup>, which was originally developed to give an explanation for the formation of the side-on coordination of a transition metal to an olefine and the related bond elongation in the olefine. Regarding the transition metal-carbonyl coordination this model derives reasoning for the relative C-O bond strength of coordinated carbonyls in general and the higher stability of end-on ( $\eta^1$ ) versus side-on ( $\eta^2$ ) coordination specifically by looking at the involved molecular orbitals and their energy in the MO energy diagram (fig. 66).

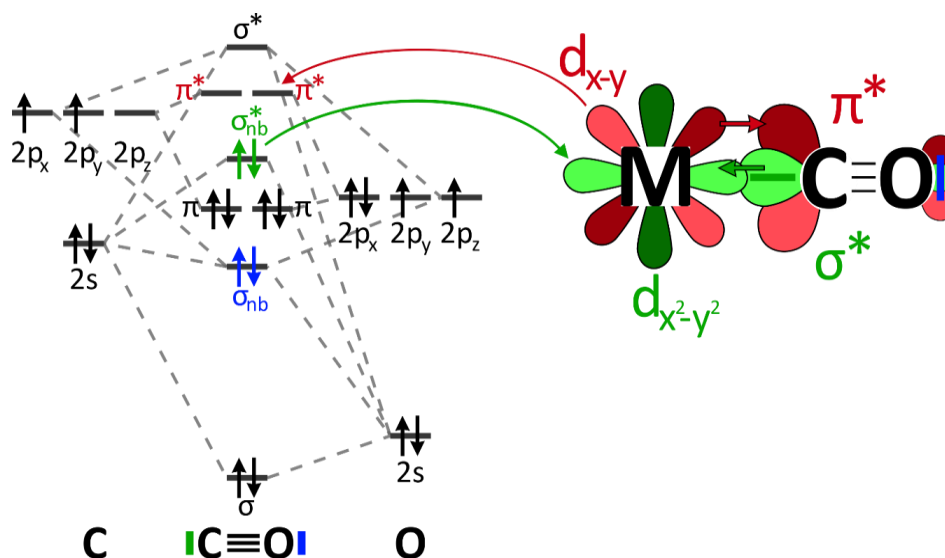
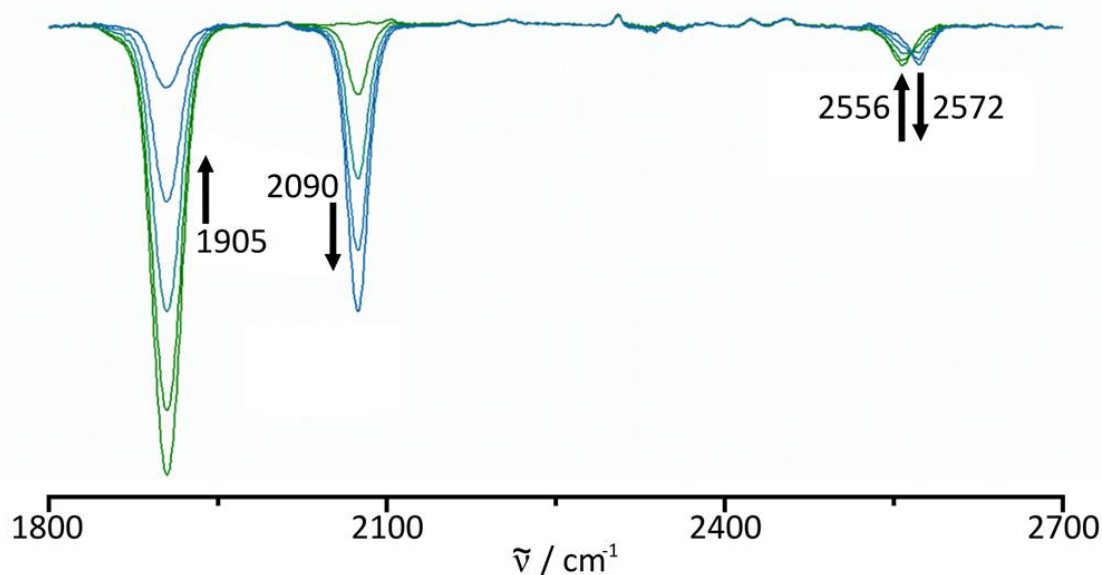


Fig. 66: molecular orbital energy diagram of carbon monoxide (left) and depiction of orbitals involved in the creation of transition metal-carbonyl bonds (right). Brighter/darker coloration of the lobes of the d- and  $\pi^*$  orbitals indicate signs of the corresponding wavefunctions.

The HOMO orbital of the carbonyl ligand is a non-bonding/slightly anti-bonding  $\sigma^*$  orbital that corresponds to the free electrons on the carbon atom in the valence bond depiction. These electrons most commonly bind to a transition metal via an empty d-orbital, usually the  $d_{x^2-y^2}$ -orbital, though s- and p-orbitals can contribute. The resulting  $\sigma$ -bond does not change the C-O bond strength significantly. However, transition metals with filled d-orbitals, which applies to transition metals in low oxidation states and in particular to W(II), can alleviate further reduction of the oxidation state due to the free electrons of the carbonyl by donating d-electron density to the anti-bonding carbonyl  $\pi^*$  orbital. This so called  $\pi$ -back-bonding further strengthens the metal-carbonyl bond at the expense of the C-O bond strength. The weakening of the C-O bond can be observed through a large down-shift of the C-O stretching vibration absorption peak in the corresponding IR spectrum from  $\tilde{\nu}_{\text{CO, gas}} = 2143.1 \text{ cm}^{-1}$  in the gas phase to considerably below  $2100 \text{ cm}^{-1}$  (examples for transition metal monocarbonyls:  $\tilde{\nu}_{\text{CO}}(\text{Ni}(\text{CO})(\text{PF}_3)_4) = 2078 \text{ cm}^{-1}$ ,  $\tilde{\nu}_{\text{CO}}(\text{Fe}(\text{CO})_{\text{ax}}(\text{PF}_3)_4) = 2035 \text{ cm}^{-1}$ <sup>[76]</sup>,  $\tilde{\nu}_{\text{CO}}(\text{Fe}(\text{CO})_{\text{eq}}(\text{PF}_3)_4) = 2006 \text{ cm}^{-1}$ <sup>[76]</sup>,  $\tilde{\nu}_{\text{CO}}(\text{Rh}(\text{CO})\text{Cl}(\text{TPP})_2) = 1975 \text{ cm}^{-1}$ <sup>[77]</sup>,  $\tilde{\nu}_{\text{CO}}(\text{Ir}(\text{CO})\text{Cl}(\text{TPP})_2) = 1961 \text{ cm}^{-1}$ <sup>[77]</sup>). Accordingly, the tungsten complexes presented here display the same shift in their ground state IR spectra ( $\tilde{\nu}_{\text{CO}}(\text{OC-W-L}) = 1905 \text{ cm}^{-1}$ ,  $\tilde{\nu}_{\text{CO}}(\text{OC-W-L-Ru}(\text{bpy})_2^+) = 1886 \text{ cm}^{-1}$ ,  $\tilde{\nu}_{\text{CO}}(\text{OC-W-L-Ir}(\text{ppy})_2) = 1880 \text{ cm}^{-1}$ ).

Keeping the MO orbital model for transition metal carbonyls in mind, one would expect a similarly large up-shift upon oxidation of the tungsten metal centre from W(II) to W(III) as it would result from the proposed metal-to-metal charge-transfer from the W(II) to the respective metal Ru(II) or Ir(III) since less electron density would be available for back-bonding into the anti-bonding carbonyl  $\pi^*$  orbital that weakens the C-O bond. Indeed, spectroelectrochemical measurements in the infrared (IR-SEC, fig. 67) show a large shift of the C-O-stretching vibration and even the B-H stretching vibration within the Tp\* ligand as the corresponding peaks at  $1905 \text{ cm}^{-1}$  and  $2556 \text{ cm}^{-1}$  disappear, while two peaks at  $2090 \text{ cm}^{-1}$  and  $2572 \text{ cm}^{-1}$  emerge upon oxidation of the W(II) (see fig. 67).

Due to the large effect of the back-bonding on the position of the C-O stretching absorption peak the carbonyl ligand is a very sensitive marker for the electron density on the connected transition metal. It is therefore commonly used to identify electronic transitions in transition metal complexes and will be of central importance for the analysis of the dynamics of the three tungsten complexes after electronic excitation.



67: IR-SEC spectra of the OC-W-L complex during oxidation from W(II) to W(III).

## 4.2.2 Mononuclear OC-W-L complex

### 4.2.2.1 Ground state UV/vis spectrum

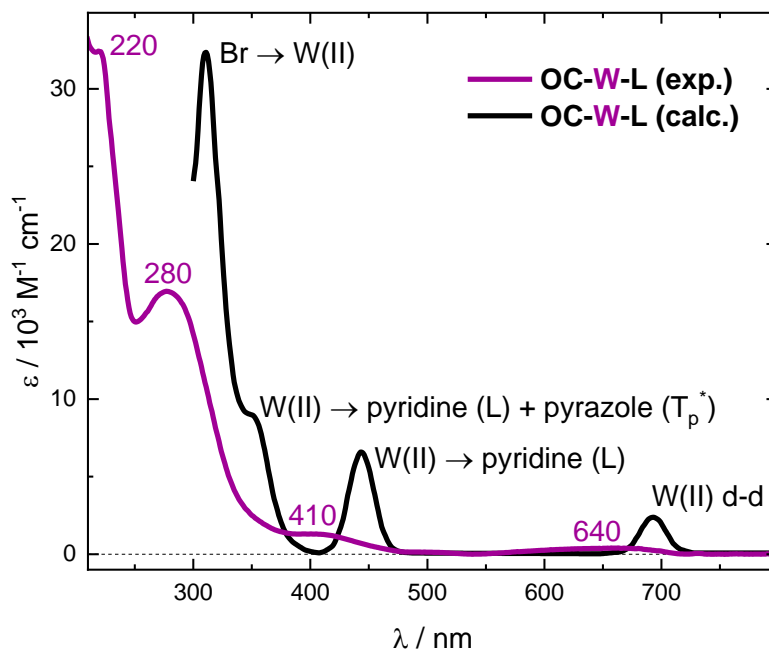


Fig. 68: ground state UV/vis spectrum of the OC-W-L complex in acetonitrile at room temperature measured by Mareike Hüttenschmidt (violet) and appropriately scaled ground state UV/vis spectrum with transition assignments calculated via TD-DFT. Data of the calculations reproduced from Hüttenschmidt et al.<sup>[73]</sup>.

In the spectral range of 200-800 nm four absorption bands can be identified in the ground state absorption UV/vis spectrum of the OC-W-L complex in acetonitrile solution (fig. 68): a weak, very broad, but well separated one at about 640 nm and three shoulders at 220 nm, 280 nm and 410 nm on the flank of the very intense ligand-based absorptions below 200 nm.

With the help of TD-DFT calculations<sup>[73]</sup> these bands can be roughly assigned, though significant mixing of states is assumed. Most of the calculated transitions above 200 nm involve the W(II) moiety. The weak low energy band is quite certainly ascribed to a forbidden MC d-d transition on the W(II), which according to calculated electron difference densities removes electron density from the  $d_{x-y}$  orbital responsible for the  $\pi$ -back bonding to the carbonyl and shifts it to the  $d_{y-z}$  or  $d_{x-z}$ -orbital (depending on the orientation of the coordinate system) overlapping with the alkyne  $\pi$ -system. The slightly stronger band at 410 nm represents a singlet-singlet MLCT transition from the tungsten to mostly the pyridyl-group of the alkyne ligand. At 280 nm an electron density shift from the W(II) to both the pyrazole-group of the  $T_p^*$  and the pyridyl-group of the alkyne ligand. Lastly, the band at 220 nm is assigned to  $Br \rightarrow W(II)$  transitions.

According to these assignments an excitation at 400 nm involves an electron density shift away from the tungsten moiety towards one of the organic ligands, which should induce a blue-shift of the C-O stretching peak in the time-resolved midIR spectrum. An ultrafast relaxation according to Kasha's rule<sup>[13]</sup> towards the MC transitions final state within the temporal resolution of the experiment is also possible, though this state would have a similar effect on the C-O stretching frequency.



### 4.2.2.2 Time-resolved UV/vis spectra

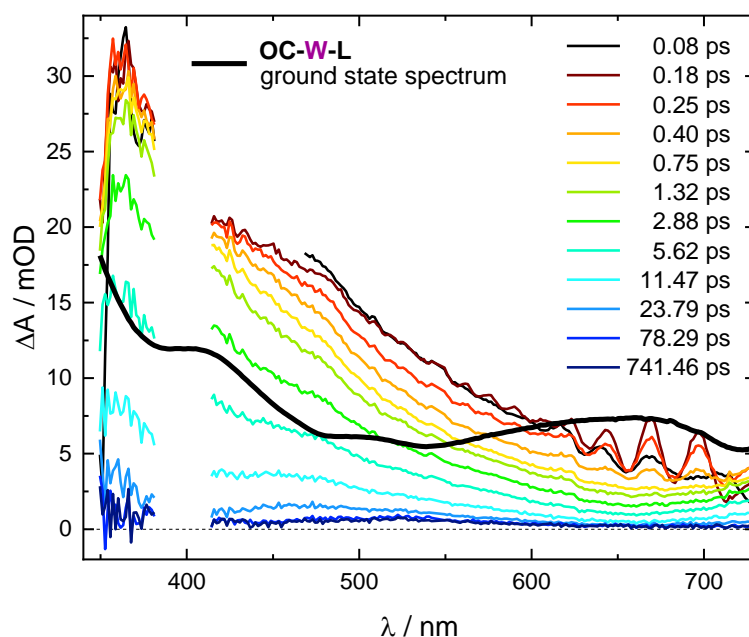


Fig. 69: time-resolved UV/vis spectra of the OC-W-L complex in acetonitrile (< 1.5 mM) at selected pump-probe delays after excitation at 400 nm (1  $\mu$ J). The ground state absorption spectrum with arbitrary scaling is included to understand the influence of the ground state bleach in the transients.

The time-resolved UV/vis spectra of the mononuclear tungsten complex OC-W-L after excitation at  $\lambda_{\text{pump}} = 400$  nm are shown in fig. 69. Right upon excitation a broad absorption is visible over the entire spectrum which seems to consist of a maximum at 362 nm with a slowly falling red-sided flank, a small positive bulge at 480 nm on top of the flank and a similarly small negative bulge above 600 nm. The latter is covered by oscillations, which are caused by a coherent artifact within the time overlap of pump and probe pulses and were not completely removable upon data correction. Within the first picosecond the maximum is slightly increasing and the bulge seems to at least maintain its shape (due to the low intensity reliable claims about an increase/decrease are not possible), while the underlying flank is decaying with a time constant of  $\tau_1 = 0.2$  ps. Then the whole spectrum is falling with a time constant of  $\tau_2 = 7.5$  ps until a weak broad band with less than 10% of the initial intensity centred at about 520 nm and an even smaller band below 450 nm (partially cut out due to the pump pulse interference) remain unchanged from about 40 ps to the end of the measurement.

The triexponential fits of the spectral decay with the three mentioned time constants in fig. 70 (left) illustrate that  $\tau_2$  is the dominant fraction of the decay. According to the DAS in fig. 70 (right) a decay with  $\tau_2$  is present at all wavelengths. The corresponding DAS is mirroring the shape of the time-resolve spectra indicating that the whole spectrum is decaying with this time constant after some initial minor transformation. The broad almost featureless shape and the time constant of 7.5 ps are typical indications for a hot ground state spectrum. The time-resolved midIR spectra will support this interpretation and even give insight into parts of the vibrational relaxation dynamics. The broad absorption is likely the vibrationally hot flank of the strong band below 350 nm. The positive bulge might be a hot band of the ground state absorption at 410 nm, the negative one might result from bleaching due to the ground state band at 640 nm.

Given that the  $\tau_2$  indeed represents vibrational relaxations of the hot ground state,  $\tau_1$  could then be the lifetime of the preceding electronically excited state. After excitation at 400 nm this state would be the result of an MLCT transition between W(II) and the alkyne ligand L according to the ground state UV/vis spectrum, though it cannot be excluded that an ultrafast relaxation into a lower excited state like the MC state happens within the time resolution of the experiment.

The long-lived residual cannot be identified due to the small, broad and featureless shape, but the time-resolved midIR spectra prove that it is not an error in the measurement and must in fact relate to at least fractions of the OC-W-L complex.

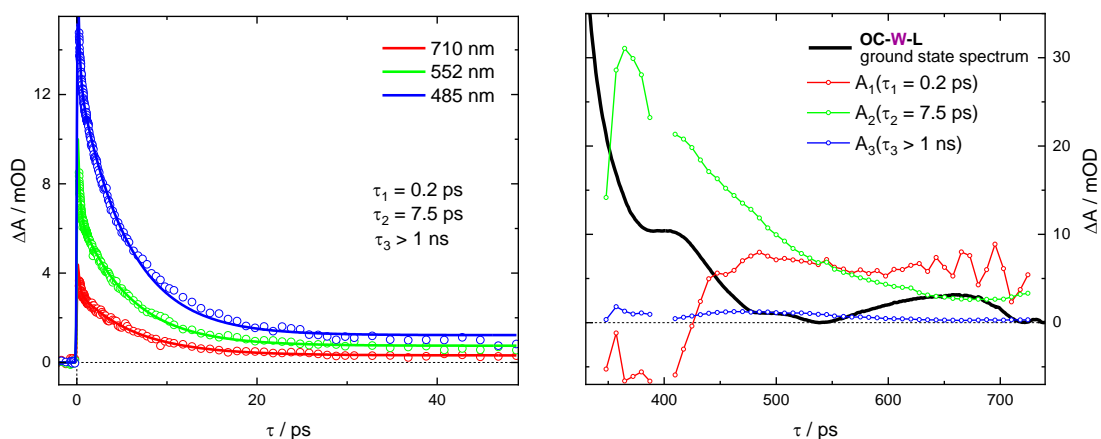


Fig. 70: transient data (circles) of the time-resolved UV/vis measurement of OC-W-L after excitation at  $\lambda_{\text{pump}} = 400$  nm at three different wavelengths and corresponding triexponential fits (solid lines) with fitted time constants (left); DAS from a global triexponential fit of the time-resolved UV/vis data with the same time constants (circles represent actual data, connecting lines are added for better visualization of the curves) including ground state absorption spectrum with arbitrary scaling to understand the shape of the bleach absorption.

### 4.2.2.3 Time-resolved midIR spectra

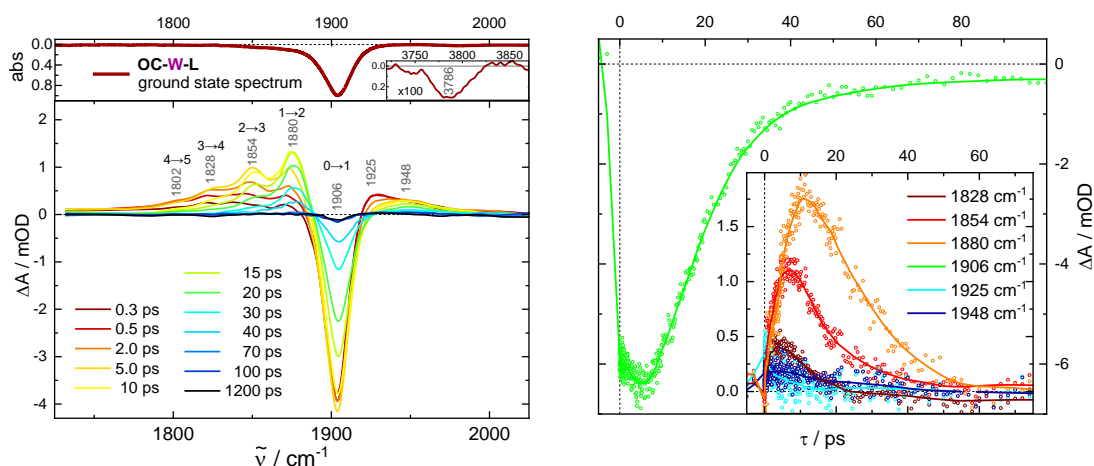


Fig. 71: normalized ground state FTIR spectrum of the OC-W-L complex at the CO stretching peak (top left) and at the corresponding first overtone (inlet left); time-resolved midIR spectra in acetonitrile ( $< 1.5$  mM) at selected pump-probe delays after excitation at 400 nm ( $1 \mu\text{J}$ ) (bottom left); transient data (circles) of the time-resolved midIR measurement of OC-W-L at the ground state bleach (right) and selected positive transient absorption peaks with solid lines to outline the average progression (inlet right).

Due to the connections via  $\pi$ -back bonding of the carbonyl group and also the alkyne ligand L to the W(II) core, excitation at 400 nm is expected to cause a noticeable blue-shift of the carbonyl stretching peak in the time-resolved midIR spectra since both the MLCT and the MC transition reduces electron density in the d-orbital that is responsible for  $\pi$ -back bonding into the antibonding  $\pi$ -orbital of the carbonyl, strengthening the C-O bond.

In fact, right after excitation at  $\lambda_{\text{pump}} = 400$  nm the time-resolved midIR spectra in fig. 71 show a small peak slightly blue-shifted to about  $1925 \text{ cm}^{-1}$  next to the very intense bleach of the C-O stretching peak at  $1906 \text{ cm}^{-1}$  (see ground state spectrum in fig. 71 (top left)). The small excited state peak is then decaying with a time constant of about  $\tau_1 = 0.5$  ps, while the bleach is not decreasing, but growing (see fig. 71 (right)) due to the overlapping excited state peak vanishing, which indicates that the carbonyl stretching vibration is not directly returning to its initial state before excitation. Within the time the excited state peak disappears another further blue-shifted very broad peak at about  $1948 \text{ cm}^{-1}$  and a series of new peaks to the low-energy side of the bleach at  $1802 \text{ cm}^{-1}$ ,  $1828 \text{ cm}^{-1}$ ,  $1854 \text{ cm}^{-1}$  and  $1880 \text{ cm}^{-1}$  emerge. The relative intensities of the latter are quite similar in the beginning, however, within several picoseconds those at lower energy gradually decrease while those at higher energy increase until almost exclusively the peak at  $1880 \text{ cm}^{-1}$  is left. After about 10 ps, meaning within the time of this transformation, all the remaining peaks of the series as well as the second blue-shifted peak decay together with the bleach indicating a return to the state pre excitation within 70 ps, however, while the series completely disappears, a residual of <5% of the bleach is left from about 70 ps to the end at 1.2 ns.

Looking at the transients of the peak series in fig. 71 (inlet right) it is apparent that with increasing energy the peaks rise and fall slower. In the spectrum this creates a relaxation cascade from low to high energy peaks. Interestingly, all peaks of the series are separated by  $26 \text{ cm}^{-1}$ , which is close to the anharmonicity of the C-O stretching vibration in tungsten monocarbonyl complexes ( $2x_e v_e = 29 \text{ cm}^{-1[77]}$ ). With this information it can be proposed that the peak series represents anharmonically shifted transitions of energetically higher vibrational states of the C-O stretching vibration in the electronic ground state. This would lead to the following interpretation of the spectra:

The initial electronically excited state quickly relaxing into the electronic ground state populates vibrational states of the C-O stretching vibration up to at least  $v = 5$  to a notable degree. From each state vibrational relaxation significantly happens only to the next energetically lower state according to the selection rule  $\Delta v = \pm 1$  for vibrational transitions (transitions  $\Delta v > \pm 1$  are possible in anharmonic vibrations, but less likely). Additionally, it can be shown that, at least within the model for the harmonic oscillator (though it is reasonable to assume the same for anharmonic vibrations at low vibrational states), the transition rates  $k_{v+1,v}$  between two states  $v+1$  and  $v$  increase linearly with the quantum number  $v^{[5]}$  (also see fig. 72 a)) according to

$$k_{v+1,v} = (v + 1) \cdot k_{10} \quad \text{with } v = 1,2,3, \dots \quad \text{eq.050}$$

Consequently, this means that coming from the initial population distribution each vibrationally excited molecule relaxes step by step to the energetically lower states, which appear delayed due to the preceding steps, and relaxes even slower with each step leading to an accumulation of molecules in the lower vibrationally excited states as can be observed in the time-resolved midIR spectra.

Since transitions to higher vibrational states from the vibrational ground state are allowed for an anharmonic oscillator, the first overtone  $v = 0 \rightarrow v+n = 2$  should be observable in the FTIR spectrum given it has sufficient intensity despite the significantly lower transition probability. According to eq. 023 using the anharmonicity  $2x_e v_e \approx 2x_0 v_0 = 26 \text{ cm}^{-1}$  derived from the time-resolved midIR spectra this transition should appear at

$$E(v+n) - E(v) = \nu_0 n - \chi_0 \nu_0 (2vn + n^2 - n) = 3786 \text{ cm}^{-1} \quad \text{eq.051}$$

and indeed, the corresponding peak can be measured at exactly this wavenumber (fig. 71 (inlet left)) in a highly concentrated solution validating the anharmonicity.

The decay time of the anharmonically shifted peaks has the same magnitude as the second time constant derived from the time-resolved UV/vis measurement that was attributed to the vibrationally hot ground state. This interpretation is still reasonable with the information from the time-resolved midIR spectra, though the difference might indicate that other modes than the C-O stretching vibration of the molecule constitute to the broadened hot ground state band.

The peak at about  $1925 \text{ cm}^{-1}$  can be connected to the excited electronic state proposed for the interpretation of the time-resolved UV/vis spectra due to its similarly short lifetime and the suitable blue-shift presumably caused by reduced electron density at the W(II) centre for both theoretically predicted possibilities (MLCT and MC).

The peak at  $1948 \text{ cm}^{-1}$  on the other hand has no straight forward interpretation. A vibrational transition in a second excited electronic state is possible and would be suitable as the observed blue-shift could be connected to one of the transitions found in the ground state UV/vis spectrum, but there is no evidence, neither spectrally nor kinetically, in the time-resolved UV/vis spectra. Another possibility could be anharmonic coupling of the C-O stretching vibration to another vibrationally excited mode of the molecule in the electronic ground state (see fig. 72 b)). This effect has already been observed for example in a rhodium dicarbonyl complex (dicarbonyl acetylacetonato rhodium(I)) with the coupling of the symmetric and asymmetric stretching vibration of the carbonyls using 2D-FTIR spectroscopy<sup>[78]</sup>. According to the model, coupled states between two different vibrational modes can exist so that a transition with lower energy for one vibration and a transition with higher energy for the other can appear. This would explain why this peak has the same decay time as the anharmonically shifted peaks, since it would vanish without the coupling partner in its required state. However, there is no concrete prove available to support the use of this model on the present data.

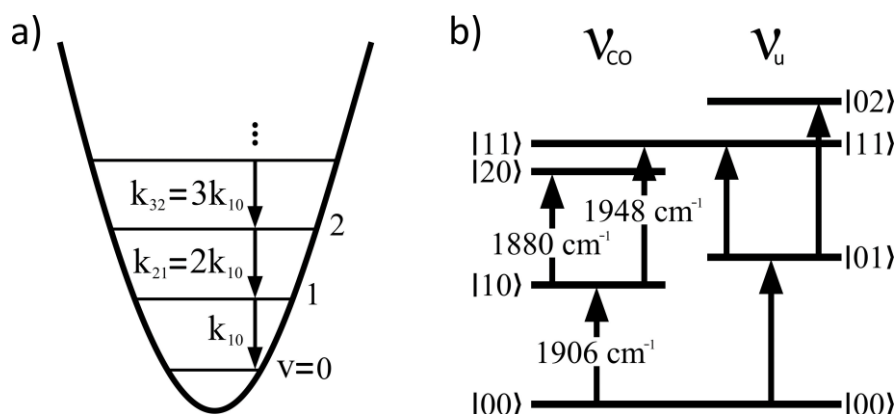


Fig. 72: energy relaxation schematic of a harmonic oscillator (a) and energy diagram for the anharmonic coupling of the C-O stretching vibration  $\nu_{CO}$  and an unknown molecular vibration  $\nu_u$  (b).

#### 4.2.2.4 Modelling of the time-resolved midIR spectra

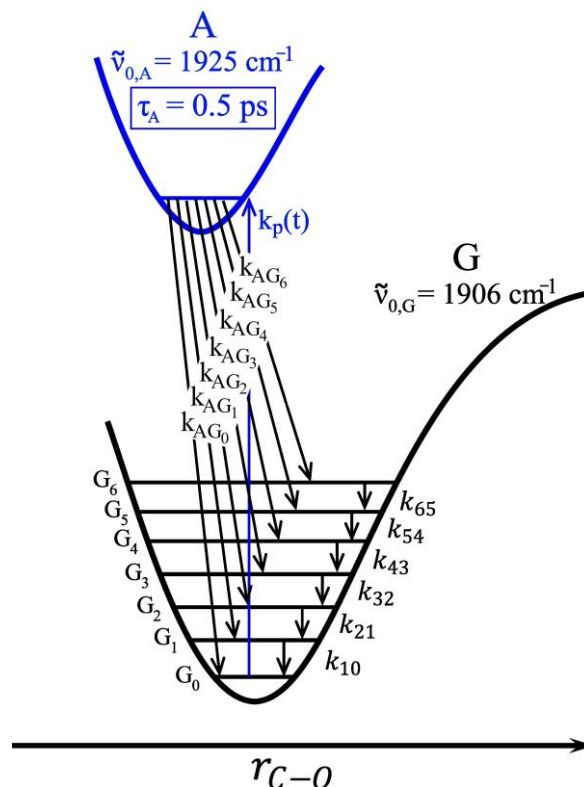


Fig. 73: Jablonski diagram for the modelling of the time-resolved midIR spectra of OC-W-L.

In order to examine the validity of the proposed relaxation dynamics especially of the vibrational relaxation cascade in the electronic ground state and potentially gain more information on the underlying mechanism, a kinetic model (see fig. 73) was constructed that is able to simulate the time-resolved midIR spectra.

In accordance with the interpretation of the data, an initial electronically excited state A with a lifetime  $\tau_A$  is proposed, which is populated from the electronic ground state by excitation with a pump pulse of gaussian shape

$$k_p(t) \sim I(t) = e^{-4\ln(2)\left(\frac{t-t_0}{\Delta t}\right)^2} \quad \text{eq.052}$$

The time-dependent intensity  $I(t)$  of the pulse in this case is equated with the pump induced transition rate  $k_p(t)$  between those states, the pulse width and temporal centre of the pulse are  $\Delta t$  and  $t_0$ .

Upon transitioning to the electronic ground state G via IC the vibrational states  $G_v$  of up to  $v=6$  are populated according to the respective rates  $k_{AG_v}$ . The inverse of the sum of these rates then constitutes the lifetime of the excited state A:

$$\begin{aligned} \tau_A &= (k_A)^{-1} \\ &= (k_{AG_0} + k_{AG_1} + k_{AG_2} + k_{AG_3} + k_{AG_4} + k_{AG_5} + k_{AG_6} + k_{AG_7})^{-1} \end{aligned} \quad \text{eq.053}$$

Each vibrational state can then transition into the next lower vibrational state with the corresponding rate  $k_{v+1,v}$  that linearly depends on  $k_{10}$  as was depicted in eq. 050 and is at the

same time also populated from the next higher vibrational state. The error of the approximation regarding the rate constants due to the anharmonicity (remember that the relation is derived for harmonic vibrations) is considered minor due to the small relative deviation of the transition energies of equivalent transitions at low vibrational states. The peak at  $1948\text{ cm}^{-1}$  was not included in this model since the focus was put on the simulation of the vibrational relaxation, which it should not affect.

From these propositions the following rate equations were established:

$$\frac{dA}{dt} = -k_{AG}A + k_p(t)G_0 \quad \text{eq.054a}$$

$$\frac{dG_6}{dt} = +k_{AG_6}A - k_{65}G_6 \quad \text{eq. 054b}$$

$$\frac{dG_5}{dt} = +k_{AG_5}A + 6k_{10}G_6 - 5k_{10}G_5 \quad \text{eq. 054c}$$

$$\frac{dG_4}{dt} = +k_{AG_4}A + 5k_{10}G_5 - 4k_{10}G_4 \quad \text{eq. 054d}$$

$$\frac{dG_3}{dt} = +k_{AG_3}A + 4k_{10}G_4 - 3k_{10}G_3 \quad \text{eq. 054e}$$

$$\frac{dG_2}{dt} = +k_{AG_2}A + 3k_{10}G_3 - 2k_{10}G_2 \quad \text{eq. 054f}$$

$$\frac{dG_1}{dt} = +k_{AG_1}A + 2k_{10}G_2 - k_{10}G_1 \quad \text{eq. 054g}$$

$$\frac{dG_0}{dt} = +k_{AG_0}A + k_{10}G_1 - k_p(t)G_0 \quad \text{eq.054h}$$

With this equation system the population of each state ( $A(t)$  and  $G_v(t)$ ) can be calculated at all times. Those are needed to simulate the time-resolved midIR spectra since a transition can only occur if the corresponding initial state is populated. Each peak is constructed using a base peak function multiplied by the current population and an absorption cross section  $\sigma_r$  relative to the ground state. It is important to notice that a transition happens both from the lower state due to absorption and, if populated, from the upper state due to stimulated emission, which is then weighted negatively.

For the peak of A at about  $1925\text{ cm}^{-1}$  a gaussian function

$$g(\tilde{\nu}, \tilde{\nu}_0, \Delta\tilde{\nu}) = e^{-4\ln(2)\left(\frac{\tilde{\nu}-\tilde{\nu}_0}{\Delta\tilde{\nu}}\right)^2} \quad \text{eq.055}$$

with the central wavenumber  $\tilde{\nu}_0$  and the line width  $\Delta\tilde{\nu}$  was used. The resulting function for the state A then is

$$Sp_A = \sigma_{r,A} \cdot A(t) \cdot g(\tilde{\nu}, \tilde{\nu}_{0,A}, \Delta\tilde{\nu}_A) \quad \text{eq.056}$$

For each transition a lineshape function corresponding to the  $v = 0 \rightarrow 1$  absorption band of the FTIR spectrum was used after it was normalized and interpolated to receive  $f_G(\tilde{\nu})$ , which was shifted by the anharmonicity of the electronic ground state  $2x_{0,G}\tilde{\nu}_{0,G}$  multiplied by the vibrational quantum number  $v$ . The transitions  $v+1 \leftrightarrow v$  were additionally weighted with a cross section  $\sigma_{v+1,v}$  according to eq. 016. Since the exact value can be included in the cross section of the ground state,  $\sigma_{10}$  was set to one to receive only the  $v$ -dependent scaling factor. Overall, the function for the simulation of the electronic ground state spectrum is

$$Sp_G = \sigma_G \cdot \sum_{v=0}^5 [G_v(t) - G_{v+1}(t)] \cdot \sigma_{v+1,v} \cdot f_G(\tilde{\nu}_{0,G} - v \cdot 2x_{0,G}\tilde{\nu}_{0,G}) \quad \text{eq.057}$$

With the two spectral functions the spectrum after pump excitation

$$S_{p_{\text{pump}}} = S_{p_A} + S_{p_G} \quad \text{eq.058}$$

and finally, by subtracting the ground state spectrum  $f_G(\tilde{\nu})$  the difference absorption spectrum

$$\Delta OD = (S_{p_{\text{pump}}} - S_{p_{\text{no pump}}}) \cdot c_{\text{scale}} = (S_{p_{\text{pump}}} - f_G(\tilde{\nu})) \cdot c_{\text{scale}} \quad \text{eq.059}$$

can be simulated. It is fitted to the measured spectra varying the parameters for the pump pulse  $\tilde{\nu}_0$  and  $\Delta\tilde{\nu}$ , peak positions  $\tilde{\nu}_{0,A}$  and width  $\Delta\tilde{\nu}_A$  of state A, peak position  $\tilde{\nu}_{0,G}$  and anharmonicity  $2x_{0,G}\tilde{\nu}_{0,G}$  of the electronic ground state G, rate constants  $k_{AGv}$  and  $k_{10}$ , the latter of which determines all other  $k_{v+1,v}$  via eq. 050, the absorption cross section of state A  $\sigma_{r,A}$  and the scaling factor of the whole spectrum  $c_{\text{scale}}$ . The result is compared to the measured spectra in fig. 74, the fitting data is shown in the appendix.

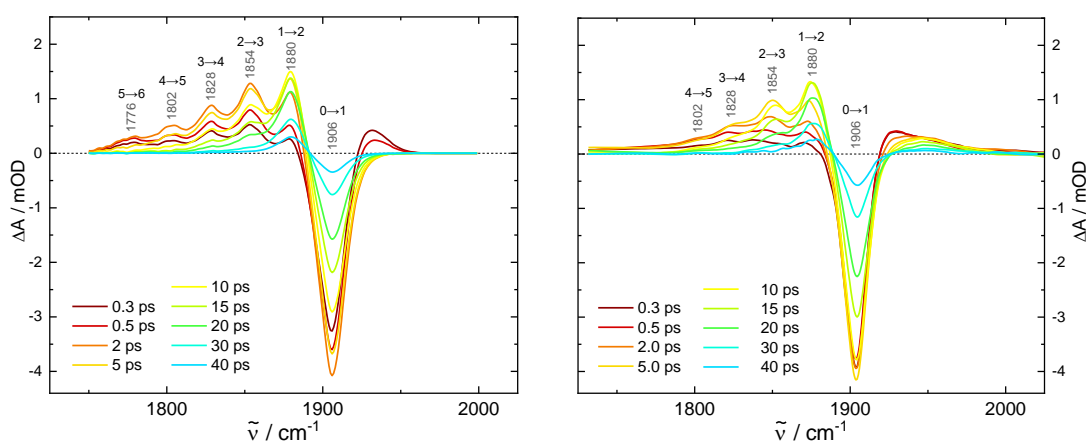


Fig. 74: Comparison of the modelled (left) to the measured (right) time-resolve midIR spectra of OC-W-L.

Overall, the simulated spectra match the measured ones quite well, especially the evolution of the anharmonically shifted peaks after the initial population of the electronic ground state, further supporting the interpretation of a relaxation cascade of excited anharmonic vibrations. Most of the differences there come from the line shapes. The peaks in the simulation that were created from the ground state FTIR spectrum are asymmetric and a bit sharper than the time-resolved midIR spectra, which were slightly smoothed, flattening the peaks. The starting intensity and growth of the bleach is also partially mismatched possibly due to an overestimation of the overlapping peak of the A state, though a more complex decay of the initial electronic states cannot be excluded.

#### 4.2.2.5 Conclusion OC-W-L complex

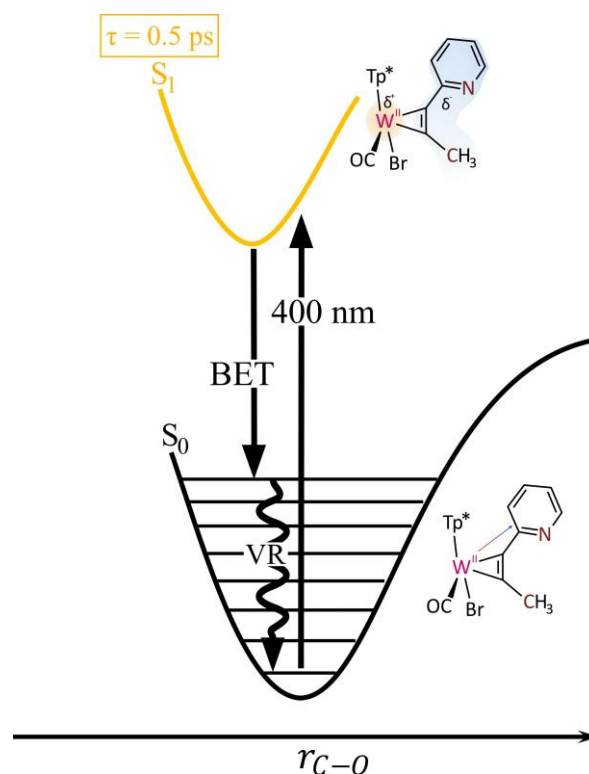


Fig. 75: Energy diagram according to the conclusions derived for the OC-W-L complex.

Both the time-resolved UV/vis and midIR spectra agree that the excitation at  $\lambda_{\text{pump}} = 400$  nm induces a transition into a very short-lived electronically excited state, that decays into the highly vibrationally excited electronic ground state. The hot ground state is indicated by broad time-resolved UV/vis spectra with a typical relaxation constant of  $\tau = 7.5$  ps and a corresponding ground state recovery at the C-O stretching vibration bleach at  $1906$   $\text{cm}^{-1}$ . The time-resolved midIR spectra even allow a closer look into the dynamics as an efficient energy transfer to the anharmonic C-O vibration leads to the population of high vibrational states up to  $v=5$  after relaxation into the electronic ground state. The anharmonicity of the vibration is supported by the appearance of the first overtone in the FTIR spectrum of the C-O stretching vibration at  $3786$   $\text{cm}^{-1}$ , which is the exact position predicted via eq. 023 using the anharmonicity  $2x_{0,G}\tilde{\nu}_{0,G} = 26$   $\text{cm}^{-1}$  derived from the shift of the peaks in the time-resolved midIR spectra, and by the good agreement with a kinetic model using simple relations for a complex system of interconnected processes.

The properties of the short-lived electronically excited state cannot be conclusively clarified. The time-resolved midIR spectra indicate a slight shift of electron density away from the W(II) moiety due to reduced electron density in the antibonding  $\pi^*$ -orbital of the carbonyl which induces a blue-shift of the C-O vibration according to the DCD model. Overall, the excited state peak is not shifted far enough to assume a full charge-transfer generating W(III), which according to the IR-SEC would be observed at about  $2090$   $\text{cm}^{-1}$  and not at  $1925$   $\text{cm}^{-1}$ . Consulting TD-DFT calculation for the assignment of the ground state UV/vis spectrum, an electron density shift to the pyridine-group of the alkyne ligand L or the pyrazole-groups in the Tp\* ligand are reasonable. A d-d transition at the tungsten, however, is also possible.



## 4.2.3 Heterobinuclear [OC-W-L-Ru(bpy)<sub>2</sub>]<sup>+</sup> complex

### 4.2.3.1 Ground state UV/vis spectrum

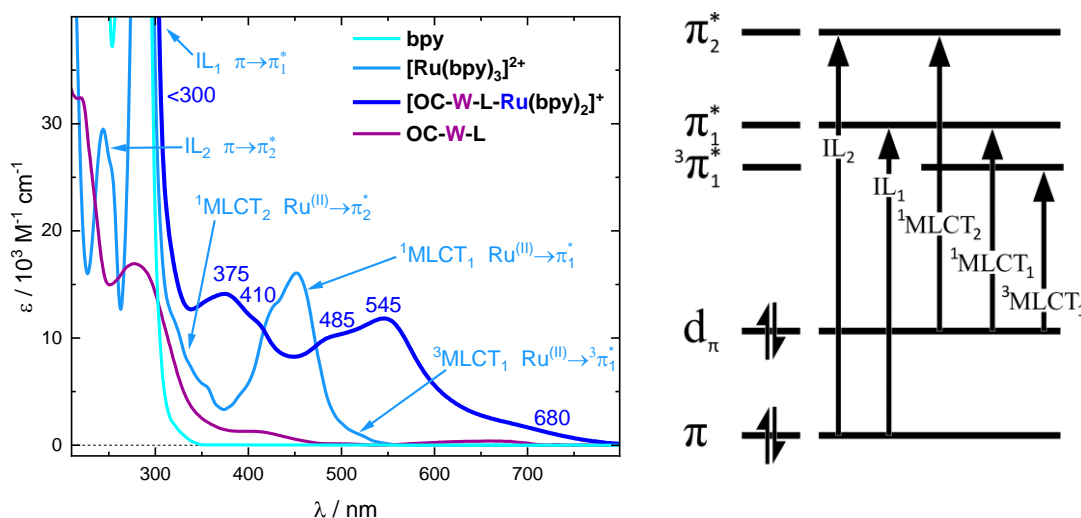


Fig. 76: left: ground state UV/vis spectrum of the [OC-W-L-Ru(bpy)<sub>2</sub>]<sup>+</sup> (dark blue) and for comparison the OC-W-L (violet) complex in acetonitrile at room temperature measured by Mareike Hüttenschmidt and appropriately scaled ground state UV/vis spectra of the bpy ligand (1 mM in THF, measured in an optically transparent thin-layer electrode (OTTLE) cell) reproduced from Krejčík et al.<sup>[79]</sup> and of [Ru(bpy)<sub>3</sub>]<sup>2+</sup> (in acetonitrile at room temperature) with transition assignments reproduced from Dongare et al.<sup>[80]</sup>; right: frequently used energy level diagram for the assignment of transitions in  $\alpha$ -diimine transition metal complexes inspired by Zális et al.<sup>[81]</sup>. Only one d-orbital of the metal with the connected ligand orbitals are depicted for simplification.

The addition of a ruthenium-bipyridyl group to the OC-W-L complex is very noticeable in the ground state UV/vis spectrum of the heterobinuclear W-Ru complex [OC-W-L-Ru(bpy)<sub>2</sub>]<sup>+</sup>. The very intense bands known from the mother complex [Ru(bpy)<sub>3</sub>]<sup>2+</sup> seemingly all are present in the spectrum of the binuclear complex, though they are shifted to lower energy (see fig. 76 left).

The low energy electronic transition bands of  $\alpha$ -diimine transition metal complexes like [Ru(bpy)<sub>3</sub>]<sup>2+</sup> are typically roughly assigned using the energy level scheme in fig. 76 (right)<sup>[81]</sup>. The bands of [Ru(bpy)<sub>3</sub>]<sup>2+</sup> below 300 nm are quite confidently ascribed to IL transitions of the bpy ligands as they also appear in the spectrum of the bare ligand (also depicted in fig. 76 left). A shoulder at its base represents an MLCT transition from a Ru(II) d-orbital to the upper bpy  $\pi^*$  orbital  $\pi_2^*$ . The most intense band in the visible range is assigned to the MLCT transition to the lower bpy  $\pi^*$  orbital  $\pi_1^*$  and a shoulder on this band belongs to a spin-forbidden transition into a triplet MLCT state.

The transitions in the absorption spectrum of the [OC-W-L-Ru(bpy)<sub>2</sub>]<sup>+</sup> complex can be interpreted accordingly. The bands below 300 nm are assigned to IL transitions of the two bpy ligands, the bands at 375 nm and 410 nm belong to a <sup>1</sup>MLCT<sub>2</sub>-like transition, the bands at 485 nm and 545 nm constitute <sup>1</sup>MLCT<sub>1</sub> transitions and the shoulder at 680 nm represents the corresponding singlet-triplet transition.

The much weaker bands of the tungsten section of the molecule overlap with those of the ruthenium-bipyridyl section or create new transitions, which is also found by TD-DFT calculations<sup>[73]</sup>. For example, the band at 680 nm and to a lesser degree the band at 410 nm are presumed to have a significant fraction of MLCT from the W(II) to the bpy ligands and the 545 nm band includes an MC transition of W(II). Those three instances indicate electronic coupling between the two metal centres. However, the calculations also emphasize the dominance of the Ru(II)  $\rightarrow$  bpy MLCT transitions in the visible range of the UV/vis spectrum.

Excitation at 400 nm can entail a multitude of transitions, but judging from the absorption coefficients of the components the most likely transition is a singlet-singlet MLCT transition from Ru(II) to the bpy ligands, which would have a rather small effect on the electron density around the W(II) and therefore also on the carbonyl stretching vibration compared to the mononuclear tungsten complex unless the contribution of MLCT transitions from W(II) to the ligands bpy and L as they are predicted by the TD-DFT calculations induce sufficient electron density shifts.

### 4.2.3.2 Time-resolved UV/vis spectra

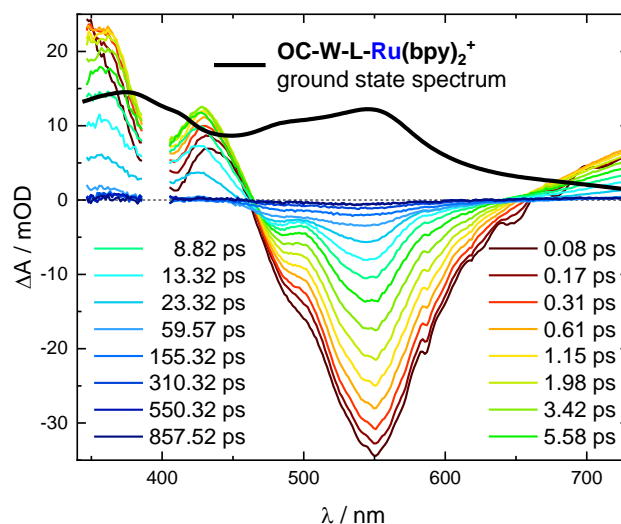


Fig. 77: time-resolved UV/vis spectra of the  $[\text{OC-W-L-Ru}(\text{bpy})_2]^+$  complex in acetonitrile ( $< 0.1$  mM) at selected pump-probe delays after excitation at 400 nm ( $0.75 \mu\text{J}$ ). The ground state absorption spectrum with arbitrary scaling is included to underpin that the negative absorbance is caused by a ground state bleach.

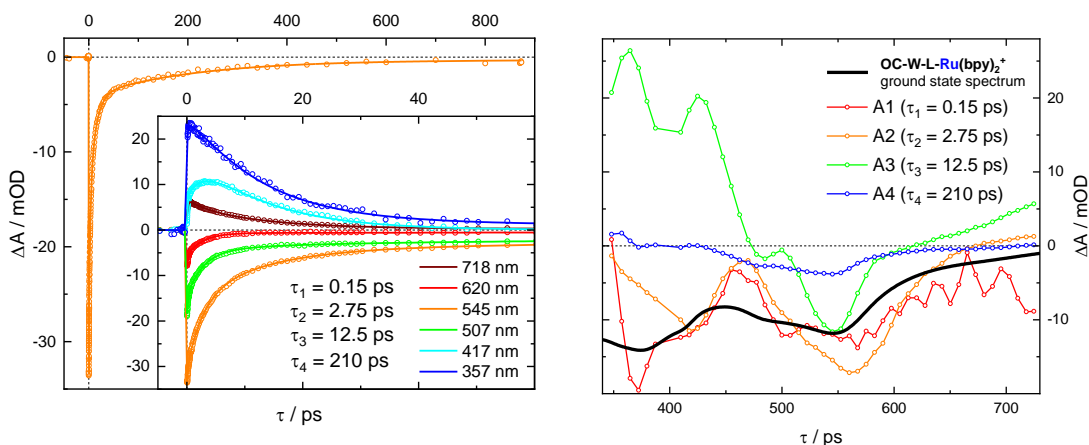


Fig. 78: transient data (circles) of the time-resolved UV/vis measurement of the  $[\text{OC-W-L-Ru}(\text{bpy})_2]^+$  complex after excitation at  $\lambda_{\text{pump}} = 400$  nm at the minimum of the ground state bleach at 545 nm (left) and several other different wavelengths (inlet left) and corresponding tetraexponential fits (solid lines) with fitted time constants (left); DAS from a global tetraexponential fit of the time-resolved UV/vis data (circles represent actual data, connecting lines are added for better visualization of the curves) including ground state absorption spectrum with arbitrary scaling to understand the shape of the bleach absorption (right).

As suspected due to the high absorption coefficient of the  $[\text{OC-W-L-Ru}(\text{bpy})_2]^+$  complex in acetonitrile at 400 nm and the generally intense absorption bands of ruthenium-bipyridyl complexes, the corresponding time-resolved UV/vis spectra after excitation at  $\lambda_{\text{pump}} = 400$  nm depicted in fig. 77 show large absorption bands considering the rather moderate pump intensity and low sample concentration.

Right after excitation a large negative signal, which can be roughly attributed to the bleaching of the ground state spectrum, appears with a minimum at 548 nm and a shoulder at 485 nm. At the same time excited state absorptions emerge to both sides: a low-energy band, whose centre is somewhere above 730 nm, and two high-energy bands at 435 nm and below 345 nm with an indent in between possibly created by a ground state bleach of the bands at 375 nm and 410 nm. Though this range is obscured by the cut-out of the pump pulse it is clearly visible in the measurements with  $\lambda_{\text{pump}} = 350$  nm and 480 nm. Within less than 1 ps ( $\tau_1 = 0.15$  ps) the negative signal loses about 20% of its intensity at the maximum. At the same time the two high-energy bands shift to 427 nm and 360 nm seemingly towards each other without changing the depth of the indent, while the former of the two ESA bands is growing. The band in the red part of the spectrum meanwhile is barely changing.

After the first picosecond the bands at 360 nm and below 730 nm start to decay while the indent between the central bleach at 548 nm and its shoulder deepens and the red flank of the bleach drops faster than its minimum. This process happens with a time constant of about  $\tau_2 = 2.75$  ps.

Finally, all bands decay to zero with a time constant of  $\tau_3 = 12.5$  ps except for the two bleach bands at 548 nm and 485 nm and the excited state band at 360 nm with roughly 5% of their initial intensity. Those bands eventually decay with  $\tau_4 = 210$  ps (see fig. 78).

Since the excitation at 400 nm presumably induces an MLCT from Ru(II) to the bpy ligands according to the TD-DFT calculations<sup>[73]</sup>, a spectrum is expected that is similar to what an electronically excited ruthenium-bipyridyl complex would produce. Indeed, the early spectra have a striking similarity to the transient spectra of  $[\text{Ru}(\text{bpy})_3]^{2+}$  measured by Yoshimura et al.<sup>[82]</sup> (as can be seen in fig. 79 left) and Kalyanasundaram<sup>[83]</sup> (not shown here), though they are stretched into the red part of the spectrum just like the ground state spectrum. By subtracting the ground state spectrum Yoshimura et al. estimated the shape of the excited state spectrum of  $[\text{Ru}(\text{bpy})_3]^{2+}$  and assigned the bands to the bipyridyl anion and the oxidized  $[\text{Ru}(\text{bpy})_3]^{3+}$  by comparison to their respective ground state spectra (also see fig. 79 left) concluding a photoinduced MLCT from Ru(II) to bpy resulting in  $[\text{Ru}^{\text{III}}(\text{bpy})_2(\text{bpy}^{\cdot-})]^{2+}$ .

By creating estimated excited state spectra from the time-resolved UV/vis spectra of the  $[\text{OC-W-L-Ru}(\text{bpy})_2]^+$  complex a similar assignment can be attempted. The three bands below 545 nm in these spectra have some semblance to those of the  $[\text{Ru}(\text{bpy})_3]^{2+}$  complex and could be assigned accordingly, but the unpredictable shifts of the components upon complexation make this attempt rather unreliable. Only the assignment of the band at 375 nm to a bipyridyl anion transition and the band at 435 nm shifting to 410 nm to a transition of  $[\text{Ru}(\text{bpy})_3]^{3+}$  is possible with some certainty supporting the MLCT from Ru(II) to bpy ligand. The small band at 500 nm can stem from both an oxidized  $[\text{Ru}(\text{bpy})_3]^{3+}$  transition as it resembles the  ${}^3\text{MLCT}_1$  band in the  $[\text{Ru}(\text{bpy})_3]^{2+}$  ground state or a  $\text{bpy}^{\cdot-}$  band. The band below 730 nm in the excited state spectra can be a transition from both components as well, a  $[\text{Ru}(\text{bpy})_3]^{3+}$  transition that is only hinted at in the ground state spectrum of Kalyanasundaram with rising absorbance above 550 nm or a  $\text{bpy}^{\cdot-}$  band stretched into the red part of the spectrum. Another possible approach arises due to the singly occupied d-orbital generated upon MLCT excitation as a low energy LMCT transition from the bpy  $\pi$ -orbital is then imaginable (see fig. 75 right). Both interpretations would support the creation of an MLCT state upon photoexcitation at 400 nm. Alternatively, since the band does not appear in the difference spectrum

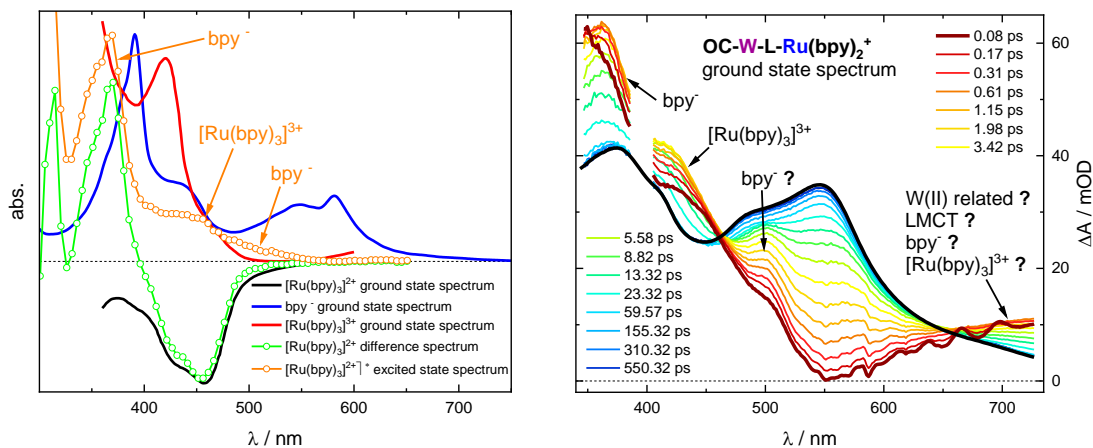


Fig. 79: left: transient absorption spectrum of  $[\text{Ru}(\text{bpy})_3]^{2+}$  in acetonitrile after laser photolysis at  $\lambda_{\text{pump}} = 532 \text{ nm}$  and excited state spectrum constructed from it by subtracting the ground state spectrum. Data reproduced from Yoshimura et al.<sup>[82]</sup>. For visualization of assignments the ground state spectrum of  $[\text{Ru}(\text{bpy})_3]^{2+}$  and  $[\text{Ru}(\text{bpy})_3]^{3+}$  reproduced from Kalyanasundaram<sup>[83]</sup> and  $\text{bpy}^-$  reproduced from Krejčík et al.<sup>[79]</sup> were added. The assignments of the excited state spectrum according to Yoshimura et al. are added in orange. Right: excited state spectra of  $[\text{OC-W-L-Ru}(\text{bpy})_2]^+$  created by subtracting the ground state spectrum scaled with one fixed factor from all time-resolved UV/vis spectra.

of  $[\text{Ru}(\text{bpy})_3]^{2+}$  of Yoshimura et al., a W(II) connected transition can also be suspected, but the involvement of the W(II) moiety in any of the transition bands can neither be excluded nor certified with the available information.

Due to the decay of the negative signal centred at 545 nm right after excitation, a perpetual return to the ground state could be assumed, however, the time-resolved midIR spectra, which will be discussed in the next chapter, call this interpretation into question as the bleach of the C-O stretching vibration is not decaying at all in the first 8 ps.

In fact, the depth of the indent between the excited state bands at 435 nm and below 345 nm is also not decaying within at least the first 6 ps. According to Zálíš et al. the spectra of the reduced and  $^1\text{MLCT}_1$  excited state of  $\alpha$ -diimine transition metal complexes have a lot of similarities to the ground state spectrum (though they emphasize that these similarities are coincidental contrary to the general believe that they are connected to weak coupling between ligands and metal, which would keep their energy levels basically unchanged upon reduction/excitation)<sup>[81]</sup>. With this knowledge the first two time constants could be related to transitions that create states, which have stronger absorption bands than the preceding state and are close to those of the ground state. Adding the ground state spectrum to the DAS of the third time constant  $\tau_3$  gives a spectrum that strongly resembles a combination of  $\text{bpy}^-$  and  $[\text{Ru}(\text{bpy})_3]^{3+}$  ground state spectrum, which indicates relaxation from the corresponding MLCT state to the ground state. For  $\tau_4$  the relaxation to the ground state is more apparent, since both the time-resolved spectra and the DAS appear very much identical to the ground state spectrum above 450 nm.

Though the exact identification of the bands in the time-resolved UV/vis spectra cannot be conclusively clarified, there is evidence that excitation at  $\lambda_{\text{pump}} = 400 \text{ nm}$  induces an MLCT from Ru(II) to a bpy ligand. Since ruthenium-bipyridyl complexes are reported to perform ultrafast ISC from the  $^1\text{MLCT}_1$  to the  $^3\text{MLCT}_1$  ( $\tau = 40 \text{ fs}$ <sup>[72]</sup> or  $\tau = 25 \text{ fs}$ <sup>[84]</sup>), it can be assumed that the first relaxation with  $\tau_1 = 0.15 \text{ ps}$  is attributed to this transition. The relatively short lifetime of the complex compared to the nano- to microseconds<sup>[72],[85],[86]</sup> that are typically observed for the  $^3\text{MLCT}_1$  state of  $[\text{Ru}(\text{bpy})_3]^{2+}$  implies additional subsequent decay pathways. Those relaxation processes, however, require more information, which will be provided by the time-resolved midIR measurements.

### 4.2.3.3 Time-resolved midIR spectra

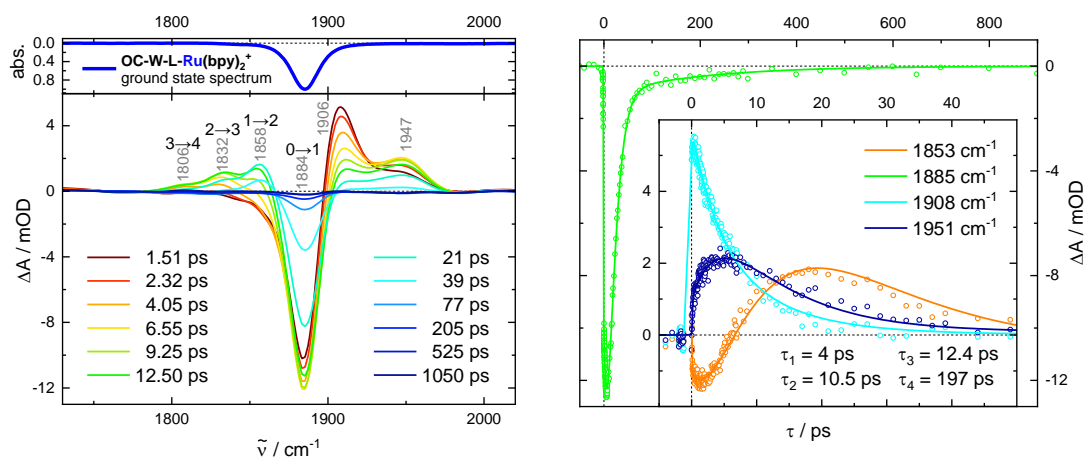


Fig. 80: normalized ground state FTIR spectrum of the  $[\text{OC-W-L-Ru}(\text{bpy})_2]^+$  complex at the CO stretching peak (top left), time-resolved midIR spectra in acetonitrile ( $< 0.1 \text{ mM}$ ) at selected pump-probe delays after excitation at  $400 \text{ nm}$  ( $0.75 \mu\text{J}$ ) (left bottom); transient data (circles) of the time-resolved midIR measurement of  $[\text{OC-W-L-Ru}(\text{bpy})_2]^+$  at the ground state bleach (right) and selected positive transient absorption peaks (inlet right) with corresponding tetraexponential fits (solid lines) and fitted time constants.

Fig. 80 (left) shows the time-resolved midIR spectra of the  $[\text{OC-W-L-Ru}(\text{bpy})_2]^+$  complex in acetonitrile around the C-O stretching absorption after excitation at  $\lambda_{\text{pump}} = 400 \text{ nm}$ . Due to significant interferences around the point of zero pump-probe delay in these measurements, the spectra before  $1.5 \text{ ps}$  are unreliable and therefore not included.

At the first available delay time at  $1.51 \text{ ps}$  the spectrum shows a bleaching of the C-O stretching vibration at  $1884 \text{ cm}^{-1}$  and two positive peaks at  $1906 \text{ cm}^{-1}$  and  $1947 \text{ cm}^{-1}$ . Since the latter grows upon the decay of the former with a time constant of  $\tau_1 = 4 \text{ ps}$  and a quasi-isosbestic point is visible, it is reasonable to speculate that a transition from one to the other, even at delays before  $1.51 \text{ ps}$ , occurs. Presumably due to some overlap with the neighbouring peak on the high-energy side the bleach initially grows within about  $10 \text{ ps}$  similar to the measurement of the OC-W-L complex.

On the low-energy side of the bleach a series of peaks with a distance between peak maxima of  $26 \text{ cm}^{-1}$  at  $1858 \text{ cm}^{-1}$ ,  $1832 \text{ cm}^{-1}$  and  $1806 \text{ cm}^{-1}$  emerges and evolves just like what was observed for the OC-W-L complex, however, they don't appear during the initial decay of the peak at  $1906 \text{ cm}^{-1}$ , but only after the peak at  $1947 \text{ cm}^{-1}$  gained some intensity, which grows to about half the size of its predecessor and then decays with a time constant of  $\tau_2 = 10.5 \text{ ps}$ .

The peak series relaxes, delayed by the previous processes, with the same cascade-like pattern as was described for the mononuclear W(II) complex within  $60 \text{ ps}$  ( $\tau_3 = 12.4 \text{ ps}$ ). At the same time the bleach decays to about  $10\%$  of its initial intensity, which decreases with a time constant of  $\tau_4 = 197 \text{ ps}$ , though a residual of about  $2\%$  remains. A rather weak peak ( $\Delta A < 0.45 \text{ mOD}$ , see fig. 81 left) decaying together with the bleach with a similar time constant to  $\tau_4$  was found at  $1701 \text{ cm}^{-1}$  that emerged simultaneously to the peak series upon the decay of the peak at  $1947 \text{ cm}^{-1}$  with  $\tau_2$  (see fig. 81 right, negative signal around  $\tau = 0 \text{ ps}$  is result of the mentioned interferences).

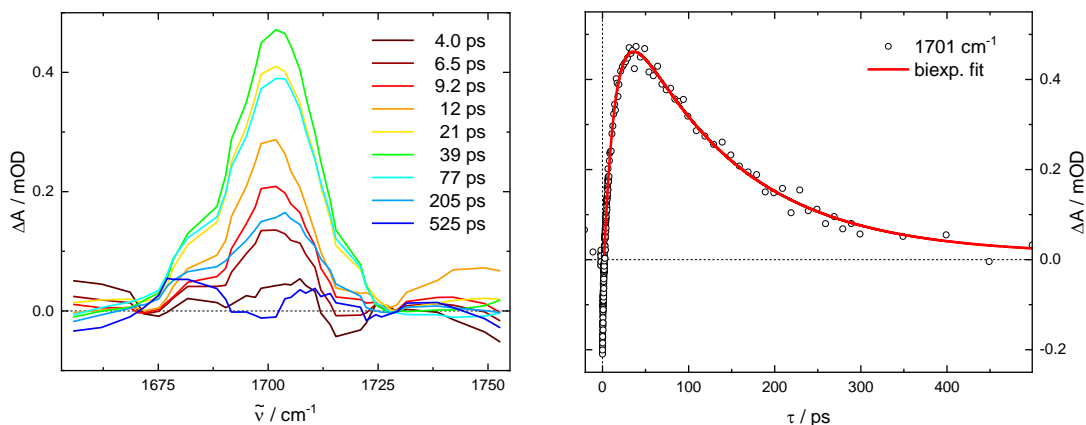


Fig. 81: time-resolved midIR spectrum of the  $[\text{OC-W-L-Ru}(\text{bpy})_2]^+$  complex at the peak at  $1701 \text{ cm}^{-1}$  (left) and corresponding time trace and biexponential fit with time constants  $\tau_1 = 13.7 \text{ ps}$  and  $\tau_2 = 128 \text{ ps}$  (right).

From the previous discussion of the OC-W-L complex it is quite evident that the peak series again represents the anharmonically shifted transitions of the vibrationally excited states ( $v=1,2,3$ ) in the electronic ground state with an anharmonicity of  $2x_e v_e = 26 \text{ cm}^{-1}$ . Diverging from that, however, the  $[\text{OC-W-L-Ru}(\text{bpy})_2]^+$  complex is not directly returning to the electronic ground state to populate these states, but passes a second electronic state that shifts the peak of the C-O vibration from  $1906 \text{ cm}^{-1}$  to  $1947 \text{ cm}^{-1}$ . Since a shift of this peak to higher energy is most likely connected to a reduction of electron density in the antibonding  $\pi$ -orbital of the carbonyl ligand and therefore in the d-orbital of the W(II) responsible for the  $\pi$ -back bonding, a corresponding electron density shift away from the W(II) should be proposed. Unlike the OC-W-L complex, however, the initial excitation, according to the interpretation of the ground state and time-resolved UV/vis spectrum, predominantly results in an MLCT transition from Ru(II) to bpy ligand. It could be assumed that, given the previous conclusion on the time-resolve UV/vis measurement is viable, the excitation creates the  $^1\text{MLCT}_1$  that quickly relaxes into the  $^3\text{MLCT}_1$ , which due to the Ru(II)  $\rightarrow$  R(III) oxidation generates reduced electron density in the vicinity of the W(II) and is therefore responsible for the first shift to  $1906 \text{ cm}^{-1}$ . Since the TD-DFT calculations of Hüttenschmidt et al.<sup>[73]</sup> indicate the possibility of a small electron density shift from W(II) to L in singlet-singlet transitions from the ground state, a similar transition connected to the electron density loss at the Ru(II) is at least imaginable. The second shift to  $1947 \text{ cm}^{-1}$  could then, again inspired by the calculations, be a shift from W(II) to the bpy ligands further removing electron density from the W(II) and due to the similar time constants be related to the second time constant  $\tau_2 = 2.75 \text{ ps}$  derived from the time-resolve UV/vis data.

From this state the relaxation path diverges into two directions: the return to the electronic ground state populating excited anharmonic vibrations of the carbonyl ligand that relax step-by-step to the vibrational ground state and the transition to a state with a peak at a wavenumber far lower than the  $0 \rightarrow 1$  transition of the bleach. Due to the lack of any absorption in the close vicinity in the ground state FTIR spectrum and especially the matching time constants of the decay of the peak at  $1947 \text{ cm}^{-1}$  and the bleach, this peak is assigned to a C-O stretching vibration. Within the DCD-model the large red-shift of  $183 \text{ cm}^{-1}$  compared to the ground state would be associated to an equally large increase in electron density in the antibonding  $\pi^*$ -orbital of the carbonyl donated from the W(II), which would effectively mean something close to a reduction to W(I). Since this is unlikely according to cyclovoltammetric analyses<sup>[73]</sup>, an alternative explanation would be appropriate. DFT calculations on  $\text{Cr}(\text{CO})_6$  (chromium is a lighter analogue of tungsten) supported by matrix isolation infrared spectroscopy of Cr in CO<sup>[87]</sup> showed a downshift of  $70 \text{ cm}^{-1}$  of the side-on  $\eta^2$  binding of CO to the metal<sup>[88]</sup>. Coupled cluster calculations on  $\text{UO}_2\text{-CO}$  even predicted

a shift of more than  $530\text{ cm}^{-1}$  for a transformation from C-bound end-on ( $\eta^1$ ) to side-on ( $\eta^2$ ) coordination<sup>[89]</sup>. No more closely related calculations or even measurements were found, but the examples show a consistent trend: the side-on coordination can dramatically downshift the C-O stretching vibration. This coordination is thermodynamically disfavoured to the end-on carbon-bonded coordination, but might be achievable from the electronically excited state. It can even be embedded into the DCD-model. Just like the side-on coordination of an alkene/alkyne to a transition metal the carbonyl donates electrons from the bonding  $\pi$ -orbital to the metal. Donating electron density from this orbital instead of the non-bonding  $\sigma_{nb}^*$  with the free electrons of the carbon largely weakens the C-O bond leading to the large downshift.

Due to the very similar decay times and fractions of the bleach, this state can safely be connected to  $\tau_4$  derived from the time-resolved UV/vis spectra. Assuming a minor influence of the coordination changes on the UV/vis spectrum, the observation of a bleach in the late spectra could indicate that the peak at  $1701\text{ cm}^{-1}$  in the time-resolved midIR might involve an electronically excited state. The decay of bleaches and excited state absorptions with  $\tau_4$  in both time-resolved UV/vis and midIR spectra indicates the eventual return to the electronic ground state and the end-on coordination of the carbonyl.

#### 4.2.3.4 Modelling of the time-resolved midIR spectra

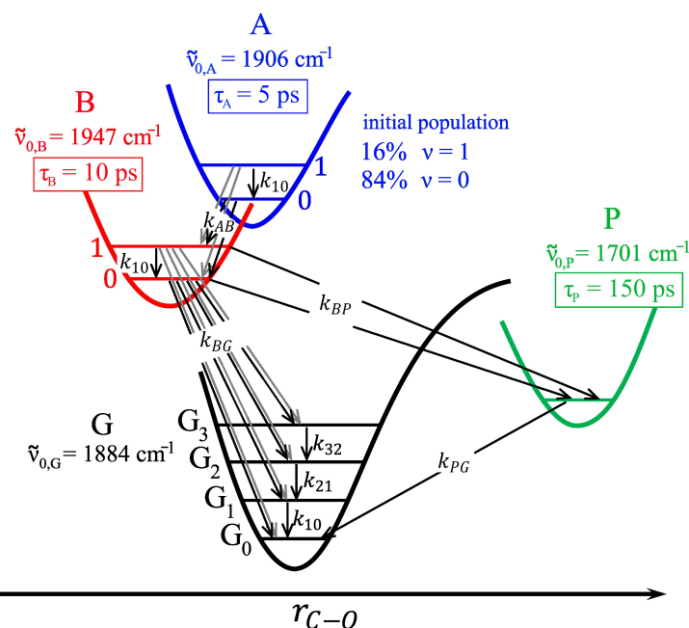


Fig. 82: Jablonski diagram for the modelling of the time-resolved midIR spectra of  $[\text{OC-W-L-Ru}(\text{bpy})_2]^+$ .

Apparently, the heterobinuclear  $[\text{OC-W-L-Ru}(\text{bpy})_2]^+$  complex can transfer energy from electronic excitation to the C-O stretching vibration similarly efficient as the mononuclear OC-W-L complex. In order to receive more detailed information from the relaxation processes connected to this vibration, the time-resolved mid IR spectra were also simulated using a kinetic model suitable for the more complex behaviour. The Jablonski diagram depicting the model is shown in fig. 82.

Since the first electronic state decaying with  $\tau_1 = 0.15\text{ ps}$  could not be recorded in the time-resolved midIR spectra due to the mentioned interferences the initial excitation via gaussian pump pulse was skipped and instead the first state visible in the time-resolved midIR spectra at  $1909\text{ cm}^{-1}$  designated with A was immediately populated. With a relaxation rate constant  $k_{AB} =$

$(\tau_A)^{-1}$  it can transition to the second excited state B related to the peak at  $\tilde{\nu}_{0,B} = 1947 \text{ cm}^{-1}$ , from which two paths branch off: relaxation to vibrationally excited states of the electronic ground state  $G_v$  up to  $v = 3$  with the related rate constants  $k_{BG_v}$  and anharmonically shifted peak maxima at

$$\tilde{\nu}_{v,G} = \tilde{\nu}_{0,G} - v \cdot 2x_{0,G}\tilde{\nu}_{0,G} \quad \text{eq.060}$$

with the anharmonicity  $2x_{0,G}\tilde{\nu}_{0,G} = 26 \text{ cm}^{-1}$  or a transition to a third electronically excited state P with  $\tilde{\nu}_{0,P} = 1701 \text{ cm}^{-1}$  with a rate constant  $k_{BP}$  that can then relax into the ground state  $G_0$  at  $\tilde{\nu}_{0,G} = 1884 \text{ cm}^{-1}$  with  $k_{PG}$ . The relaxation rate constants of both paths constitute the lifetime of state B according to

$$\tau_B = (k_B)^{-1} = (k_{BG} + k_{BP})^{-1} = (k_{BG_0} + k_{BG_1} + k_{BG_2} + k_{BG_3} + k_{BP})^{-1} \quad \text{eq.061}$$

An approximation again was applied to the relaxation rate constants  $k_{v+1,v}$  of the  $G_v$  states using eq. 050.

Since it was not possible to adequately fit the initial growth of the bleach and the indent between the peaks at  $1906 \text{ cm}^{-1}$  and  $1947 \text{ cm}^{-1}$  by using a broad peak width, an anharmonically downshifted vibrationally excited state for both state A and B were added to the model. The two vibrational states of A called  $A_1$  and  $A_0$  were populated in a ratio 16%:84%.  $A_1$  can relax into  $A_0$  and both vibrational states of A can transition to both vibrational states of B,  $B_1$  and  $B_0$ , the former of which can relax to the latter. Both  $B_1$  and  $B_0$  can then transition to the excited electronic state P and the vibrationally excited states of G.

For further simplification of this rather complex model the relaxation rate constants between  $A_1$  and  $A_0$  and  $B_1$  and  $B_0$  were assumed to equate to  $k_{10}$  and the rate constants towards the same state, for example from  $A_1$  and  $A_0$  to  $B_1$ , were assumed equal, which makes the relaxation rate for A

$$k_A = k_{AB_1} + k_{AB_0} \quad \text{eq.062}$$

The application of the other rate constants was unaffected by the addition of the anharmonically shifted peaks of A and B.

According to this model, the following set of rate equations were built:

$$\frac{dA_1}{dt} = -k_{10}A_1 - k_A A_1 \quad \text{eq.063a}$$

$$\frac{dA_0}{dt} = +k_{10}A_1 - k_A A_0 \quad \text{eq. 063b}$$

$$\frac{dB_1}{dt} = -k_{10}B_1 - k_B B_1 + k_{AB_1}(A_0 + A_1) \quad \text{eq. 063c}$$

$$\frac{dB_0}{dt} = +k_{10}B_1 - k_B B_0 + k_{AB_0}(A_0 + A_1) \quad \text{eq. 063d}$$

$$\frac{dP}{dt} = +k_{BP}B_1 + k_{BP}B_0 - k_P P \quad \text{eq. 063e}$$

$$\frac{dG_3}{dt} = -3k_{10}G_3 + k_{BG_3}(B_0 + B_1) \quad \text{eq. 063f}$$

$$\frac{dG_2}{dt} = -2k_{10}G_2 + 3k_{10}G_3 + k_{BG_2}(B_0 + B_1) \quad \text{eq. 063g}$$

$$\frac{dG_1}{dt} = -k_{10}G_1 + 2k_{10}G_2 + k_{BG_1}(B_0 + B_1) \quad \text{eq. 063h}$$

$$\frac{dG_0}{dt} = k_{10}G_1 + k_{BG_0}(B_0 + B_1) + k_P P \quad \text{eq. 063i}$$



Using the time dependent population of the states received by numerically solving the equation system, the spectra were then generated similar to the those of the OC-W-L complex. The spectrum of the ground state consisting of the bleach and the corresponding anharmonically shifted via  $\sigma_{v+1,v}$  according to eq. 016. weighed vibrationally excited state peaks was built from the normalized and interpolated ground state FTIR spectrum  $f_G(\tilde{\nu} - v \cdot 2x_{0,G}\tilde{\nu}_{0,G})$ :

$$Sp_G = \sigma_G \cdot \sum_{v=0}^3 [G_v(t) - G_{v+1}(t)] \cdot \sigma_{v+1,v} \cdot f_G(\tilde{\nu}_{0,G} - v \cdot 2x_{0,G}\tilde{\nu}_{0,G}) \quad \text{eq.064}$$

The excited state spectra of A, B and P on the other hand were created with gaussian functions.

$$Sp_A = \sigma_{r,A} \cdot \left\{ \begin{array}{l} [A_0(t) - A_1(t)] \cdot \sigma_{10} \cdot g(\tilde{\nu}, \tilde{\nu}_{0,A}, \Delta\tilde{\nu}_A) \\ + A_1(t) \cdot 2\sigma_{10} \cdot g(\tilde{\nu}, \tilde{\nu}_{0,A} - 2x_{0,A}\tilde{\nu}_{0,A}, \Delta\tilde{\nu}_A) \end{array} \right\} \quad \text{eq.065}$$

$$Sp_B = \sigma_{r,B} \cdot \left\{ \begin{array}{l} [B_0(t) - B_1(t)] \cdot \sigma_{10} \cdot g(\tilde{\nu}, \tilde{\nu}_{0,B}, \Delta\tilde{\nu}_B) \\ + B_1(t) \cdot 2\sigma_{10} \cdot g(\tilde{\nu}, \tilde{\nu}_{0,B} - 2x_{0,B}\tilde{\nu}_{0,B}, \Delta\tilde{\nu}_B) \end{array} \right\} \quad \text{eq.066}$$

$$Sp_P = \sigma_{r,P} \cdot P(t) \cdot g(\tilde{\nu}, \tilde{\nu}_{0,P}, \Delta\tilde{\nu}_P) \quad \text{eq.067}$$

Addition of the four spectra gives the spectrum after pump excitation

$$Sp_{pump} = Sp_A + Sp_B + Sp_G \quad \text{eq.068}$$

and subtraction of the ground state spectrum  $f_G(\tilde{\nu})$  according to eq. 059 the difference absorption spectrum.

The following parameters were then varied for the fit: the vibrational relaxation constant  $k_{10}$ , the relaxation rate constants  $k_{AB_1}$  and  $k_{AB_0}$  of A related by eq. 062,  $k_{BG_v}$  and  $k_{BP}$  of B related by eq. 061 and  $k_{PG}$  of P, central peak positions  $\tilde{\nu}_{0,A}$ ,  $\tilde{\nu}_{0,B}$ ,  $\tilde{\nu}_{0,P}$  and  $\tilde{\nu}_{0,G}$ , of A, B, P and G and peak widths  $\Delta\tilde{\nu}_A$ ,  $\Delta\tilde{\nu}_B$ ,  $\Delta\tilde{\nu}_P$  and  $\Delta\tilde{\nu}_G$  of A, B and P, relative cross sections  $\sigma_{r,A}$ ,  $\sigma_{r,B}$  and  $\sigma_{r,P}$  of A, B and P, cross section of the anharmonically shifted peaks relative to their corresponding  $0 \rightarrow 1$  transition according to eq. 016 and the scaling factor for the difference spectrum  $c_{scale}$ .

The resulting spectra are shown in fig. 83 next to the measured ones. The agreement at the bleach and the anharmonically shifted peak series is excellent further supporting the assignment. The gained time constants  $\tau_A = 5$  ps,  $\tau_B = 10$  ps and  $\tau_P = 150$  ps are also in very good agreement with the experimental data of both time-resolved UV/vis ( $\tau_2 = 2.75$  ps,  $\tau_3 = 12.5$  ps and  $\tau_4 = 210$  ps) and midIR spectroscopy ( $\tau_1 = 4$  ps,  $\tau_2 = 10$  ps and  $\tau_4 = 197$  ps). The discrepancy at the  $1 \rightarrow 2$  transition is a result of the difference between bleach and FTIR spectrum and appearance of more intense peaks in the simulation is again owed to the shape of the peak maxima.

Similar to the OC-W-L spectra the high-energy side of the bleach is not matching properly. Though the general development of both peaks is reproduced, first peak decaying in favour of the second, the former decays too fast, while the latter grows too slowly. Potentially, there is another state involved in the population of the second state, the first state performs some sort of transformation changing the relaxation rate or another mechanism is interfering. Nonetheless, the relaxation into the electronic ground state is delayed correctly and the vibrational relaxation is simulated properly.

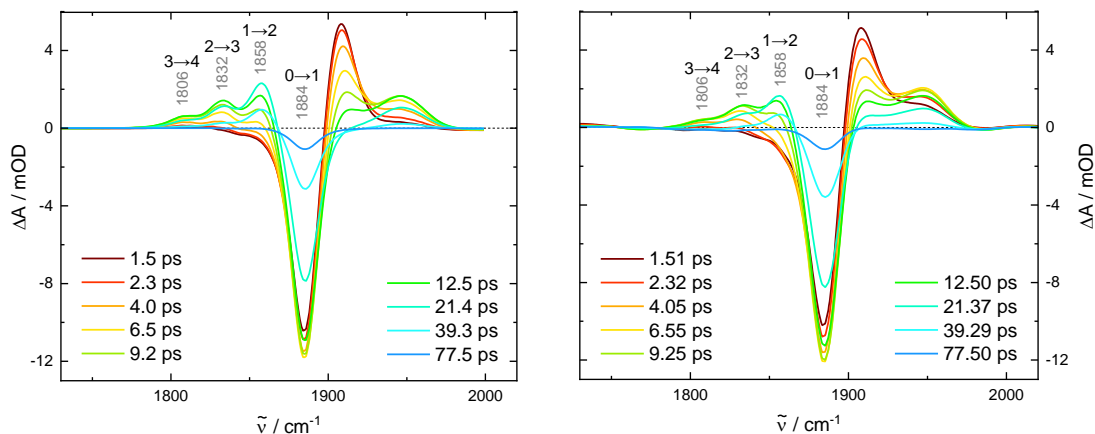


Fig. 83: Comparison of the modelled (left) to the measured (right) time-resolve midIR spectra of  $[\text{OC-W-L-Ru}(\text{bpy})_2]^+$ .

#### 4.2.3.5 Conclusion $[\text{OC-W-L-Ru}(\text{bpy})_2]^+$ complex

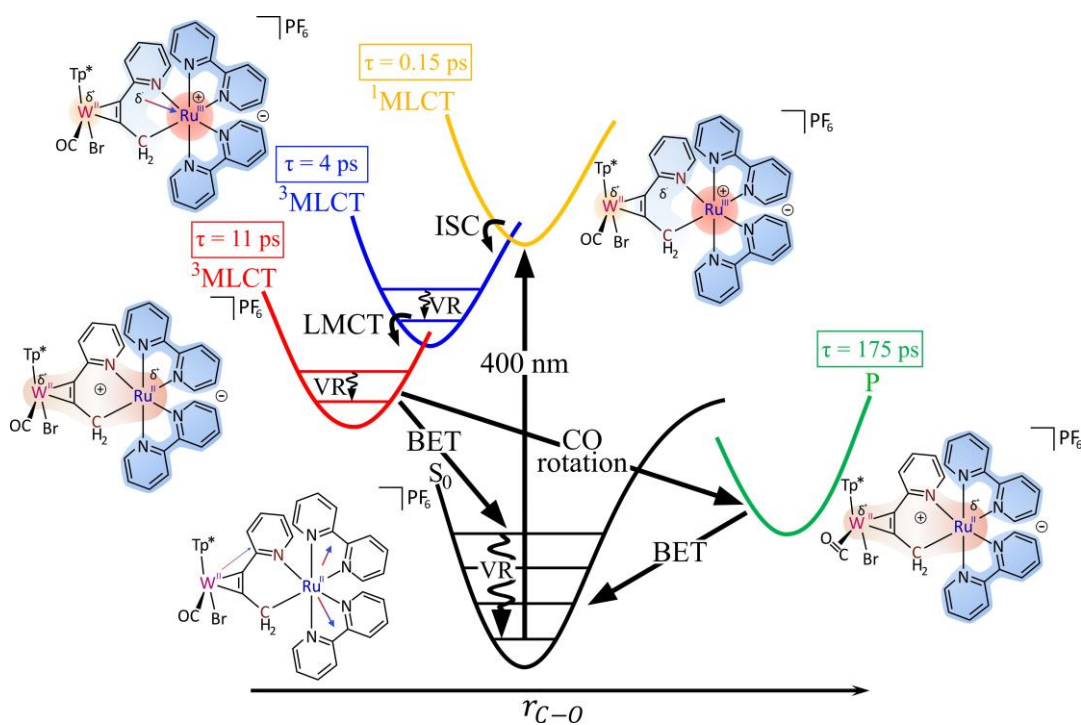


Fig. 84: Energy diagram according to the conclusions derived for the  $[\text{OC-W-L-Ru}(\text{bpy})_2]^+$  complex.

Similar to the mononuclear OC-W-L complex excitation of the  $[\text{OC-W-L-Ru}(\text{bpy})_2]^+$  complex at  $\lambda_{\text{pump}} = 400 \text{ nm}$  generates a vibrationally excited electronic ground state that evidently populates the anharmonic carbonyl stretching vibration up to  $\nu = 3$  according to the time-resolved midIR spectra, however, the path towards this population is much more complicated.

Excitation at 400 nm predominantly induces a transition to a  $^1\text{MLCT}$  state via charge transfer from Ru(II) to bpy as can be deduced by comparing the ground state UV/vis spectrum of  $[\text{OC-W-L-Ru}(\text{bpy})_2]^+$  to that of  $[\text{Ru}(\text{bpy})_3]^{2+}$  and TD-DFT calculation. The time-resolved UV/vis spectra support this assumption. They show many similarities to time-resolved spectra of  $[\text{Ru}(\text{bpy})_3]^{2+}$  known for such an MLCT transition and the bands can with some certainty be assigned to Ru(III) and  $\text{bpy}^-$ . Over time the spectrum only marginally changes implying that all subsequent states include Ru(III) and  $\text{bpy}^-$  to some extent. A first decay with  $\tau_1 = 0.15$  ps can be safely attributed to the ultrafast ISC well known from  $[\text{Ru}(\text{bpy})_3]^{2+}$ , but contrary to this simple analogue  $[\text{OC-W-L-Ru}(\text{bpy})_2]^+$  has a rather short lifetime. It relaxes with three more time constants that cannot be identified further with the time-resolved UV/vis data.

The time-resolved midIR spectra offer more information. The first state cannot be observed due to the mentioned interferences. Two blue-shifted C-O stretching vibration peaks at  $1909\text{ cm}^{-1}$  and  $1947\text{ cm}^{-1}$  consecutively appear next to the ground state bleach at  $1884\text{ cm}^{-1}$  before the anharmonic ground state vibrations are rising, indicating a two-step transfer away from the W(II) moiety. Again, full oxidation from W(II) to W(III) can be excluded due to the small shifts, but what electron density shifts happen can only be guessed. The first peak can be connected to the first  $^3\text{MLCT}$  via the lifetime of  $\tau = 4$  ps. Due to a similar shift in the OC-W-L complex spectra a similar interpretation for could be used: an electron density shift towards the pyridine-group in the alkyne ligand L. However, this shift could also be simply caused by the positive charge of the Ru(III) in the vicinity of the W(II) that has to exist simultaneously according to the time-resolved UV/vis spectra. The second peak shift could represent a shift of the additional electron density on L towards the Ru(III) in a weak LMCT creating a partial positive charge on both the tungsten and the ruthenium compared to the ground state while the bpy ligands hold the negative charge. The result is another  $^3\text{MLCT}$  state. Alternatively, an electron density shift from W(II) to the bpy ligands is also plausible since such a transition is at least deemed possible from the ground state according to TD-DFT calculations.

During the decay of the second peak the anharmonic ground state vibrations and a peak at  $1701\text{ cm}^{-1}$  emerge. The latter is safely identified as a C-O stretching vibration due to having the same relaxation time as the corresponding bleach, but it has an unusually far downshift indicating a great weakening of the C-O bond. Since a reduction of the tungsten is thermodynamically unfavourable according to cyclovoltammetric data, side-on coordination is proposed to explain this shift. This interpretation is in agreement with the DCD-model and supported by theoretical calculations and a measurement of matrix isolation infrared spectroscopy of Cr in CO. The relaxation of this state into the ground state is completed after about 800 ps.

The  $\text{Ru}(\text{bpy})_2$  moiety in its function as a photosensitizer successfully increased the intensity of the ground state UV/vis spectrum and both the time-resolved UV/vis and midIR spectra. A reduction in electron density at the W(II) was clearly observed, but a full MMCT from W(II) to Ru(III) cannot be concluded. The vibrational excitation of an anharmonic C-O vibration upon electronic relaxation into the ground state similar to the OC-W-L complex was also observed, but is less efficient, likely due to the longer-lived preceding states introducing losses during the relaxation processes. Interestingly, one of these electronic states gave access to a new state of the C-O stretching vibration, which for now is assumed to be the result of side-on coordination.

## 4.2.4 Heterobinuclear OC-W-L-Ir(ppy)<sub>2</sub> complex

### 4.2.4.1 Ground state UV/vis spectrum

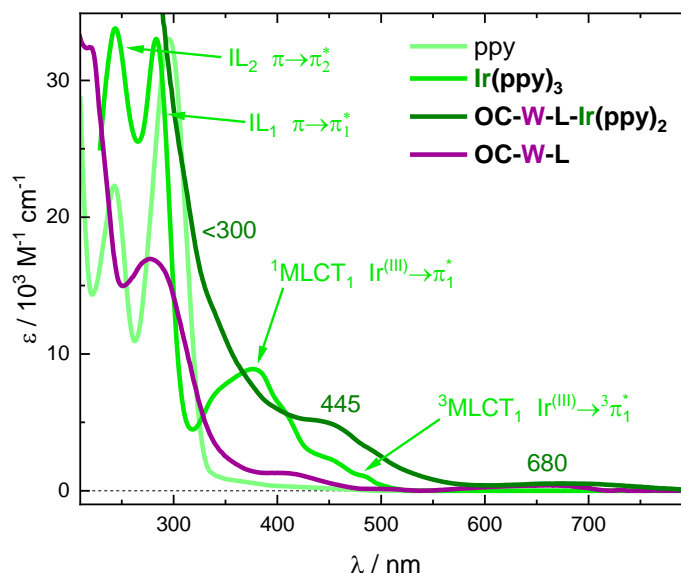


Fig. 85: left: ground state UV/vis spectrum of the OC-W-L-Ir(ppy)<sub>2</sub> (dark green) and for comparison the OC-W-L (violet) complex in acetonitrile at room temperature measured by Mareike Hüttenschmidt and appropriately scaled ground state UV/vis spectra of the ppy ligand reproduced from spectrabase<sup>[90]</sup> and of Ir(ppy)<sub>3</sub> (in dichloromethane at 300 K) with transition assignments reproduced from Hofbeck and Yersin<sup>[92]</sup>.

The Ir(ppy)<sub>2</sub>-group in the OC-W-L-Ir(ppy)<sub>2</sub> complex is structurally and electronically very similar to the Ru(bpy)<sub>2</sub>-group. Accordingly, the interpretation of the ground state UV/vis spectrum in fig. DT entails the same transitions. Bands below 300 nm are assigned to IL  $\pi \rightarrow \pi^*$  transitions, which can also be derived from comparison to the spectrum of the free ppy ligand in fig. 85, though theoretical calculations of Brahim and Daniel<sup>[92]</sup> imply strong mixing of MLCT states, the structured band at 375 nm comes from an MLCT between the Ir d-electrons and the ppy  $\pi$ -system <sup>1</sup>MLCT<sub>1</sub> and the low energy shoulder belongs to the corresponding forbidden singlet-triplet transition <sup>3</sup>MLCT<sub>1</sub><sup>[91]</sup>.

In contrast to the [OC-W-L-Ru(bpy)<sub>2</sub>]<sup>+</sup> complex, however, the spectrum of the OC-W-L-Ir(ppy)<sub>2</sub> complex does not have much resemblance to the Ir(ppy)<sub>2</sub> spectrum (see fig. 85) as almost all bands are merged into one another. It shows a broad, weak band at 680 nm and a band at 445 nm on the foot of a very large band below 300 nm. A small shoulder at 340 nm is also visible. The high-energy absorptions can be attributed to the IL transitions and the weak low-energy band is most likely the forbidden d-d transition of the W(II). The bands at 445 nm and 340 nm, however, cannot be assigned with much certainty. Either the <sup>1</sup>MLCT<sub>1</sub> and <sup>3</sup>MLCT<sub>1</sub> of the Ir(ppy)<sub>2</sub> moiety and the W(II)  $\rightarrow$  pyridine (L) transition of the W(II) moiety can contribute. Since the heavy iridium is known for state mixing due to configuration interaction and spin-orbit coupling<sup>[91]</sup> other more complex transitions are plausible. Unfortunately, no theoretical calculations are available for this complex for some guidance. Following the example of the similar [OC-W-L-Ru(bpy)<sub>2</sub>]<sup>+</sup> complex, one of the MLCT from Ir(III) to ppy with some simultaneous MLCT from W(II) to L can be expected upon excitation at 400 nm.

#### 4.2.4.2 Time-resolved UV/vis spectra

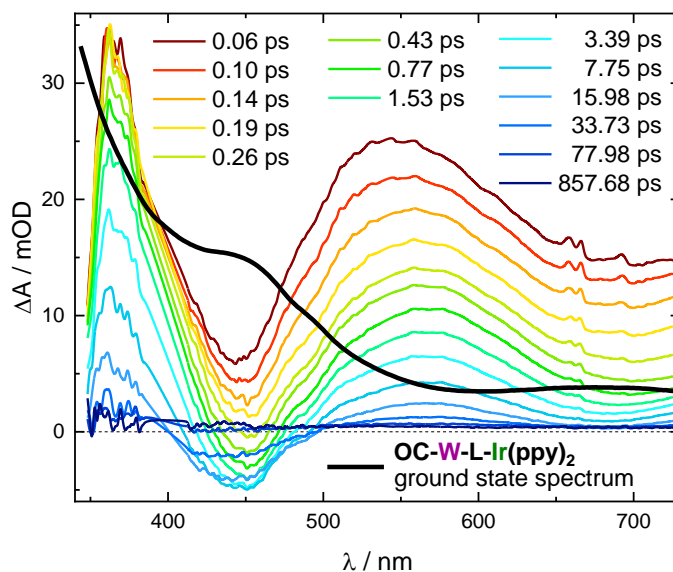


Fig. 86: time-resolved UV/vis spectra of the OC-W-L-Ir(ppy)<sub>2</sub> complex in acetonitrile (< 0.5 mM) at selected pump-probe delays after excitation at 400 nm (0.8 μJ). The ground state absorption spectrum with arbitrary scaling is included to understand the shape of the bleach absorption.

Similar to the [OC-W-L-Ru(bpy)<sub>2</sub>]<sup>+</sup> complex, excitation of the OC-W-L-Ir(ppy)<sub>2</sub> complex at  $\lambda_{\text{pump}} = 400$  nm also creates very intense time-resolved UV/vis spectra, which are shown in fig. 86.

Right after excitation positive difference absorption appears over the whole spectrum intercepted by the ground state bleach at 445 nm and below 350 nm creating ESA bands with maxima at 365 nm, 542 nm, and above 730 nm that transform with a time-constant of  $\tau_1 = 0.14$  ps losing about 40% of the intensity of the band at 542 nm, whose maximum shifts to 565 nm, while the band at 365 nm basically doesn't change. Those spectra have a lot of similarities with the excited state spectrum of iridium-phenylpyridyl-complexes like for example [Ir(ppy)<sub>2</sub>(bpy)]<sup>+</sup> (see fig. 88), which are assigned to the <sup>3</sup>MLCT state<sup>[93]</sup>. This state is typically populated via ISC from a preceding <sup>1</sup>MLCT that decays within less than 100 fs<sup>[94],[95]</sup>. Accordingly, the very first spectra can be assigned to the <sup>1</sup>MLCT state generated via charge-transfer from Ir(III) to ppy that transition to the triplet state with  $\tau_1$ .

After the initial transformation the whole spectrum decays with three more time constants  $\tau_2 = 2.75$  ps,  $\tau_3 = 8$  ps and  $\tau_4 = 28$  ps (see fig. 87). Just like the [OC-W-L-Ru(bpy)<sub>2</sub>]<sup>+</sup> complex, however, the bleach of the C-O stretching vibration in the time-resolved midIR spectra only decays after a few picoseconds. In the time-resolved UV/vis spectra the bleach is also barely changing in depth while its minimum drops below zero difference absorption. A similar explanation as for the [OC-W-L-Ru(bpy)<sub>2</sub>]<sup>+</sup> complex could be applied here: the excited state spectra are very similar to the ground state spectra and every transition creates a state with weaker absorption bands resulting in a reduction of difference absorption that is visible as a decay without repopulation of the ground state. Assumptions about the assignment of specific bands to [Ir(IV)(ppy)<sub>2</sub>]<sup>+</sup> and ppy<sup>2-</sup> according to the proposed MLCT by analogy with the analysis of [OC-W-L-Ru(bpy)<sub>2</sub>]<sup>+</sup> could be made, but the required data could not be acquired. Further information on that will be derived from the time-resolved midIR spectra.

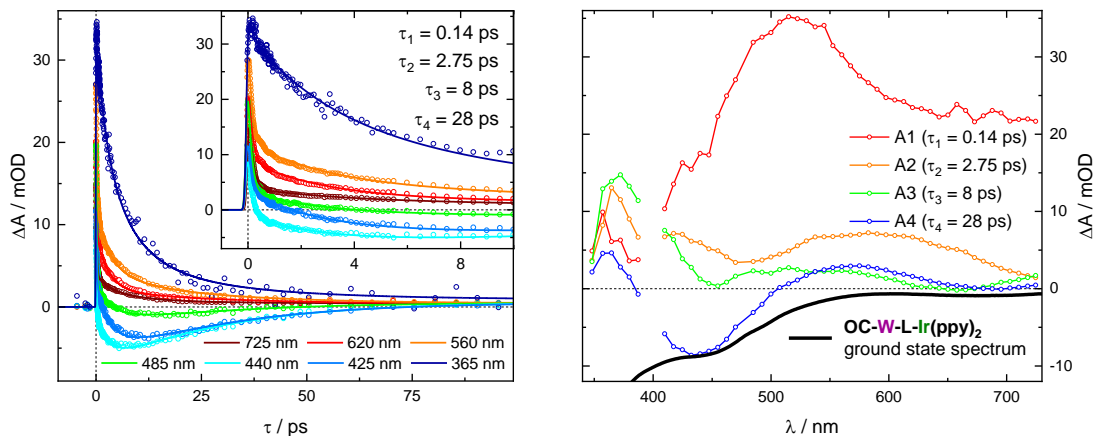


Fig. 87: transient data (circles) of the time-resolved UV/vis measurement of the OC-W-L-Ir(ppy)<sub>2</sub> complex after excitation at  $\lambda_{\text{pump}} = 400 \text{ nm}$  at the minimum of the ground state bleach at several different wavelengths and corresponding tetraexponential fits (solid lines) with fitted time constants; DAS from a global tetraexponential fit of the time-resolved UV/vis data with the same time constants (circles represent actual data, connecting lines are added for better visualization of the curves) including ground state absorption spectrum with arbitrary scaling to understand the shape of the bleach absorption.

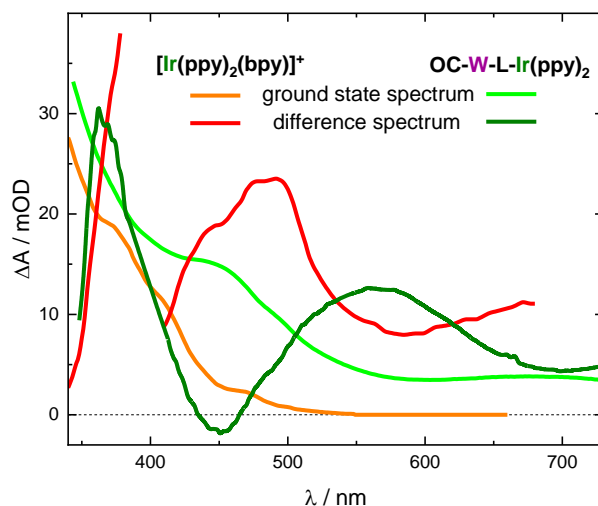


Fig. 88: comparison of the time-resolved UV/vis spectra of the OC-W-L-Ir(ppy)<sub>2</sub> in acetonitrile 430 fs after excitation at 400 nm and [Ir(ppy)<sub>2</sub>(bpy)]<sup>+</sup> in acetonitrile 500 fs after excitation at 388 nm reproduced after Tschierlei et al.<sup>[93]</sup> with corresponding ground state absorption spectra with arbitrary.

### 4.2.4.3 Time-resolved midIR spectra

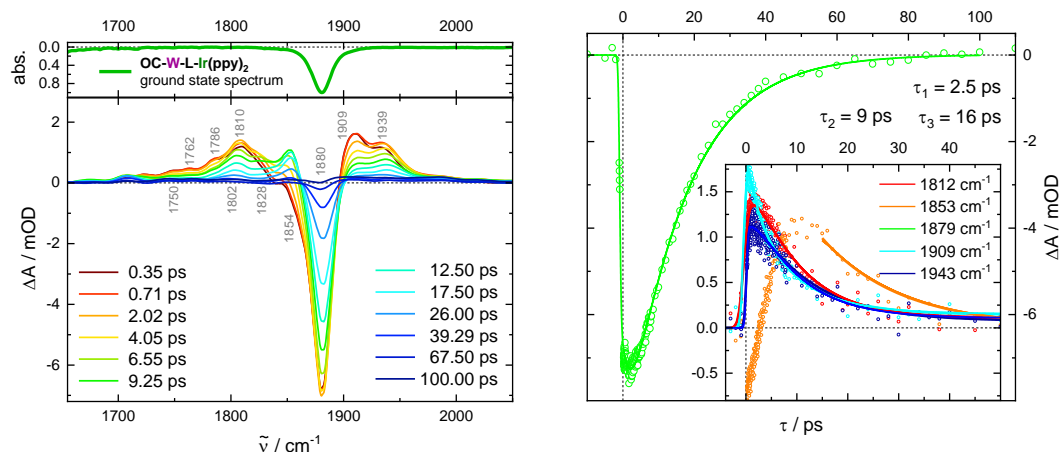


Fig. 89: normalized ground state FTIR spectrum of the OC-**W**-L-Ir(ppy)<sub>2</sub> complex at the CO stretching peak (top left); time-resolved midIR spectra in acetonitrile (< 0.5 mM) at selected pump-probe delays after excitation at 400 nm (0.7 μJ) (left bottom); transient data (circles) of the time-resolved midIR measurement of OC-**W**-L-Ir(ppy)<sub>2</sub> at the ground state bleach (right) and selected positive transient absorption peaks (inlet right) with corresponding tetraexponential fits (solid lines) and fitted time constants.

The time-resolved midIR spectra of the OC-**W**-L-Ir(ppy)<sub>2</sub> complex depicted in fig. 89 are even more similar to those of the [OC-**W**-L-Ru(bpy)<sub>2</sub>]<sup>+</sup> than the time-resolved UV/vis spectra. Upon excitation a peak at 1909 cm<sup>-1</sup> appears blue-shifted from the C-O stretching vibration bleach at 1880 cm<sup>-1</sup>. A second further blue-shifted peak at 1939 cm<sup>-1</sup> is already visible in the first spectrum at 350 fs, though similar to the corresponding peak of the [OC-**W**-L-Ru(bpy)<sub>2</sub>]<sup>+</sup> complex it can be assumed that this peak is not formed right after excitation, but grows upon the decay of the first peak since this process can be observed in the following picoseconds as well.

Different to the ruthenium-bipyridyl analogue, a third peak at 1810 cm<sup>-1</sup> red-shifted from the bleach is visible in the first spectrum that has a similar intensity at its maximum as the second peak and grows and decays with the same time constants of  $\tau_1 = 2.5$  ps,  $\tau_2 = 9$  ps. On the low-energy side two smaller peaks at 1786 cm<sup>-1</sup> and 1762 cm<sup>-1</sup> can be identified. The uniform distance between the three peaks could imply the population of higher vibrational states of an anharmonic vibration in the corresponding excited state with an anharmonicity of  $2x_0\tilde{\nu}_0 = 24$  cm<sup>-1</sup>.

During the late stages of the growth of the peaks at 1939 cm<sup>-1</sup> and 1810 cm<sup>-1</sup>, meaning as soon as the corresponding states are considerably populated, the familiar series of peaks of the anharmonic C-O stretching vibration of the ground state can be identified. Due to the high number of peaks overlapping in the area only the peaks at 1854 cm<sup>-1</sup> and 1828 cm<sup>-1</sup> can be located properly, but two further peaks at 1802 cm<sup>-1</sup> and 1750 cm<sup>-1</sup> are at least discernible. The anharmonicity of  $2x_0\tilde{\nu}_0 = 26$  cm<sup>-1</sup> derived from the peak distances is in accordance with the data from the other two complexes. The decay mechanism of these peaks presumably is the same as well, but the overlap of the peaks and the lower quality of the measurement prevent a closer analysis, which is also the reason, why the spectra were not simulated like those of the other samples. Alternatively, the decay of the bleach and the first anharmonically shifted peak were fitted to receive a rough estimation of the relaxation time of  $\tau_3 = 16$  ps.

Due to the remarkable similarity of the time-resolved midIR spectra of the OC-**W**-L-Ir(ppy)<sub>2</sub> and the [OC-**W**-L-Ru(bpy)<sub>2</sub>]<sup>+</sup> complex it is appropriate to apply the same interpretations to the peaks. Accordingly, the first peak at 1909 cm<sup>-1</sup> is assigned to an Ir(III) → ppy<sup>-</sup> <sup>3</sup>MLCT state with some electron density shifted from W(II) to the pyridyl-group of the L ligand and the second one at 1939 cm<sup>-1</sup> to a subsequent shift of the excess electron density on L to the Ir(III) core further reducing electron density from W(II) strengthening the C-O bond.

The third peak at  $1810\text{ cm}^{-1}$  must entail a weakening of the C-O bond. A side-on coordination to the iridium would be an option considering a downshift of exactly  $70\text{ cm}^{-1}$  was predicted for  $\text{Cr}(\text{CO})_6$  using DFT calculations. Alternatively, an LLCT from a ppy ligand to the alkyne ligand L is also plausible considering L was designed to imitate a ppy ligand and an LLCT was already proposed for an  $[\text{Ir}(\text{ppy})_2(\text{bpy})]^+$  complex<sup>[93]</sup>.

#### 4.2.4.4 Conclusion OC-W-L-Ir(ppy)<sub>2</sub> complex

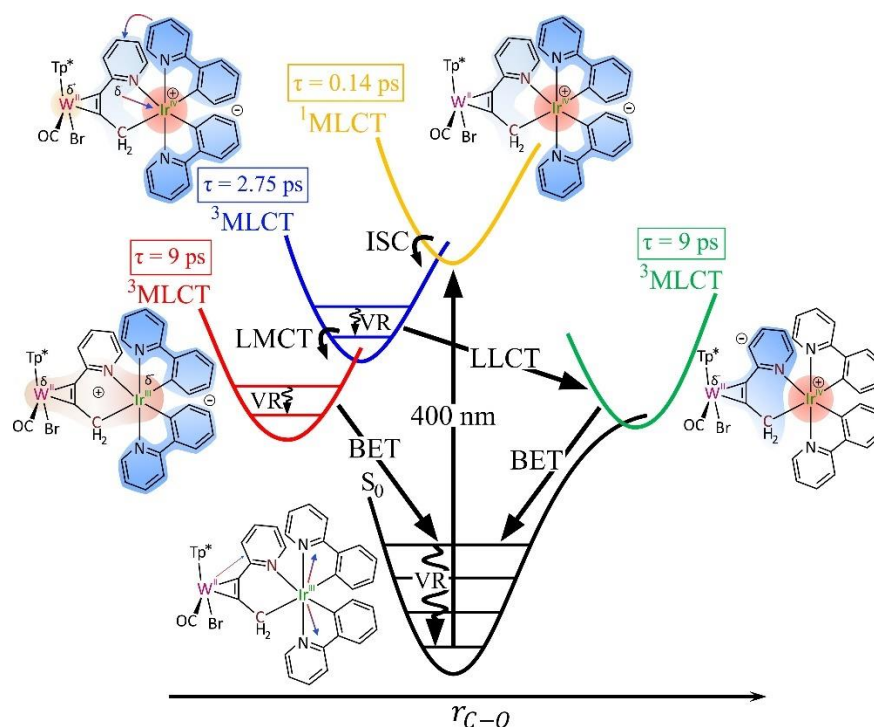


Fig. 90: Energy diagram according to the conclusions derived for the OC-W-L-Ir(ppy)<sub>2</sub> complex.

Just like the  $[\text{OC-W-L-Ru}(\text{bpy})_2]^+$  complex there was no clear evidence for an MMCT in the measurements of the OC-W-L-Ir(ppy)<sub>2</sub> complex. The time-resolved UV/vis data show a typical spectrum for an iridium phenylpyridyl complex in its <sup>3</sup>MLCT, but unlike its mononuclear homolog, it has a rather short lifetime, which indicates an additional relaxation path in the heterobinuclear complex apart from the typically observed phosphorescence. From the time-resolved midIR spectra two relaxation paths have to be considered, since the carbonyl marker indicates one state with less and one with more electron density in its antibonding  $\pi^*$ -orbital. The former is analogous to the Ru(II) analogue assigned to an LMCT from alkyne ligand L to Ir(IV), but can also be a slight shift of electron density from W(II) to Ir(IV). For the latter both an LLCT from ppy to ppy-like alkyne ligand L and a side-on coordination of the carbonyl are plausible and supported by relevant data<sup>[87],[88],[89],[93]</sup>. Relaxation to the electronic ground state leads to vibrational excitation of the anharmonic carbonyl stretching vibration.



## 5 Appendix

A1: Fitting data for the modelling of [OC-W-L-Ru(bpy)<sub>2</sub>]<sup>+</sup>

rate constants:

$$\begin{aligned}
 k_A &= k_{AB_1} + k_{AB_0} = 0.192 \text{ ps}^{-1} \approx (5.2 \text{ ps})^{-1} \\
 k_{BG} &= k_{BG_0} + k_{BG_1} + k_{BG_2} + k_{BG_3} = 0.089 \text{ ps}^{-1} \approx (11.261 \text{ ps})^{-1} \\
 k_B &= k_{BG} + k_{BP} = 0.1008 \text{ ps}^{-1} \approx (9.92 \text{ ps})^{-1} \\
 k_P &= k_{PG_0} = 0.0066 \text{ ps}^{-1} \approx (150 \text{ ps})^{-1} \\
 k_{10} &= 0.1333 \text{ ps}^{-1} \approx (7.5 \text{ ps})^{-1} \\
 k_{AB_1} &= 0.08 \text{ ps}^{-1} \approx (12.5 \text{ ps})^{-1} \\
 k_{AB_0} &= 0.112 \text{ ps}^{-1} \approx (8.93 \text{ ps})^{-1} \\
 k_{BP} &= 0.012 \text{ ps}^{-1} \approx (83.33 \text{ ps})^{-1} \\
 k_{BG_3} &= 0.0084 \text{ ps}^{-1} \approx (119 \text{ ps})^{-1} \\
 k_{BG_2} &= 0.0204 \text{ ps}^{-1} \approx (49 \text{ ps})^{-1} \\
 k_{BG_1} &= 0.03 \text{ ps}^{-1} \approx (33.33 \text{ ps})^{-1} \\
 k_{BG_0} &= 0.03 \text{ ps}^{-1} \approx (33.33 \text{ ps})^{-1}
 \end{aligned}$$

peak center:

$$\begin{aligned}
 \tilde{\nu}_{0,A} &= 1906 \text{ cm}^{-1} \\
 \tilde{\nu}_{0,B} &= 1947 \text{ cm}^{-1} \\
 \tilde{\nu}_{0,P} &= 1701 \text{ cm}^{-1} \\
 \tilde{\nu}_{0,G} &= 1885 \text{ cm}^{-1}
 \end{aligned}$$

peak width at half-height:

$$\begin{aligned}
 \Delta\tilde{\nu}_A &= 21 \text{ cm}^{-1} \\
 \Delta\tilde{\nu}_B &= 33 \text{ cm}^{-1} \\
 \Delta\tilde{\nu}_P &= 23 \text{ cm}^{-1} \\
 \Delta\tilde{\nu}_G &= 24.5 \text{ cm}^{-1}
 \end{aligned}$$

integrated cross sections rel. to S<sub>0</sub>:

$$\begin{aligned}
 \sigma_{r,A} &= 0.69 \\
 \sigma_{r,B} &= 0.65 \\
 \sigma_{r,P} &= 0.35
 \end{aligned}$$

anharmonicity constant:

$$\begin{aligned}
 2\chi_{0,A}\tilde{\nu}_{0,A} &= 22 \text{ cm}^{-1} \\
 2\chi_{0,B}\tilde{\nu}_{0,B} &= 35 \text{ cm}^{-1} \\
 2\chi_{0,G}\tilde{\nu}_{0,G} &= 26 \text{ cm}^{-1}
 \end{aligned}$$

scaling factor to match measured data:

$$c_{scale} = 1.05$$

dependence of vib. Cross section on vib. Quatum state v:

$$\sigma_{v+1,v} = (v + 1)\sigma_{10}, v = 1, 2, \dots$$

quantum yield:

$$\Phi_P = \frac{k_{BP}}{k_{BP} + k_{BG}} = 11.9\%$$

A2: Fitting data for the modelling of OC-W-L.

rate constants:

$$k_p(t) \sim I(t) = e^{-4 \ln(2) \left(\frac{t-t_0}{\Delta\tau}\right)^2} \quad t_0 = 1 \text{ ps} \quad \Delta\tau = 0.3 \text{ ps}$$

$$k_A = k_{AG_0} + k_{AG_1} + k_{AG_2} + k_{AG_3} + k_{AG_4} + k_{AG_5} + k_{AG_6} + k_{AG_7} = 2 \text{ ps}^{-1} \approx (0.5 \text{ ps})^{-1}$$

$$k_{AG_6} = 0.0 \text{ ps}^{-1}$$

$$k_{AG_5} = 0.047 \text{ ps}^{-1} \approx (21.3 \text{ ps})^{-1}$$

$$k_{AG_4} = 0.103 \text{ ps}^{-1} \approx (9.7 \text{ ps})^{-1}$$

$$k_{AG_3} = 0.23 \text{ ps}^{-1} \approx (4.35 \text{ ps})^{-1}$$

$$k_{AG_2} = 0.554 \text{ ps}^{-1} \approx (1.8 \text{ ps})^{-1}$$

$$k_{AG_1} = 1.068 \text{ ps}^{-1} \approx (0.94 \text{ ps})^{-1}$$

$$k_{AG_0} = 0.0 \text{ ps}^{-1}$$

$$k_{10} = 0.083 \text{ ps}^{-1} \approx (12 \text{ ps})^{-1}$$

integrated cross sections rel. to S<sub>0</sub>:

$$\sigma_{r,A} = 0.49$$

peak center:

$$\tilde{\nu}_{0,A} = 1925 \text{ cm}^{-1}$$

$$\tilde{\nu}_{0,G} = 1909 \text{ cm}^{-1}$$

peak width at half-height:

$$\Delta\tilde{\nu}_A = 30 \text{ cm}^{-1}$$

$$\Delta\tilde{\nu}_G = 20 \text{ cm}^{-1}$$

anharmonicity constant:

$$2\chi_{0,G}\tilde{\nu}_{0,G} = 26 \text{ cm}^{-1}$$

scaling factor to match measured data:

$$c_{scale} = 3.66$$

## 6 References

- [1] N. Bohr, *Phil. Mag.* **1913**, 6, 26, 1-25
- [2] M. Klessinger, J. Michl, *Lichtabsorption und Photochemie organischer Moleküle*, VCH Verlagsgesellschaft, Weinheim, **1989**
- [3] W. Kaim, S. Ernst, S. Kohlmann, *Chemie in unserer Zeit* **1987**, 21, 50-58
- [4] P. W. Atkins, *Physikalische Chemie*, 2. Korrigierter Nachdruck, VCH Verlagsgesellschaft mbH, Weinheim, **1990**
- [5] E. E. Nikitin, J. Troe, *Phys. Chem. Chem. Phys.* **2008**, 10, 1483-1501
- [6] G. Herzberg, *Molecular Spectra and Molecular Structure I. Spectra of Diatomic Molecules*, Second Edition, Van Nostrand Reinhold Company, Litton Educational Publishing Inc., **1950**
- [7] Beer, *Ann. Phys.* **1852**, 162, 78-88
- [8] M. J. Weber, D. Milam, W. L. Smith, *Opt. Eng.* **1978**, 17, 5, 463-469
- [9] A.-L. Calendron, H. Çankaya, G. Cirimi, F. X. Kärtner, *Opt. Express* **2015**, 23, 13866-13879
- [10] P. Herr, F. Glaser, L. A. Büldt, C. B. Larsen, O. S. Wenger, *J. Am. Chem. Soc.* **2019**, 141, 14394–14402
- [11] X. Cui, J. Zhao, Z. Mohmood, C. Zhang, *Chem. Rec.* **2016**, 16, 173–188
- [12] Y. Y. Chia, M. G. Tay, *Dalton Trans.* **2014**, 43, 13159–13168
- [13] M. Kasha, *Discuss. Faraday. Soc* **1950**, 9, 14-19
- [14] A. Walter, PhD thesis, Georg-August-university Göttingen, **2014**
- [15] J. Ahrens, PhD thesis, Georg-August-university Göttingen, **2017**
- [16] P. Hamm, A. Kaindl, J. Stenger, *Opt. Lett.* **2000**, 25, 1798–1800
- [17] R. A. Kaindl, M. Wurm, K. Reimann, P. Hamm, A. M. Weiner, M. Woerner, *J. Opt. Soc. Am. B* **2000**, 17, 2086–2094
- [18] H. W. Hahn, Master thesis, Georg-August university Göttingen, **2014**
- [19] H. Vennekate, PhD thesis, Georg-August-university Göttingen, **2014**
- [20] C. Reichardt, PhD thesis, Georg-August-university Göttingen, **2007**
- [21] P. Wagener, PhD thesis, Georg-August-university Göttingen, **2008**
- [22] <https://www.nrel.gov/pv/interactive-cell-efficiency.html>, last visited 25.06.2023, 22:19
- [23] M. Green, E. Dunlop, J. Hohl-Ebinger, M. Yoshita, N. Kopidakis, X. Hao, *Prog. Photovolt. Res. Appl.* **2021**, 29, 3–15
- [24] H. Tang, Y. Bai, H. Zhao, X. Qin, Z. Hu, C. Zhou, F. Huang, Y. Cao, *Interface Engineering for Highly Efficient Organic Solar Cells*, *Adv. Mater.* **2023**, accepted article

- [25] V. May, O. Kühn, Charge and Energy Transfer Dynamics in Molecular Systems, Wiley-VCH, Berlin, **2000**
- [26] S. Ganta, J.-H. Bortler, C. Drechsler, J. J. Holstein, D. Schwarzer, G. H. Clever, *Org. Chem. Front.* **2022**, 9, 5485-5493
- [27] V. Croue, S. Goeb, M. Salle, *Chem. Commun.* **2015**, 51, 7275-7289
- [28] K. Mahata, P. D. Frischmann, F. Würthner, *J. Am. Chem. Soc.* **2013**, 135, 15656-15661
- [29] D. M. Engelhard, S. Freye, K. Grohe, M. John, Guido H. Clever, *Angew. Chem. Int. Ed.* **2012**, 51, 4747-4750
- [30] P. L. Boulas, M. Gomez-Kaifer, L. Echegoyen, *Angew. Chem. Int. Ed.* **1998**, 37, 216-247
- [31] H.-B. Yang, K Ghosh, Y. Zhao, B. H. Northrop, M. M. Lyndon, D. C. Muddiman, H. S. White, P. J. Stang, *J. Am. Chem. Soc.* **2008**, 130, 839-841
- [32] J.-F. Ayme, J. E. Beves, C. J. Campbella, D. A. Leigh, *Chem. Soc. Rev.* **2013**, 42, 1700-1712
- [33] R. S. Forgan, J.-P. Sauvage, J. F. Stoddart, *Chem. Rev.* **2011**, 111, 5434-5464
- [34] M. Frank, J. Ahrens, I. Bejenke, M. Krick, D. Schwarzer, G. H. Clever, *J. Am. Chem. Soc.* **2016**, 138, 8279-8287
- [35] J. Ahrens, M. Frank, G. H. Clever, D. Schwarzer, *Phys. Chem. Chem. Phys.* **2017**, 19, 13596-13603
- [36] M. Frank, J. Hey, I. Balcioğlu, Y.-S. Chen, D. Stalke, T. Suenobu, S. Fukuzumi, H. Frauendorf, G. H. Clever, *Angew. Chem. Int. Ed.* **2013**, 52, 10102-10106.
- [37] W.-W. Zhang, W.-L. Mao, Y.-X. Hu, Z.-Q. Tian, Z.-L. Wang, Q.-J. Meng, *J. Phys. Chem. A* **2009**, 113, 37
- [38] J. Shirdel, A. Penzkofer, R. Procházka, Z. Shen, J. Daub, *Chem. Phys.* **2007**, 336, 1-13
- [39] S. Bay, T. Villnow, G. Ryseck, V. Rai-Constapel, P. Gilch, T. J. J. Müller, *Chem. Plus. Chem.* **2013**, 78, 137-141
- [40] Y. Iida, *Bull. Chem. Soc. Jpn.* **1971**, 44, 3, 663-667
- [41] J. Liu, L. Li, R. Xu, K. Zhang, M. Ouyang, W. Li, X. Lv, C. Zhang, *ACS Appl. Polym. Mater.* **2019**, 1, 1081-1087
- [42] J. Tessarolo, H. Lee, E. Sakuda, K. Umakoshi, G. H. Clever, *J. Am. Chem. Soc.* **2021**, 143, 6339-6344
- [43] C. S. Krämer, T. J. J. Müller, *Eur. J. Org. Chem.* **2003**, 3534-3548
- [44] M. Sailer, M. Nonnenmacher, T. Oeser, T. J. J. Müller, *Eur. J. Org. Chem.* **2006**, 423-435.
- [45] T. M. P. Gerbich, PhD. Thesis, Julius-Maximilians university Würzburg, **2015**
- [46] A. Kuboyama, *Spec. Bull. Chem. Soc. Jpn.* **1964**, 37, 1540.1544
- [47] S. Arathi Rani, J. Sobhanadri, T. A. Prasada Rao, *Spectrochim. Acta A* **1995**, 51, 2473-2479
- [48] S. Dufresne, L. Callaghan, W. G. Skene, *J. Phys. Chem. B* **2009**, 113, 15541-15549

- [49] L. A. Estrada, J. E. Yarnell, D. C. Neckers, *J. Phys. Chem. A* **2011**, 115, 6366-6375
- [50] N. A. Kukhta, D. A. da Silva Filho, D. Volyniuk, J. V. Grazulevicius, G. Sini, *Chem. Mater.* **2017**, 29, 1695-1707
- [51] T. Kobayashi, S. Nagakura, *Chem. Phys. Lett.* **1976**, 43, 3, 429-434
- [52] H. Kuroda, T. L. Kunii, *Theoret. Chim. Acta (Berl.)* **1967**, 9, 51-56
- [53] T. Gerbich, J. Herterich, J. Köhler, I. Fischer, *J. Phys. Chem. A* **2014**, 118, 1397-1402
- [54] C.-W. Chang, T. I. Sølling, Eric W.-G. Diau, *Chem. Phys. Lett.* **2017**, 686, 218-222
- [55] A. Behrendt, S. M. Couchman, J. C. Jeffery, J. A. McCleverty, M. D. Ward, *J. Chem. Soc. Dalton. Trans.* **1999**, 4349-4355
- [56] D. H. Eargle jun., *J. Chem. Soc. B* **1970**, 1556-1560
- [57] Y. Fukui, K. Ohta, K. Tominaga, *Faraday Discuss.* **2015**, 177, 65-75
- [58] P. Gayathri, M. Pannipara, A. G. Al-Sehemi, S. P. Anthony, *New J. Chem.* **2020**, 44, 8680-8696
- [59] S. Amthor, B. Noller, C. Lambert, *Chem. Phys.* **2005**, 316, 141-152
- [60] A. Heckmann, Dümmler, J. Pauli, M. Margraf, J. Köhler, D. Stich, C. Lambert, I. Fischer, U. Resch-Genger, *J. Phys. Chem. C* **2009**, 113, 20958-20966
- [61] K. D. Belfield, K. J. Schafer, W. Mourad, B. A. Reinhardt, *J. Org. Chem.* **2000**, 65, 15, 4475-4481
- [62] K.D. Belfield, M.V. Bondar, O.V. Przhonska, K.J. Schafer, W. Mourad, *J. Lumin.* **2002**, 97, 141-146
- [63] L. Yang, J.-K. Feng, Y. Liao, A.-M. Ren, *Opt. Mater.* **2007**, 29, 642-650
- [64] S. Dümmler, W. Roth, I. Fischer, A. Heckmann, C. Lambert, *Chem. Phys. Lett.* **2005**, 408, 264-268
- [65] J. Köhler, T. Quast, J. Buback, I. Fischer, T. Brixner, P. Nuernberger, B. Geiß, J. Mager, C. Lambert, *Phys. Chem. Chem. Phys.* **2012**, 14, 11081-11089
- [66] M. Holzapfel, C. Lambert, *J. Phys. Chem. C* **2008**, 112, 1227-1243
- [67] Y. Tamai, H. Ohkita, H. Benten, S. Ito, *Chem. Mater.* **2014**, 26, 2733-2742
- [68] M. U. Munshi, G. Berden, J. Martens, J. Oomens, *Phys. Chem. Chem. Phys.* **2017**, 19, 19881-19889
- [69] R. S. K. A. Gamage, A. J. McQuillan, B. M. Peake, *J. Chem. Soc. Faraday Trans.* **1991**, 87, 22, 3653-3660
- [70] A. Bedini, E. De Laurentiis, B. Sur, V. Maurino, C. Minero, M. Brigante, G. Mailhot, D. Vione, *Photochem. Photobiol. Sci.* **2012**, 11, 1445-1453
- [71] G. Buntinx, R. Naskrecki, C. Didierjean, *J. Phys. Chem. A* **1997**, 101, 47, 8768-8777
- [72] A. Cannizzo, F. van Mourik, W. Gawelda, G. Zgrablic, C. Bressler, M. Chergui, *Angew. Chem. Int. Ed.* **2006**, 45, 3174-3176

- [73] M. Hüttenschmidt, H. Lange, M. A. A. Cordero, A. Villinger, S. Lochbrunner, W. W. Seidel, *Dalton Trans.* **2022**, 51, 852-856
- [74] M. J. Dewar, *S. Bull. Soc. Chim. Fr.* **1951**, 18, 3-4, C71-C79
- [75] J. Chatt, L. A. Duncanson, *J. Chem. Soc.* **1953**, 3, 2939–2942
- [76] H. Haas; R. K. Sheline, *J. Chem. Phys.* 1967, 47, 2996–3021
- [77] E.J. Heilweil, R.R. Cavanagh, J.C. Stephenson, *Chem. Phys. Lett.* **1987**, 134, 2, 181-188
- [78] O. Golonzka, M. Khalil, N. Demirdöven, A. Tokmakoff, *J. Chem. Phys.* **2001**, 115, 10814–10828
- [79] M. Krejčík , A. A. Vlček, *J. Electroanal. Chem.* **1991**, 313, 243-257
- [80] P. Dongare, B. D. B. Myron, L. Wang, D. W. Thompson, T. J. Meyer, *Coord. Chem. Rev.* **2017**, 345, 86-107
- [81] S. Záliš, C. Consani, A. El Nahhas, A. Cannizzo, M. Chergui, F. Hartl, A. Vlček Jr., *Inorg. Chim. Acta* **2011**, 374, 578–585
- [82] A. Yoshimura, M. Z. Hoffman, H. Sun, *J. Photochem. Photobiol. A: Chem.* **1993**, 70, 29-33
- [83] K. Kalyanasundaram, *Coord. Chem. Rev.* **1982**, 46, 159-244
- [84] C. Bhasikuttan, M. Suzuki, S. Nakashima, T. Okada, *J. Am. Chem. Soc.* **2002**, 124, 8398-8405
- [85] N. H. Damrauer, G. Cerullo, A. Yeh, T. R. Boussie, C. V. Shank, J. K. McCusker, *Science* **1997**, 275, 5296, 54-57
- [86] K. M. Omberg, J. R. Schoonover, J. A. Treadway, R. M. Leasure, R. B. Dyer, T. J. Meyer, *J. Am. Chem. Soc.* **1997**, 119, 7013-7018
- [87] E. P. Kuendig, G. A. Ozin, *J. Am. Chem. Soc.* **1974**, 96, 12, 3820–3823
- [88] Q. Zhang, H. Kuwabara, W. J. Potscavage Jr., S. Huang, Y. Hatae, T. Shibata, C. Adachi, *J. Am. Chem. Soc.* **2014**, 136, 18070–18081
- [89] R. Feng, E. D. Glendening, K. A. Peterson, *Inorg. Chem.* 2020, 59, 4753-4763
- [90] <https://spectrabase.com/spectrum/4LKiDq4cFnF>, last visited 29.06.2023, 11:54
- [91] T. Hofbeck, H. Yersin, *Inorg. Chem.* **2010**, 49, 9290–9299
- [92] H. Brahim, C. Daniel, *Comput. Theor. Chem.* **2014**, 1040–1041, 219–229
- [93] S. Tschierlei, A. Neubauer, N. Rockstroh, M. Karnahl, P. Schwarzbach, H. Junge, M. Beller, S. Lochbrunner, *Phys. Chem. Chem. Phys.* **2016**, 18, 10682-10687
- [94] G. J. Hedley, A. Ruseckas, I. D. W. Samuel, *J. Phys. Chem. A* **2009**, 113, 1, 2-4
- [95] K.-C. Tang, K. L. Liu, I-C. Chen, *Chem. Phys. Lett.* **2004**, 386, 437–441

## 7 Acknowledgements

I went to hell and back while working on this thesis. Sometimes it was fun, sometimes frustrating, sometimes I learned a lot and other times I was completely overwhelmed. That is why I'm especially eager to thank those people, who I wouldn't have been able to get through with it without.

First and foremost, I want to thank Prof. Dr. Dirk Schwarzer for supervising and mentoring me during this thesis, teaching me a lot about the theoretical and technical intricacies of laser techniques, molecular spectroscopy and connected fields and having a lot of interesting, in-depth discussions and at the same time a practically infinite amount of patience and understanding. Those parts of the work were the most valuable as they not only pushed me forward quite a lot, but also motivated me like nothing else through the frustrating parts. Without him this thesis would not have been possible and I'm really grateful for that.

Secondly, I want to thank Prof. Dr. Sven Schneider, not just for being part of my thesis committee and examination board and doing the second review of this thesis, but for introducing me to the inorganic section of my work, providing me with the first projects I worked on and my first discussions in a cooperative project. Those experience opened up my perception of how cooperations can and should work and how the inorganic chemist's point of view can differ from that of the physical chemist. Also, I want to thank him for supporting my frequent asking for extensions and in general for taking so long with this thesis.

Then I want to thank Prof. Dr. Inke Siewert for being part of my thesis committee and examination board, supporting all of my extension requests with the same patience, but also for the project that produces my first paper. This was a long overdue milestone in my career and connected to my first discussion where I had the feeling to talk at eye level with an experienced scientist. I really appreciated that.

Concerning the first project group regarding the cage complexes, I want to thank Prof. Dr. Guido Clever for the cooperation on these projects and Dr. Jacopo Tassarolo, Dr. Kai Wu and Dr. Sudhakar Ganta for providing the samples, measuring the ground state spectra and performing the theoretical calculation and especially Jacopo and Kai for personally visiting Göttingen to deliver the samples and discuss the results.

Regarding the binuclear W(II)-Ru(II)/Ir(III) complexes I want to thank Prof. Dr. Wolfram Seidel, who pitched us this unexpectedly interesting project at a time I wasn't even sure if I have sufficient material for a PhD thesis (after already 4 years of work!), and Dr. Mareike Hüttenschmidt, who created the samples and provided a lot of reliable data on them. I very much appreciate having this project in my thesis.

A special thanks goes to my predecessor Dr. Jennifer Zimara, former Ahrens, who introduced me to the laser systems and helped me with my first measurement. I also want to thank Dr. Hendrik Vennekate, who created the program used for the time-resolved midIR data processing and took some time to modify it for my purposes.

An equally special thanks goes to Reinhard Bürsing, Birgit Freyberg, especially Tim Diedrichs, who gave a lot of technical support even at busy hours and went out of their way to help with any difficulties. Especially Tim was an invaluable help during my thesis work both technically and mentally. His drive and enthusiasm every now and then rubbed off on me and helped me regain motivation.

Overall, I want to thank the members of the Wodtke group, who I frequently ran into and had a lot of off-work-topic conversations. I want to especially highlight Daniel (Danny) Crowley, Dr. Sascha Kandratsenka, Dr. Sven Kaufmann, Anna-Maria Schönemann, Dr. Nils Hertl, Dr. Jan Altschäffel, Dr. Kim Papendorf and Inge Dreger from the MPINAT and Dr. Tim Schäfer, Arved Dorst and Dr. Georg Westphal from the IPC. In this context I also want to thank Prof. Dr. Alec Wodtke for having me in his group and organizing quite enjoyable retreats and other group events.

I also want to thank those people, who supported me outside of my professional context during the thesis. At first, I want to thank Jessica Landgraf and Sven Herbers for their emotional support as the closest people to me in my life. Then I want to thank my parents Manfred and Sonja Borter, who supported me emotionally and financially during my darkest hours, and my siblings Marc, Tamara and Tim, who had a lot of patience with me and sometimes helped me to get out of my head.

Finally, I want to thank the Deutsche Forschungsgesellschaft (DFG) for the financial support through the Sonderforschungsbereich (SFB) and collaborative research centre (CRC) 1073.

In the end only one is left: I thank my fluffy ninja kitty Milly. I miss you!



## 8 Curriculum vitae

1997 – 2009	High school Isernhagen
2010 – 2014	Bachelor of Science chemistry, Leibniz university Hannover, “Rotationsspektrum von Oxacycloheptan”
2013 – 2017	Master of Science material and nano science, Leibniz university Hannover, „Femtosekundenspektroskopie an gelösten Elektronen in unpolaren Fluiden“
2019 – 2021	Correspondence course laser technology
2017 – 2023	PhD, Georg-August university Göttingen,  “Femtosecond spectroscopy of charge-transfer dynamics in self- assembled Pd(II) based donor-acceptor/host-guest cages and heterobinuclear alkyne-bridged W(II)-Ru(II) and W(II)-Ir(III) complexes”

## 9 Publications

L. A. Paul, N. C. Röttcher, J. Zimara, J.-H. Borter, J.-P. Du, D. Schwarzer, R. A. Mata, I. Siewert; Photochemical Properties of  $\text{Re}(\text{CO})_3$  Complexes with and without a Local Proton Source and Implications for  $\text{CO}_2$  Reduction Catalysis; *Organometallics* 2020, 39, 2405–2414

B. Schluschaß, J.-H. Borter, S. Rupp, S. Demeshko, C. Herwig, C. Limberg, N. A. Maciulis, J. Schneider, C. Würtele, V. Krewald, D. Schwarzer, S. Schneider; Cyanate Formation via Photolytic Splitting of Dinitrogen; *JACS Au* 2021, 1, 879–894

S. Ganta, J.-H. Borter, C. Drechsler, J. J. Holstein, D. Schwarzer, G. H. Clever; Photoinduced host-to-guest electron transfer in a self-assembled coordination cage; *Org. Chem. Front.* 2022, 9, 5485–5493

M. Oelschlegel, S.-A. Hua, L. Schmid, P. Marquetand, A. Bäck, J.-H. Borter, J. Lücken, S. Dechert, O. S. Wenger, I. Siewert, D. Schwarzer, L. González, F. Meyer; Luminescent Iridium Complexes with a Sulfurated Bipyridine Ligand: PCET Thermochemistry of the Disulfide Unit and Photophysical Properties; *Inorg. Chem.* 2022, 61, 35, 13944–13955